

**NEW DYNAMIC SUBGRID-SCALE MODELLING APPROACHES
FOR LARGE EDDY SIMULATION AND RESOLVED STATISTICAL
GEOMETRY OF WALL-BOUNDED TURBULENT SHEAR FLOW**

A Thesis Submitted to
the College of Graduate Studies and Research
in Partial Fulfillment of the Requirements
for the Degree of Doctor of Philosophy
in the Department of Mechanical Engineering
University of Saskatchewan
Saskatoon, Saskatchewan

by

BingChen Wang

Permission to Use

In presenting this thesis in partial fulfillment of the requirements for a Post-graduate degree from the University of Saskatchewan, I agree that the Libraries of this University may make it freely available for inspection. I further agree that permission for copying of this thesis in any manner, in whole or in part, for scholarly purposes may be granted by the professor or professors who supervised my thesis work or, in their absence, by the Head of the Department or the Dean of the College in which my thesis work was done. It is understood that any copying or publication or use of this thesis or parts thereof for financial gain shall not be allowed without my written permission. It is also understood that due recognition shall be given to me and to the University of Saskatchewan in any scholarly use which may be made of any material in my thesis.

Requests for permission to copy or to make other use of material in this thesis in whole or part should be addressed to:

Head of the Department of Mechanical Engineering
University of Saskatchewan
Saskatoon, Saskatchewan, Canada
S7N 5A9

Abstract

This dissertation consists of two parts, i.e. dynamic approaches for subgrid-scale (SGS) stress modelling for large eddy simulation and advanced assessment of the resolved scale motions related to turbulence geometrical statistics and topologies. The numerical simulations are based on turbulent Couette flow.

The first part of the dissertation presents four contributions to the development of dynamic SGS models. The conventional integral type dynamic localization SGS model is in the form of a Fredholm integral equation of the second kind. This model is mathematically consistent, but demanding in computational cost. An efficient solution scheme has been developed to solve the integral system for turbulence with homogeneous dimensions. Current approaches to the dynamic two-parameter mixed model (DMM2) are mathematically inconsistent. As a second contribution, the DMM2 has been optimized and a modelling system of two integral equations has been rigorously obtained. The third contribution relates to the development of a novel dynamic localization procedure for the Smagorinsky model using the functional variational method. A sufficient and necessary condition for localization is obtained and a Picard's integral equation for the model coefficient is deduced. Finally, a new dynamic nonlinear SGS stress model (DNM) based on Speziale's quadratic constitutive relation [J. Fluid Mech., **178**, p.459, 1987] is proposed. The DNM allows for a nonlinear anisotropic representation of the SGS stress, and exhibits a significant local stability and flexibility in self-calibration.

In the second part, the invariant properties of the resolved velocity gradient tensor are studied using recently developed methodologies, i.e. turbulence geometrical statistics and topology. The study is *a posteriori* based on the proposed DNM, which is different than most of the current *a priori* approaches based on experimental or DNS databases. The performance of the DNM is further validated in terms of its capability of simulating advanced geometrical and topological features of resolved scale motions. Phenomenological results include, e.g. the positively skewed resolved

enstrophy generation, the alignment between the vorticity and vortex stretching vectors, and the pear-shape joint probability function contour in the tensorial invariant phase plane. The wall anisotropic effect on these results is also examined.

Acknowledgements

I would like to express my profound appreciation to my supervisor, Professor Donald J. Bergstrom, for his guidance in the area of fluids science, encouragement on creative thinking, teaching in English, and help when I was in need both in academic and non-academic areas. I would also like to express my appreciation to his wife Mrs. Naomi Bergstrom and the rest of the family for their warm invitations to their home and genuine friendship.

I sincerely thank Professor James D. Bugg for his teaching in experimental fluid mechanics, and generous help and advice when I was in shock for the first time teaching Canadian undergraduate students as an independent lecturer. I would also like to thank the other advisory committee members, Professors David Sumner and Malcolm Reeves for their valuable academic advice.

My sincere thanks to Professors Robert W. Besant, Glen Watson, Allan T. Dolovich, Kamiel S. Gabriel, Madan M. Gupta, and Arnold E. Krause for their sound instruction in graduate classes, help in English, and professional representation of the Canadian educational system.

I enjoyed the experience of working as a teaching assistant to Professors P. Barry Hertz, Richard T. Burton and Trever G. Crowe, and also as a laboratory demonstrator in cooperation with Mr. David M. Deutscher. I appreciate their help and generosity in passing valuable knowledge and experience to me. I would also like to thank Mr. Ian Macphedran and his colleagues at the Engineering Computer Centre for their assistance in using the computer facilities.

I would like to thank the Department of Mechanical Engineering for providing me a sound research environment. Special thanks to the previous secretary Mrs. Iptisam Alexanders (Halim) who offered a generous help when I first applied for my Ph.D. program and after I settled down in Saskatoon. I would like to thank the university graduate student association and various university committees that I have served on, for providing me an opportunity to understand the Canadian culture and

operation of the university system.

I am grateful to my friend and mathematical teacher, Dr. Fang-Xiang Wu, for his enlightening guidance in mathematics and valuable critiques on the mathematical-physical approaches of my research work related to this dissertation. My special thanks to my dear friends and elders, Peter and Arlene Block, for their teaching, love and exemplary strength for seeking the truth. I would like to acknowledge the help and fellowship from other graduate students. I am deeply grateful to all the friends I have made in Saskatoon for bringing me so many joyful moments.

Funding for this research, provided as a scholarship from the University of Saskatchewan and research stipend from my supervisor's NSERC grant, is gratefully acknowledged.

I would take this opportunity to thank all my previous and current teachers throughout my entire student career for their teaching and enlightening.

Consistent and unconditional support, encouragement and love from all my family, especially from my paternal grandmother who is still so memorably kind, is necessary for anything that is potentially glimmering in this dissertation.

Dedicated to my loving parents

献给父母大人

Table of Contents

Permission to Use	i
Abstract	ii
Acknowledgements	iv
Dedication	vi
Table of Contents	vii
List of Tables	xiii
List of Figures	xiv
Nomenclature	xx
1 Introduction	1
1.1 Motivation	1
1.2 Method of Large Eddy Simulation and the SGS Stress Decomposition	4
1.3 Conventional SGS Modelling Approaches	5
1.3.1 Scale Similarity Model	6
1.3.2 Dynamic SGS Viscosity Model	7
1.3.3 Integral Type Localization Approach	11

1.4	Linear Boussinesq Constitutive Relation and Its Limitations	12
1.5	An Improved Criterion for SGS Models	13
1.6	Outline of the Dissertation	15
2	Numerical Algorithm and Test Problem	18
2.1	Algorithm for the Numerical Calculation	18
2.2	Discrete Filters	22
2.3	Test Problem	23
3	An Efficient Solution Scheme for Applying the Integral Type Dynamic Localization Subgrid-Scale Model in Turbulence with Homogeneous Directions	26
3.1	Introduction	26
3.2	A Direct Solution Scheme for the ILDM	27
3.3	Results of Numerical Simulations	31
3.4	Conclusions	41
4	An Integral Type Localization Dynamic Two-Parameter Subgrid-Scale Model: Formulation and Simulation	42
4.1	Introduction	42
4.2	Mixed Models	44
4.2.1	Bardina's Mixed Model	44
4.2.2	The C_L - C_S Type Mixed Models	45
4.3	A New Integral Type Localization DMM2	48
4.3.1	Model Development	48
4.3.2	An Iterative Solver	51
4.4	Results of Numerical Simulations	53

4.4.1	Predicted Features of Turbulent Couette Flow	53
4.4.2	SGS Kinetic Energy Production and Backscatter	58
4.5	Conclusions	61
5	Consistent Localization and the Constitutive Relation of the Dynamic Smagorinsky Subgrid-Scale Stress Model	62
5.1	Introduction	62
5.2	A Sufficient and Necessary Condition for the Localization Dynamic Smagorinsky Model	63
5.2.1	A Necessary Condition for Localization	65
5.2.2	Proof of Sufficiency	68
5.2.3	Theoretical Application of the OC	70
5.2.3.1	Restriction to Constant Distribution of $C_S^N(\mathbf{x}, \mathbf{x}_0)$. .	72
5.2.3.2	Restriction to Identical Distribution of $C_S^N(\mathbf{x}, \mathbf{x}_0)$. .	74
5.3	Results of Numerical Simulations	75
5.3.1	An Efficient Solver for the Picard's Integral Equation	76
5.3.2	Basic Flow Features and Discussion	78
5.3.3	Rate of SGS TKE Production, Modulus of Filtered Strain Rate Tensor, Model Coefficient and SGS Viscosity	83
5.4	Conclusions	89
6	A Novel Dynamic Nonlinear Subgrid Scale Stress Model	93
6.1	Introduction	93
6.2	A New Dynamic Nonlinear Model	96
6.3	Analysis of Numerical Results	99
6.3.1	Basic Features of the Flow	100

6.3.2	Numerical Stability of the Model	103
6.3.3	Model Coefficients	106
6.4	Geometrical Characteristics of the DNM	108
6.4.1	Conventions on the Tensorial Eigensystem	109
6.4.2	Tensorial Alignment Feature of the DNM in Contrast to the Linear Smagorinsky Type Models	110
6.5	Properties of the Eigensystem	118
6.5.1	An Eigensystem Identity	118
6.5.2	Mapping Characteristics of the Eigensystem Identity	120
6.5.3	Situation of Multiple Roots	124
6.6	Characteristics of the SGS TKE Production Rate	125
6.6.1	Backscatter	125
6.6.2	Rate of SGS TKE Production Due to the 2nd and 3rd Nonlinear Constituent Terms	129
6.7	Conclusions	132
7	Turbulence Geometrical Statistics	135
7.1	Introduction	135
7.2	Basic Concepts Related to the Velocity Gradient Tensor	136
7.3	Several Classical Topics in Turbulence Geometrical Statistics	140
7.3.1	Geometrical Alignments	140
7.3.2	Relative Principal Values	141
7.4	Numerical Results on Geometrical Alignments	144
7.4.1	Results on Helicity	144
7.4.2	Results on Alignment between Vorticity and Eigenvectors	145

7.4.3	Results on Enstrophy and Enstrophy Generation	154
7.5	Numerical Results on the Relative Principal Values	159
7.6	Conclusions	166
8	Tensorial Invariants and Turbulence Topology	170
8.1	Introduction	170
8.2	Basic Concepts Related to Tensorial Invariants and Flow Topologies	171
8.3	Numerical Results on Turbulence Topologies	175
8.3.1	Flow Topologies Related to Invariants of the Resolved Velocity Gradient Tensor	175
8.3.2	Flow Topologies Related to the Invariants of the Resolved Strain Rate Tensor	180
8.3.3	Statistical Expectations of Resolved Quantities and Flow Topol- ogy	185
8.3.3.1	Characteristics of the Expectation of Resolved Enstro- phy	186
8.3.3.2	Characteristics of the Expectation of Resolved Enstro- phy Generation	192
8.3.3.3	Characteristics of the Expectation of Resolved SGS TKE Production Rate	197
8.4	Conclusions	200
9	Conclusions and Future Work	205
9.1	Review of Major Contributions	205
9.2	Comments on Future Studies	213
	References	216

Appendix	237
A Formulations and Singularity Condition for the DNM	238
B Orthogonal and Rotation Matrices	242
B.1 Similar and Orthogonal Transformations	242
B.2 Rotation Matrix	243
C Transport Equations for the Moments of the Strain Rate Tensor and Vorticity Vector	245

List of Tables

3.1	Comparison of the computational cost	31
5.1	Absolute and relative computational cost ($Re = 2600$)	78
5.2	Near-wall cubic behavior of the resolved Reynolds shear stress ($Re = 1500$).	82
6.1	Absolute and relative computational cost ($Re = 2600$)	99
6.2	Averaged tensorial alignment between \bar{S}_{ij} and the 2nd and 3rd nonlinear terms ($Re = 2600$, 66^3 nodes).	114
6.3	Averaged tensorial alignment between $-\tau_{ij}$ and the nonlinear terms ($Re = 2600$, 66^3 nodes).	117
6.4	Instantaneous tensorial eigensystem for the 1st and 3rd nonlinear terms ($Re = 2600$).	121
6.5	Mapping scenarios for the tensorial eigensystems between \mathbf{S} and $\mathbf{\Gamma}$ (Distinct eigen-roots)	122

List of Figures

2.1	Sketch of the collocated grid system in the x_1 – x_2 plane.	20
3.1	Averaged distribution of C_S in the wall-normal direction.	32
3.2	Averaged SGS viscosity distribution in the wall-normal direction. . .	32
3.3	Averaged non-dimensional velocity profile ($Re = 2600$).	33
3.4	Averaged velocity profile using wall coordinates ($Re = 2600$).	34
3.5	Averaged velocity profile using wall coordinates ($Re = 4762$).	34
3.6	Resolved streamwise turbulence intensities ($Re = 2600$).	35
3.7	Resolved streamwise turbulence intensities ($Re = 4762$).	35
3.8	Resolved Reynolds shear stress distribution ($Re = 2600$).	36
3.9	Resolved Reynolds shear stress distribution ($Re = 4762$).	36
3.10	Averaged rate of SGS TKE production.	39
3.11	Averaged rate of the resolved TKE dissipation.	39
3.12	Ratio of the rate of SGS TKE production to the rate of resolved viscous dissipation.	40
3.13	Instantaneous contours of the spanwise vorticity $\bar{\omega}_3$ ($Re = 2600$). . . .	40
4.1	Convergence performance of the solver ($Re = 2600$).	53
4.2	Dimensionless mean velocity profile ($Re = 2600$).	53
4.3	Mean velocity profile using wall coordinates ($Re = 2600$).	54
4.4	Averaged resolved turbulence intensities ($Re = 2600$).	54

4.5	Averaged resolved Reynolds shear stress distribution ($Re = 2600$). . .	55
4.6	Comparison of the friction coefficient.	55
4.7	Averaged distribution of C_L in the wall-normal direction ($Re = 2600$). .	56
4.8	Averaged distribution of C_S in the wall-normal direction ($Re = 2600$). .	56
4.9	Instantaneous velocity field in the central x_1 - x_2 plane ($Re = 2600$). . .	57
4.10	Instantaneous velocity and vorticity fields in the central x_2 - x_3 plane ($Re = 2600$).	57
4.11	Averaged SGS TKE production rate ($Re = 2600$).	59
4.12	Instantaneous \mathcal{P}_r distribution with maximal peaks ($Re = 2600$; Rela- tive location in the homogeneous plane: $x_1/L_1 = 0.728$, $x_3/L_3 = 0.880$). .	59
4.13	Instantaneous \mathcal{P}_r distribution with moderate peaks ($Re = 2600$; Rela- tive location in the homogeneous plane: $x_1/L_1 = 0.989$, $x_3/L_3 = 0.663$). .	60
4.14	Averaged viscous dissipation of the filtered motions ($Re = 2600$). . . .	60
5.1	Mean non-dimensional velocity profile (66^3 nodes).	79
5.2	Mean velocity profile in wall coordinates (66^3 nodes).	79
5.3	Averaged wall-normal distribution of resolved turbulence intensities (66^3 nodes).	80
5.4	Averaged wall-normal profile of resolved Reynolds shear stress (66^3 nodes).	81
5.5	Variation of the skin-friction coefficient C_f with Reynolds number (66^3 nodes).	81
5.6	Averaged rate of SGS TKE production in the wall-normal direction (66^3 nodes).	84
5.7	Grid effect on the rate of SGS TKE production ($Re = 2600$).	84
5.8	Resolved viscous dissipation in the wall-normal direction (66^3 nodes). .	86

5.9	Resolved viscous dissipation rate in the core region (66^3 nodes).	86
5.10	Mean distribution of the model coefficient in the wall-normal direction (66^3 nodes).	87
5.11	Grid effect on model coefficient ($Re = 2600$).	87
5.12	Mean SGS viscosity profile in the wall-normal direction (66^3 nodes).	88
5.13	Grid effect on SGS viscosity ($Re = 2600$).	88
6.1	Mean velocity profile using wall coordinates.	101
6.2	Mean velocity profile using wall coordinates ($Re = 4762$).	101
6.3	Resolved streamwise turbulence intensities ($Re = 2600$).	102
6.4	Resolved streamwise turbulence intensities ($Re = 4762$).	102
6.5	Budget of shear stresses ($Re = 2600$). VIS: viscous shear stress $\nu\langle\bar{u}_{1,2}\rangle/u_\tau^2$, SGS: subgrid shear stress $-\langle\tau_{12}\rangle/u_\tau^2$, RRS: resolved Reynolds shear stress, $-\langle\bar{u}_1''\bar{u}_2\rangle/u_\tau^2$, TOT: total shear stress.	103
6.6	Resolved Reynolds shear stress distribution.	103
6.7	Averaged condition number $\text{cond}(\mathbf{A})$ along the wall-normal direction (66^3 nodes).	105
6.8	Distribution of model coefficients in the wall-normal direction.	107
6.9	Sensitivity of the model coefficients to the grid size ($Re = 2600$).	107
6.10	Instantaneous wall-normal distribution of the coefficients at central location: $x_1/L_1 = x_2/L_2 = 0.49$ ($Re = 2600$, 48^3 nodes).	107
6.11	Averaged angles between the eigenvectors of the filtered strain rate tensor and second constituent term ($\bar{S}_{ij}, \gamma_{ij}$) for the case of 66^3 nodes.	113
6.12	Averaged angles between the eigenvectors of the filtered strain rate tensor and third constituent term (\bar{S}_{ij}, η_{ij}) for the case of 66^3 nodes.	113

6.13	Averaged angles between the eigenvectors of the negative SGS stress and first constituent term $(-\tau_{ij}, \beta_{ij})$ or $(-\tau_{ij}, \bar{S}_{ij})$ for the case of 66^3 nodes.	115
6.14	Averaged angles between the eigenvectors of the negative SGS stress and second constituent term $(-\tau_{ij}, \gamma_{ij})$ for the case of 66^3 nodes. . . .	115
6.15	Averaged angles between the eigenvectors of the negative SGS stress and third constituent term $(-\tau_{ij}, \eta_{ij})$ for the case of 66^3 nodes. . . .	116
6.16	Scenarios for the mapping relation of the eigensystem identity.	120
6.17	Mean profile of the non-dimensional SGS TKE production rate predicted using the DNM (66^3 nodes).	126
6.18	Instantaneous distribution of the non-dimensional SGS TKE production rate ($Re = 2600$, 66^3 nodes; relative location in the homogeneous plane: $x_1/L_1 = 0.570$ and $x_3/L_3 = 0.367$ for (a), $x_1/L_1 = 0.602$ and $x_3/L_3 = 0.461$ for (b)).	127
6.19	Instantaneous distribution of the non-dimensional SGS TKE production rate ($Re = 4762$, 66^3 nodes; relative location in the homogeneous plane: $x_1/L_1 = 0.383$ and $x_3/L_3 = 0.477$ for (a), $x_1/L_1 = 0.289$ and $x_3/L_3 = 0.180$ for (b)).	128
7.1	Time-averaged PF of resolved relative helicity density $\bar{h}_n = \cos(\bar{\mathbf{u}}, \bar{\boldsymbol{\omega}})$ ($Re = 2600$).	145
7.2	Averaged angle between the vorticity vector and eigenvectors.	147
7.3	Time-averaged PF of the angle between the vorticity vector and the eigenvectors of filtered strain rate tensor ($Re = 2600$).	148
7.4	Time-averaged PF of the angle between the vorticity vector and eigenvectors of the negative SGS stress tensor ($Re = 2600$).	149
7.5	Time-averaged JPF between the $\Theta(\bar{\boldsymbol{\omega}}, \mathbf{e}_{S\beta})$ and $\Theta(\bar{\boldsymbol{\omega}}, \mathbf{e}_{S\gamma})$ ($Re = 2600$).	151
7.6	The spherical triangle related to a vector and an orthonormal triad.	152

7.7	Time-averaged JPF between $\Theta(\bar{\omega}, \mathbf{e}_{-\tau\beta})$ and $\Theta(\bar{\omega}, \mathbf{e}_{-\tau\gamma})$ ($Re = 2600$).	153
7.8	Time-averaged PF of the resolved normalized enstrophy generation $\bar{\sigma}_n = \cos(\bar{\omega}, \bar{\mathbf{w}})$ ($Re = 2600$).	155
7.9	Time-averaged JPF between $\bar{\omega}^2/\langle\bar{\omega}^2\rangle$ and $ \cos(\bar{\omega}, \mathbf{e}_{S\beta}) $ ($Re = 2600$).	156
7.10	Time-averaged JPF between $\bar{\omega}^2/\langle\bar{\omega}^2\rangle$ and $\bar{\sigma}_n = \cos(\bar{\omega}, \bar{\mathbf{w}})$ ($Re = 2600$).	157
7.11	Averaged ratio between the eigenvalues of the negative SGS stress and three constituent tensors.	160
7.12	Time-averaged β^* -PF for the eigenvalue ratio of \bar{S}_{ij} ($Re = 2600$).	162
7.13	Time-averaged (β/α) -PF for the eigenvalue ratio of \bar{S}_{ij} ($Re = 2600$).	162
7.14	Time-averaged s^* -PF for the eigenvalue ratio of \bar{S}_{ij} ($Re = 2600$).	163
7.15	Time-averaged JPF between the relative eigenvalues of the negative SGS stress tensor ($Re = 2600$).	165
8.1	Solution space for invariants Q_A and R_A with lines corresponding to constant values of the discriminant D_A . The different subdomains are labelled according to the terminology of Chong and Perry [58].	173
8.2	Time-averaged JPF between invariants $Q_{A\Delta}^+$ and $R_{A\Delta}^+$ of the filtered velocity gradient tensor ($Re = 2600$).	178
8.3	Time-averaged JPF between invariants $Q_{S\Delta}^+$ and $R_{S\Delta}^+$ of the filtered strain rate tensor ($Re = 2600$).	183
8.4	Time-averaged expectation of resolved non-dimensional enstrophy $(\bar{\omega}^2)_E$ associated with invariants $Q_{A\Delta}^+$ and $R_{A\Delta}^+$ ($Re = 2600$).	187
8.5	Time-averaged expectation of resolved non-dimensional enstrophy $(\bar{\omega}^2)_E$ associated with invariants $Q_{S\Delta}^+$ and $R_{S\Delta}^+$ ($Re = 2600$).	188
8.6	Plane and time-averaged profile for non-dimensional enstrophy.	191

8.7	Time-averaged expectation of resolved non-dimensional enstrophy generation σ_E associated with invariants $Q_{A\Delta}^+$ and $R_{A\Delta}^+$ for $Re = 2600$ (positive values: solid lines, negative values: dashed line).	193
8.8	Time-averaged expectation of the resolved non-dimensional enstrophy generation σ_E associated with invariants $Q_{S\Delta}^+$ and $R_{S\Delta}^+$ for $Re = 2600$ (positive values: solid lines, negative values: dashed line).	194
8.9	Time-averaged expectation of the resolved non-dimensional SGS TKE production rate \mathcal{P}_{rE} in the logarithmic region for $Re = 2600$	198
8.10	Time-averaged expectation of the resolved non-dimensional SGS TKE production rate \mathcal{P}_{rE} in the logarithmic region for $Re = 2600$ (Forward scatter \mathcal{P}_{rE}^+ and backward scatter \mathcal{P}_{rE}^- have been separated indicated by the solid and dashed contours, respectively).	198
8.11	Time-averaged expectation of the resolved SGS TKE production rate \mathcal{P}_{rE} in the $Q_{A\Delta}$ - $R_{A\Delta}$ phase plane ($x_2^+ = 77.2$, $Re = 2600$).	199
8.12	Time-averaged expectation of the resolved SGS TKE production rate \mathcal{P}_{rE} in the $Q_{S\Delta}$ - $R_{S\Delta}$ phase plane ($x_2^+ = 77.2$, $Re = 2600$).	199

Nomenclature

English Symbols

a_l, a_q, a_r	filter coefficients
a'	coefficient for the pressure correction equation
\mathcal{A}	constant for the near-wall cubic law
A, B	constants for the logarithmic law; or sides of a spherical triangle
$\mathbf{A}, \mathbf{B}, \mathbf{C}$	matrices
A_i	cross-sectional area of the control volume perpendicular to the i -th dimension
A_{ij}	velocity gradient tensor: $u_{i,j}$
A_k^J, A_q^J	coefficients for solver in the J -th homogeneous layer
b'	source term for the pressure correction equation
B_{ij}	tensor: $\bar{u}_i \bar{u}_j - \bar{\bar{u}}_i \bar{\bar{u}}_j$
\mathcal{B}_{ij}	tensor: $\tau_{kj,ik}$
C	side of a spherical triangle
\mathcal{C}	set of all continuous functions
C_B	coefficient for the filtered Bardina's model
C_f	friction coefficient
C_{ij}	cross stress: $\overline{u'_i \bar{u}_j} + \overline{\bar{u}_i u'_j}$
C_{ij}^m	modified cross stress: $\overline{u'_i \bar{u}_j} + \overline{\bar{u}_i u'_j} - \overline{u'_i \bar{\bar{u}}_j} - \overline{\bar{\bar{u}}_i u'_j}$
C_L	coefficient for the scale similarity SGS stress model
C_m, C_n	coefficients for the dynamic nonlinear SGS stress model: C_S, C_W, C_N
C_N	coefficient for the dynamic nonlinear SGS stress model
C_r	coefficient for Bardina's scale-similarity SGS stress model

C_S	coefficient for the Smagorinsky type SGS stress model
$C_S(\mathbf{x}, \mathbf{x}_0)$	Smagorinsky model coefficient, a function of \mathbf{x} for a specific location \mathbf{x}_0
$\{C_S^{\aleph}\}$	set of optimal Smagorinsky model coefficient functions
$\{C_S^{\aleph 0}\}$	set of optimal Smagorinsky model coefficients
C_W	coefficient for the dynamic nonlinear SGS stress model
d	constant
$d(x_2^+)$	near-wall damping function
D_A, D_S	discriminants
$D_t(\cdot)$	material derivative: $(\dot{\cdot}) + u_j \cdot (\cdot)_{,j}$
\mathbf{e}, \mathbf{e}'	orthonormal eigenvectors
$E(\cdot)$	statistical expectation
E_{ij}	local error tensor function
f	a function of space
\mathcal{F}	integral error functional
F_{ij}^m, F_{ij}^n	differential tensorial functions: M_{ij} , W_{ij} and N_{ij}
G^k	coefficients, functions of irreducible tensorial invariants
$G(\mathbf{x}, \mathbf{y})$	filter kernel function
h	half channel height
h_n	relative helicity: $\cos \Theta(\mathbf{u}, \boldsymbol{\omega})$
H	helicity (density): $u_i \omega_i$
H_i	combination of the convection-diffusion terms of the N-S equations
\mathcal{H}_{ij}	tensor: $L_{ij}^V - \tilde{L}_{ij}^m$
\mathcal{H}_{ij}^Z	tensor: $L_{ij}^Z - \tilde{L}_{ij}^m$
\mathcal{H}_{ij}	tensor: combination of the deviatoric pressure Hessian and viscous diffusion terms
$\mathcal{K}, \mathcal{K}_A, \mathcal{K}_T$	filter kernel functions
k	wavenumber; turbulence kinetic energy; or index: $k = 1, 2, \dots$
i	index: $i = 1, 2, \dots$; or imaginary unit $\sqrt{-1}$
\mathbf{I}_d	identity matrix (tensor)

I_m	invariants of tensors ($m = 1 \sim 6$)
\mathcal{I}_{S2}	strain product, an invariant of S_{ij} : $S_{ij}S_{ji}$
\mathcal{I}_{S3}	strain skewness, an invariant of S_{ij} : $S_{ik}S_{kj}S_{ji}$
j	index: $j = 1, 2, \dots$
L_1, L_2, L_3	dimensions of the physical domain
L_{ij}	Leonard stress: $\overline{\bar{u}_i \bar{u}_j} - \bar{u}_i \bar{u}_j$
L_{ij}^m	modified Leonard stress: $\overline{\bar{u}_i \bar{u}_j} - \bar{\bar{u}}_i \bar{\bar{u}}_j$
L_{ij}^Z, L_{ij}^V	resolved stresses to account for the scale similarity effect
\mathcal{L}_{ij}	resolved Leonard-type stress: $\widetilde{\bar{u}_i \bar{u}_j} - \tilde{\bar{u}}_i \tilde{\bar{u}}_j$
\mathcal{L}_{ij}^{appr}	element of the tensorial approximation space for the resolved Leonard-type stress
\mathcal{L}_{ij}^{proj}	projection of the resolved Leonard-type stress in the tensorial approximation space
m	index: $m = 1, 2, \dots$
M_{ij}	differential tensorial function: $\alpha_{ij} - \tilde{\beta}_{ij}$
M'_{ij}	tensorial intensity function: $\alpha_{ij}(\mathbf{y})\delta_D(\mathbf{x}_0, \mathbf{y}) - \beta_{ij}(\mathbf{y})G(\mathbf{x}_0, \mathbf{y})$
\mathfrak{M}_o	local tensorial approximation space for the Leonard stress at \mathbf{x}_0
\mathfrak{M}_L^{rev}	local tensorial approximation space of the revised conventional dynamic approach
\mathfrak{M}_L^{orig}	original approximation tensorial function space of Lilly's approach
n	index: $n = 1, 2, \dots$
N	number of the nodes for a 1-D discrete filter stencil
N^3	total number of nodes of the discrete physical domain
N_B	number of bins for statistics
N_{ij}	differential tensorial function: $\zeta_{ij} - \tilde{\eta}_{ij}$
p	pressure
P	probability (function)
P_A	invariant of the velocity gradient tensor
P_S	invariant of the strain rate tensor
\mathcal{P}_r	rate of production of SGS turbulence kinetic energy

$\mathring{\mathcal{P}}_{rN}$	scalar due to the contraction of tensors
\mathbf{q}	Euler equivalent axis
Q	local error density function
\mathcal{Q}	local error density functional
Q_A	invariant of the velocity gradient tensor
Q_S	invariant of the strain rate tensor
r_a	eigenvalue ratio: β_S/α_S
R	orthogonal matrix; or orthonormal rotation matrix
\mathfrak{R}	set of real numbers
\mathfrak{R}_n	set for all $n \times n$ matrices over \mathfrak{R}
R_3	truncation error
R_A	invariant of the velocity gradient tensor
R_{CL}, R_{CS}, R_S	relaxation factors
Re	Reynolds number: $U_h \cdot 2h/\nu$
Re_F	critical Reynolds number for fully developed channel flow
Re_T	transitional Reynolds number for turbulence to be sustained
Re_τ	Reynolds number: $u_\tau \cdot h/\nu$
R_{ij}	SGS Reynolds stress: $\overline{u'_i u'_j}$
R_{ij}^m	modified SGS Reynolds stress: $\overline{u'_i u'_j} - \bar{u}'_i \bar{u}'_j$
R_S	invariant of the strain rate tensor
s_i	discrete statistical sample points
s^*	nondimensional parameter
\mathbf{S}	matrix: $[\bar{S}_{ij}]$
S^J	source term for the solver in the J -th homogeneous layer
S_{ij}	strain rate tensor
t	time
Δt	time step
\mathbf{T}	matrix
$\mathbf{T}^{(i)}$	independent symmetric tensorial elements related to the products of \mathbf{S} and $\mathbf{\Omega}$ ($i = 1 \sim 11$)

T_{ij}	test-grid level SGS stress
u_i	the i -th velocity component
u_τ	friction velocity: $\sqrt{\tau_w/\rho}$
u'_i	SGS velocity component: $u'_i = u_i - \bar{u}_i$
\bar{u}''_i	residual velocity: $\bar{u}''_i = \bar{u}_i - \langle \bar{u}_i \rangle$
u_i^+	nondimensional velocity component: $\langle u_i \rangle / u_\tau$
U_h	half velocity difference between the two plates of a channel
$-\langle \bar{u}''_1 \bar{u}_2 \rangle$	resolved Reynolds shear stress for LES of channel flow
$-\langle u'_1 u'_2 \rangle_t$	Reynolds shear stress
\mathbf{v}	vector
$V_n(\mathfrak{R})$	n-dimensional vector space associated with \mathfrak{R}
ΔV	control volume
\mathbf{w}	vortex stretching vector: $w_i = \omega_j S_{ij}$
W_{ij}	differential tensorial function: $\lambda_{ij} - \tilde{\gamma}_{ij}$
x, y, z	3-D Cartesian coordinates
$\mathbf{x}, \mathbf{y}, \mathbf{z}$	3-D Cartesian vectors
x_i, x'_i	coordinates ($i = 1, 2, 3$)
Δx_i	grid size in the x_i direction
x_2^+	wall coordinate: $x_2 u_\tau / \nu$

Greek Symbols

α	largest eigenvalue of a second order tensor
α_{ij}	tensor: $2\tilde{\Delta}^2 \tilde{S} \tilde{S}_{ij}$
β	intermediate eigenvalue of a second order tensor
β_{ij}	tensor: $2\bar{\Delta}^2 \bar{S} \bar{S}_{ij}$
β^*	nondimensional parameter
γ	smallest eigenvalue of a second order tensor
γ_{ij}	grid level constituent tensor: $2\bar{\Delta}^2 (\bar{S}_{ik} \bar{\Omega}_{kj} - \bar{\Omega}_{ik} \bar{S}_{kj})$

$\mathbf{\Gamma}$	matrix: $\mathbf{T}^{(2)*}$
$\delta(\cdot), \delta^n(\cdot)$	first and n -th order variational operations
$\delta_D(\mathbf{x}, \mathbf{y})$	Dirac delta function
δ_{ij}	Kronecker delta
Δ	mesh or filter size
ϵ	ratio between the cut-off sizes of the test-grid and grid filters: $\tilde{\Delta}/\bar{\Delta}$
ε_{ijk}	Levi-Civita permutation symbol
ε_r	resolved dissipation rate
$\mathcal{E}, \mathcal{E}'$	orthonormal frame bases: $[\mathbf{e}_1, \mathbf{e}_2, \mathbf{e}_3]$ and $[\mathbf{e}'_1, \mathbf{e}'_2, \mathbf{e}'_3]$, respectively
$\mathcal{E}_{ij}(\mathbf{x}, \mathbf{x}_0)$	local error tensor, a function of \mathbf{x} for a specific location \mathbf{x}_0
ζ_{ij}	test-grid level constituent tensor: $4\tilde{\Delta}^2(\tilde{\bar{S}}_{ik}\tilde{\bar{S}}_{kj} - \frac{1}{3}\tilde{\bar{S}}_{mn}\tilde{\bar{S}}_{nm}\delta_{ij})$
η	sufficiently small real number
η_{ij}	grid level constituent tensor: $4\bar{\Delta}^2(\bar{S}_{ik}\bar{S}_{kj} - \frac{1}{3}\bar{S}_{mn}\bar{S}_{nm}\delta_{ij})$
Θ	angle
λ	eigenvalue
λ_{ij}	test-grid level constituent tensor: $2\tilde{\Delta}^2(\tilde{\bar{S}}_{ik}\tilde{\bar{\Omega}}_{kj} - \tilde{\bar{\Omega}}_{ik}\tilde{\bar{S}}_{kj})$
$\Lambda_\alpha, \Lambda_\beta, \Lambda_\gamma$	principal angles between two eigenframes
μ	coefficient of viscosity
ν	kinematic viscosity
ν_{sgs}	subgrid-scale viscosity
ν_T	eddy viscosity
Π	resolved scalar quantity
ρ	density
σ	enstrophy generation: $\boldsymbol{\omega} \cdot \mathbf{w}$
σ_n	normalized enstrophy generation: $\cos \Theta(\boldsymbol{\omega}, \mathbf{w})$
Σ	the physical field domain
ς	sufficiently small real number
τ	shear stress
τ_{ij}	grid level SGS stress
τ_w	wall friction stress

Υ	solution space for the model coefficients
χ	Euler rotational angle
$\psi(\mathbf{x}, \mathbf{y})$	non-symmetric kernel function
$\boldsymbol{\omega}$	vorticity vector: $\omega_i = \varepsilon_{ijk}\Omega_{kj}$
ω^2	enstrophy: $\omega_i\omega_i$
$\boldsymbol{\Omega}$	matrix: $[\bar{\Omega}_{ij}]$
Ω_{ij}	rotation rate tensor

Subscripts and Superscripts

$()_1$	streamwise component
$()_2$	wall-normal component
$()_3$	spanwise component
$()_A$	quantity related to the velocity gradient tensor
$()_b$	component at the back face of the control volume
$()_B$	component at the back neighbor node
$()_e$	component at the east face of the control volume
$()_E$	component at the east neighbor node; or statistical expectation
$()_f$	component at the front face of the control volume
$()_F$	component at the front neighbor node
$()_n$	component at the north face of the control volume
$()_N$	component at the north neighbor node; or component related to the 3rd nonlinear constituent term η_{ij}
$()_P$	component at the central node
$()_w$	component at the west face of the control volume
$()_W$	component at the west neighbor node; or component related to the 2nd nonlinear constituent term γ_{ij}
$()_S$	component related to the 1st constituent term β_{ij} (or \bar{S}_{ij})
$()_{ij}$	tensor: $i, j = 1, 2, 3$

$()_i$	vector component: $i = 1, 2, 3$
$()_{,i}$	spatial derivative: $\partial()/\partial x_i$
$()_{i,j}$	spatial derivative: $\partial()_i/\partial x_j$
$()_{ij}^*$	tracefree form of a tensor
$()^{I,J,K}$	indices for a discrete location
$()^n$	result at the n -th time step
$()^T$	transpose of a matrix or vector
$()^{-1}$	inverse of a matrix
$()_\alpha$	component related to the largest eigenvalue of a tensor
$()_\beta$	component related to the intermediate eigenvalue of a tensor
$()_\gamma$	component related to the smallest eigenvalue of a tensor
$()^\mathbb{K}$	the optimal result
$()_\Delta$	component at the filtered scale of motion
$()^\star$	intermediate result between two time steps
$\check{()}$	random variable
$\dot{()}$	time derivative: $\partial()/\partial t$
$\overline{()}$	grid level filter; or resolved quantity
$\widetilde{()}$	test-grid level filter
$()'$	SGS or temporal residual component
$()''$	residual component relative to the plane and time averaged value
$()^+$	wall coordinates; or forward scatter
$()^-$	backscatter
$\langle \rangle$	plane and time averaged quantity; or spatially averaged quantity
$\langle \rangle_c$	conditional expectations
$\langle \rangle_p$	plane averaged quantity
$\langle \rangle_t$	time averaged quantity

Abbreviations

1-D	One-Dimensional
2-D	Two-Dimensional
3-D	Three-Dimensional
ADI	Alternative Direction Implicit solver
CFD	Computational Fluid Dynamics
CMM1	Constant One-Parameter Mixed Model
CMM2	Constant Two-Parameter Mixed Model
CPU	Central Processing Unit
CTDMA	Cyclic Tri-Diagonal Matrix Algorithm
DEC	Distribution Equation for the dynamic localization model Coefficient
DM	Dynamic Smagorinsky Model
DMM	Dynamic Mixed Model
DMM1	Dynamic One-parameter Mixed Model
DMM2	Dynamic Two-Parameter Mixed Model
DNM	Dynamic Nonlinear SGS stress Model
DNS	Direct Numerical Simulation
DSM1	Dynamic One-Parameter Smagorinsky Model (equivalent to DM)
FIE2	Fredholm Integral Equation of the Second kind
HPIV	Holographic Particle Image Velocimetry
ILDm	Integral-type Localization DM
ILDsm1	Integral type Localization DSM1
ILDMM2	Integral type Localization DMM2
IOC	Integral form of the OC
ISI	Incomplete Spatial Invariance
JPF	Joint Probability Function
LES	Large Eddy Simulation
MM	Mixed Model
MM2	Two-Parameter Mixed Model

NP	Neighbor Points
N-S	Navier-Stokes
OC	Orthogonal Condition
PC	Personal Computer
PDMA	Penta-Diagonal Matrix Algorithm
PDS	Penta-Diagonal banded linear System
PF	Probability Function
PIE	Picard's Integral Equation
PIV	Particle Image Velocimetry
QTD	Quasi-Two-Dimensional
RANS	Reynolds Averaged Navier-Stokes method
SGS	SubGrid-Scale
SM	Smagorinsky SGS stress Model
T/TS	computer Time for each Time Step
TDMA	Tri-Diagonal Matrix Algorithm
TDS	Tri-Diagonal banded linear System
TKE	Turbulence Kinetic Energy

Chapter 1

Introduction

*“Observe the motion of the water surface, which resembles that of hair, that has two motions: one due to the weight of the shaft, the other to the shape of the curls; thus, water has **eddying motions**, one part of which is due to the **principal current**, the other to the **random and reverse motions**.”*

—Leonardo da Vinci (1510) [1]

“Even after 100 years, turbulence studies are still in their infancy. We are naturalists, observing butterflies in the wild. We are still discovering how turbulence behaves, in many respects. We do have a crude, practical, working understanding of many turbulence phenomena but certainly nothing approaching a comprehensive theory, and nothing that will provide predictions of an accuracy demanded by the designers.”

—John L. Lumley and Akiva M. Yaglom (2001) [2]

1.1 Motivation

The last quarter of the 19th century was a remarkable time in the human history of fluids science and engineering as modern scientific methodologies were formally introduced into turbulence studies through a dozen pioneering papers linked to a group of legendary names such as Joseph Valentin Boussinesq, Osborne Reynolds, and John William Strutt, Third Baron Rayleigh [2–9]. Among these pioneering contributions,

Osborne Reynolds' famous experiment (1883) [4] was from a scientific point of view, a milestone for discovering the laminar and turbulent states of a flow (although according to Monin and Yaglom [3], the discussion of these two flow states can be traced back to the first half of the 19th century.). One hundred and twenty years has passed since the beginning of modern turbulence studies. The nature of turbulence is still far from being unveiled, and unlike many other branches of physics, a standard research methodology for the study of turbulence has not yet been well established. Although the comment of Lumley and Yaglom (2001) [2] (see the citation above) might be true that 'a comprehensive theory that provides predictions of an accuracy demanded by the designers *will* stay sealed', the past century has witnessed a tremendous growth of human knowledge in turbulence (e.g. Kolmogorov's theory of 1941) and achievements related to its engineering application (e.g. the aircraft and automobile engine industries).

In the past thirty years, due to the rapid advancement of modern computational theories and facilities, Computational Fluid Dynamics (CFD) has become one of the most significant research approaches in turbulence study. It has made available data that were never measurable previously, e.g. the unobtruded velocity and instantaneous pressure fields. There are basically two purposes for research in CFD [10]. The first relates to fundamental studies including numerical algorithms, physical mechanisms of flows and mathematical models (if needed) that reflect these mechanisms. The second type of research serves the need of engineering analysis and design based on knowledge obtained from the first type of research. Currently, three major CFD methodologies are used for studying turbulent flows: the Reynolds Averaged Navier-Stokes method (RANS), Large Eddy Simulation (LES), and Direct Numerical Simulation (DNS).

The DNS approach which began with Orszag and Patterson [11] in 1972, is free from any semi-empirical turbulence modelling and resolves all the scales of motions, including the smallest dynamically active Kolmogorov scale, both spatially and temporally. This approach requires a computational cost proportional to Re^3 (where the Reynolds number Re is based on an integral scale of the flow). Therefore, due to

the limitation of computational resources, DNS is still mainly used for low Reynolds number flow investigations. In contrast, the RANS approach, which has a longer history than DNS, is based on the temporal *Reynolds decomposition*^a [5]. Since motions at all wavenumbers have not been resolved in the RANS approach, it heavily relies on semi-empirical turbulence modelling closures. However, it is computationally efficient and can be applied for calculating high Reynolds number flows. The LES approach originally introduced by Smagorinsky in 1962–1963 [2, 12, 13] and followed by Deardorff [14] and Schumann [15, 16], balances the computational ambition and cost of RANS and DNS. In LES, all the field-dominant anisotropic large scale motions above a certain cut-off size (usually much larger than the Kolmogorov scale) are resolved directly in a time-accurate manner, while the small scale or SubGrid-Scale (SGS) motions are assumed to be homogeneous and universal such that some semi-empirical methods can be applied to model the SGS effects.

Since the pioneering works of the 1960's, the LES technique has been advancing with remarkable speed. It has been widely studied using both theoretical test flows with simple geometries and practical engineering flows with complex geometries [17]. Much progress has been made in developing and validating the SGS models, among which influential contributions include the scale-similarity model of Bardina [18], the dynamic model of Germano *et al.* [19] and Lilly [20], the spectral eddy viscosity model of Kraichnan [21], the structure function model of Métais and Lesieur [22], and the *a priori* validation of SGS models using DNS data [18, 23, 24] or experimental measurements [25–27] (see Adrian's report [28] and the paper by Tao *et al.* [29]). There is no intention to review here all the LES methodologies of the past 40 years, since some comprehensive works [1, 10, 17, 28, 30–32] are already available for this purpose. However, the new trends of LES of turbulence that closely relate to this research will be revisited in a detailed manner in the appropriate chapters to follow.

In general, this dissertation seeks improved LES approaches for turbulence studies, which can offer a relatively high computational efficiency, account for the

^aThe observation of Leonardo da Vinci (1510), cited at the beginning of the chapter, can be viewed as the precursor of the Reynolds decomposition technique [1].

nonlinear nature of turbulence in the SGS models, predict turbulence topologies and near-wall anisotropy of wall-bounded turbulent flows, and reflect the generic tensorial geometrical characteristics of the SGS stress, filtered velocity gradient, strain rate and rotation rate tensors. The research has been generally carried out at a fundamental level in terms of physics, which serves the first type of CFD research as mentioned previously.

1.2 Method of Large Eddy Simulation and the SGS Stress Decomposition

In LES, large and small scale structures of the turbulence are distinguished by introducing a filter

$$\bar{f}(\mathbf{x}) = \int_{-\infty}^{\infty} f(\mathbf{y})G(\mathbf{x}, \mathbf{y})d\mathbf{y} \quad (1.1)$$

For incompressible flows, the filtered continuity and Navier-Stokes (N-S) equations, respectively, take the following forms:

$$\bar{u}_{i,i} = 0 \quad (1.2)$$

$$\dot{\bar{u}}_i + (\bar{u}_i \bar{u}_j)_{,j} = -\bar{p}_{,i} / \rho - \tau_{ij,j} + \nu \bar{u}_{i,jj} \quad (1.3)$$

After filtering, the *grid-level* (\bar{G} -level) *SGS stress*

$$\tau_{ij} = \overline{u_i u_j} - \bar{u}_i \bar{u}_j \quad (1.4)$$

appears in Eq.(1.3) and has to be modelled. Recent reviews of different SGS stress models can be found in the Refs. [1, 10, 32]. Applying the classical *Leonard decomposition*, the SGS stress τ_{ij} can be decomposed into three parts

$$\tau_{ij} = L_{ij} + C_{ij} + R_{ij} \quad (1.5)$$

where

$$L_{ij} = \overline{u_i u_j} - \bar{u}_i \bar{u}_j \quad (1.5a)$$

$$C_{ij} = \overline{u'_i \bar{u}_j} + \overline{\bar{u}_i u'_j} \quad (1.5b)$$

$$R_{ij} = \overline{u'_i u'_j} \quad (1.5c)$$

denote the *Leonard stress*, *cross stress* and *SGS Reynolds stress* tensors, respectively. In developing these equations, the instantaneous velocity has been decomposed as follows: $u_i = \bar{u}_i + u'_i$, where a prime is used to indicate the unresolved SGS component. By requiring each stress term to be *Galilean invariant* (inertial-frame invariant under any translation), Germano [33] proposed the following modified method for decomposing the SGS stress τ_{ij}

$$\tau_{ij} = L_{ij}^m + C_{ij}^m + R_{ij}^m \quad (1.6)$$

where

$$L_{ij}^m = \overline{\bar{u}_i \bar{u}_j} - \bar{\bar{u}}_i \bar{\bar{u}}_j \quad (1.6a)$$

$$C_{ij}^m = \overline{\bar{u}'_i \bar{u}_j} + \overline{\bar{u}_i \bar{u}'_j} - \bar{\bar{u}'_i} \bar{\bar{u}}_j - \bar{\bar{u}}_i \bar{\bar{u}'_j} \quad (1.6b)$$

$$R_{ij}^m = \overline{\bar{u}'_i \bar{u}'_j} - \bar{\bar{u}'_i} \bar{\bar{u}'_j} \quad (1.6c)$$

As will be shown in the following context, the decomposition of SGS stress tensor is directly linked to the SGS modelling procedure.

1.3 Conventional SGS Modelling Approaches

In this section, the conventional scale-similarity model and (dynamic) Smagorinsky SGS viscosity model are revisited as a preparation for future discussion. However, surveys on other SGS modelling approaches related to the new SGS models to be proposed will be presented in specific detail in the chapters to follow.

1.3.1 Scale Similarity Model

The *scale similarity SGS stress model* is based on the observation that the smallest grid scale motion is similar to that at the largest SGS scale. The scale similarity model of Bardina [18, 34] assumes the cross and SGS Reynolds stresses to take the following forms:

$$C_{ij} \approx \bar{u}_i(\bar{u}_j - \bar{\bar{u}}_j) + \bar{u}_j(\bar{u}_i - \bar{\bar{u}}_i) \quad (1.7)$$

$$R_{ij} \approx (\bar{u}_i - \bar{\bar{u}}_i)(\bar{u}_j - \bar{\bar{u}}_j) \quad (1.8)$$

whence

$$C_{ij} + R_{ij} \approx \bar{u}_i\bar{u}_j - \bar{\bar{u}}_i\bar{\bar{u}}_j \stackrel{\text{def}}{=} B_{ij} \quad (1.9)$$

Therefore, the constitutive relation of the similarity model given by Eq.(1.5) reads

$$\tau_{ij} \approx L_{ij} + B_{ij} = \overline{\bar{u}_i\bar{u}_j} - \bar{\bar{u}}_i\bar{\bar{u}}_j \equiv L_{ij}^m \quad (1.10)$$

Based on their Particle Image Velocimetry (PIV) measurements in a round jet, Liu *et al.* [25] provided empirical support for the idea of scale similarity in LES. They observed the following stress similarity phenomenon:

$$\tau_{ij} = C_L \mathcal{L}_{ij} = C_L(\widetilde{\bar{u}_i\bar{u}_j} - \tilde{\bar{u}}_i\tilde{\bar{u}}_j) \quad (1.11)$$

where C_L is the coefficient for the scale similarity SGS stress model, the tilde represents the *test-grid filtering process* and $\mathcal{L}_{ij} = \widetilde{\bar{u}_i\bar{u}_j} - \tilde{\bar{u}}_i\tilde{\bar{u}}_j$ is the *resolved Leonard-type stress*. Discussions on the value of C_L can be found in the papers by Sagaut and Grohens [35], and Meneveau and Katz [31]. This model can reflect the backscatter in a reasonable manner, however it is not dissipative enough to make the calculation stable. Variations of the scale-similarity models for an improved performance will be discussed in chapter 4.

1.3.2 Dynamic SGS Viscosity Model

The conventional *Dynamic Smagorinsky SGS stress Model* (DM) introduced by Germano *et al.* [19] and modified by Lilly [20] was a breakthrough and continues to be popular in the LES community. The modified DM has been successfully used for predicting various incompressible and compressible flows (e.g. Moin *et al.* [36], Zang *et al.* [37] and Piomelli [38]). Moin *et al.* [36] extended this dynamic modelling procedure to the scalar (energy) transport process. In the DM approach, the constitutive relation between the grid-level SGS stress is expressed as

$$\tau_{ij}^* = \tau_{ij} - \frac{\delta_{ij}}{3}\tau_{kk} = -2C_S\bar{\Delta}^2|\bar{S}|\bar{S}_{ij} \quad (1.12)$$

where C_S is the coefficient for the Smagorinsky type models, the asterisk is used to indicate the tracefree form of a tensor and δ_{ij} is the Kronecker delta. The *SGS viscosity* related to Eq.(1.12) is defined as

$$\nu_{sgs} = C_S\bar{\Delta}^2|\bar{S}| \quad (1.13)$$

It should be indicated that the LES approach is intrinsically different from the RANS approach in that the motions larger than the filter size are resolved using the unsteady calculation. Thus the level of the SGS viscosity (ν_{sgs}) is much smaller (possibly two or three orders depending on the specific test problem) than that for the *eddy viscosity* (ν_T) in the RANS approach.

Originally [13], C_S^2 instead of C_S was used in Eq.(1.12), so that the model was purely dissipative and numerically robust. The *resolved strain rate tensor* appearing in the above equations has the form of

$$\bar{S}_{ij} = \frac{1}{2}(\bar{u}_{i,j} + \bar{u}_{j,i}) \quad (1.14)$$

and its magnitude is evaluated by $|\bar{S}| = (2\bar{S}_{ij}\bar{S}_{ij})^{1/2}$.

The original Smagorinsky approach [13] has some drawbacks, e.g. the model ‘constant’ C_S is not a self-adjusting flow dependent parameter, it does not account for backscatter of the SGS *Turbulent Kinetic Energy* (TKE), it yields inaccurate predictions of near-wall flow, and the adoption of an additional artificial near-wall damping function is always necessary in the simulation. Germano *et al.* [19] proposed a dynamic SGS model by introducing a second test-grid-level filtering process. The \bar{G} -level SGS stress still retains the original form of the Smagorinsky model, however, C_S is no longer a constant, but rather a function of time and space. A new *test-grid-level* (\tilde{G} -level) *SGS stress*, T_{ij} , appears due to the second filter adopted,

$$T_{ij} = \widetilde{u_i u_j} - \tilde{u}_i \tilde{u}_j \quad (1.15)$$

where the test-grid filtering process is based on a characteristic filter size of $\tilde{\Delta}$. Typically [19], the scaling factor, $\epsilon = \tilde{\Delta}/\bar{\Delta}$, is set to 2. Similar to the approach for τ_{ij}^* , the constitutive relation between T_{ij}^* and \tilde{S}_{ij} can be modelled as

$$T_{ij}^* = T_{ij} - \frac{\delta_{ij}}{3} T_{kk} = -2C_S \tilde{\Delta}^2 \left| \tilde{S} \right| \tilde{S}_{ij} \quad (1.16)$$

The two SGS stresses, i.e. τ_{ij} and T_{ij} , are related by the *Germano identity* [19], defined as

$$\mathcal{L}_{ij} = T_{ij} - \tilde{\tau}_{ij} \quad (1.17)$$

Substituting Eqs.(1.12) and (1.16) into the tracefree form of Eq.(1.17), the following equation is obtained

$$\mathcal{L}_{ij}^* = -\alpha_{ij} C_S + \widetilde{\beta_{ij} C_S} \quad (1.18)$$

where

$$\alpha_{ij} = 2\tilde{\Delta}^2 \left| \tilde{S} \right| \tilde{S}_{ij} \quad (1.19)$$

$$\beta_{ij} = 2\bar{\Delta}^2 \left| \bar{S} \right| \bar{S}_{ij} \quad (1.20)$$

At any specific spatial position, Eq.(1.18) represents five independent instantaneous equations for the single unknown, C_S . Therefore, Eq.(1.18) is an over-determined

system, and consequently an exact solution for C_S does not exist and a residual tensor exists between the right and left hand sides of Eq.(1.18). However, an optimal value for C_S can be obtained by minimizing the *local error density function*, which is a function of space at each time step, defined as

$$Q = E_{ij}E_{ij} \quad (1.21)$$

where E_{ij} is the *local error tensor*, based on the residual of Eq.(1.18), i.e.

$$E_{ij} = \mathcal{L}_{ij}^* + \alpha_{ij}C_S - \widetilde{\beta_{ij}C_S} \quad (1.22)$$

From the theory of approximation [39], it is understood that the above optimization approach seeks the *projection* of \mathcal{L}_{ij}^* in the specified *tensorial approximation space of the model*, \mathfrak{M}_L^{orig} (which will be discussed later in subsection 5.2.3). The projection then represents the ‘best substitute’ for \mathcal{L}_{ij}^* , i.e.

$$\mathcal{L}_{ij}^* \approx \mathcal{L}_{ij}^{proj*} = -\alpha_{ij}C_S^{\aleph} + \widetilde{\beta_{ij}C_S^{\aleph}} \quad (1.23)$$

where the superscript \aleph represents the optimal result^b. Using the above concepts and Eq.(1.22), the local error tensor, which has the minimal norm Q_{min} , takes the following form:

$$E_{ij} = \mathcal{L}_{ij}^* - \mathcal{L}_{ij}^{proj*} \quad (1.24)$$

The difficulty in minimizing Q comes from the filtered term in Eq.(1.22), i.e. $\widetilde{\beta_{ij}C_S}$. Germano *et al.* [19] and Lilly [20] both used an assumption of *Incomplete Spatial Invariance* (ISI), which assumes that C_S is spatially invariant so that it can be extracted from this filtering operation. However, C_S is assumed to be spatially variant in the other parts of the model. Therefore, a *mathematical inconsistency* emerges, i.e. the treatments of C_S in the 2nd and 3rd terms on the right hand side of Eq.(1.22) are

^bThroughout this dissertation, the superscript \aleph is used only when it is necessary to avoid possible confusion. It is frequently used in chapter 5.

different. Nevertheless, with this assumption, Eq.(1.22) can be simplified to

$$E_{ij} = \mathcal{L}_{ij}^* + M_{ij}C_S \quad (1.25)$$

where

$$M_{ij} = \alpha_{ij} - \tilde{\beta}_{ij} \quad (1.26)$$

The physical meaning of α_{ij} , β_{ij} , M_{ij} and \mathcal{L}_{ij}^{proj*} will be discussed further in section 5.2. Minimizing Q using the least squares method and noting that the trace of \mathcal{L}_{ij} vanishes, then yields the conventional dynamic Smagorinsky SGS model coefficient of Lilly [20]

$$C_S^{\mathfrak{N}}(\mathbf{x}) = - \frac{M_{ij}\mathcal{L}_{ij}}{M_{mn}M_{mn}} \quad (1.27)$$

It should be indicated that the above optimization procedure to obtain Eq.(1.27) is based on the minimal residual of the Germano identity, which was the first and is still the most popular criterion in the dynamic SGS modelling procedure. However, it is not the only choice. Other criteria involving different types of identities include: the kinetic energy identity originally introduced by Cabot and utilized by Ghosal *et al.* [40], a new identity involving an explicit filter and its inverse by Kuerten *et al.* [41], the generalized Germano identity by Sagaut [10], and the vector identity by Morinishi and Vasilyev [42]. The Germano identity itself began to attract scrutiny immediately after the classical papers of Germano *et al.* [19] and Lilly [20] were published. Some relevant research papers include Ronchi *et al.* [43], Meneveau and Katz [44], Kuerten *et al.* [41], and Brun and Friedrich [45]. Using Taylor series expansions, Brun and Friedrich [45] extensively studied the grid-level SGS stress tensor τ_{ij} , test-grid level SGS stress tensor T_{ij} and Germano identity. The errors involved in SGS stress terms were specified in their study and the corresponding corrections to the stress terms have been quantified. Nevertheless, the criterion of the minimal residual of the Germano identity will be used exclusively in the optimization procedures of the SGS modelling approaches throughout this dissertation.

1.3.3 Integral Type Localization Approach

As mentioned previously, in both the DM approaches of Germano *et al.* [19] and Lilly [20], the assumption of ISI treats the filtering term $\widetilde{\beta_{ij}C_S}$ separately from the rest of the model. On observing this mathematical inconsistency, Ghosal *et al.* [40] minimized a global error functional using the functional variational method without adopting the *a priori* assumption of ISI to handle $\widetilde{\beta_{ij}C_S}$. They obtained a rigorous *Integral-type Localization Dynamic Smagorinsky type Model* (ILDm) in the form of a Fredholm Integral Equation of the Second kind (FIE2). The global error functional adopted in their approach was defined as

$$\mathcal{F}(C_S) = \int_{-\infty}^{\infty} Q d\mathbf{x} = \int_{-\infty}^{\infty} E_{ij}E_{ij} d\mathbf{x} \quad (1.28)$$

To find the ‘best’ spatial distribution of C_S , such that the global error functional \mathcal{F} is minimal, the variation of \mathcal{F} must vanish. This results in a Fredholm integral equation of the third kind or Picard’s Integral Equation (PIE) (Kondo [46], Golberg [47]), given by

$$\alpha_{ij}(\mathbf{x})E_{ij}(\mathbf{x}) - \beta_{ij}(\mathbf{x}) \int_{-\infty}^{\infty} E_{ij}(\mathbf{y})G(\mathbf{y}, \mathbf{x})d\mathbf{y} = 0 \quad (1.29)$$

which can be further rewritten in the form of a Fredholm integral equation of the second kind

$$f(\mathbf{x}) = C_S(\mathbf{x}) - \int_{-\infty}^{\infty} \mathcal{K}(\mathbf{x}, \mathbf{y})C_S(\mathbf{y})d\mathbf{y} \quad (1.30)$$

where

$$f(\mathbf{x}) = -\frac{1}{\alpha_{ij}(\mathbf{x})\alpha_{ij}(\mathbf{x})} \left[\alpha_{ij}(\mathbf{x})\mathcal{L}_{ij}(\mathbf{x}) - \beta_{ij}(\mathbf{x}) \int_{-\infty}^{\infty} \mathcal{L}_{ij}(\mathbf{y})G(\mathbf{y}, \mathbf{x})d\mathbf{y} \right] \quad (1.31)$$

$$\mathcal{K}(\mathbf{x}, \mathbf{y}) = \frac{\mathcal{K}_A(\mathbf{x}, \mathbf{y}) + \mathcal{K}_A(\mathbf{y}, \mathbf{x}) - \mathcal{K}_T(\mathbf{x}, \mathbf{y})}{\alpha_{ij}(\mathbf{x})\alpha_{ij}(\mathbf{x})} \quad (1.32)$$

and

$$\mathcal{K}_A(\mathbf{x}, \mathbf{y}) = \alpha_{ij}(\mathbf{x})\beta_{ij}(\mathbf{y})G(\mathbf{x}, \mathbf{y}) \quad (1.33)$$

$$\mathcal{K}_T(\mathbf{x}, \mathbf{y}) = \beta_{ij}(\mathbf{x})\beta_{ij}(\mathbf{y}) \int_{-\infty}^{\infty} G(\mathbf{z}, \mathbf{x})G(\mathbf{z}, \mathbf{y})d\mathbf{z} \quad (1.34)$$

If $\alpha_{ij}(\mathbf{x})\alpha_{ij}(\mathbf{x}) \neq 0$, Eq.(1.29) is equivalent to (1.30). In the optimization approach of Ghosal *et al.* [40], a global integration in Eq.(1.28) is necessary to extract the function δC_S from the filtering term $\widetilde{\beta_{ij}\delta C_S}$, so that Eq.(1.29) can be obtained using functional variational theory. However, as will be shown in chapter 5, the author has found that the local error density function Q can be minimized *directly* by introducing the Dirac delta function without adopting such an additional global integration.

1.4 Linear Boussinesq Constitutive Relation and Its Limitations

In both the LES and RANS communities, the Boussinesq hypothesis is often used for constructing a linear constitutive relation between the unknown stress term and resolved strain rate tensor for (SGS-) eddy-viscosity type models. Generally, the linear Boussinesq (SGS-) eddy-viscosity type model is advantageous for its simplicity and robustness, however, as noted by Pope [32], it is improperly based on a molecular transport analogy, which results in a linear relation between the stress and strain rate tensors. Such a molecular process is intrinsically different than the physics of the turbulent motions to be modelled.

The conventional Smagorinsky constitutive relation [12, 13] is based on the Boussinesq hypothesis. Compared with the original Smagorinsky model, a significant theoretical improvement of the Smagorinsky type DM of Germano *et al.* [19] and Lilly [20], and the ILDM of Ghosal *et al.* [40] is that both models are freed from any empirical constants and wall damping functions. However, the DM and ILDM have a few drawbacks due to the Smagorinsky constitutive relation adopted in their modelling approaches: (i) similar to the original Smagorinsky model, it assumes equilibrium between dissipation and production of the SGS TKE and requires the principal axes of the SGS stress tensor τ_{ij} to be aligned with those of the resolved

strain rate tensor \bar{S}_{ij} , which then gives an inadequate representation of the SGS stress components [48]; (ii) the model can result in an unrealistic SGS dissipative effect if the model coefficient is restricted to be positive; (iii) a potential numerical instability can arise due to excessive backscatter of the SGS TKE if the model coefficient is allowed to be negative [38, 49]; and (iv) specific to the DM, there is an additional shortcoming: it is not bounded and admits a possible singularity when the denominator of the formulation ($M_{ij}M_{ij}$) becomes very small [10, 38]. A plane averaging technique has often been adopted (when a homogeneous plane exists) for the DM to avoid numerical instability due to either excessive backscatter or potential singular situation of the modelling formulation [19, 36, 38, 49, 50].

Obviously, the first drawback of the DM and ILDM, i.e. the strict alignment between the τ_{ij} and \bar{S}_{ij} is a direct result of the adoption of the Boussinesq hypothesis. However, it will be demonstrated in chapter 6 that the other three drawbacks are also related to this hypothesis, and a model's performance can be significantly improved if this canonical hypothesis is abandoned in formulating its constitutive relation.

1.5 An Improved Criterion for SGS Models

In the past twenty years, the rapid development of two new branches of fluid dynamics, i.e. *turbulence geometrical statistics* [51–55] and *turbulence topology* [56–58], have brought many new insights into the turbulence community. For instance, Kerr [54] and Ashurst *et al.* [55] discovered a strong tendency of alignment between the vorticity and the intermediate eigenvector of the strain rate tensor, Lund and Rogers [59] discovered that a state of axisymmetric expansion is the most probable flow configuration for isotropic turbulence, and Chong and Perry [56, 58] introduced turbulence topology using the theories of tensorial invariants and nonlinear physics. These new methodologies have helped fluid dynamicists to develop an improved understanding of turbulence phenomena, such as the helical nature of turbulence [53, 60–62], invariant features of the velocity gradient tensor, topological characteristics of turbu-

lence [56–58, 63–74], vortex alignments and stretching [52, 54, 55, 75–91], local intermittency and small-scale vortical structure [51, 92–95], vortex identification [96–98], geometrical description of the eigensystem of the SGS stress and filtered strain rate tensors [29, 99, 100], and methods for constructing improved SGS models based on local vortical structures [101–107].

Currently in both the RANS and LES communities, when one studies a new modelling approach using the *a posteriori* numerical approach, focus is often on the model’s capability of predicting the turbulence features in terms of the magnitude of a parameter, such as the mean velocity profile (using semi-logarithmic wall-coordinates) and the associated distributions of turbulence intensity and shear stress. It should be pointed out that the magnitude and orientation are *equally important* in determining the properties of a tensor such as the Reynolds stress tensor, SGS stress tensor, strain rate tensor, and rotation rate tensor, which then influence the solution set of the momentum equation. Therefore, it is advocated by this and other recent research [70] that future improved CFD modelling studies should include consideration of the tensorial geometrical relations between the known and unknown terms in the constitutive relation such that a model can mimic not only the scaling features, e.g. the logarithmic law, but also the tensorial geometrical features, e.g. the alignment pattern between the vorticity and vortex stretching vectors.

The improved CFD modelling criterion proposed above is based on the advanced requirement that a model should reflect the nonlinear nature, structures and physical processes of the flow, such as vortex stretching, vorticity alignment, and backscatter of TKE from the subgrid scale to the filtered scale. The mechanism of these physical phenomena and processes have been investigated fruitfully in both turbulence topology and geometrical statistics, and some results are already conclusive, e.g. ‘backscatter is not generated by a negative eddy viscosity, but rather the interchange mechanism of the eigenvector alignment (of a constituent tensor formed by the velocity gradients)’ [100]. Thus it is apparent that models founded on the linear Boussinesq constitutive relation, e.g. the conventional DM [19, 20], cannot satisfy this improved criterion, since a linear Boussinesq constitutive relation only offers one

possibility that the SGS stress is strictly aligned with the filtered strain rate tensor. Consequently, these type of models are inadequate for simulating a physical process that is strongly based on tensorial alignments, e.g. backscatter. In this dissertation, a new dynamic nonlinear anisotropic SGS model will be proposed, with the aim of achieving an improved performance (in comparison with the DM and ILDM) in accordance with the improved CFD modelling criterion proposed above.

1.6 Outline of the Dissertation

The objective of this dissertation is to investigate various new dynamic SGS modelling approaches and turbulence phenomenologies of the resolved-scale motions for wall-bounded turbulent shear flows. Both the linear Smagorinsky and nonlinear constitutive relations for the SGS stress models are studied. Turbulence phenomenologies of the resolved-scale motions are investigated using such recently developed methodologies as turbulence geometrical statistics and topology.

The organization of this dissertation is outlined as follows. In chapter 2, the numerical algorithm for the governing equations, discrete filtering scheme and test problem are introduced. From chapter 2 to chapter 5, improved dynamic SGS modelling formulations based on a linear Smagorinsky constitutive relation are investigated. In chapter 3, two efficient direct solution schemes based on the 2-D and 3-D discrete filters of Sagaut and Grohens [35] are proposed to solve the ILDM (FIE2) of Ghosal *et al.* [40] for turbulence with two homogeneous dimensions. In chapter 4, a new localization dynamic two-parameter mixed model is formulated using functional variational methods. In the proposed dynamic localization modelling procedure for the two-parameter mixed model, the mathematical inconsistency due to the assumption of ISI adopted in the current modelling approaches found in the literature is removed, and a system of two integral equations is obtained, which determines the instantaneous optimal spatial distribution of the two model coefficients. In chapter 5, a sufficient and necessary condition for localizing the Smagorinsky SGS stress model

is proposed, which is in the form of an orthogonal condition (OC) and controls the localization model coefficient for the dynamic Smagorinsky SGS model. The OC is useful for dynamic SGS modelling optimization, since it unifies a few conventional modelling formulations and also results in a new dynamic SGS stress model in the form of Picard’s integral equation (PIE). The proposed PIE has one less convolution operation than the FIE2 introduced previously by Ghosal *et al.* [40], and therefore is less expensive in numerical simulation. Also in chapter 5, the construction of the tensorial approximation space for the projection of the Leonard stress is discussed, which is essential to the optimization methods adopted for deriving the dynamic localization models.

From chapter 6 to chapter 8, a novel nonlinear dynamic SGS stress modelling approach is considered, and turbulence features of both the resolved and subgrid scale motions predicted using the proposed dynamic nonlinear model are investigated. In chapter 6, a three-parameter Dynamic Nonlinear Model (DNM) based on the quadratic constitutive relation of Speziale [108, 109] is formulated and tested. Also in this chapter, the tensorial characteristics of the proposed nonlinear model are investigated, including the backscatter phenomenon, relative alignment between the principal axes of the SGS stress and filtered strain rate tensor, and related local sheetlike, tubelike, 2-D, axisymmetric expansion, and axisymmetric compression flow configurations. In chapter 7, results on turbulence geometrical statistics are presented. The statistical features investigated in this chapter are based on a LES Couette flow database generated using the proposed DNM. The physical quantities and phenomena studied in this chapter include helicity and helical structure, enstrophy, enstrophy generation and vortex stretching, local quasi 2-D state of turbulence, relative eigenvalue ratios of the filtered strain rate tensor, geometrical alignment between vorticity and the eigenvector corresponding to the intermediate eigenvalue of the filtered strain rate tensor, and that between vorticity and the vortex stretching vectors. In chapter 8, turbulence topological features based on the resolved tensorial invariants are explored using statistical methods. The sample data are also based on LES of Couette flow using the proposed DNM and the results in turn confirm

the performance of the DNM by comparing them to those reported in the literature. The obtained phenomenological results include the pear-shape contour of the joint probability function of the invariants of the resolved velocity gradient tensor, and illustrations of the statistical expectation of resolved enstrophy, enstrophy generation, and SGS TKE production rate in the phase plane of tensorial invariants. Finally in chapter 9, a summary of major contributions and a discussion of future research directions are presented.

Chapter 2

Numerical Algorithm and Test Problem

2.1 Algorithm for the Numerical Calculation

As described in the works by Piomelli [1], and Ferziger and Perić [110], the fractional step methods have become rather popular in LES and DNS calculations. There are a variety of fractional step algorithms due to the vast number of approaches to time and space discretization. In this study, the governing equations (1.2) and (1.3) are solved using an algorithm based on the fractional step method and second order Adams-Bashforth scheme introduced by Chorin [111] and Kim and Moin [112], and the pressure correction technique of Huang [113]. The development of the computational code for this research was based on a preliminary code inherited from the advisor of this dissertation, Dr. Donald J. Bergstrom, which adopted a basic conventional Smagorinsky model [13].

The filtered momentum equation (1.3) can be re-written as

$$\dot{\bar{u}}_i = H_i - \bar{p}_{,i} / \rho \quad (2.1)$$

where H_i is a combination of the convection and diffusion terms, i.e.

$$H_i = -(\bar{u}_i \bar{u}_j + \tau_{ij})_{,j} + \nu \bar{u}_{i,jj} \quad (2.2)$$

Use of a two-step fractional step method and second order Adams-Bashforth scheme

splits Eq.(2.1) into the following two equations in terms of time-advancement:

$$\begin{cases} \rho \frac{\bar{u}_i^* - \bar{u}_i^{(n)}}{\Delta t} = \frac{1}{2}[3H_i^{(n)} - H_i^{(n-1)}] \\ \rho \frac{\bar{u}_i^{(n+1)} - \bar{u}_i^*}{\Delta t} = -\bar{p}_{,i}^{(n+1)} \end{cases} \quad (2.3)$$

where n indicates the current time step and the superscript \star indicates an intermediate result between two time steps. In the above scheme, the new velocity $\bar{u}_i^{(n+1)}$ is calculated using the new pressure gradient $-\bar{p}_{,i}^{(n+1)}$. According to Ferziger and Perić [110], the pressure gradient can also be split into two parts in the time advancement, i.e. half of the old pressure gradient $-\frac{1}{2}\bar{p}_{,i}^{(n)}$ goes to the first equation of (2.3) to calculate \bar{u}_i^* and the other half of the new pressure gradient $-\frac{1}{2}\bar{p}_{,i}^{(n+1)}$ is used to update the velocity field $\bar{u}_i^{(n+1)}$. Both methods were tested in the simulations and no obvious difference was observed in terms of the statistics of the quantities being calculated. The numerical results presented in this dissertation are based on the scheme shown in Eqs.(2.3). In the numerical process of solving for the velocity field, periodic boundary conditions are applied in the streamwise (x_1) and spanwise (x_3) directions, while the no-slip boundary condition is applied in the wall-normal direction (x_2). The finite volume method is used throughout the discretization procedures and the spatial discretization schemes adopted are of second order accuracy. One fictitious node is used on each side of the discrete computational domain.

The new pressure field used for updating the velocity field in the second equation of (2.3) can be obtained from the filtered continuity equation (1.2) using a pressure correction method [113]. The finite volume method is applied to discretize the filtered continuity equation on a uniform collocated grid system, i.e.

$$\int_b^f \int_s^n \int_w^e \left(\frac{\partial \bar{u}_1}{\partial x_1} + \frac{\partial \bar{u}_2}{\partial x_2} + \frac{\partial \bar{u}_3}{\partial x_3} \right) dx_1 dx_2 dx_3 = 0 \quad (2.4)$$

which results in the following discrete system:

$$(\bar{u}_e - \bar{u}_w)A_1 + (\bar{u}_n - \bar{u}_s)A_2 + (\bar{u}_f - \bar{u}_b)A_3 = 0 \quad (2.5)$$

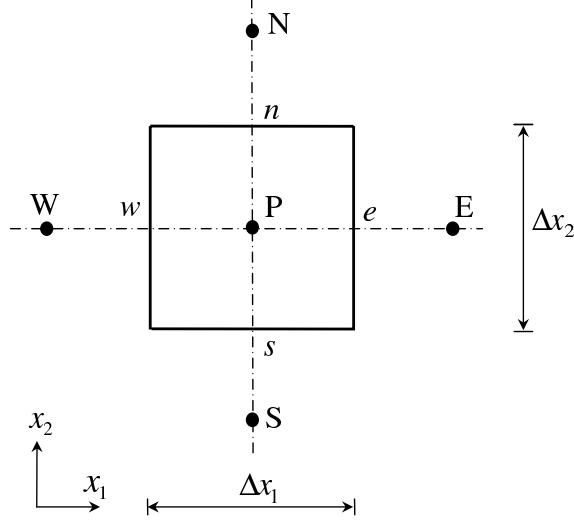


FIGURE 2.1: Sketch of the collocated grid system in the x_1 - x_2 plane.

where the symbols ‘e’ and ‘w’ represent ‘east’ and ‘west’ face-locations on the two sides of the central node in the x_1 direction, respectively. Similarly, ‘n’ and ‘s’ represent ‘north’ and ‘south’ in the x_2 direction, while ‘f’ and ‘b’ represent ‘front’ and ‘back’ in the x_3 direction, respectively (see Fig. 2.1). $A_1 = \Delta x_2 \cdot \Delta x_3$ is the cross-sectional area of the control volume perpendicular to the x_1 direction, and A_2 and A_3 are the cross-sectional areas perpendicular to the x_2 and x_3 directions, respectively.

The velocity field \bar{u}_i^* obtained from the first equation of (2.3) does not necessarily satisfy continuity over the control volume. Thus, a velocity correction is made so that continuity can be satisfied. A conventional approach is to link the flux velocities at the face-location to the difference of the nodal pressure correction field values, i.e.

$$\left\{ \begin{array}{l} \bar{u}_e = \bar{u}_e^* + \frac{A_1 \Delta t}{\rho \Delta V} (\bar{p}'_P - \bar{p}'_E) \\ \bar{u}_w = \bar{u}_w^* + \frac{A_1 \Delta t}{\rho \Delta V} (\bar{p}'_W - \bar{p}'_P) \\ \dots\dots\dots \\ \bar{u}_b = \bar{u}_b^* + \frac{A_3 \Delta t}{\rho \Delta V} (\bar{p}'_B - \bar{p}'_P) \end{array} \right. \quad (2.6)$$

where, $\Delta V = \Delta x_1 \cdot \Delta x_2 \cdot \Delta x_3$ is the volume, and the uppercase subscripts indicate nodal variables, e.g. the subscript ‘P’ represents the central node, ‘E’ represents the

‘East’ neighbor node in the x_1 direction, etc. By substituting the above equations into Eq.(2.5), the following discrete equation for the pressure correction field is obtained:

$$a'_P \bar{p}'_P = \sum a'_{NP} \bar{p}'_{NP} + b' \quad (2.7)$$

where the subscript NP represents the six neighbor nodes, a'_{NP} and a'_P are discrete coefficients of the form

$$\begin{aligned} a'_E = a'_W = \frac{(A_1)^2 \Delta t}{\Delta V}, \quad a'_N = a'_S = \frac{(A_2)^2 \Delta t}{\Delta V}, \quad a'_F = a'_B = \frac{(A_3)^2 \Delta t}{\Delta V} \\ a'_P = \sum a'_{NP} \end{aligned} \quad (2.8)$$

and b' is the source term given by

$$b' = -\rho [A_1(\bar{u}_e^* - \bar{u}_w^*) + A_2(\bar{u}_n^* - \bar{u}_s^*) + A_3(\bar{u}_f^* - \bar{u}_b^*)] \quad (2.9)$$

In order to solve Eq.(2.7), the intermediate flux velocity $\bar{u}_e^*, \dots, \bar{u}_b^*$ at each face must be evaluated from the known intermediate velocity $\bar{u}_E^*, \dots, \bar{u}_B^*$ and pressure $\bar{p}^{(n)}$ at each node, e.g.

$$\bar{u}_e^* = \frac{1}{2}(\bar{u}_P^* + \bar{u}_E^*) + \frac{A_1 \Delta t}{\rho \Delta V}(\bar{p}_P - \bar{p}_E) \quad (2.10)$$

From the solution of Eq.(2.7), the updated nodal pressure field can be obtained via a ‘correction’ as follows:

$$\bar{p}^{(n+1)} = \bar{p}^{(n)} + \bar{p}' \quad (2.11)$$

The corrected pressure field is used to solve the second fractional-step equation in (2.3) to obtain the new velocity field.

Equation (2.7) is typically a discrete Poisson equation, which is well-known for its critical role in the overall numerical algorithm due to high computational cost of solving it. Although several highly efficient multigrid solvers have been developed for solving this discrete Poisson equation [114], they were actually not used in the numerical simulations reported in this dissertation. Instead, a simple ADI (alternative direction implicit) solver based on a TDMA (tri-diagonal matrix algorithm) in the

wall-normal (x_2) direction and CTDMA (cyclic tri-diagonal matrix algorithm) [115] in the periodical (x_1 and x_3) directions was used. Such a choice was based on the fact that the multigrid schemes adopted [114] are expensive in terms of memory consumption, while the ADI solver uses much less memory and still does a good job in Couette flow simulations. For example, it can reduce the global residual of the discrete Poisson system to an order of 10^{-12} using about 20–25 iterations once a fully developed turbulence field is established, with the maximum Courant number ($|u| \cdot \Delta t / \Delta x$) set to be 0.3. All the simulations performed for this dissertation were initiated from a previously obtained fully developed turbulent flow field.

2.2 Discrete Filters

In dynamic SGS modelling approaches, an explicit discrete filter is required for the test-grid level filtering process. The discrete Gaussian filters introduced by Sagaut and Grohens [35] are used throughout this dissertation. They proposed two methods to construct a 3-D filtering convolution using a 1-D discrete filter. The discrete convolution constructed using a linear combination method has the following form:

$$\tilde{f}(I, J, K) = \frac{1}{3} \sum_{l=-N}^N a_l [f(I+l, J, K) + f(I, J+l, K) + f(I, J, K+l)] \quad (2.12)$$

while that constructed using the product method has the following form:

$$\tilde{f}(I, J, K) = \sum_{l=-N}^N \sum_{m=-N}^N \sum_{n=-N}^N a_l a_m a_n f(I+l, J+m, K+n) \quad (2.13)$$

where $N = 1$ for a three point stencil (2nd order accuracy) and $N = 2$ for a five point stencil (4th order accuracy), and a_l , a_m and a_n represents the filter coefficients for the 1-D discrete filter.

Obviously, the cost of the product method is about two orders higher than

that of the linear combination method. For the discrete filter, the linear combination method is more often used in LES, e.g. Zang *et al.* [37], Najjar and Tafti [116], and Morinishi and Vasilyev [50]. In this study, without an otherwise specification, the boundary field is processed using a 2nd order discrete Gaussian filter, while the internal field is processed with a 4th order discrete Gaussian filter. The 1-D discrete forms for the 2nd and 4th order Gaussian filters given by Sagaut and Grohens [35] are, respectively,

$$\tilde{f}(I) = \frac{1}{24}\epsilon^2 [f(I+1) + f(I-1)] + \frac{1}{12}(12 - \epsilon^2)f(I) \quad (2.14)$$

and

$$\begin{aligned} \tilde{f}(I) = & \frac{\epsilon^4 - 4\epsilon^2}{1152} [f(I+2) + f(I-2)] \\ & + \frac{16\epsilon^2 - \epsilon^4}{288} [f(I+1) + f(I-1)] + \frac{\epsilon^4 - 20\epsilon^2 + 192}{192} f(I) \end{aligned} \quad (2.15)$$

where $\epsilon = \tilde{\Delta}/\bar{\Delta}$ represents the ratio between the cut-off sizes of the test-grid and grid filters, which is set to $\epsilon = 2$ following the conventional approach [19]. An evaluation of the effect of different values for ϵ can be found in papers by Najjar and Tafti [116], Lund [117], and Sagaut and Grohens [35]. It is interesting to observe that with the choice of $\epsilon = 2$, the discrete filtering scheme of 2nd order accuracy (Eq.(2.14)) becomes identical to that of 4th order accuracy (Eq.(2.15)).

2.3 Test Problem

Throughout this dissertation, the numerical tests were performed using turbulent Couette flow. It is a canonical test problem for wall-bounded anisotropic shear driven turbulence, which has been studied both experimentally [118–124] and numerically [124–132].

The transitional Reynolds number (lowest Reynolds number for which turbulence can be sustained) for Couette flow is $Re_T \approx 600$ according to Leutheusser and

Chu [119], while $Re_T \approx 720$ (or $Re_{\tau T} \approx 26$) according to other studies [122, 124, 125, 127]. The two Reynolds numbers mentioned above are defined as $Re = U_h(2h)/\nu$ and $Re_\tau = u_\tau h/\nu$. Here, h is the half channel height, U_h is one half of the velocity difference between the two plates, u_τ is the wall friction velocity defined as $u_\tau = (\tau_w/\rho)^{1/2}$, and $\tau_w = (\mu \bar{u}_{1,2})_{wall}$ represents the wall shear stress. The critical Reynolds number for fully developed turbulent Couette flow [124] is $Re_F \approx 1000$ or $Re_{\tau F} \approx 35$. It should be noted that although pressure driven Poiseuille channel flow has exactly the same physical geometry as shear driven Couette channel flow, its transitional Reynolds number for turbulence to be sustained and critical Reynolds number for turbulence to be fully developed are much higher. For Poiseuille channel flows, Patel and Head [133] found the transitional Reynolds number at which a log law with universal constants can be observed is about $Re_{\tau T} \approx 104$, while according to Eckelmann [134], Kim *et al.* [135], and Jiménez and Moin [136], the critical Reynolds number for fully developed flow is $Re_{\tau F} \approx 142$. Thus, both the transitional and critical Reynolds numbers for pressure driven Poiseuille channel flow are about four times those for shear driven Couette flow ($104/26 \approx 142/35 \approx 4$).

To resolve the turbulence field for $Re = 2600$, Bech *et al.* [124] used $256 \times 70 \times 256$ nodes (non-uniform in the wall-normal direction) in DNS for a field domain of $10\pi h \times 2h \times 4\pi h$, while Kim and Menon [131, 132] used $48 \times 48 \times 32$ (non-uniform in the wall-normal direction) in LES for a field domain of $4\pi h \times 2h \times 2\pi h$. In this study, the physical domain is $L_1 \times L_2 \times L_3 = 24h \times 2h \times 12h$ in chapter 4 and $8\pi h \times 2h \times 4\pi h$ in chapters 3 and 5–8, where the half channel height h is set to be 10 mm . Three uniform grid systems with a different number of control volumes are used, i.e. 34^3 in chapters 5 and 6, 48^3 in chapters 4–8 and 66^3 in chapters 3, 5 and 6. The Reynolds numbers tested ranged from $Re = 1500$ to 7050 (from $2.1Re_T$ to $9.8Re_T$). The statistics are based on 6000 time steps in chapters 3 and 6, 2000 time steps in chapter 4, 5000 time steps in chapter 5, and 4000 time steps in chapters 7 and 8. The different choices of the physical domain sizes and time steps for statistics are not due to any special consideration of the physics, but instead arise from the fact that the simulations reported in different chapters were carried out as independent

research projects spread over a period of approximately four years. The results of the simulations for testing the new SGS modelling approaches presented in chapters 3–8 are compared with those calculated using conventional SGS models, as well as both the DNS and experimental results reported in the literature.

Chapter 3

An Efficient Solution Scheme for Applying the Integral Type Dynamic Localization Subgrid-Scale Model in Turbulence with Homogeneous Directions

3.1 Introduction

In chapter 1, the Integral type Localization Dynamic Smagorinsky type Model (ILDm) of Ghosal *et al.* [40] was introduced. The ILDM does not rely on the assumption of ISI and is mathematically rigorous, however, it has the complex form of a Fredholm Integral Equation of the Second kind (FIE2). A preconditioning relaxation iterative scheme was implemented by Ghosal *et al.* [40] and Carati *et al.* [137] to solve the FIE2. It was estimated that the CPU time for solving the ILDM is four times that of the DM [49]. Piomelli and Liu [49] estimated that the cost for solving the FIE2 is similar to that for solving the Poisson equation for the pressure field, which can be relatively expensive. They observed that C_S is a fairly slowly-varying function of time, and proposed an approximate explicit scheme to localize the DM. Their approximate localization model avoids the costly process of solving the FIE2 and has been successfully tested using rotating channel flow.

One of the major objectives of this chapter is to apply the discrete filter proposed by Sagaut and Grohens [35] to directly solve the FIE2 of Ghosal *et al.* [40], in a manner that avoids using the conventional iterative solver [40, 137] or approximate scheme [49]. It will be shown later that the cost of using the proposed direct solver for the ILDM is about the same as that for the DM in the case of turbulent flow bounded by parallel walls. This chapter is organized as follows. The numerical scheme of the direct solver for the FIE2 is discussed in section 3.2. Numerical results are analyzed in section 3.3, and conclusions are presented in section 3.4.

3.2 A Direct Solution Scheme for the ILDM

In an approach slightly different than that of Ghosal *et al.* [40] and Carati *et al.* [137], the Picard's integral equation (PIE) Eq.(1.29) is used directly in the solution strategy developed below.

For turbulence with a statistically homogeneous plane, the plane averaging technique is often adopted to obtain a stable solution of $C_S(x_2)$. This is based on the assumption that C_S varies only in the wall-normal direction and is homogeneous in the other two directions. Generally speaking, this assumption holds, if (i) such a spatially averaged distribution for C_S exists statistically, and (ii) the instantaneous plane distribution is sufficiently close to the plane averaged profile. From Eq.(1.12), it is understood that for an SGS viscosity model, both C_S and \bar{S}_{ij} determine the SGS effects. Condition (i) is a prerequisite for using a plane averaging approach. Condition (ii) prohibits any instantaneous variations of C_S from its averaged value and relies solely on \bar{S}_{ij} to account for the instantaneous unresolved scales of motions through Eq.(1.12). Notwithstanding the fact that condition (ii) is unrealistic, the plane averaging technique does avoid the singularity problem and has been successfully used in a variety of different simulations [19, 36, 38, 50]. Integrating both sides of the PIE over the homogeneous plane, and then on substituting the expression for three-point discrete Gaussian filter of Sagaut and Grohens [35], i.e. Eq.(2.14), the

following discrete system is obtained:

$$\begin{aligned}
& \langle \alpha_{ij} \mathcal{L}_{ij}^* \rangle_p - \langle \beta_{ij} \tilde{\mathcal{L}}_{ij}^* \rangle_p + \langle \alpha_{ij} \alpha_{ij} \rangle_p C_S^J \\
& - \frac{1}{3} \left[\sum_{q=-1}^1 a_q \left\langle \alpha_{ij} \left(\beta_{ij}^{I+q,J,K} + \beta_{ij}^{I,J,K+q} \right) \right\rangle_p C_S^J + \sum_{q=-1}^1 a_q \left\langle \alpha_{ij} \beta_{ij}^{I,J+q,K} \right\rangle_p C_S^{J+q} \right] \\
& - \frac{1}{3} \left[\sum_{q=-1}^1 a_q \left\langle \beta_{ij} \left(\alpha_{ij}^{I+q,J,K} + \alpha_{ij}^{I,J,K+q} \right) \right\rangle_p C_S^J + \sum_{q=-1}^1 a_q \left\langle \beta_{ij} \alpha_{ij}^{I,J+q,K} \right\rangle_p C_S^{J+q} \right] \\
& + \frac{1}{3} \sum_{q=-1}^1 \frac{a_q}{d} \left\{ \left[\sum_{r=-1}^1 a_r \left\langle \beta_{ij} \left(\beta_{ij}^{I+q+r,J,K} + \beta_{ij}^{I+q,J,K+r} \right) \right\rangle_p C_S^J \right. \right. \\
& \quad \left. \left. + \left(\sum_{r=-1}^1 a_r \left\langle \beta_{ij} \beta_{ij}^{I+q,J+q,K} \right\rangle_p C_S^{J+q} \right)^* \right] \right. \\
& + \left[\sum_{r=-1}^1 a_r \left\langle \beta_{ij} \left(\beta_{ij}^{I+r,J+q,K} + \beta_{ij}^{I,J+q,K+r} \right) \right\rangle_p C_S^{J+q} + \left(\sum_{r=-1}^1 a_r \left\langle \beta_{ij} \beta_{ij}^{I,J+q+r,K} \right\rangle_p C_S^{J+q+r} \right)^* \right] \\
& \left. + \left[\sum_{r=-1}^1 a_r \left\langle \beta_{ij} \left(\beta_{ij}^{I+r,J,K+q} + \beta_{ij}^{I,J,K+q+r} \right) \right\rangle_p C_S^J + \left(\sum_{r=-1}^1 a_r \left\langle \beta_{ij} \beta_{ij}^{I,J+r,K+q} \right\rangle_p C_S^{J+r} \right)^* \right] \right\} \\
& = 0
\end{aligned} \tag{3.1}$$

where $d = 3$, and $\langle \cdot \rangle_p = \iint \cdot dx_1 dx_3$ represents the plane integral. For tensors without a superscript spatial index, the default spatial location is the central node (I, J, K) , e.g. α_{ij} represents $\alpha_{ij}^{I,J,K}$. The solution, C_S^J , to Eq.(3.1) is the model coefficient for the J -th homogeneous plane. The above equation can be readily rearranged into a Penta-Diagonal banded linear System (PDS), which can be directly solved using a Penta-Diagonal Matrix Algorithm (PDMA)

$$\sum_{k=-2}^2 A_k^J C_S^{J+k} = S^J \tag{3.2}$$

where A_k^J represents the coefficients and $S^J = -\langle \alpha_{ij} \mathcal{L}_{ij}^* \rangle_p + \langle \beta_{ij} \tilde{\mathcal{L}}_{ij}^* \rangle_p$ is the source term.

The complexity of Eq.(3.1) is mainly due to the last term enclosed in the braces

$\{\cdot\}$, which is the 3-D discrete form of the double test-grid filtered term $\widetilde{\widetilde{\beta_{ij}C_S}}$ contained in Eq.(1.29). It should be noted that the discrete modelling formulation, e.g. Eq.(3.2), relies on the specific discrete filter adopted and therefore can take various forms other than the PDS obtained. In some approaches presented in the literature (e.g. Morinishi and Vasilyev [50], and Kravchenko *et al.* [138]), only a 2-D filter is applied in the homogeneous plane for turbulence with two homogenous dimensions. A 2-D discrete filter can be constructed from Eq.(2.12) as follows

$$\tilde{f}(I, J, K) = \frac{1}{2} \sum_{l=-N}^N a_l [f(I+l, J, K) + f(I, J, K+l)] \quad (3.3)$$

Unlike the 3-D filter, a 2-D filter in the homogeneous plane does not allow information to be exchanged directly in the wall-normal direction between two different homogeneous layers. However, if a mixed scheme is used, which applies a 2-D discrete filter to the inner filtering process and a 3-D filter to the outer filtering process for $\widetilde{\widetilde{\beta_{ij}C_S}}$, Eq.(3.1) can be much simplified: d becomes 2, the terms indicated by \ast vanish, and Eq.(3.2) reduces to a Tri-Diagonal banded linear System (TDS), which can be easily solved using a TDMA. Compared with the purely 2-D filtering solution schemes found in the literature as mentioned earlier, both the PDS and TDS approaches being proposed allow two adjacent homogeneous layers to communicate field information. Also, since the PDS and TDS are solved only in the wall-normal direction once for each time step, the extra cost for the PDMA and TDMA is insignificant.

In order to solve the PDS and TDS, the boundary conditions for C_S and \bar{S}_{ij} (for β_{ij}) have to be specified. Since the viscous effect dominates in the vicinity of the wall, we require that $C_S|_{wall} = 0$. At the wall, \bar{S}_{ij} takes the following form (see Pope [32]):

$$\bar{S}_{ij} |_{wall} = \frac{1}{2} \begin{bmatrix} 0 & \bar{u}_{1,2} & 0 \\ \bar{u}_{1,2} & 0 & \bar{u}_{3,2} \\ 0 & \bar{u}_{3,2} & 0 \end{bmatrix}_{wall} \quad (3.4)$$

The value of $\bar{u}_{1,2}$ can be estimated using empirical wall friction coefficient correlations. Numerical tests indicates that statistically $\bar{u}_{3,2} \ll \bar{u}_{1,2}$ at the wall due to the fact that the instantaneous value of \bar{u}_3 does not have a preference in either the positive or negative direction of x_3 . Thus, it was found that an initial assumption of $\bar{u}_{3,2} |_{wall} \approx 0$ can give realistic (preliminary) results. For turbulent Couette flow, the following experimental wall friction law introduced by Aydin and Leutheusser [121] can be used to obtain the preliminary field:

$$C_f^{-1/2} = 3.54 \ln(2 Re C_f^{1/2}) + 4.1 \quad (3.5)$$

where C_f is the friction coefficient, defined as

$$C_f = \tau_w / (2\rho U_h^2) = (u_\tau / U_h)^2 / 2 \quad (3.6)$$

In this research, the above approximate method was used at the beginning of the simulation. Once a realistic turbulence field had been established, the plane averaged values of $\bar{u}_{1,2} |_{wall}$ and $\bar{u}_{3,2} |_{wall}$ were determined explicitly using the velocity field obtained from the previous time step. Since only one outer fictitious node is used outside of the flow region, the penta-diagonal equation is applicable to all interior nodes except for the fictitious node and the first interior node next to the wall. To solve the PDS, the boundary condition specified previously was used for the fictitious node and the tri-diagonal equation was applied at the first interior node.

As indicated by Carati *et al.* [137], the relative computational cost for different dynamic models is difficult to quantify in a precise manner due to its dependence on the computer configuration and details of the code. Nonetheless, Table 3.1 provides an estimate of the computational cost of different SGS models, including the proposed TDS, PDS, the conventional DM [20], the conventional Smagorinsky Model (SM) with a constant model coefficient [13], and the Dynamic Two-parameter Mixed SGS stress Model (DMM2) introduced by Morinishi and Vasilyev [50]. A comparison was made using the same code structure and initial velocity and pressure fields. The cost was

TABLE 3.1: Comparison of the computational cost

Model	Time per loop (s)	Ratio
SM	28.4	0.53
DM	53.8	1
ILDm (PDS)	56.6	1.05
ILDm (TDS)	55.5	1.03
DMM2	80.2	1.49

measured using the averaged computer time for each time step relative to that of the conventional DM of Lilly. An IBM PC (Pentium IV-2GHz) was used to run the test. From Table 3.1 it is found that the cost for solving the ILDM of Ghosal *et al.* [40] can be reduced to the same order of that for the DM of Lilly, i.e. $ILDm : DM \approx 1 : 1$. Thus, the direct solver provides a practical way to handle the ILDM [40] in turbulence with two homogenous directions, especially for such canonical test flows as turbulent Couette and Poiseuille plane channel flows.

3.3 Results of Numerical Simulations

To validate the proposed discrete scheme for the ILDM, numerical tests have been performed using turbulent Couette flow. Figure 3.1 illustrates the plane and time averaged distribution of C_S in the wall-normal direction. The conventional model constant for the Smagorinsky model, which uses C_S^2 instead of C_S in its definition, generally ranges from 0.065 to 0.12 [1, 139]. From Fig. 3.1 it is observed that the dynamic coefficient predicted by the model vanishes at the wall. For $Re = 2600$, the value of $C_S^{1/2}$ in the core region is 0.078 for the TDS, 0.085 for the PDS, and 0.086 for the DM. For $Re = 4762$, the value of $C_S^{1/2}$ in the core region is 0.051 for the TDS, 0.062 for the PDS, and 0.061 for the DM. By comparison, all of these values lie either within or just below the range of values of the conventional Smagorinsky constant. Fig. 3.1 indicates that in terms of the prediction for C_S , the performance of the PDS

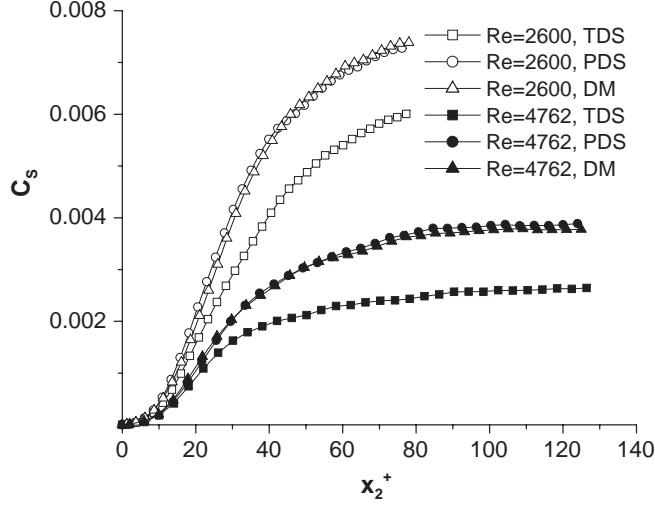


FIGURE 3.1: Averaged distribution of C_s in the wall-normal direction.

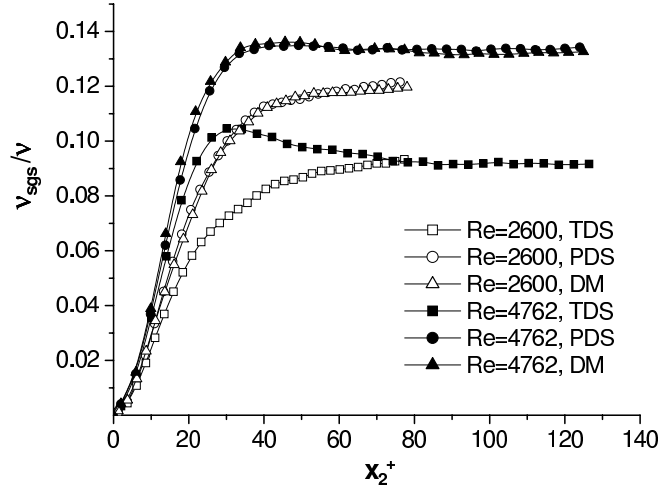


FIGURE 3.2: Averaged SGS viscosity distribution in the wall-normal direction.

scheme approaches more closely to that of the DM than the TDS scheme in the core region. As shown in Fig. 3.2, this conclusion can be extended to the prediction of the SGS viscosity. One possible explanation for this phenomenon is that both the PDS and DM use 3-D filters for the non-boundary nodes, while the TDS uses a mixed filtering scheme based on both 2-D and 3-D filters over the entire domain as discussed earlier. From Fig. 3.2 it is observed that ν_{sgs} vanishes at the wall, which is consistent with the fact that the viscous shear is dominant near the wall. One may have already observed from Fig. 3.1 that for all three modelling schemes, the value of

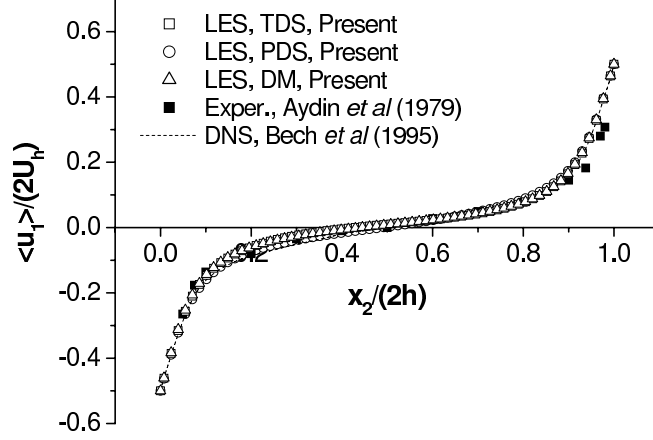


FIGURE 3.3: Averaged non-dimensional velocity profile ($Re = 2600$).

the coefficient C_S for the higher Reynolds number is smaller than that for the lower Reynolds number. However, as shown in Fig. 3.2, the value of the SGS viscosity ν_{sgs} for the higher Reynolds number is larger than that for the lower Reynolds number. From the modelling constitutive equation (1.12) it is understood that ν_{sgs} , which includes information on both C_S and the magnitude of \bar{S}_{ij} , plays a more significant role than C_S (alone) in determining the level of the SGS stress τ_{ij} .

Figure 3.3 shows the mean streamwise velocity profile of $\langle \bar{u}_1 \rangle$ at $Re = 2600$. Here, $\langle \cdot \rangle$ represents a plane and time averaging operation. The velocity profiles obtained using both the TDS and PDS are in good agreement with the experimental result of Aydin and Leutheusser [120] and DNS result of Bech *et al.* [124]. Figures 3.4 and 3.5 plot the mean velocity profiles at the two different Reynolds numbers using wall coordinates, and compare them with the experimental result of Aydin and Leutheusser [121] and the classical two-layer wall-law of von Kármán [140], i.e.

$$\begin{cases} u_1^+ = x_2^+ & (x_2^+ \leq 5) \\ u_1^+ = 2.5 \ln(x_2^+) + 5.5 & (x_2^+ > 30) \end{cases} \quad (3.7)$$

where $u_1^+ = \langle \bar{u}_1 \rangle / u_\tau$ and $x_2^+ = x_2 u_\tau / \nu$.

Figures 3.6 and 3.7 compare the resolved streamwise turbulence intensities with the experimental and DNS results reported in the literature. In *a posteriori* LES

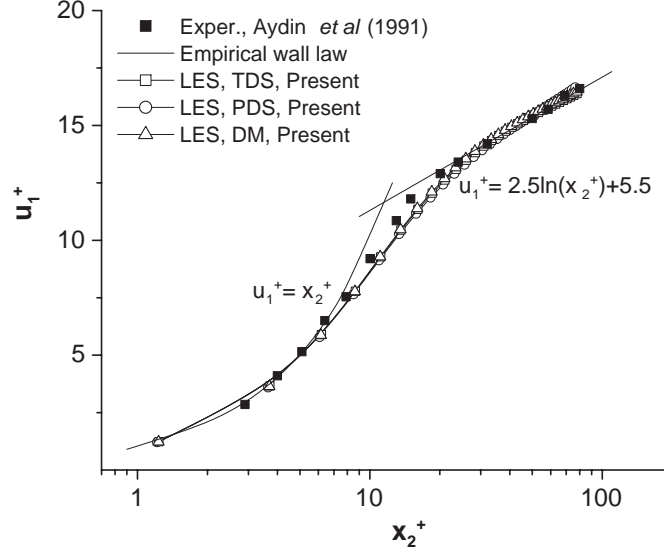


FIGURE 3.4: Averaged velocity profile using wall coordinates ($Re = 2600$).

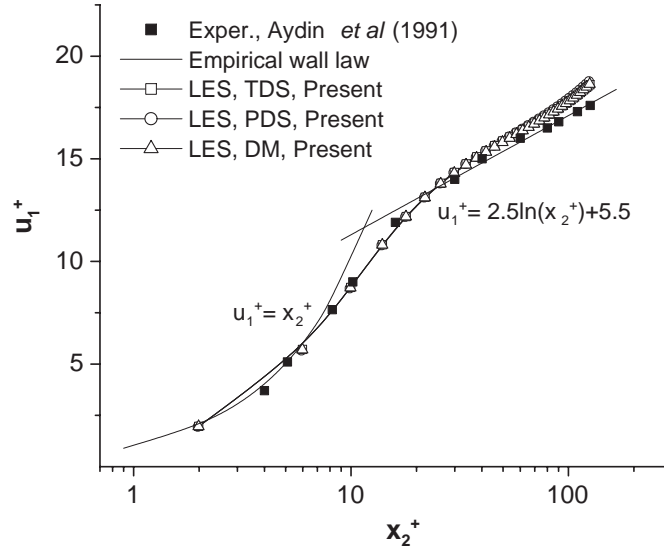


FIGURE 3.5: Averaged velocity profile using wall coordinates ($Re = 4762$).

testing, it is common to compare the predicted streamwise intensity with experimental and DNS results, and a good agreement is often observed [49, 138, 141–146]. It should be recognized, however, that the results obtained from these different approaches are not conceptually equivalent [32] and some researchers [19, 147] compare the LES result with filtered DNS data to minimize the conceptual difference due to the inherent filtering effect of the LES approach. As pointed out by Kravchenko *et al.* [138],

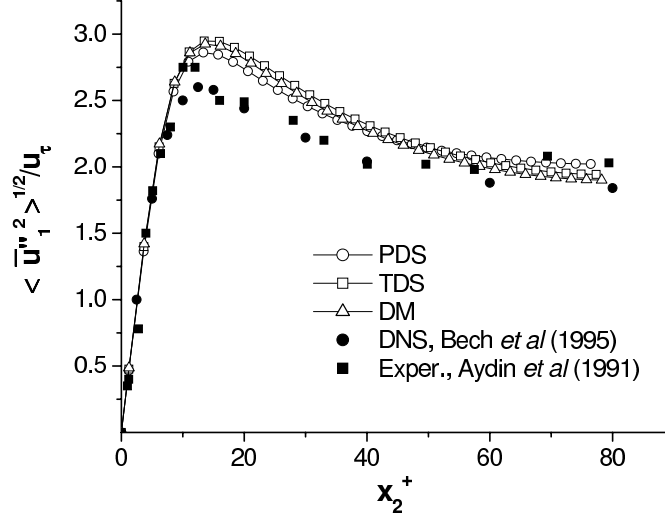


FIGURE 3.6: Resolved streamwise turbulence intensities ($Re = 2600$).

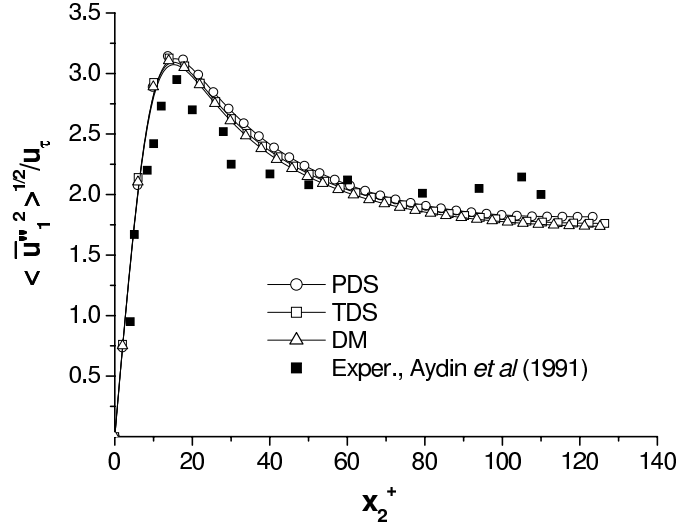


FIGURE 3.7: Resolved streamwise turbulence intensities ($Re = 4762$).

the value of the streamwise turbulence intensity predicted using a coarse grid LES computation is expected to be slightly higher than the experimental and DNS results. The residual velocity component shown in Figs. 3.6 and 3.7 is defined as $\bar{u}_i'' = \bar{u}_i - \langle \bar{u}_i \rangle$. For the TDS, PDS and DM approaches, the peak value of $\langle \bar{u}_1''^2 \rangle^{1/2} / u_\tau$ is about 2.8 at $x_2^+ = 14$ for $Re = 2600$; and about 3.1 at $x_2^+ = 15$ for $Re = 4762$. These values are close to but slightly higher than those reported by Bech *et al.* [124], i.e. 2.6 at $x_2^+ \approx 12$ for $Re = 2600$, and also those reported by Aydin and Leutheusser [121], i.e. 2.8 at $x_2^+ \approx 11$ for $Re = 2600$ and 2.9 at $x_2^+ \approx 16$ for $Re = 4762$.

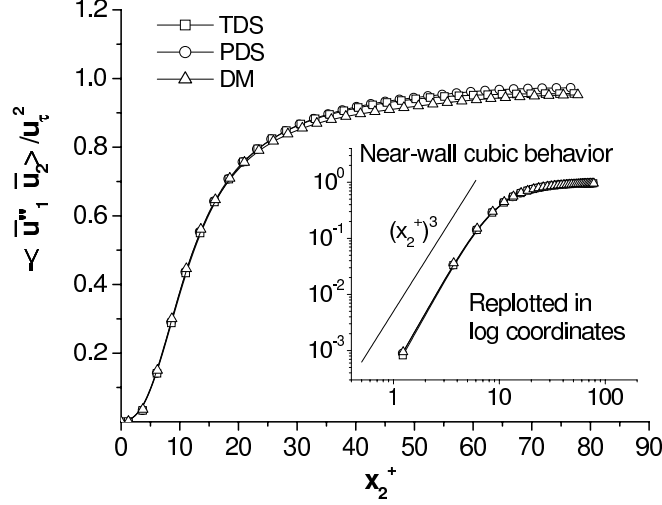


FIGURE 3.8: Resolved Reynolds shear stress distribution ($Re = 2600$).

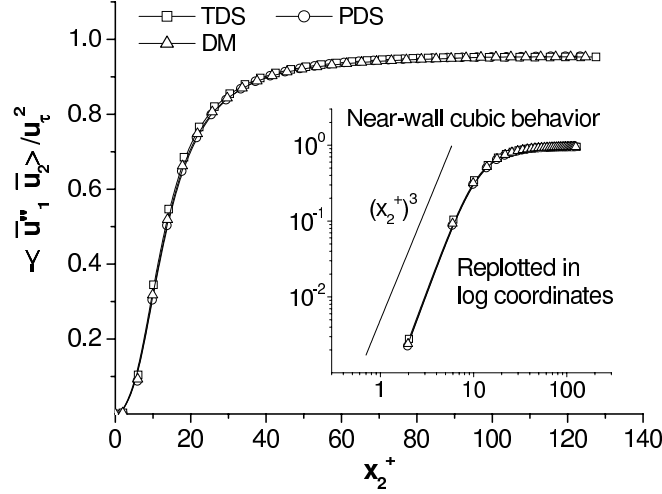


FIGURE 3.9: Resolved Reynolds shear stress distribution ($Re = 4762$).

Figures 3.8 and 3.9 show the resolved Reynolds shear stress distribution in the wall-normal direction. Plane turbulent Couette flow has the unique feature of a constant shear stress distribution, i.e.

$$\mu \cdot \langle \bar{u}_{1,2} \rangle - \rho \langle \bar{u}''_1 \bar{u}''_2 \rangle - \rho \langle \tau_{12} \rangle \approx \tau_{wall} = \rho u_\tau^2 \quad (3.8)$$

The three items on the left hand side of this equation represent the averaged *resolved viscous shear stress*, *resolved Reynolds shear stress* and *subgrid scale shear stress*, respectively. The above approximate equation is obtained from the filtered streamwise

momentum equation based on several assumptions: the flow is steady and homogeneous in the x_1 - x_3 plane, and the mean resolved and SGS velocities normal to the homogeneous plane are zero [141, 143], i.e. $\langle \bar{u}_2 \rangle = 0$ and $\langle \bar{u}_2'' \rangle = 0$. It has been shown both theoretically [3] and numerically [135] that the Reynolds shear stress varies in a cubic manner in the near-wall region. Analysis of the cubic behavior of the resolved Reynolds shear stress for the (dynamic) Smagorinsky type SGS models can be found in the works by Piomelli [1, 38] and Pope [32]. From Figs. 3.8 and 3.9, it is observed that the resolved Reynolds stress diminishes in the vicinity of the wall following the cubic law, i.e. $-\langle \bar{u}_1'' \bar{u}_2 \rangle \propto x_2^{+3}$ for $0 \leq x_2^+ < 5$. In the core region, the resolved Reynolds shear stress becomes dominant, with a value close to unity. It is noted that although the predicted profiles of C_S and ν_{sgs} differ somewhat for the PDS and TDS in the core region, both solution schemes give very similar predictions for the plane and time averaged velocity and resolved Reynolds shear stress profiles. This is because the SGS stress as given by the modelling constitutive relation, i.e. Eq.(1.12), is determined not only by ν_{sgs} (or C_S), but also by the filtered strain rate tensor in terms of its tensorial orientation and magnitude.

The *rate of SGS kinetic energy production* \mathcal{P}_r and the *rate of resolved viscous dissipation* ε_r represent two sinks for the TKE of the filtered scale motions, which are defined as [32]

$$\mathcal{P}_r = -\tau_{ij}^* \bar{S}_{ij} \quad (3.9)$$

and

$$\varepsilon_r = 2\nu \bar{S}_{ij} \bar{S}_{ij} \quad (3.10)$$

respectively. Overall, the term \mathcal{P}_r has a positive value, which represents a net TKE cascade from the filtered to the subgrid scales of motions. However, locally it can have an instantaneous negative value, which indicates a reverse process of the TKE cascade from the residual subgrid scale to the large filtered scale. There is an inconsistency regarding the name of this term in the LES community, and sometimes it is referred to as the SGS dissipation denoted by ε_{sgs} or Π_{sgs} . The author would agree with Pope [32] that it is more appropriate to name it as the rate of SGS TKE production

for a number of reasons: (i) unlike the true dissipation, it represents the rate of transfer of kinetic energy from the filtered motions to the residual motions through an inviscid and inertial process; (ii) it is purely dissipative only for the conventional single-constant-parameter Smagorinsky SGS viscosity model [13] which does not allow for inertial inviscid backscatter; (iii) in physics, when a specific amount of TKE is backscattered from the subgrid to the filtered scales, it is not necessary for all of this TKE to be exactly returned to the subgrid scale via forward scatter but instead some of it could optionally be transported through mechanisms such as advection and diffusion by the filtered scale motions [1,10,32]; and finally (iv) the definition, Eq.(3.9), is analogous to the production term due to the deviatoric part of the Reynolds stress tensor in RANS, i.e. $-\langle u'_i u'_j \rangle_t^* \cdot \langle S_{ij} \rangle_t$, which functions similarly as a TKE source for the (temporal) residual motions. Here $\langle \cdot \rangle_t$ represents the ensemble average used in the classical Reynolds decomposition.

It should be indicated that different SGS models implement different methods to represent SGS TKE transfer between the filtered and subgrid scales via \mathcal{P}_r . The backscatter phenomenon cannot be well simulated using the method presented in this chapter due to the adopted Smagorinsky type SGS model and plane average method. More adequate representation of backscatter will be investigated using mixed and nonlinear SGS modelling approaches later in chapters 4, 6 and 8.

Figure 3.10 shows both the dimensional and nondimensional plane and time averaged distribution of \mathcal{P}_r along the wall-normal direction. From the figure, it is observed that the prediction for \mathcal{P}_r of the PDS is close to that of the DM. The peak value occurs at $x_2^+ = 11$ for $Re = 2600$ and $x_2^+ = 12$ for $Re = 4762$. Figure 3.11 plots the plane and time averaged ε_r distribution obtained using the TDS, PDS and DM. Both the dimensional and non-dimensional plots indicate a peak that grows dramatically in the near-wall region within $x_2^+ < 30$. From previous analysis of the near-wall behavior of \bar{S}_{ij} , it is understood that this peak of resolved viscous dissipation is mainly attributed to the resolved near-wall velocity gradient component $\bar{u}_{1,2}$. Figure 3.12 shows the plane and time averaged ratio of \mathcal{P}_r to ε_r , which indicates the relative amount of the TKE dissipative effect at the filtered scale due to the two

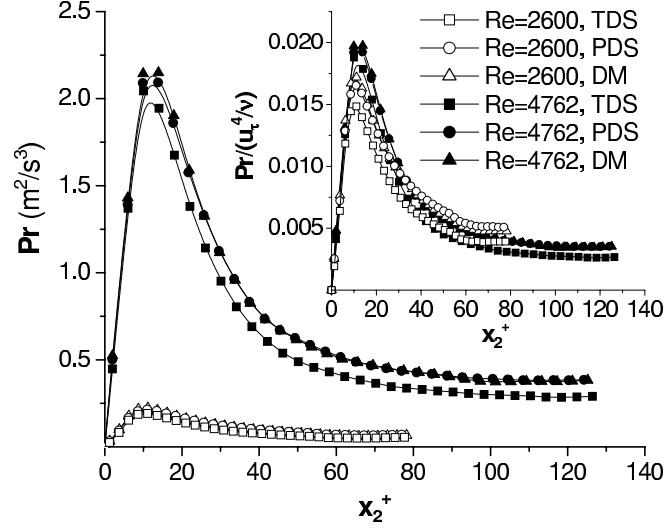


FIGURE 3.10: Averaged rate of SGS TKE production.

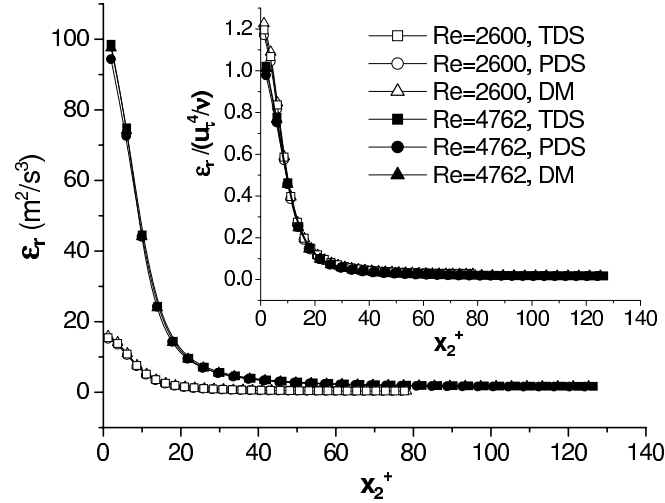


FIGURE 3.11: Averaged rate of the resolved TKE dissipation.

sinks. Obviously, the resolved viscous effect (ε_r) overwhelms the inertial inviscid effect (\mathcal{P}_r) in the near-wall region. However, the inertial inviscid effect keeps increasing relative to the resolved viscous effect as the distance from the wall increases, and the ratio of these two effects becomes relatively constant in the core region. For $Re = 2600$, the stable value of $\mathcal{P}_r/\varepsilon_r$ in the core region is about 14% for the TDS, and 18% for the PDS and DM. For $Re = 4762$ this value is 17% for the TDS, and 24% for the PDS and DM. Again, the prediction of the PDS is closer to that of the DM than that of the TDS for this parameter.

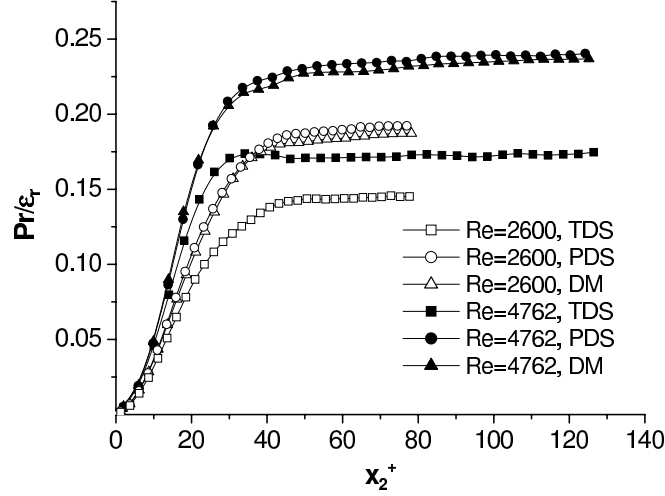


FIGURE 3.12: Ratio of the rate of SGS TKE production to the rate of resolved viscous dissipation.

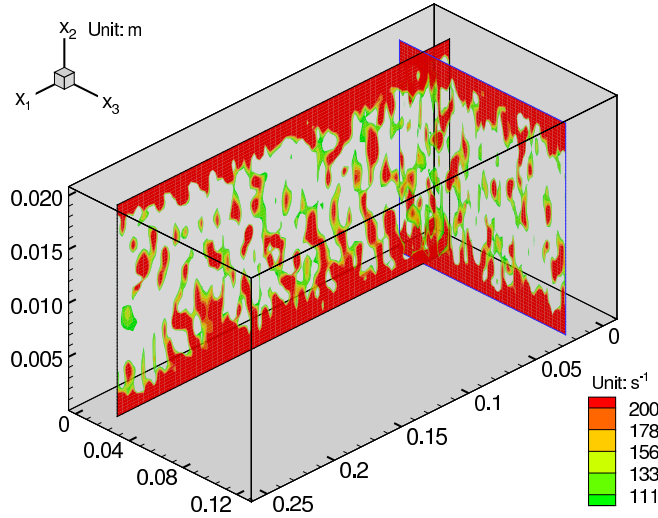


FIGURE 3.13: Instantaneous contours of the spanwise vorticity $\bar{\omega}_3$ ($Re = 2600$).

Finally, Fig. 3.13 shows the magnitude of the spanwise vorticity in the x_1 - x_2 and x_2 - x_3 planes predicted using the PDS for $Re = 2600$. Clearly, the vorticity strength is larger in the near-wall region than in the core region. Also, as illustrated in the figure, some eddy structures can be identified in the near-wall region from the vorticity magnitude contours shown within a carefully selected vorticity magnitude range.

3.4 Conclusions

In order to apply the integral type dynamic localization model (ILDm) [40] for practical simulations of turbulence with two homogeneous dimensions, two efficient direct solution schemes have been developed to solve the integral system, i.e. a five-point scheme (PDS) and a three-point scheme (TDS) based on the 3-D and 2-D discrete filters of Sagaut and Grohens [35]. The CPU time for solving the ILDM of Ghosal *et al.* [40] using the TDS and PDS is thereby reduced to the same order as that for the DM of Lilly [20], which is substantially less than that for the conventional iterative solver [49, 137].

Turbulent Couette flow is used in numerical simulations to validate the proposed approach. The proposed solver can predict prototypical features such as the logarithmic velocity profile, resolved Reynolds shear stress and streamwise turbulence intensity. In the core region, the performance of the PDS is closer to that of the DM than that of the TDS, in terms of predictions of the plane and time averaged wall-normal distribution of the model coefficient, SGS viscosity, and rate of SGS TKE production. However, in terms of predictions for the resolved velocity profile, shear stress, streamwise turbulence intensity, and viscous dissipation, the performance of the TDS, PDS and DM are all very similar. In the vicinity of the wall, the TDS, PDS and DM yield a similar prediction for all the turbulent quantities mentioned above. The author would point out that the direct solution schemes for the ILDM proposed in this chapter are only appropriate for turbulent flows with two homogeneous dimensions, and a generalized “fast solver” for non-homogeneous turbulence based on a different discrete filtering scheme remains yet to be developed.

Chapter 4

An Integral Type Localization Dynamic Two-Parameter Subgrid-Scale Model: Formulation and Simulation

4.1 Introduction

In this chapter, the so-called *Mixed Models* (MM) for the SGS stresses are investigated. There are a few different types of MM depending on the method used for decomposing the SGS stresses and the constitutive relation selected for building the corresponding model. The most popular approach combines the modified Leonard stress (different researchers may have different definitions, featured by the coefficient C_L) with an SGS viscosity model (featured by the coefficient C_S). Studies of the C_L - C_S *mixed model* include the works of Zang *et al.* [37], Liu *et al.* [25], Vreman *et al.* [148], Salvetti and Banerjee [48], Horiuti [143], Sarghini *et al.* [146], Meneveau and Katz [44], and Morinishi and Vasilyev [50]. Horiuti [143] observed that the predicted magnitude of the backscatter of TKE using Bardina's scale similarity model is larger than the DNS value. To overcome this drawback inherent to the model, Horiuti [143] proposed the so-called *filtered Bardina's model*, which approximates the SGS Reynolds stress as: $R_{ij} \approx C_B \overline{(\bar{u}_i - \bar{u}_i)(\bar{u}_j - \bar{u}_j)}$. Based on the coefficient C_B , Horiuti [143] also developed a general dynamic three-parameter mixed model, i.e. the *dynamic C_L - C_B - C_S mixed model*. However, this model is demanding in computa-

tional cost, since it requires a 3×3 matrix system composed of terms with complex filtering processes to be solved at each node. For practical purposes, Horiuti [143] investigated two dynamic two-parameter mixed models, i.e. the C_L - C_S and C_B - C_S models, which are obtained from the general dynamic C_L - C_B - C_S model using some specific restrictions. Notwithstanding the existence of other types of mixed models, this chapter will focus on the popular C_L - C_S type *Dynamic Two-parameter Mixed Models* (DMM2).

As it is well known in the classical optimization procedures of Germano *et al.* [19] and Lilly [20] for obtaining the *Dynamic One-parameter Smagorinsky Model* (DSM1 or simply DM) using the least squares method, a mathematical inconsistency exists in processing a filtering term. Such a mathematical inconsistency was removed by Ghosal *et al.* [40] in their consistent localization approach using the functional variational method. Similar to the one-parameter case, in current approaches using the DMM2, a mathematical inconsistency also exists and thus far the DMM2 has not been strictly localized. A major objective of this chapter is to deduce a new optimal localization DMM2 and eliminate the mathematical inconsistency following the approach used for the DSM1 by Ghosal *et al.* [40].

This chapter is organized as follows. In section 4.2, the mixed models, especially the C_L - C_S type mixed model (and its two base models) will be reviewed. In section 4.3, a new localization DMM2 will be strictly developed using the functional variational method. In section 4.4, results of the numerical simulation of turbulent Couette flow will be presented. Conclusions will be summarized in section 4.5.

4.2 Mixed Models

In this section, the idea of the mixed SGS model proposed by Bardina [18,34] will first be summarized, and then the C_L – C_S type mixed models encountered in the literature will be reviewed.

4.2.1 Bardina’s Mixed Model

To build the scale similarity model, Bardina [18,34] utilized information from the strain rate tensor \bar{S}_{ij} and tensor B_{ij} (see Eq.(1.9)), i.e.

$$\tau_{ij} = C_r(B_{ij} - \frac{1}{3}B_{kk}\bar{S}_{ij}) \quad (4.1)$$

where C_r is a model constant, which according to Speziale [149], should be 1 in order to keep the model’s Galilean invariance. From Eq.(4.1) it is understood that the scale similarity model of Bardina [18,34] is actually a *Constant One-parameter Mixed Model* (CMM1), consisting of two elements, i.e. B_{ij} and $B_{kk}\bar{S}_{ij}$. The second term can be generally understood as an SGS viscosity model, for its tensorial alignment is controlled by \bar{S}_{ij} and the term B_{kk} functions in a similar way to the classical Smagorinsky SGS viscosity. Bardina [18] also extensively studied different types of SGS viscosity models. He concluded that the scale-similarity model gives a good representation of the local SGS Reynolds stresses, however, is almost non-dissipative and hence does not provide a mean energy balance. In contrast, the SGS viscosity model provides a proper mean energy balance, but is incapable of predicting the correct SGS Reynolds stresses. To overcome the weaknesses of both modelling approaches, Bardina [18] introduced the idea of a *Two-parameter Mixed Model* (MM2) into the LES community. His model relies on the classical Leonard’s SGS stress decomposition and *Constant Two-parameter Mixed Model* (CMM2), i.e.

$$\begin{aligned} \tau_{ij}^* &= -2\nu_t\bar{S}_{ij} + C_r B_{ij}^* \\ &= -2C_S\bar{\Delta}^2|\bar{S}|\bar{S}_{ij} + C_r(\bar{u}_i\bar{u}_j - \bar{\bar{u}}_i\bar{\bar{u}}_j)^* \end{aligned} \quad (4.2)$$

where the two constant parameters are determined as $C_S = 0.165 \sim 0.19$ and $C_r = 1.1$, respectively. Based on Germano's modified decomposition (Eq.(1.6)), Horiuti [142,143,150] extensively investigated the scale similarity model. He revised Bardina's model as a *Dynamic One-parameter Mixed Model* (DMM1)

$$\tau_{ij}^* = L_{ij}^{m*} + (C_B - 1)[(\bar{u}_i - \bar{\bar{u}}_i)(\bar{u}_j - \bar{\bar{u}}_j)]^* \quad (4.3)$$

where C_B was determined using the standard dynamic procedure of Germano *et al.* [19] and Lilly [20]. By comparison with the DNS data, Horiuti [143] also indicated that one drawback of Bardina's scale similarity model is that it over-predicts the backscatter and underestimates the dissipation. It should be indicated that both Bardina's original CMM2 (Eq.(4.2)) and the DMM1 (Eq.(4.3)) revised by Horiuti [143] are not of the C_L – C_S type. The CMM2 of Bardina [18] relies on both the SGS viscosity and the combined effect of C_{ij} and R_{ij} , i.e. B_{ij} . However, the DMM1 of Horiuti [143] mixes the explicit modified Leonard term and the approximate SGS Reynolds stress term introduced by Bardina [18] (see Eq.(1.8)).

4.2.2 The C_L – C_S Type Mixed Models

The essential idea of the C_L – C_S mixed model is to let the SGS viscosity model and the scale similarity model work dynamically as a remedy for each other so that both backscatter and dissipation can be correctly predicted. The C_L – C_S type mixed models found in the literature can be generally categorized as follows: (1) DMM1, (2) CMM2, and (3) DMM2.

The first C_L – C_S type DMM1 was introduced by Zang *et al.* [37]. In their modelling approach, the combined effect of the C_{ij}^m and R_{ij}^m is approximated using the Smagorinsky model, while L_{ij}^{m*} is calculated directly. Therefore, the tracefree \bar{G} -level stress is

$$\tau_{ij}^* = -2C_S \bar{\Delta}^2 |\bar{S}| \bar{S}_{ij} + L_{ij}^{m*} \quad (4.4)$$

while the tracefree \tilde{G} -level stress is given by

$$T_{ij}^* = -2C_S \tilde{\Delta}^2 \left| \tilde{S} \right| \tilde{S}_{ij} + L_{ij}^{Z*} \quad (4.5)$$

where L_{ij}^Z is a \tilde{G} -level modified Leonard type stress defined by Zang *et al.* [37] as

$$L_{ij}^Z = (\widetilde{\bar{u}_i \bar{u}_j} - \tilde{\bar{u}}_i \tilde{\bar{u}}_j) \quad (4.6)$$

Following the dynamic procedure of Lilly [20] and using the assumption of ISI, Zang *et al.* [37] obtained the following DMM1 coefficient:

$$C_S = -\frac{(\mathcal{L}_{ij}^* - \mathcal{H}_{ij}^{Z*})M_{ij}}{M_{ij}M_{ij}} \quad (4.7)$$

where

$$\mathcal{H}_{ij}^Z = L_{ij}^Z - \tilde{L}_{ij}^m = \widetilde{\bar{u}_i \bar{u}_j} - \tilde{\bar{u}}_i \tilde{\bar{u}}_j \quad (4.8)$$

Vreman *et al.* [148] proposed that the \bar{G} -level stress τ_{ij} should be entirely expressed using \bar{u} and the \tilde{G} -level stress T_{ij}^* should be entirely expressed using \tilde{u} . In their opinion, the term T_{ij}^* introduced by Zang *et al.* [37], i.e. Eq.(4.5), is inconsistent because its SGS viscosity part relies on \tilde{u} , however, its similarity part, L_{ij}^Z , is based on \bar{u} . Vreman *et al.* [148] proposed an improved C_L - C_S type DMM1 by modifying the similarity part of the \tilde{G} -level stress as follows

$$L_{ij}^V = \widetilde{\tilde{u}_i \tilde{u}_j} - \tilde{\bar{u}}_i \tilde{\bar{u}}_j \quad (4.9)$$

Consequently, in their modified model, \mathcal{H}_{ij}^Z is replaced by

$$\begin{aligned} \mathcal{H}_{ij} &= L_{ij}^V - \tilde{L}_{ij}^m \\ &= \left(\widetilde{\tilde{u}_i \tilde{u}_j} - \tilde{\bar{u}}_i \tilde{\bar{u}}_j \right) - \left(\widetilde{\bar{u}_i \bar{u}_j} - \bar{\bar{u}}_i \bar{\bar{u}}_j \right) \end{aligned} \quad (4.10)$$

Later, Vreman *et al.* [147] performed an extensive study of this DMM1 in comparison with five other SGS models using a weakly compressible turbulent mixing layer flow.

Their DMM1 showed a mechanism to mimic the backscatter of energy from the sub-grid to the resolved scales, although the predicted value was found to be a bit lower than the filtered DNS results.

Liu *et al.* [25] proposed a C_L – C_S type CMM2, which is

$$\tau_{ij} = -2C_S^2 \bar{\Delta}^2 |\bar{S}| \bar{S}_{ij} + C_L \mathcal{L}_{ij} \quad (4.11)$$

By analyzing PIV data, Liu *et al.* [25] determined that $C_S = 0.1 \sim 0.2$ and $C_L = 1$. It should be noted that C_S^2 in the above model strictly constrains the SGS viscosity part of the mixed model to be purely dissipative. Thus, the possibility of backscatter and numerical instability due to a negative value of C_S (when the SGS viscosity part is defined as $-2C_S \bar{\Delta}^2 |\bar{S}| \bar{S}_{ij}$) is avoided.

Salvetti and Banerjee [48] first applied the dynamic procedure to the two-parameter mixed model and obtained a C_L – C_S type DMM2. Since their work was carried out almost at the same time as Vreman *et al.* [148], they did not incorporate the idea of the modified L_{ij}^V and \mathcal{H}_{ij} into their work. This step was accomplished later by Horiuti (1997), and Morinishi and Vasilyev [50], as will be discussed shortly. The similarity part of the \tilde{G} -level stress tensor of Salvetti and Banerjee [48] was still based on the definition of Zang *et al.* [37],

$$T_{ij}^* = -2C_S \tilde{\Delta}^2 |\tilde{S}| \tilde{S}_{ij} + C_L L_{ij}^{Z*} \quad (4.12)$$

and their \tilde{G} -level stress takes the following form based on L_{ij}^m :

$$\tau_{ij}^* = -2C_S \bar{\Delta}^2 |\bar{S}| \bar{S}_{ij} + C_L L_{ij}^{m*} \quad (4.13)$$

Consequently, \mathcal{H}_{ij}^Z instead of \mathcal{H}_{ij} was still used in their model. Applying the least squares method and the assumption of ISI, the result of Salvetti and Banerjee [48]

for incompressible flow can be rewritten using matrices as

$$\begin{bmatrix} \mathcal{H}_{ij}^{Z*} \mathcal{H}_{ij}^{Z*} & -\mathcal{H}_{ij}^{Z*} M_{ij} \\ -\mathcal{H}_{ij}^{Z*} M_{ij} & M_{ij} M_{ij} \end{bmatrix} \cdot \begin{bmatrix} C_L \\ C_S \end{bmatrix} = \begin{bmatrix} \mathcal{L}_{ij}^* \mathcal{H}_{ij}^{Z*} \\ -\mathcal{L}_{ij}^* M_{ij} \end{bmatrix} \quad (4.14)$$

By adopting the improved definition of the $\tilde{\tilde{G}}$ -level stress of Vreman *et al.* [148], i.e. L_{ij}^V (Eq.(4.9)), Horiuti [143], and Morinishi and Vasilyev [50] revisited the DMM2 of Salvetti and Banerjee [48], and provided a modified C_L – C_S type DMM2 under the assumption of ISI. The system for the model coefficients is the same as given by Eq.(4.14), except that \mathcal{H}_{ij} was used to replace \mathcal{H}_{ij}^Z . Two methods for increasing the numerical stability were also adopted in the approach of Morinishi and Vasilyev [50], i.e. (i) similar to the idea of Liu *et al.* [25], C_S^2 was used to restrict the SGS viscosity coefficient to be positive, and (ii) a spatial averaging was applied to each term in the system equation (4.14) in the homogeneous plane.

4.3 A New Integral Type Localization DMM2

As discussed previously, in the approach of Ghosal *et al.* [40], a dynamic model in the form of a FIE2 controls the instantaneous spatial optimal distribution of the single model coefficient C_S , and it is therefore called by its inventors a *localization* DSM1. The objective of this section is to similarly propose a new optimal C_L – C_S type DMM2, which should also be mathematically consistent.

4.3.1 Model Development

The \bar{G} -level and $\tilde{\tilde{G}}$ -level SGS stresses introduced by Morinishi and Vasilyev [50], are adopted to build and optimize the new DMM2, i.e. Eq.(4.13) is used for τ_{ij}^* and

$$T_{ij}^* = -2C_S \tilde{\tilde{\Delta}}^2 \left| \tilde{\tilde{S}} \right| \tilde{\tilde{S}}_{ij} + C_L L_{ij}^{V*} \quad (4.15)$$

is used for T_{ij}^* . Using the definitions in Eqs.(4.13) and (4.15), the traceless form of the Germano identity can be expressed specifically as

$$\mathcal{L}_{ij}^* = C_L \mathcal{H}_{ij}^* - C_S \alpha_{ij} + \widetilde{\beta_{ij} C_S} \quad (4.16)$$

The local error tensor function is still defined as the residual of Eq.(4.16) and adopts the following form due to the presence of C_L :

$$E_{ij}(C_L, C_S, \mathbf{x}) = \mathcal{L}_{ij}^* - C_L \mathcal{H}_{ij}^* + C_S \alpha_{ij} - \widetilde{\beta_{ij} C_S} \quad (4.17)$$

The definition of the local error density function Q remains as the contraction of E_{ij} , as shown in Eq.(1.21).

Similar to the difficulty encountered in the optimization process for the DSM1 introduced by Lilly [20], the difficulty for optimizing the DMM2 using the variational method mainly comes from the treatment of the filtered term, i.e. $\widetilde{\beta_{ij} C_S}$. As discussed previously, in the DMM community, this difficulty has usually been avoided by using the assumption of ISI, which assumes C_S to be a constant in $\widetilde{\beta_{ij} C_S}$ so that it can be readily extracted from this filtering process and thus Q can be minimized using the least squares method. However, this treatment makes the definition and property of C_S mathematically inconsistent in the third and fourth terms on the right hand side of Eq.(4.17). This mathematical inconsistency can be avoided by minimizing the integral of the local error function, which is a functional of C_L and C_S

$$\mathcal{F}(C_S, C_L) = \int_{\Sigma} E_{ij} E_{ij} d\mathbf{x} \quad (4.18)$$

where the symbol Σ represents the physical domain.

According to functional variational theory, the integral error functional \mathcal{F} is minimal if the following variational conditions hold:

$$\begin{cases} \delta \mathcal{F} |_{C_L} = 2 \int_{-\infty}^{\infty} E_{ij} \delta E_{ij} |_{C_L} d\mathbf{x} = 0 \\ \delta \mathcal{F} |_{C_S} = 2 \int_{-\infty}^{\infty} E_{ij} \delta E_{ij} |_{C_S} d\mathbf{x} = 0 \end{cases} \quad (4.19)$$

Substituting (4.17) into δE_{ij} in the above equations to obtain

$$\begin{cases} 2 \int_{-\infty}^{\infty} E_{ij}(-\mathcal{H}_{ij}^*) \delta C_L d\mathbf{x} = 0 \\ 2 \int_{-\infty}^{\infty} E_{ij}(\alpha_{ij} \delta C_S - \widetilde{\beta_{ij} \delta C_S}) d\mathbf{x} = 0 \end{cases} \quad (4.20)$$

On inverting the sequence of integration in the second equation and renaming the variables, the following system is obtained

$$\begin{cases} \int_{-\infty}^{\infty} E_{ij} \mathcal{H}_{ij}^* \cdot \delta C_L d\mathbf{x} = 0 \\ \int_{-\infty}^{\infty} [\alpha_{ij} E_{ij} - \beta_{ij} \int_{-\infty}^{\infty} E_{ij} G(\mathbf{y}, \mathbf{x}) d\mathbf{y}] \cdot \delta C_S d\mathbf{x} = 0 \end{cases} \quad (4.21)$$

for all δC_L and $\delta C_S \in \Upsilon$, where Υ is the solution space for the model coefficients. Thus the following system must hold:

$$\begin{cases} E_{ij}(\mathbf{x}) \mathcal{H}_{ij}^*(\mathbf{x}) = 0 \\ \alpha_{ij}(\mathbf{x}) E_{ij}(\mathbf{x}) - \beta_{ij}(\mathbf{x}) \int_{-\infty}^{\infty} E_{ij}(\mathbf{y}) G(\mathbf{y}, \mathbf{x}) d\mathbf{y} = 0 \end{cases} \quad (4.22)$$

which governs the optimal distribution of the two model coefficients. As such, the goal of localization has been achieved and the mathematical inconsistency is removed. If $\alpha_{ij}(\mathbf{x})\alpha_{ij}(\mathbf{x}) \neq 0$, the second equation can be rearranged as a Fredholm equation of the second kind, which is similar to the result obtained by Ghosal *et al.* (1995) in the one-parameter case. The governing system (4.22) has two integral equations with two unknown functions, i.e. C_S and C_L . No special assumptions have yet been made and thus this governing system holds for both homogeneous and non-homogeneous turbulent flows. This new model is based on minimizing the functional \mathcal{F} , the integral form of the error function Q , and thus it will be referred to as an *Integral type Localization Dynamic Two-parameter Mixed Model* (ILDMM2). For the same reason, the author would also suggest referring to the optimal DSM1 of Ghosal *et al.* [40] as an *Integral type Localization DSM1* (ILDMM1). For the ILDMM2, both the Smagorinsky and similarity parts can account for backscatter of SGS TKE from small-scale to large-scale motions. However, excessive backscatter of SGS TKE may

result in instability. An option which attempts to prevent this potential instability is to introduce the restriction of $C_S \geq 0$ into the above system, and only allow the similarity part to be responsible for backscatter.

4.3.2 An Iterative Solver

On substituting the definition of E_{ij} , i.e. Eq.(4.17), Eq.(4.22) becomes a complex integral system involving a number of convolutions. Solving this integral system also becomes a challenging problem, which determines the practicability of the proposed ILDMM2. The system given by Eq.(4.22) can be rearranged as follows

$$\begin{bmatrix} A_{11} & A_{12} \\ A_{21} & A_{22} \end{bmatrix} \cdot \begin{bmatrix} C_L \\ C_S \end{bmatrix} = \begin{bmatrix} B_1 \\ B_2 \end{bmatrix} \quad (4.23)$$

or $\mathbf{AC} = \mathbf{B}$ for brevity. Here,

$$\begin{bmatrix} A_{11} & A_{12} \\ A_{21} & A_{22} \end{bmatrix} = \begin{bmatrix} \mathcal{H}_{ij}^* \mathcal{H}_{ij}^* & -\mathcal{H}_{ij}^* \alpha_{ij} \\ -\mathcal{H}_{ij}^* \alpha_{ij} & \alpha_{ij} \alpha_{ij} \end{bmatrix} \quad (4.24)$$

$$B_1 = \mathcal{H}_{ij}^*(\mathbf{x}) \mathcal{L}_{ij}^*(\mathbf{x}) - \mathcal{H}_{ij}^*(\mathbf{x}) \int_{-\infty}^{\infty} \beta_{ij}(\mathbf{y}) C_S(\mathbf{y}) G(\mathbf{x}, \mathbf{y}) d\mathbf{y} \quad (4.25)$$

and

$$\begin{aligned} B_2 = & -\alpha_{ij}(\mathbf{x}) \mathcal{L}_{ij}^*(\mathbf{x}) \\ & + \alpha_{ij}(\mathbf{x}) \int_{-\infty}^{\infty} \beta_{ij}(\mathbf{y}) C_S(\mathbf{y}) G(\mathbf{x}, \mathbf{y}) d\mathbf{y} \\ & + \beta_{ij}(\mathbf{x}) \int_{-\infty}^{\infty} \mathcal{L}_{ij}^*(\mathbf{y}) G(\mathbf{y}, \mathbf{x}) d\mathbf{y} \\ & - \beta_{ij}(\mathbf{x}) \int_{-\infty}^{\infty} \mathcal{H}_{ij}^*(\mathbf{y}) C_L(\mathbf{y}) \cdot G(\mathbf{y}, \mathbf{x}) d\mathbf{y} \\ & + \beta_{ij}(\mathbf{x}) \int_{-\infty}^{\infty} \alpha_{ij}(\mathbf{y}) C_S(\mathbf{y}) G(\mathbf{y}, \mathbf{x}) d\mathbf{y} \\ & - \beta_{ij}(\mathbf{x}) \int_{-\infty}^{\infty} \int_{-\infty}^{\infty} \beta_{ij}(\mathbf{z}) C_S(\mathbf{z}) G(\mathbf{y}, \mathbf{z}) \cdot G(\mathbf{y}, \mathbf{x}) d\mathbf{z} d\mathbf{y} \end{aligned} \quad (4.26)$$

The instantaneous integral system (4.23) can be solved using the following relaxation scheme:

$$\begin{bmatrix} C_L \\ C_S \end{bmatrix}^{new} = \begin{bmatrix} C_L \\ C_S \end{bmatrix}^{old} + R_S \left\{ \frac{1}{A_{11}A_{22} - A_{12}A_{21}} \cdot \begin{bmatrix} B_1A_{22} - B_2A_{12} \\ B_2A_{11} - B_1A_{21} \end{bmatrix} - \begin{bmatrix} C_L \\ C_S \end{bmatrix}^{old} \right\} \quad (4.27)$$

where R_S is an iterative relaxation factor for correcting the instantaneous coefficients, which can be flexibly chosen within the range $(0.6 \sim 1)$. To increase the stability of the entire system, a second relaxation scheme is adopted between two adjacent time steps, i.e. $n - 1$ and n :

$$\begin{bmatrix} C_L \\ C_S \end{bmatrix}^{(n)} = \begin{bmatrix} C_L \\ C_S \end{bmatrix}^{(n-1)} + \begin{bmatrix} R_{C_L} & 0 \\ 0 & R_{C_S} \end{bmatrix} \cdot \left\{ \begin{bmatrix} C_L \\ C_S \end{bmatrix}^{(n)} - \begin{bmatrix} C_L \\ C_S \end{bmatrix}^{(n-1)} \right\} \quad (4.28)$$

where R_{C_L} and R_{C_S} are the relaxation factors both set to be 0.8. Figure 4.1 shows that the solver demonstrates an exponential convergence performance at the beginning of the iteration, which is often observed in linear systems. Figure 4.1 was obtained with $R_S = 0.8$. The residual shown in the figure is the residual of Eq.(4.23), which is

$$\begin{aligned} \text{Res} &= \sum_{i,j,k} \|\mathbf{AC} - \mathbf{B}\|_{i,j,k} \\ &= \sum_{i,j,k} \left[(A_{11}C_L + A_{12}C_S - B_1)^2 + (A_{21}C_L + A_{22}C_S - B_2)^2 \right]_{i,j,k}^{0.5} \end{aligned} \quad (4.29)$$

where i, j, k run through the entire domain of 46^3 internal nodes. The residual after the first iteration is 1.51×10^5 , and drops to 1.85 by the 11th iteration. Figure 4.1 indicates that the proposed iterative solver is capable of decreasing the residual by 5 orders of magnitude. Ten iterations were used in the numerical test, which gave a final residual of about 1.88 (1.94×10^{-5} at each node).

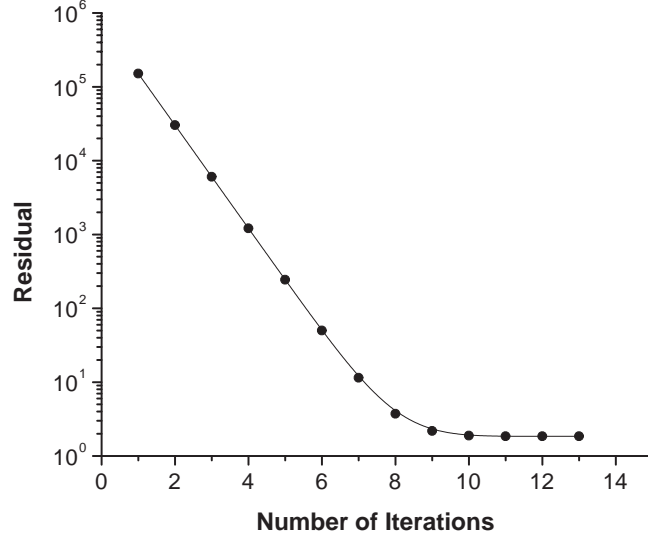


FIGURE 4.1: Convergence performance of the solver ($Re = 2600$).

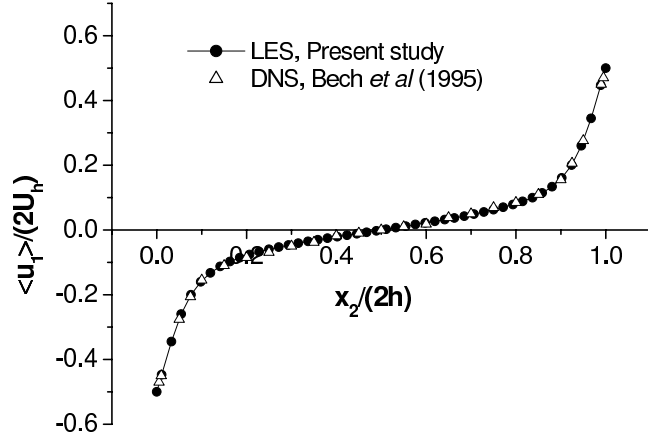


FIGURE 4.2: Dimensionless mean velocity profile ($Re = 2600$).

4.4 Results of Numerical Simulations

4.4.1 Predicted Features of Turbulent Couette Flow

Figure 4.2 shows the profile of mean streamwise velocity along the wall-normal direction, obtained using both spatial averaging in the homogeneous plane and time averaging for 2000 time steps. The velocity profile is in good agreement with the DNS result obtained by Bech *et al.* [124]. Figure 4.3 plots the mean velocity profile

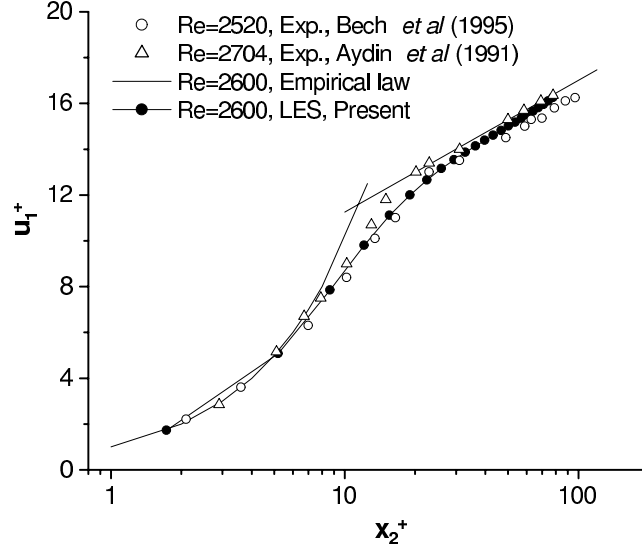


FIGURE 4.3: Mean velocity profile using wall coordinates ($Re = 2600$).

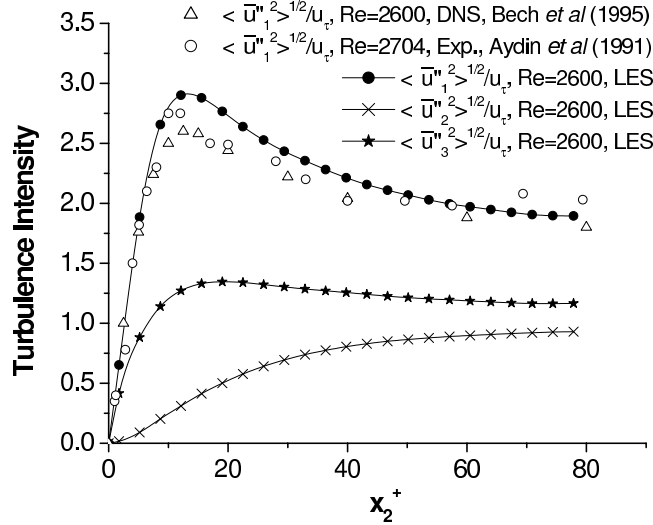


FIGURE 4.4: Averaged resolved turbulence intensities ($Re = 2600$).

using wall coordinates, which is shown to agree well with the experimental results of Aydin and Leutheusser [121] and Bech *et al.* [124], and von Kármán's classical empirical relation for wall-bounded turbulent flows, i.e. Eq.(3.7).

Figure 4.4 compares the resolved turbulence intensities for the three velocity components and indicates that the streamwise component dominates the turbulence kinetic energy. The characteristic anisotropy of the three fluctuating velocity components persists into the core region. Figure 4.5 gives the resolved Reynolds shear stress

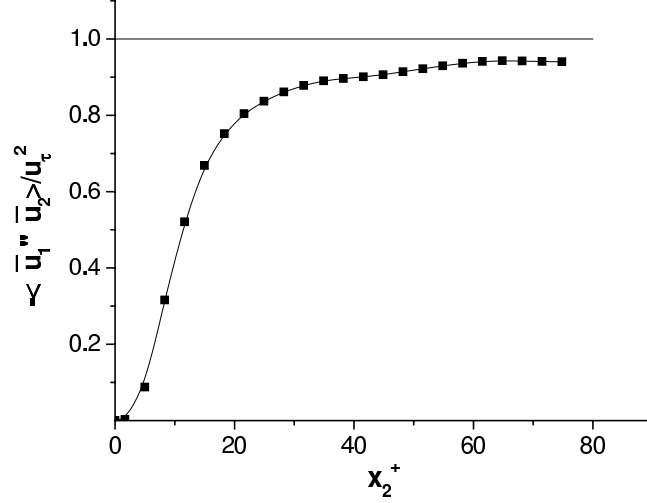


FIGURE 4.5: Averaged resolved Reynolds shear stress distribution ($Re = 2600$).

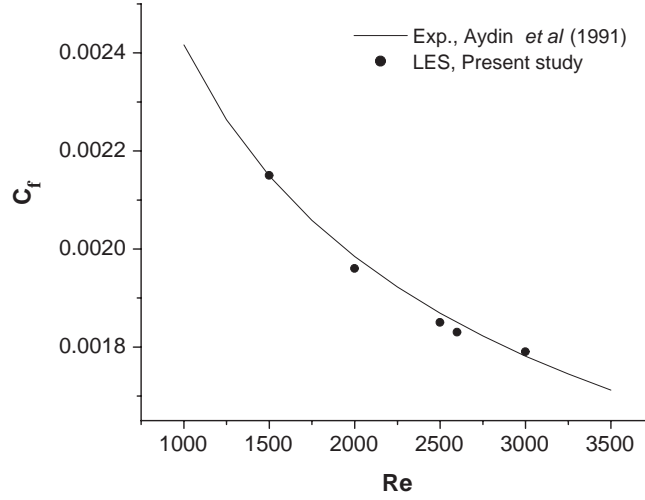


FIGURE 4.6: Comparison of the friction coefficient.

distribution in the wall-normal direction. At the center of the channel, $-\langle \bar{u}_1'' \bar{u}_2'' \rangle / u_\tau^2$ is less than but close to 1, as shown in Figure 4.5. Figure 4.6 compares the friction coefficient predicted using the proposed ILDM2 with the experimental wall friction law of Aydin and Leutheusser [121], i.e. Eq.(3.5), which shows good agreement.

Figures 4.7 and 4.8 plot the averaged distributions of C_L and C_S in the wall-normal direction. In the literature, the range of C_L for the scale similarity models varies from 0.45 to 1 (Sagaut and Grohens [35], and Meneveau and Katz [31]). Figure 4.7 indicates that for the proposed ILDM2, C_L has a peak value of 0.26 at

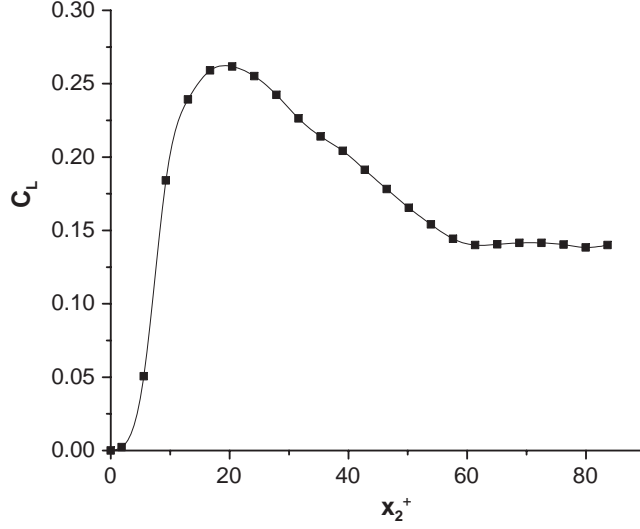


FIGURE 4.7: Averaged distribution of C_L in the wall-normal direction ($Re = 2600$).

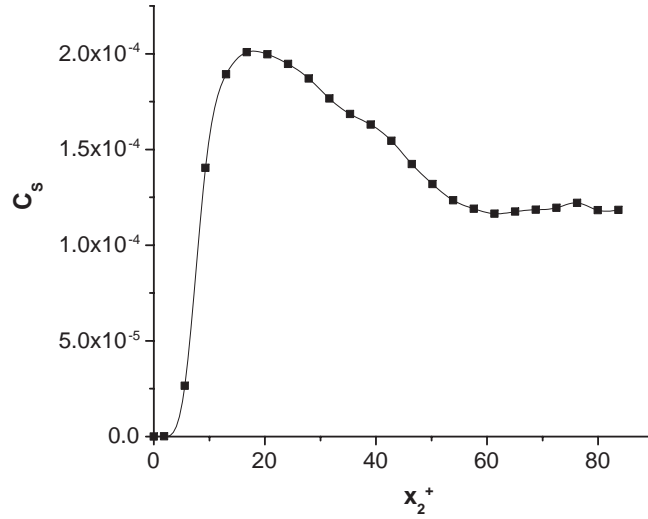


FIGURE 4.8: Averaged distribution of C_S in the wall-normal direction ($Re = 2600$).

$x_2^+ \approx 18$ and is about 0.14 in the central region. The conventional value for the Smagorinsky model coefficient, which uses C_S^2 instead of C_S in defining the SGS viscosity, ranges from 0.065 to 0.12 [1,139]. Figure 4.8 shows that $|C_S|^{1/2}$ of the ILDMM2 has a peak value of 0.014 at $x_2^+ \approx 18$ and is about 0.011 in the central region, which values are only 10 ~ 20% of that of the conventional Smagorinsky model coefficient as indicated above. The ILDMM2 developed in this chapter has two self-adjusting dynamic coefficients, which allows more flexibility (degrees of freedom) in the values of

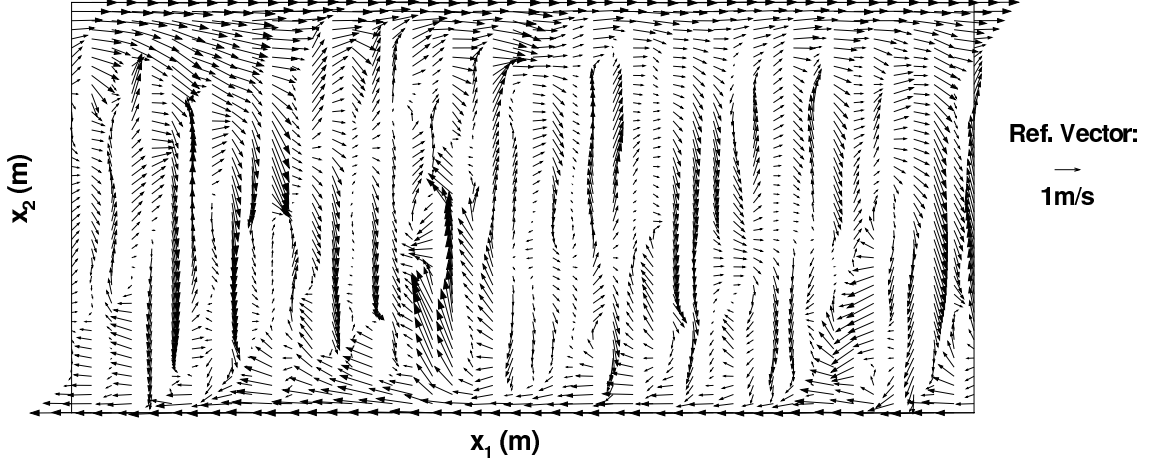


FIGURE 4.9: Instantaneous velocity field in the central x_1 - x_2 plane ($Re = 2600$).

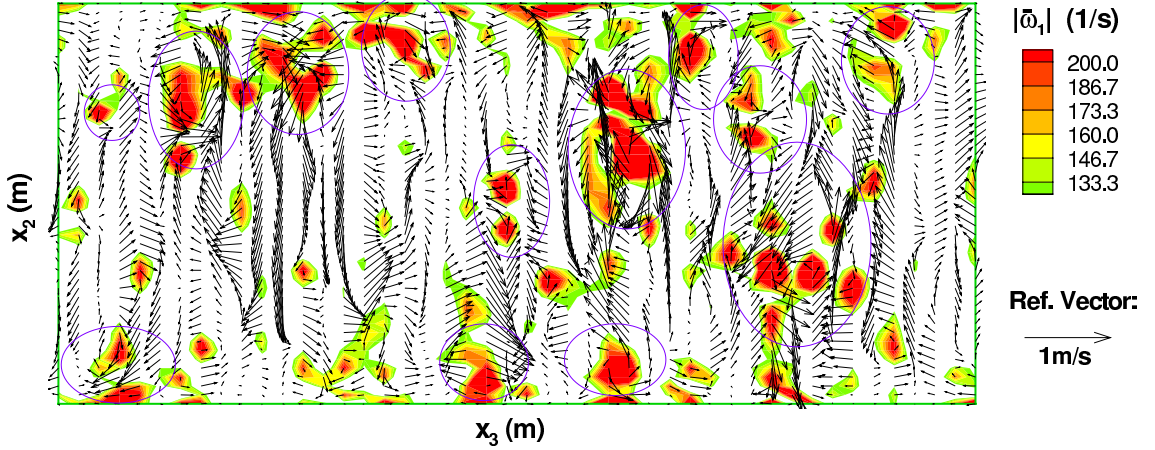


FIGURE 4.10: Instantaneous velocity and vorticity fields in the central x_2 - x_3 plane ($Re = 2600$).

the coefficients. This suggests the existence of multiple possibilities for the coefficient distributions. For example, we have at least the following special cases which can be deduced from the ILDMM2 and are reported to work well for some specific flows in the literature: if $C_L \equiv 0$, the ILDMM2 reduces to the DSM1 (e.g. Lilly [20]); if $C_S \equiv 0$, the model reduces to a scale similarity model (e.g. Bardina [18]); if $C_L \equiv 1$, the model reduces to a DMM1 (e.g. Zang *et al.* [37], and Vreman *et al.* [148]); and if $C_L \equiv 0$ and $C_S \equiv \text{constant}$, the model reduces to the classical Smagorinsky model [13].

Although a strict definition of a vortex is still lacking, a high vorticity modulus

is a candidate for vortex identification, especially in free shear flows [151]. Comte *et al.* [152] specifically studied coherent structures of mixing layers using the contours of streamwise vorticity. Figures 4.9 and 4.10 show instantaneous 2-D velocity fields in the x_1 - x_2 and x_2 - x_3 planes. In Fig. 4.10, streamwise vorticity contours are also used to locate the vortices. Major vortices (indicated by circles) appear to agree quite well with the spiralling streamlines suggested by the velocity vectors.

4.4.2 SGS Kinetic Energy Production and Backscatter

Modelling of the SGS stress, τ_{ij} , is one of the central topics in LES. It builds the interaction between the filtered and residual scale motions. One of the most important issues in this interaction is the transfer of TKE. The SGS TKE production rate \mathcal{P}_r for the proposed ILDMM2 becomes

$$\begin{aligned}\mathcal{P}_r &= -\tau_{ij}^* \bar{S}_{ij} \\ &= -\left[C_L (\overline{\bar{u}_i \bar{u}_j} - \bar{\bar{u}_i} \bar{\bar{u}_j})^* - 2C_S \bar{\Delta}^2 |\bar{S}| \bar{S}_{ij} \right] \cdot \bar{S}_{ij}\end{aligned}\tag{4.30}$$

and the resolved TKE dissipation of the filtered scale is defined in Eq.(3.10). For the ILDMM2 concerned in this research, backscatter can be triggered by either the scale similarity or the SGS viscosity part. In the latter case, backscatter is due to negative values of C_S . Carati *et al.* [137] studied the latter case using a DSM1 and found that a negative C_S can bring numerical instability. As indicated earlier, in this study, a restriction is placed on C_S , i.e. $C_S \geq 0$ and only the similarity part is allowed to account for backscatter.

Figure 4.11 shows the plane and time averaged distribution of \mathcal{P}_r along the wall-normal direction. \mathcal{P}_r peaks in the boundary region and levels off in the center. Obviously, the statistical approach used in Fig. 4.11 obscures any information on instantaneous backscatter. Figures 4.12 and 4.13 are based on the instantaneous field at two different locations, where the phenomenon of backscatter is clearly shown. Figure 4.12, which was obtained by searching for the maximum peak value of $-\mathcal{P}_r$, shows two adjacent large positive and negative peaks. This is an interesting phe-

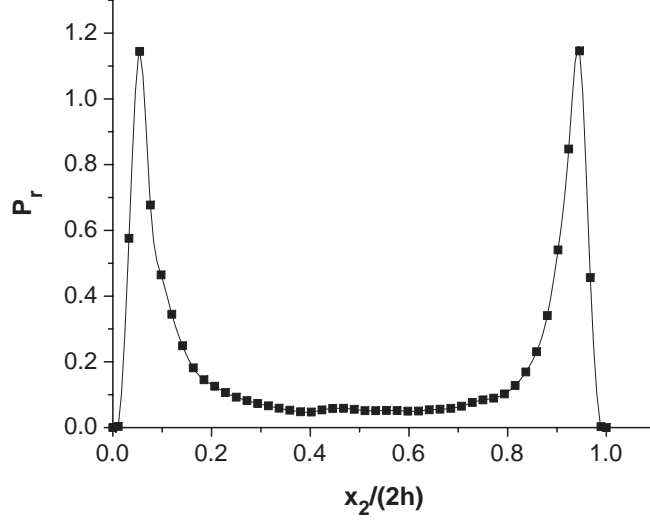


FIGURE 4.11: Averaged SGS TKE production rate ($Re = 2600$).

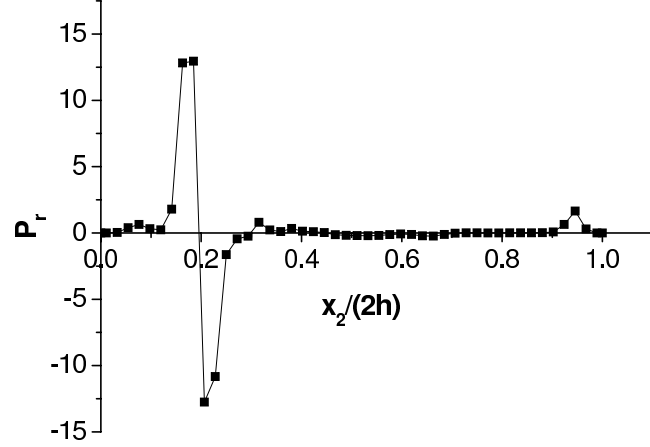


FIGURE 4.12: Instantaneous \mathcal{P}_r distribution with maximal peaks ($Re = 2600$; Relative location in the homogeneous plane: $x_1/L_1 = 0.728$, $x_3/L_3 = 0.880$).

nomenon and its mechanism might be explained as follows. At the location of the large positive \mathcal{P}_r peak, a large amount of TKE is being transferred from the resolved to residual subgrid scale motions. If this TKE far exceeds the dissipation capability of the SGS viscosity part of the ILDM2, the similarity part is instantaneously triggered to transfer the excessive TKE back to the filtered scale, which then produces the large negative \mathcal{P}_r peak. These two peaks are very close to each other spatially, however they are not in the same homogeneous layer, which suggests that the motions and interactions of eddies play a key role in the spatial transport of TKE. The author

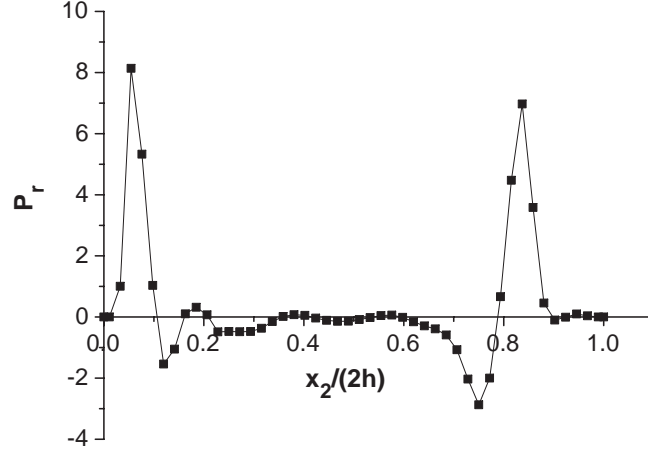


FIGURE 4.13: Instantaneous \mathcal{P}_r distribution with moderate peaks ($Re = 2600$; Relative location in the homogeneous plane: $x_1/L_1 = 0.989$, $x_3/L_3 = 0.663$).

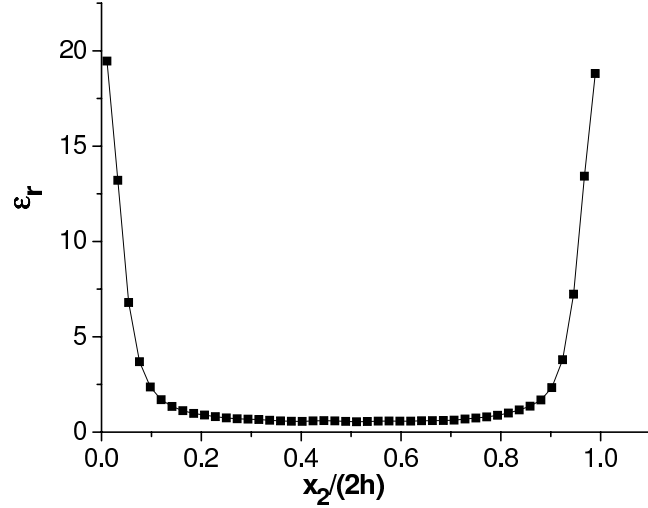


FIGURE 4.14: Averaged viscous dissipation of the filtered motions ($Re = 2600$).

has checked dozens of instantaneous figures for the \mathcal{P}_r distribution. Although it is not yet conclusive, it is commonly found that wherever an intense positive peak is located, there is always a negative peak nearby to backscatter the excessive TKE. This feature can also be observed in Fig. 4.13, although the strength of the peaks is smaller than that in Fig. 4.12. In Fig. 4.13, both forward and backward cascades of TKE transfer along the entire wall-normal direction can be clearly observed.

Finally, Fig. 4.14 gives the plane and time averaged profile of the viscous dissipation rate of the resolved scale motions. The mechanism of the resolved viscous

dissipation ε_r is totally different than that of \mathcal{P}_r in that it is purely due to viscous effects, can only be positive, and serves as a sink for the TKE of the large filtered motions.

4.5 Conclusions

The previous contributions of other researchers on the C_L – C_S type dynamic mixed models (DMM) have been briefly reviewed illustrating the evolution of the Leonard type stress terms adopted in the DMM modelling approaches. An integral type localization dynamic two-parameter mixed model (ILDMM2) has been developed. It is obtained by minimizing the integral error functional of the modified DMM2 using the functional variational method. The classical assumption of incomplete spatial invariance (ISI) adopted in many previous studies (e.g., Zang *et al.* [37], Salvetti and Banerjee [48], Horiuti [143], Meneveau and Katz [44], Morinishi and Vasilyev [50]) is not used and thus the mathematical inconsistency has been removed. A system of two integral equations has been obtained, which governs the instantaneous optimal spatial distribution of the two model coefficients of the DMM2.

The proposed ILDMM2 is demonstrated to work very well in a numerical simulation of turbulent Couette flow using a relatively coarse grid. It can successfully predict many pertinent features such as the logarithmic velocity profile and the correct level of the friction coefficient. Due to the adoption of the scale similarity model, the ILDMM2 has the desirable effect of balancing the dissipation and backscatter of the SGS TKE. From a survey of the instantaneous distributions of the SGS TKE production rate, it was observed that wherever there is an intense TKE cascade from the filtered scale to the residual subgrid scale, there is typically an instantaneous strong response from the scale similarity part of the model to backscatter the excessive TKE from the subgrid to the filtered scale.

Chapter 5

Consistent Localization and the Constitutive Relation of the Dynamic Smagorinsky Subgrid-Scale Stress Model

5.1 Introduction

As discussed in the previous two chapters, the first localization dynamic Smagorinsky SGS model in the form of a FIE2 was obtained by Ghosal *et al.* [40] based on minimizing a residual functional, which is the integral of the modulus of the residual tensor of the Germano identity over the entire domain. The FIE2 determines the optimal spatial distribution of the model coefficient and avoids the mathematical inconsistency encountered in the conventional dynamic modelling approaches of Germano *et al.* [19] and Lilly [20]. By introducing the SGS kinetic energy transport equation (k -equation) and using a similar global variational method, Ghosal *et al.* [40] reformulated their integral equation and developed a new dynamic localization model. The latter reformulated model prohibits instability due to the occasional excessive backscatter of SGS TKE and is weakly realizable with $k \geq 0$. Menon *et al.* [153], Kim and Menon [131, 132], and Pallares and Davidson [154] also tested a different k -equation dynamic localization model, which is based on the similarity behavior observed in the experiment of Liu *et al.* [25] and the least squares method of optimization adopted by Lilly [20]. Carati *et al.* [137] developed a different dynamic

localization stochastic model by introducing an eddy force term into the SGS model to account for the backscatter of SGS TKE. Similar to the approach of Ghosal *et al.* [40], Carati *et al.* [137] achieved the goal of localization by minimizing a globally integrated residual. The ILDMM2 proposed and tested in chapter 4 was also optimized by minimizing the globally integrated residual of the Germano identity in accordance with the functional variational method.

Notwithstanding the alternative approaches detailed above [132, 137, 153–155], the dynamic Smagorinsky model remains to be one of the most popular dynamic SGS modelling approaches in LES. Making use of the observation that C_S is a fairly slowly varying function of time, Piomelli and Liu [49] proposed an approximate extrapolation scheme to localize the dynamic Smagorinsky model. Although their approximate method is not rigorously compatible with variational theory, it has the benefit of avoiding the large computational cost required for solving a FIE2 [40], and has been successfully tested using a rotating channel flow.

A common feature of the global optimization technique is that it minimizes the residual integrated over the general domain (usually an integral type functional), which does not necessarily ensure the local residual to be minimal. One of the objectives of this chapter is to minimize the local residual directly, avoiding such a global integration and yet maintaining mathematical consistency.

5.2 A Sufficient and Necessary Condition for the Localization Dynamic Smagorinsky Model

Although some approximate localization methods are available, e.g. the conventional DM [20] based on the assumption of ISI and the integral type localization model obtained by minimizing the integral of Q over the entire domain [40], a consistent mathematical method for directly minimizing Q is not yet available in the literature. The philosophical idea for finding such a direct consistent localization approach (to be addressed in the following section) is borrowed from solid mechanics, which utilizes the

Dirac delta function $\delta_D(\mathbf{x}, \mathbf{y})$ as a tool to treat local effects, e.g. the local concentrated non-continuous forces and moments, so that they can be generally included in the continuous differential or integral governing equations and be treated in the same way as other globally continuous effects or forces.

In order to find the extremum value of Q directly using the functional variational method following the above idea, it is necessary to redefine the quantities E_{ij} and Q , using the symbols \mathcal{E}_{ij} and \mathcal{Q} to indicate their modified definitions, respectively. Based on Eq.(1.22), the definition for the local error tensor can be modified as

$$\mathcal{E}_{ij}(\mathbf{x}, \mathbf{x}_0) = \mathcal{L}_{ij}^*(\mathbf{x}_0) + \alpha_{ij}(\mathbf{x}_0)C_S(\mathbf{x}, \mathbf{x}_0) - \int_{-\infty}^{\infty} \beta_{ij}(\mathbf{y})C_S(\mathbf{y}, \mathbf{x}_0)G(\mathbf{x}_0, \mathbf{y})d\mathbf{y} \quad (5.1)$$

where $C_S(\mathbf{x}, \mathbf{x}_0)$ and $\mathcal{E}_{ij}(\mathbf{x}, \mathbf{x}_0)$ represent, respectively, the model coefficient function and local error tensor function of \mathbf{x} for a *specific* location \mathbf{x}_0 . The variable \mathbf{x} runs over the entire computational domain (Σ) and these two 3-D spatial functions are specific for the given location $\mathbf{x}_0 \in \Sigma$. The local error density retains a similar form to Eq.(1.21), however, it becomes a functional of $C_S(\mathbf{x}, \mathbf{x}_0)$, using the following fixed point mapping:

$$\mathcal{Q}(C_S(\mathbf{x}_0, \mathbf{x}_0)) = \mathcal{E}_{ij}(\mathbf{x}, \mathbf{x}_0) \cdot \mathcal{E}_{ij}(\mathbf{x}, \mathbf{x}_0) \big|_{\mathbf{x}=\mathbf{x}_0} \quad (5.2)$$

which varies only with the function $C_S(\mathbf{x}, \mathbf{x}_0)$ at a given location \mathbf{x}_0 . The variational problem then can be defined as follows: at each location $\mathbf{x}_0 \in \Sigma$, find an optimal function $C_S^{\mathbb{N}}(\mathbf{x}, \mathbf{x}_0) \in \Upsilon$ such that $\mathcal{Q}(C_S^{\mathbb{N}}(\mathbf{x}_0, \mathbf{x}_0))$ is minimal. Here, $C_S^{\mathbb{N}}(\mathbf{x}_0, \mathbf{x}_0)$ is the localization (optimal) model coefficient and Υ represents the function space for $C_S(\mathbf{x}, \mathbf{x}_0)$. All $C_S^{\mathbb{N}}(\mathbf{x}, \mathbf{x}_0)$ for different locations generate a *set of optimal coefficient functions*

$$\{C_S^{\mathbb{N}}\} = \{C_S^{\mathbb{N}}(\mathbf{x}, \mathbf{x}_0) \mid \mathcal{Q}(C_S^{\mathbb{N}}(\mathbf{x}_0, \mathbf{x}_0)) \leq \mathcal{Q}(C_S(\mathbf{x}_0, \mathbf{x}_0)), \forall C_S(\mathbf{x}, \mathbf{x}_0) \in \Upsilon, \forall \mathbf{x}_0 \in \Sigma\} \quad (5.3)$$

and all $C_S^{\mathbb{N}}(\mathbf{x}_0, \mathbf{x}_0)$, $\forall \mathbf{x}_0 \in \Sigma$, generate a *set of optimal model coefficients*, which taken

together represent a 3-D optimal distribution of C_S , i.e.

$$\{C_S^{\aleph 0}\} = \{C_S^{\aleph}(\mathbf{x}_0, \mathbf{x}_0) \mid \mathcal{Q}(C_S^{\aleph}(\mathbf{x}_0, \mathbf{x}_0)) \leq \mathcal{Q}(C_S(\mathbf{x}_0, \mathbf{x}_0)), \forall C_S(\mathbf{x}, \mathbf{x}_0) \in \Upsilon, \forall \mathbf{x}_0 \in \Sigma\} \quad (5.4)$$

which retains a function mapping (surjective) from the spatial domain Σ to the image set $\{C_S^{\aleph 0}\}$. Thus, unlike the traditional approach of searching for one optimal function $C_S(\mathbf{x})$ for the entire domain at each time step, the new approach will look for the optimal function set and the set of the optimal model coefficients, i.e. $\{C_S^{\aleph}\}$ and $\{C_S^{\aleph 0}\}$, respectively. These two sets are *uncountable* in the continuous case, while have at least N^3 independent elements in the discrete case, where N^3 represents the total number of discrete nodes. Although conceptually more complex than the traditional approach, this new way of regarding the model coefficient C_S does not change its role in determining the SGS stress defined by Eq.(1.12) within the classical framework of the Smagorinsky constitutive relation, and as will be shown later, it is actually more flexible in terms of mathematics. Furthermore, some general formulations and useful physical concepts can be derived using this new approach.

This section is organized in the following way: in subsection 5.2.1, a necessary condition for localization in the form of an orthogonal condition will be derived; in subsection 5.2.2, the necessary condition obtained in subsection 5.2.1 will also be proven to be sufficient for localization, and a theorem for localization will be derived; in subsection 5.2.3, various theoretical applications of the theorem will be explored, specifically those that result in the conventional models of Lilly [20] and Ghosal *et al.* [40], and also a new Picard's integral equation.

5.2.1 A Necessary Condition for Localization

With the re-defined expressions for $\mathcal{E}_{ij}(\mathbf{x}, \mathbf{x}_0)$, $\mathcal{Q}(C_S(\mathbf{x}_0, \mathbf{x}_0))$, $\{C_S^{\aleph}\}$, and $\{C_S^{\aleph 0}\}$, it is possible to begin the procedure of optimization for the variational problem defined

previously. Let the first order variation of \mathcal{Q} vanish, i.e.

$$\delta\mathcal{Q} = 2\mathcal{E}_{ij}\delta\mathcal{E}_{ij} = 0 \quad (5.5)$$

$\forall \mathbf{x}_0 \in \Sigma$. Considering Eqs.(5.1) and (5.2), the above equation becomes

$$\mathcal{E}_{ij}(\mathbf{x}_0, \mathbf{x}_0) \cdot \left[\alpha_{ij}(\mathbf{x}_0)\delta C_S(\mathbf{x}_0, \mathbf{x}_0) - \int_{-\infty}^{\infty} \beta_{ij}(\mathbf{y})\delta C_S(\mathbf{y}, \mathbf{x}_0)G(\mathbf{x}_0, \mathbf{y})d\mathbf{y} \right] = 0 \quad (5.6)$$

The *Dirac delta function* $\delta_D(\mathbf{x}, \mathbf{y})$ has the property: $\phi(\mathbf{x}) = \int_{-\infty}^{\infty} \phi(\mathbf{y})\delta_D(\mathbf{x}, \mathbf{y})d\mathbf{y}$, such that Eq.(5.6) can be expressed as

$$\int_{-\infty}^{\infty} \mathcal{E}_{ij}(\mathbf{x}_0, \mathbf{x}_0) \cdot [\alpha_{ij}(\mathbf{y})\delta_D(\mathbf{x}_0, \mathbf{y}) - \beta_{ij}(\mathbf{y})G(\mathbf{x}_0, \mathbf{y})] \cdot \delta C_S(\mathbf{y}, \mathbf{x}_0) \cdot d\mathbf{y} = 0 \quad (5.7)$$

$\forall \delta C_S(\mathbf{y}, \mathbf{x}_0) \in \Upsilon$. Therefore, the following relation must hold:

$$\mathcal{E}_{ij}(\mathbf{x}_0, \mathbf{x}_0) \cdot [\alpha_{ij}(\mathbf{y})\delta_D(\mathbf{x}_0, \mathbf{y}) - \beta_{ij}(\mathbf{y})G(\mathbf{x}_0, \mathbf{y})] = 0 \quad (5.8)$$

$\forall \mathbf{x}_0 \in \Sigma$, or more briefly

$$\mathcal{E}_{ij}M'_{ij} = 0 \quad (5.9)$$

where $\mathcal{E}_{ij} = \mathcal{E}_{ij}(\mathbf{x}_0, \mathbf{x}_0)$, and

$$M'_{ij} = M'_{ij}(\mathbf{y}, \mathbf{x}_0) = \alpha_{ij}(\mathbf{y})\delta_D(\mathbf{x}_0, \mathbf{y}) - \beta_{ij}(\mathbf{y})G(\mathbf{x}_0, \mathbf{y}) \quad (5.10)$$

Because of the Dirac delta function contained in its first term, M'_{ij} is a *generalized function* [156] of \mathbf{y} at a given location \mathbf{x}_0 . In view of the convolution contained in \mathcal{E}_{ij} (see Eq.(5.1)), Eq.(5.9) is actually an integral equation with respect to $C_S(\mathbf{x}, \mathbf{x}_0)$. Eq.(5.9) also indicates an elegant *Orthogonal Condition* (OC) between the local residual stress (or stress error tensor) \mathcal{E}_{ij} and the tensor M'_{ij} at any given location \mathbf{x}_0 . This OC is a necessary condition for making the functional \mathcal{Q} minimal and as such represents a Distribution Equation for the dynamic localization model Coefficient (DEC) for this Smagorinsky type SGS stress model.

The following is an attempt to provide an interpretation for the previously discussed tensors M'_{ij} and \mathcal{L}_{ij}^{proj*} , and also the tensors α_{ij} and β_{ij} which are frequently encountered in the literature. In order to understand the physical meaning of these tensors, we need to revisit some basic concepts given in subsection 1.3.2. From comparison of the constitutive relations given by Eq.(1.12) and Eq.(1.20), we understand that at each time step, β_{ij} acts as the ‘*base stress tensor function*’ (function of space) for the grid-level SGS stress τ_{ij}^* , which is then obtained by weighting β_{ij} with $(-C_S)$. Similarly, α_{ij} can be regarded as a ‘*base stress tensor function*’ for the test-grid level SGS stress T_{ij}^* at each time step. Both α_{ij} and β_{ij} are related to the filtered strain rate tensor \bar{S}_{ij} . Extensive discussions on the integrity bases and invariants related to the strain rate tensor, and the tensorial spaces for the Reynolds and SGS stresses, can be found in references [109,139,157–162]. Recall that the tracefree Leonard stress term \mathcal{L}_{ij}^* in the Germano identity (Eq.(1.17)) can be approximated by Eq.(1.23) using the SGS models given by Eq.(1.12) and (1.16). Equation (1.23) indicates that \mathcal{L}_{ij}^* is approximated using α_{ij} and β_{ij} by a linear weighting operation involving $C_S^{\aleph}(\mathbf{x}, \mathbf{x}_0)$. From the definition of M'_{ij} , the following elegant constructive relation between \mathcal{L}_{ij}^{proj*} and M'_{ij} can be readily obtained:

$$\mathcal{L}_{ij}^{proj*}(\mathbf{x}_0) = - \int_{-\infty}^{\infty} C_S^{\aleph}(\mathbf{y}, \mathbf{x}_0) M'_{ij}(\mathbf{y}, \mathbf{x}_0) \cdot d\mathbf{y} \quad (5.11)$$

$\forall \mathbf{x}_0 \in \Sigma$. From the point of view of approximation theory, the variational problem defined previously can be equivalently expressed as follows: at a given location \mathbf{x}_0 , find $C_S^{\aleph}(\mathbf{x}, \mathbf{x}_0) \in \Upsilon$ for the projection of $\mathcal{L}_{ij}^*(\mathbf{x}_0)$ in the specified approximation stress tensor space \mathfrak{M}_o , i.e. $\mathcal{L}_{ij}^{proj*}(\mathbf{x}_0) \in \mathfrak{M}_o$, such that the ‘error’ ($\mathcal{E}_{ij}(\mathbf{x}_0, \mathbf{x}_0)$) is orthogonal to \mathfrak{M}_o (see Eq.(5.9)). Here, \mathfrak{M}_o is a *local tensorial approximation space* for the Leonard stress at \mathbf{x}_0 , constructed as

$$\begin{aligned} \mathfrak{M}_o &= \mathfrak{M}_o(\mathbf{x}_0) \\ &= \left\{ \mathcal{L}_{ij}^{appr*}(\mathbf{x}_0) \left| \mathcal{L}_{ij}^{appr*}(\mathbf{x}_0) = - \int_{-\infty}^{\infty} C_S(\mathbf{y}, \mathbf{x}_0) M'_{ij}(\mathbf{y}, \mathbf{x}_0) d\mathbf{y}, \forall C_S(\mathbf{x}, \mathbf{x}_0) \in \Upsilon, \mathbf{y} \in \Sigma \right. \right\} \end{aligned} \quad (5.12)$$

Obviously, $\mathcal{L}_{ij}^{appr*}(\mathbf{x}_0)$, the *element* of the local tensorial approximation space for the Leonard stress, is a functional of $C_S(\mathbf{y}, \mathbf{x}_0)$ at the location $\mathbf{x}_0 \in \Sigma$, and the space \mathfrak{M}_o is specific for \mathbf{x}_0 . The above variational problem requires that $\mathcal{E}_{ij}(\mathbf{x}_0, \mathbf{x}_0)$ be orthogonal to any element in \mathfrak{M}_o , which can be easily validated using Eq.(5.9) as follows:

$$\mathcal{E}_{ij}(\mathbf{x}_0, \mathbf{x}_0) \cdot \mathcal{L}_{ij}^{appr*}(\mathbf{x}_0) = - \int_{-\infty}^{\infty} C_S(\mathbf{y}, \mathbf{x}_0) \cdot \mathcal{E}_{ij}(\mathbf{x}_0, \mathbf{x}_0) \cdot M'_{ij}(\mathbf{y}, \mathbf{x}_0) \cdot d\mathbf{y} \equiv 0 \quad (5.13)$$

$$\forall \mathcal{L}_{ij}^{appr*}(\mathbf{x}_0) \in \mathfrak{M}_o.$$

Eq.(5.12) clearly shows an linear constructive relation between $\mathcal{L}_{ij}^{appr*}(\mathbf{x}_0)$ and M'_{ij} , weighted by $C_S(\mathbf{y}, \mathbf{x}_0) \cdot d\mathbf{y}$ in a 3-D continuous case. Considering the difference in units between $\mathcal{L}_{ij}^{appr*}(\mathbf{x}_0)$ and M'_{ij} , M'_{ij} can thus be understood as the ‘*tensorial intensity function*’ for the local elementary approximation Leonard stress $\mathcal{L}_{ij}^{appr*}(\mathbf{x}_0)$. Since $\alpha_{ij}(\mathbf{x}_0) = \int_{-\infty}^{\infty} \alpha_{ij}(\mathbf{y}) \delta_D(\mathbf{x}_0, \mathbf{y}) d\mathbf{y}$, the first term of M'_{ij} , i.e. $\alpha_{ij}(\mathbf{y}) \delta_D(\mathbf{x}_0, \mathbf{y})$ in Eq.(5.10), reflects the contribution of the *local* test-grid level stress (indicated by α_{ij}) to the local value of $\mathcal{L}_{ij}^{appr*}(\mathbf{x}_0)$ because of the sharp localization effect of the Dirac delta function at \mathbf{x}_0 . Similarly, the second term, $\beta_{ij}(\mathbf{y}) G(\mathbf{x}_0, \mathbf{y})$, reflects the contribution of the grid-level stress (indicated by β_{ij}) at *all* locations to the local value of $\mathcal{L}_{ij}^{appr*}(\mathbf{x}_0)$ using the filter kernel function $G(\mathbf{x}_0, \mathbf{y})$ as a weight at \mathbf{x}_0 .

Since the reverse procedure from Eq.(5.8) to (5.5) also strictly holds, the OC (Eq.(5.9)) is equivalent to the variational condition (Eq.(5.5)). In mathematics [163], the variational condition (Eq.(5.5)) is regarded as a necessary condition for functional minimization. However, in the following section, it will be proven that the variational condition (Eq.(5.5)) and the OC (Eq.(5.9)) are not only necessary but also sufficient for minimizing the local error functional \mathcal{Q} .

5.2.2 Proof of Sufficiency

Solutions obtained from the variational condition (Eq.(5.5)) or the OC or DEC (Eq.(5.9)), can be *extremum functions*, or non-extremum *inflection* or *saddle* ‘points’ (functions, actually) for the local error functional $\mathcal{Q}(C_S(\mathbf{x}_0, \mathbf{x}_0))$. To investigate the

sufficient condition for the minimal \mathcal{Q} , its second and higher order variations must be considered. Assuming that $\mathcal{Q}[C_S(\mathbf{x}_0, \mathbf{x}_0) + \eta\delta C_S(\mathbf{x}_0, \mathbf{x}_0)]$ is at least three times differentiable with respect to η , where η is all sufficiently small numbers near 0, then the following results for the 2nd and n-th order variations can be readily obtained from their definitions [163]:

$$\begin{aligned}\delta^2\mathcal{Q}(C_S(\mathbf{x}_0, \mathbf{x}_0), \eta\delta C_S(\mathbf{x}_0, \mathbf{x}_0)) &= \left. \frac{d^2}{d\eta^2}\mathcal{Q}(C_S(\mathbf{x}_0, \mathbf{x}_0) + \eta\delta C_S(\mathbf{x}_0, \mathbf{x}_0)) \right|_{\eta=0} \\ &= 2\delta\mathcal{E}_{ij}\delta\mathcal{E}_{ij} \geq 0\end{aligned}\quad (5.14)$$

$$\delta^n\mathcal{Q}(C_S(\mathbf{x}_0, \mathbf{x}_0), \eta\delta C_S(\mathbf{x}_0, \mathbf{x}_0)) = \left. \frac{d^n}{d\eta^n}\mathcal{Q}[C_S(\mathbf{x}_0, \mathbf{x}_0) + \eta\delta C_S(\mathbf{x}_0, \mathbf{x}_0)] \right|_{\eta=0} \equiv 0 \quad (5.15)$$

at any given location \mathbf{x}_0 and for $n \geq 3$.

Suppose that the function $C_S^{\aleph}(\mathbf{x}, \mathbf{x}_0)$ is a solution of the OC, which makes the first order variation of \mathcal{Q} vanish. The possibility for $C_S^{\aleph}(\mathbf{x}, \mathbf{x}_0)$ to be an inflection ‘point’ can be excluded by condition (5.14), which does not allow the sign of $\delta^2\mathcal{Q}$ to change at $C_S^{\aleph}(\mathbf{x}, \mathbf{x}_0)$. It can be shown that the functional \mathcal{Q} can be expanded using its variations in the following manner [163]:

$$\begin{aligned}\mathcal{Q}(C_S^{\aleph}(\mathbf{x}_0, \mathbf{x}_0) + \eta\delta C_S(\mathbf{x}_0, \mathbf{x}_0)) &= \\ \sum_{n=0}^3 \frac{\eta^n}{n!} \delta^n\mathcal{Q}(C_S^{\aleph}(\mathbf{x}_0, \mathbf{x}_0), \delta C_S(\mathbf{x}_0, \mathbf{x}_0)) &+ R_3(C_S^{\aleph}(\mathbf{x}_0, \mathbf{x}_0), \delta C_S(\mathbf{x}_0, \mathbf{x}_0), \eta)\end{aligned}\quad (5.16)$$

where $R_3 = R_3(C_S^{\aleph}(\mathbf{x}_0, \mathbf{x}_0), \delta C_S(\mathbf{x}_0, \mathbf{x}_0), \eta)$ is the truncation error, which is restricted by

$$|R_3| \leq \frac{|\eta|^3}{3!} \max_{|\varsigma| \leq |\eta|} \left| \frac{d^3}{d\varsigma^3} \mathcal{Q}(C_S^{\aleph}(\mathbf{x}_0, \mathbf{x}_0) + \varsigma\delta C_S(\mathbf{x}_0, \mathbf{x}_0)) - \delta^3\mathcal{Q}(C_S^{\aleph}(\mathbf{x}_0, \mathbf{x}_0), \delta C_S(\mathbf{x}_0, \mathbf{x}_0)) \right| \quad (5.17)$$

$\forall \eta$ and ς near zero. Since the third order derivative and variation vanish as shown in Eq.(5.15), we know that $|R_3| \equiv 0$. This result can also be understood in the following intuitive way: from Eqs.(5.1) and (5.2), we understand that $\mathcal{Q} = \mathcal{E}_{ij}\mathcal{E}_{ij}$ is a second order functional of $C_S(\mathbf{x}, \mathbf{x}_0)$ and thus its third and higher order variations

must vanish and $|R_3| \equiv 0$. Considering that the first order variation vanishes, then Eq.(5.16) can be simplified to

$$\mathcal{Q}(C_S^{\mathbb{N}}(\mathbf{x}_0, \mathbf{x}_0) + \eta \delta C_S(\mathbf{x}_0, \mathbf{x}_0)) = \mathcal{Q}(C_S^{\mathbb{N}}(\mathbf{x}_0, \mathbf{x}_0)) + \frac{\eta^2}{2!} \delta^2 \mathcal{Q}(C_S^{\mathbb{N}}(\mathbf{x}_0, \mathbf{x}_0), \delta C_S(\mathbf{x}_0, \mathbf{x}_0)) \quad (5.18)$$

Using (5.14), we obtain

$$\mathcal{Q}(C_S^{\mathbb{N}}(\mathbf{x}_0, \mathbf{x}_0) + \eta \delta C_S(\mathbf{x}_0, \mathbf{x}_0)) \geq \mathcal{Q}(C_S^{\mathbb{N}}(\mathbf{x}_0, \mathbf{x}_0)) \quad (5.19)$$

The above result clearly indicates that at any given location \mathbf{x}_0 , $C_S^{\mathbb{N}}(\mathbf{x}, \mathbf{x}_0)$ which satisfies the necessary condition will only allow \mathcal{Q} to be locally minimal. Thus the variational condition and its equivalent expression, i.e. the OC or DEC, are not only necessary but also sufficient for minimizing the local error functional \mathcal{Q} . The possibility for $C_S^{\mathbb{N}}(\mathbf{x}, \mathbf{x}_0)$ to be a saddle point has automatically been excluded, because Eq.(5.19) prohibits $[\mathcal{Q}(C_S^{\mathbb{N}}(\mathbf{x}_0, \mathbf{x}_0) + \eta \delta C_S(\mathbf{x}_0, \mathbf{x}_0)) - \mathcal{Q}(C_S^{\mathbb{N}}(\mathbf{x}_0, \mathbf{x}_0))]$ to change sign at $C_S^{\mathbb{N}}(\mathbf{x}, \mathbf{x}_0)$.

The principal result of subsections 5.2.1 and 5.2.2, i.e. the sufficient and necessary condition in the form of the OC or DEC (Eq.(5.9)), for localizing the dynamic Smagorinsky model can be briefly summarized by the following theorem:

Theorem: For the dynamic Smagorinsky SGS stress model, the local error density functional \mathcal{Q} at a given location \mathbf{x}_0 , is minimum, if and only if $\mathcal{E}_{ij} M'_{ij} = 0$.

5.2.3 Theoretical Application of the OC

Integrating both sides of the OC in terms of \mathbf{y} over the entire domain, results in

$$\mathcal{E}_{ij}(\mathbf{x}_0, \mathbf{x}_0) \cdot [\alpha_{ij}(\mathbf{x}_0) - \tilde{\beta}_{ij}(\mathbf{x}_0)] = 0 \quad (5.20)$$

$\forall \mathbf{x}_0 \in \Sigma$. Applying the definition of M_{ij} given in Eq.(1.26), the above relation simplifies to

$$\mathcal{E}_{ij} M_{ij} = 0 \quad (5.21)$$

which is the *Integral form of the Orthogonal Condition* (IOC) at any given location \mathbf{x}_0 . M_{ij} is another frequently encountered tensor in the literature, which in view of the previous discussion, can be explained in general terms as the difference between the test-grid level SGS base stress and the filtered grid-level SGS base stress, i.e. $\alpha_{ij} - \tilde{\beta}_{ij}$. Although an additional integration has been performed in obtaining Eq.(5.20) from the OC, the result still retains some implications of the original variational problem, which now requires the local error tensor \mathcal{E}_{ij} to be orthogonal to M_{ij} at a given location \mathbf{x}_0 . An elegant linear constructive relation between M'_{ij} and M_{ij} can be obtained from Eq.(5.10) as follows

$$M_{ij}(\mathbf{x}_0) = \int_{-\infty}^{\infty} M'_{ij} d\mathbf{y} \quad (5.22)$$

at a given location \mathbf{x}_0 . The application of the above equation will be explored in subsection 5.2.3.1.

Substituting \mathcal{E}_{ij} as defined in Eq.(5.1) into the IOC, we obtain

$$\begin{aligned} & \mathcal{L}_{ij}^*(\mathbf{x}_0)M_{ij}(\mathbf{x}_0) + \alpha_{ij}(\mathbf{x}_0)M_{ij}(\mathbf{x}_0)C_S(\mathbf{x}_0, \mathbf{x}_0) \\ & - M_{ij}(\mathbf{x}_0) \int_{-\infty}^{\infty} \beta_{ij}(\mathbf{y})C_S(\mathbf{y}, \mathbf{x}_0)G(\mathbf{x}_0, \mathbf{y})d\mathbf{y} = 0 \end{aligned} \quad (5.23)$$

which is an integral equation that governs the optimal function $C_S^{\mathbb{N}}(\mathbf{x}, \mathbf{x}_0)$ at a given location \mathbf{x}_0 . However, this is not a regular integral equation in that $C_S^{\mathbb{N}}(\mathbf{x}, \mathbf{x}_0)$ can in principle be different at every \mathbf{x}_0 , which means that the integral equation needs to be solved at all N^3 discrete nodes for the independent optimal functions. In general, this would be impractical for a numerical simulation. Fortunately, some useful special solutions have been found. The solution to this integral system, Eq.(5.23), is obviously non-unique, for it admits at least the following three useful special theoretical solutions under different restrictions. However, a complete investigation of the properties of the OC and IOC and their applications is beyond the scope of this dissertation.

5.2.3.1 Restriction to Constant Distribution of $C_S^{\aleph}(\mathbf{x}, \mathbf{x}_0)$

If $C_S^{\aleph}(\mathbf{x}, \mathbf{x}_0) \equiv C_S^{\aleph}(\mathbf{x}_0, \mathbf{x}_0)$, i.e. $C_S^{\aleph}(\mathbf{x}, \mathbf{x}_0)$ has a 3-D spatially constant distribution with respect to \mathbf{x} at each \mathbf{x}_0 , $\{C_S^{\aleph}\}$ then becomes a set consisting of independent constant functions. Thus Eq.(5.23) becomes

$$[\mathcal{L}_{ij}^*(\mathbf{x}_0) + M_{ij}(\mathbf{x}_0)C_S^{\aleph}(\mathbf{x}_0, \mathbf{x}_0)] \cdot M_{ij}(\mathbf{x}_0) = 0 \quad (5.24)$$

from which we can obtain

$$C_S^{\aleph}(\mathbf{x}_0, \mathbf{x}_0) = -\frac{M_{ij}(\mathbf{x}_0)\mathcal{L}_{ij}(\mathbf{x}_0)}{M_{ij}(\mathbf{x}_0)M_{ij}(\mathbf{x}_0)} \quad (5.25)$$

$\forall \mathbf{x}_0 \in \Sigma$. Clearly, the above result obtained using the revised approach is the same as the conventional DM formulation of Lilly [20], i.e. Eq.(1.27), except for the conceptual difference that here we are looking for an optimal coefficient set $\{C_S^{\aleph 0}\}$ instead of the conventional single optimal coefficient function $C_S^{\aleph}(\mathbf{x})$. However, this conceptual difference does not result in any difference between Eq.(1.27) and Eq.(5.25) for calculating the value of the local DM coefficient. The constant functions are independent (and can be different) at each different \mathbf{x}_0 , such that $\{C_S^{\aleph 0}\}$ can still yield a non-constant optimal distribution of the model coefficient over the entire domain. Thus, the conventional assumption of ISI is not the only way to obtain Lilly's result. From the above approach, it is further understood that Lilly's result can be generalized as a special solution of the IOC. The restriction condition of the new approach based on the set $\{C_S^{\aleph 0}\}$ is weaker than the conventional [19, 20] assumption of ISI, and thus provides a method for obtaining Lilly's result in a mathematically consistent way. This is due to the fact that in comparison with the conventional approach [19, 20] for a single optimal function $C_S^{\aleph}(\mathbf{x})$, the new approach has the advantage of allowing the freedom to choose an independent optimal function at each position to compose $\{C_S^{\aleph 0}\}$.

An alternative consistent approach to obtain Lilly's formulation can start from the construction equation for \mathcal{L}_{ij}^{proj*} , i.e. Eq.(5.11). Under the restriction condi-

tion considered, we know that $C_S(\mathbf{y}, \mathbf{x}_0)$ is independent of \mathbf{y} at a given location \mathbf{x}_0 . Therefore, using Eq.(5.22), Eq.(5.11) becomes

$$\mathcal{L}_{ij}^{proj*}(\mathbf{x}_0) = -C_S^{\aleph}(\mathbf{x}_0, \mathbf{x}_0)M_{ij}(\mathbf{x}_0) \quad (5.26)$$

which has a specific meaning in physics, i.e. the projected Leonard stress $\mathcal{L}_{ij}^{proj*}(\mathbf{x}_0)$ can be generated from the tensor $M_{ij}(\mathbf{x}_0)$ using the coefficient $-C_S^{\aleph}(\mathbf{x}_0, \mathbf{x}_0)$ as a weight. From the theory of approximation, an orthogonal relation must exist between \mathcal{E}_{ij} and $\mathcal{L}_{ij}^{proj*}(\mathbf{x}_0)$, i.e. $\mathcal{E}_{ij} \cdot \mathcal{L}_{ij}^{proj*}(\mathbf{x}_0) = 0$, or

$$-\left[\mathcal{L}_{ij}^*(\mathbf{x}_0) - \mathcal{L}_{ij}^{proj*}(\mathbf{x}_0)\right] \cdot C_S^{\aleph}(\mathbf{x}_0, \mathbf{x}_0)M_{ij}(\mathbf{x}_0) = 0 \quad (5.27)$$

The above equation yields two solutions, i.e. a trivial solution of $C_S^{\aleph}(\mathbf{x}_0, \mathbf{x}_0) \equiv 0$, and an orthogonal relation of $[\mathcal{L}_{ij}^*(\mathbf{x}_0) - \mathcal{L}_{ij}^{proj*}(\mathbf{x}_0)] \cdot M_{ij}(\mathbf{x}_0) = 0$ which upon substituting Eq.(5.26) results in Eqs.(5.24) and Eq.(5.25), the revised conventional dynamic SGS model of Lilly [20] proposed previously. Therefore, besides the general interpretation given at the beginning of subsection 5.2.3, $M_{ij}(\mathbf{x}_0)$ can be further identified from Eq.(5.26) as a ‘*base stress tensor*’ for the local elementary approximation Leonard stress $\mathcal{L}_{ij}^{appr*}(\mathbf{x}_0)$ in the specific case of the revised conventional dynamic SGS modelling (Eq.(5.25)) considered. Therefore, under the restriction, the revised conventional dynamic approach of Lilly [20] seeks $C_S^{\aleph}(\mathbf{x}_0, \mathbf{x}_0)$ to generate $\mathcal{L}_{ij}^{proj*}(\mathbf{x}_0)$ in the local tensorial approximation space constructed by

$$\begin{aligned} \mathfrak{M}_L^{rev} &= \mathfrak{M}_L^{rev}(\mathbf{x}_0) \\ &= \left\{ \mathcal{L}_{ij}^{appr*}(\mathbf{x}_0) \left| \mathcal{L}_{ij}^{appr*}(\mathbf{x}_0) = -C_S(\mathbf{x}_0, \mathbf{x}_0)M_{ij}(\mathbf{x}_0), \forall C_S(\mathbf{x}_0, \mathbf{x}_0) \in \mathfrak{R} \right. \right\} \end{aligned} \quad (5.28)$$

where \mathfrak{R} is the set of all real numbers. Clearly, $\mathfrak{M}_L^{rev} \subseteq \mathfrak{M}_o$ at \mathbf{x}_0 . It should be noted that the above interpretation of Lilly’s tensorial approximation space for the Leonard stress is mathematically consistent because Eq.(5.26) is obtained from Eq.(5.11) and discussions were made locally for \mathbf{x}_0 . However, if we use the original assumption of ISI [19,20] and begin from Eq.(1.25), we can find the original approximation tensorial

function space of Lilly's approach [20] for the Leonard stress, following a similar procedure of analysis, i.e.

$$\mathfrak{M}_L^{orig} = \left\{ \mathcal{L}_{ij}^{appr*}(\mathbf{x}) \left| \mathcal{L}_{ij}^{appr*}(\mathbf{x}) = -C_S(\mathbf{x})M_{ij}(\mathbf{x}), \forall C_S(\mathbf{x}) \in \mathcal{C}(\Sigma), \mathbf{x} \in \Sigma \right. \right\} \quad (5.29)$$

where $\mathcal{C}(\Sigma)$ represents the set of all continuous functions over the domain Σ . It is easy to show that in this specific case of Lilly's original approach [20], the orthogonal relation is $E_{ij}(\mathbf{x})M_{ij}(\mathbf{x}) = 0$, and similarly, $M_{ij}(\mathbf{x})$ serves as a '*base stress tensor function*' for $\mathcal{L}_{ij}^{appr*}(\mathbf{x})$ weighted by $-C_S(\mathbf{x})$.

5.2.3.2 Restriction to Identical Distribution of $C_S^{\aleph}(\mathbf{x}, \mathbf{x}_0)$

(1) Picard's Integral Equation

If $C_S^{\aleph}(\mathbf{x}, \mathbf{x}_0)$ has the same 3-D spatial distribution for each \mathbf{x}_0 , the elements of the set $\{C_S^{\aleph}\}$ become identical, i.e. $C_S^{\aleph}(\mathbf{x}, \mathbf{x}_a) \equiv C_S^{\aleph}(\mathbf{x}, \mathbf{x}_b)$, $\forall \mathbf{x}, \mathbf{x}_a$ and $\mathbf{x}_b \in \Sigma$ ($\mathbf{x}_a \neq \mathbf{x}_b$ is possible). This simplifies the problem to the traditional approach of searching for a single optimal coefficient function $C_S^{\aleph}(\mathbf{x})$ over the entire domain, instead of a special optimal function $C_S^{\aleph}(\mathbf{x}, \mathbf{x}_0)$ for each \mathbf{x}_0 . This is a desirable feature and Eq.(5.23) becomes a regular integral equation, which is a Fredholm integral equation of the third kind or Picard's Integral Equation [46] (PIE), i.e.

$$\mathcal{L}_{ij}^*(\mathbf{x})M_{ij}(\mathbf{x}) + \alpha_{ij}(\mathbf{x})M_{ij}(\mathbf{x})C_S(\mathbf{x}) - M_{ij}(\mathbf{x}) \int_{-\infty}^{\infty} \beta_{ij}(\mathbf{y})C_S(\mathbf{y})G(\mathbf{x}, \mathbf{y})d\mathbf{y} = 0 \quad (5.30)$$

where the replacement of \mathbf{x}_0 by \mathbf{x} is valid, since the equation holds $\forall \mathbf{x}_0 \in \Sigma$. In the case of $\alpha_{ij}(\mathbf{x})M_{ij}(\mathbf{x}) \neq 0$, this Fredholm integral equation of the third kind or the PIE can be further rearranged into a Fredholm integral equation of the second kind:

$$f(\mathbf{x}) = C_S(\mathbf{x}) + \int_{-\infty}^{\infty} \psi(\mathbf{x}, \mathbf{y})C_S(\mathbf{y})d\mathbf{y} \quad (5.31)$$

where

$$f(\mathbf{x}) = -\frac{\mathcal{L}_{ij}^*(\mathbf{x})M_{ij}(\mathbf{x})}{\alpha_{ij}(\mathbf{x})M_{ij}(\mathbf{x})} \quad (5.32)$$

and the non-symmetric kernel function is:

$$\psi(\mathbf{x}, \mathbf{y}) = -\frac{M_{ij}(\mathbf{x})\beta_{ij}(\mathbf{y})}{\alpha_{ij}(\mathbf{x})M_{ij}(\mathbf{x})}G(\mathbf{x}, \mathbf{y}) \quad (5.33)$$

(2) Fredholm Integral Equation of the Second Kind of Ghosal *et al.*

The above integral equation was obtained using the IOC, which is different than the Fredholm integral equation of the second kind obtained by Ghosal *et al.* [40]. The fact that the result of Ghosal *et al.* [40] is also a special solution of the OC under the condition of the identical distribution solution of $C_S^N(\mathbf{x}, \mathbf{x}_0)$ can be demonstrated as follows. We have observed that the formulation of the OC is not symmetric in terms of \mathbf{x}_0 and \mathbf{y} . Under the restriction of identical distribution, $\mathcal{E}_{ij}(\mathbf{x}_0, \mathbf{x}_0)$ can then be reduced to $E_{ij}(\mathbf{x}_0)$ and the OC becomes integrable in terms of \mathbf{x}_0 , and thus we obtain

$$\int_{-\infty}^{\infty} E_{ij}(\mathbf{x}_0)\alpha_{ij}(\mathbf{y})\delta_D(\mathbf{x}_0, \mathbf{y})d\mathbf{x}_0 - \int_{-\infty}^{\infty} E_{ij}(\mathbf{x}_0)\beta_{ij}(\mathbf{y})G(\mathbf{x}_0, \mathbf{y})d\mathbf{x}_0 = 0 \quad (5.34)$$

which can be further rearranged into Eq.(1.29), the result of Ghosal *et al.* [40] as discussed previously.

Considering the definition of E_{ij} , i.e. Eq.(1.22), we observe that Eq.(1.29) has one extra integral operation compared with Eqs.(5.30) and (5.31). Thus, the new Picard's integral equation Eq.(5.30) proposed in this subsection is less costly in computation than the conventional Fredholm integral equation of the second kind of Ghosal *et al.* [40].

5.3 Results of Numerical Simulations

In the previous theoretical application of the OC, we obtained several modelling formulations including the conventional results of Lilly [20] and Ghosal *et al.* [40], as well as a new PIE (Eq.(5.30)). Since validations of those conventional models have already been reported in the literature [19, 20, 36, 38, 40, 49, 116, 137], we will focus on the numerical validation of the new PIE in this study (although the DM of Lilly [20]

is used for comparison). It should be noted that the main purpose for presenting the formulation of the PIE in the previous section and its related numerical results in this section, is to demonstrate one theoretical and practical application of the OC, the major conclusion of this chapter.

5.3.1 An Efficient Solver for the Picard's Integral Equation

Similar to the Fredholm integral equation of the second kind of Ghosal *et al.* [40], the PIE only needs to be solved once at one time step for the entire domain. The difficulty in solving this integral equation pertains to the 3-D convolution term, which involves the unknown C_S . Piomelli and Liu [49] observed that C_S changes very slowly with the advancement of time. Thus, the following explicit scheme for Eq.(5.30) could be used to obtain an approximate solution:

$$C_S^{new}(\mathbf{x}) = -\frac{\mathcal{L}_{ij}^*(\mathbf{x})M_{ij}(\mathbf{x})}{\alpha_{ij}(\mathbf{x})M_{ij}(\mathbf{x})} + \frac{M_{ij}(\mathbf{x})}{\alpha_{ij}(\mathbf{x})M_{ij}(\mathbf{x})} \int_{-\infty}^{\infty} \beta_{ij}(\mathbf{y})C_S^{old}(\mathbf{y})G(\mathbf{x}, \mathbf{y})d\mathbf{y} = 0 \quad (5.35)$$

Also since the PIE holds locally at any point, the above scheme may also be used to perform a local iterative solution. However, instead of using this approximate explicit scheme, a highly efficient direct implicit solver was developed to solve the PIE following a similar procedure used in chapter 3 or Ref. [164]. By substituting the 2nd order accurate discrete Gaussian filter of Sagaut and Grohens [35], i.e. Eqs.(2.12) and (2.14) into Eq.(5.30) and averaging the result in the homogeneous plane, the following discrete system can be obtained:

$$\begin{aligned} & \left\{ \langle \alpha_{mn} M_{mn} \rangle_p - \frac{a_0}{3} \langle M_{mn} \beta_{mn} \rangle_p \right. \\ & \left. - \frac{1}{3} \sum_{q=-1}^1 a_q [\langle M_{mn} \beta_{mn}^{I+q, J, K} \rangle_p + \langle M_{mn} \beta_{mn}^{I, J, K+q} \rangle_p] \right\} C_S^J \\ & - \frac{a_{-1}}{3} \langle M_{mn} \beta_{mn}^{I, J-1, K} \rangle_p C_S^{J-1} - \frac{a_1}{3} \langle M_{mn} \beta_{mn}^{I, J+1, K} \rangle_p C_S^{J+1} + \langle M_{mn} \mathcal{L}_{mn}^* \rangle_p \\ & = 0 \end{aligned} \quad (5.36)$$

where $\langle \cdot \rangle_p = \iint \cdot dx_1 dx_3$ represents the plane integral operation, and C_S^J is the model coefficient for the J -th homogeneous plane. The above equation is a 1-D tri-diagonal banded linear system for C_S^J , i.e.

$$\sum_{q=-1}^1 A_q^J C_S^{J+q} + S^J = 0 \quad (5.37)$$

which can be readily solved using the TDMA. Here, A_q^J and S^J represent the coefficients and source term contained in Eq.(5.36), respectively. The boundary condition is set as $C_S = 0$ at the wall. From a physical point of view, C_S influences the magnitude of the SGS viscosity ($\nu_{sgs} = C_S \bar{\Delta}^2 |\bar{S}|$). Therefore, this boundary condition is compatible with the notion that viscous shear is dominant in the vicinity of the wall. Since the computational cost of the TDMA is trivial, the above proposed direct implicit solver is expected to give both high efficiency and accuracy. Although a relative computational cost for different dynamic models is difficult to quantify in a precise manner due to its dependence on the computer configuration and details of the code as indicated earlier, it is meaningful to evaluate the computational cost of the proposed PIE in comparison with those for the standard DM of Lilly [20] and the conventional constant-parameter Smagorinsky model (SM) [13]. The comparative study was performed with the same code structure, and initial velocity and pressure fields. The cost was measured using the averaged computer Time for each Time Step (T/TS) relative to that of the DM. An ALC PC (Pentium IV-2.66GHz) was used to perform the computations for the relative cost analysis. Table 5.1 indicates that the T/TS for the SM is only about 54—63% that of the standard DM, while the proposed PIE generally costs only 2—4% more in terms of T/TS than the standard DM, indicating that the additional cost is negligible.

It should be pointed out that since this highly efficient implicit solver takes advantage of the existence of a homogeneous plane, it is not applicable to a general case where a 2-D homogeneous plane does not exist. For such a general 3-D non-homogeneous case, the discrete filter of Sagaut and Grohens [35] can still be used for discretizing the PIE (Eq.(5.30)) which then becomes a discrete Poisson type equation

TABLE 5.1: Absolute and relative computational cost ($Re = 2600$)

Grid	66^3 nodes		48^3 nodes		34^3 nodes	
Cost	T/TS (s)	Ratio	T/TS (s)	Ratio	T/TS (s)	Ratio
PIE	43.1	1.04	16.0	1.03	4.4	1.02
DM	41.5	1	15.6	1	4.3	1
SM	22.5	0.54	8.7	0.56	2.7	0.63

involving a 7-node stencil (one central node and one neighbor node on each side). As opposed to solving such a discrete Poisson type equation, another option for obtaining a localized solution in the general case is to implement a local iterative solver (e.g. Eq.(5.35)) similar to the preconditioning iterative scheme used by Ghosal *et al.* [40]. Both the discrete Poisson type solution scheme and the iterative solution scheme have the advantage of being applicable to a general 3-D non-homogeneous flow as well as retaining the concept of a strictly local solution for the PIE. However, they are anticipated to be computationally much more expensive.

5.3.2 Basic Flow Features and Discussion

In this subsection, the features of turbulent Couette flow predicted by the LES using the proposed localization model will be presented. Figure 5.1 shows the non-dimensional velocity profiles obtained for the three Reynolds numbers of 2600, 4762 and 7050. Although the differences in the velocity profiles for the Reynolds number of $Re = 2600$ are very small, the LES result is closer to the DNS result of Bech *et al.* [124] than the experimental data of Aydin and Leutheusser [120]. As expected, the velocity profile at $Re = 7050$ has a narrower wall region than those at $Re = 4762$ and $Re = 2600$. The simulation data presented in Fig. 5.1 are replotted in Fig. 5.2 using wall coordinates. The prediction for the near-wall velocity profile generally agrees with the experimental results of Robertson and Johnson [118], Bech *et al.* [124], Aydin and Leutheusser [121], as well as the classical two layer wall law of von Kármán [140]

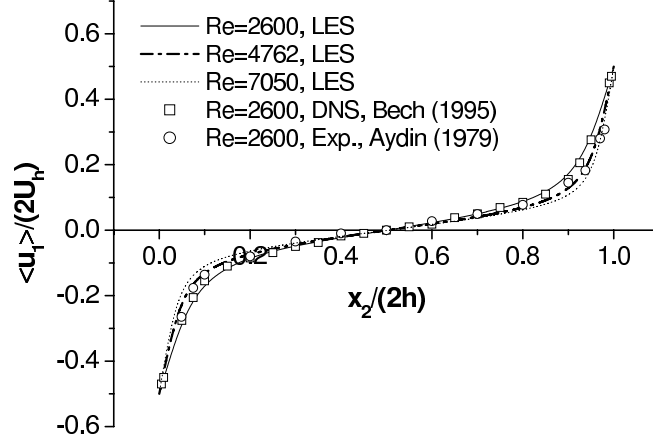


FIGURE 5.1: Mean non-dimensional velocity profile (66^3 nodes).

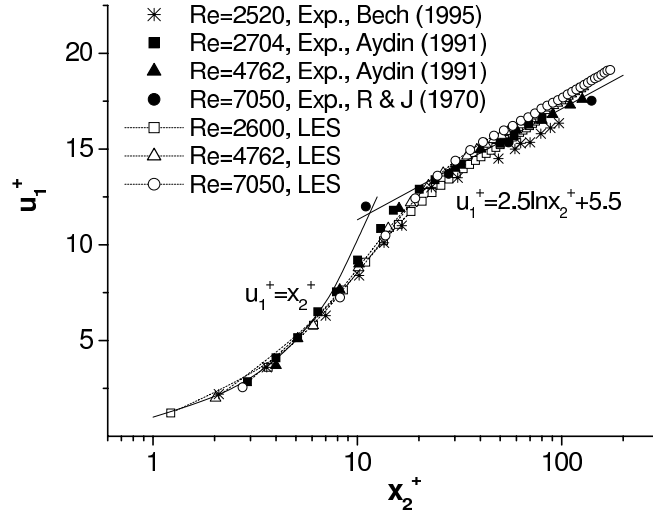


FIGURE 5.2: Mean velocity profile in wall coordinates (66^3 nodes).

given by Eq.(3.7).

Figure 5.3(a)–(c) illustrates the wall-normal distributions of the three resolved turbulence intensity components for three different Reynolds numbers, respectively. The peak value for $\langle \bar{u}_1''^2 \rangle^{1/2} / u_\tau$ appears at $x_2^+ = 13$ for $Re = 2600$, $x_2^+ = 15$ for $Re = 4762$ and $x_2^+ = 16$ for $Re = 7050$. These agree approximately with the locations $x_2^+ = 12$ for $Re = 2600$ reported by Bech *et al.* [124], $x_2^+ = 11 \sim 16$ for $Re = 2600$ and 4762 reported by Aydin and Leutheusser [121], and $x_2^+ \approx 16$ for $Re = 7050$ reported by Robertson and Johnson [118]. Figure 5.3 also indicates that the magnitudes of the peak values of the spanwise and wall-normal components of the turbulence intensities

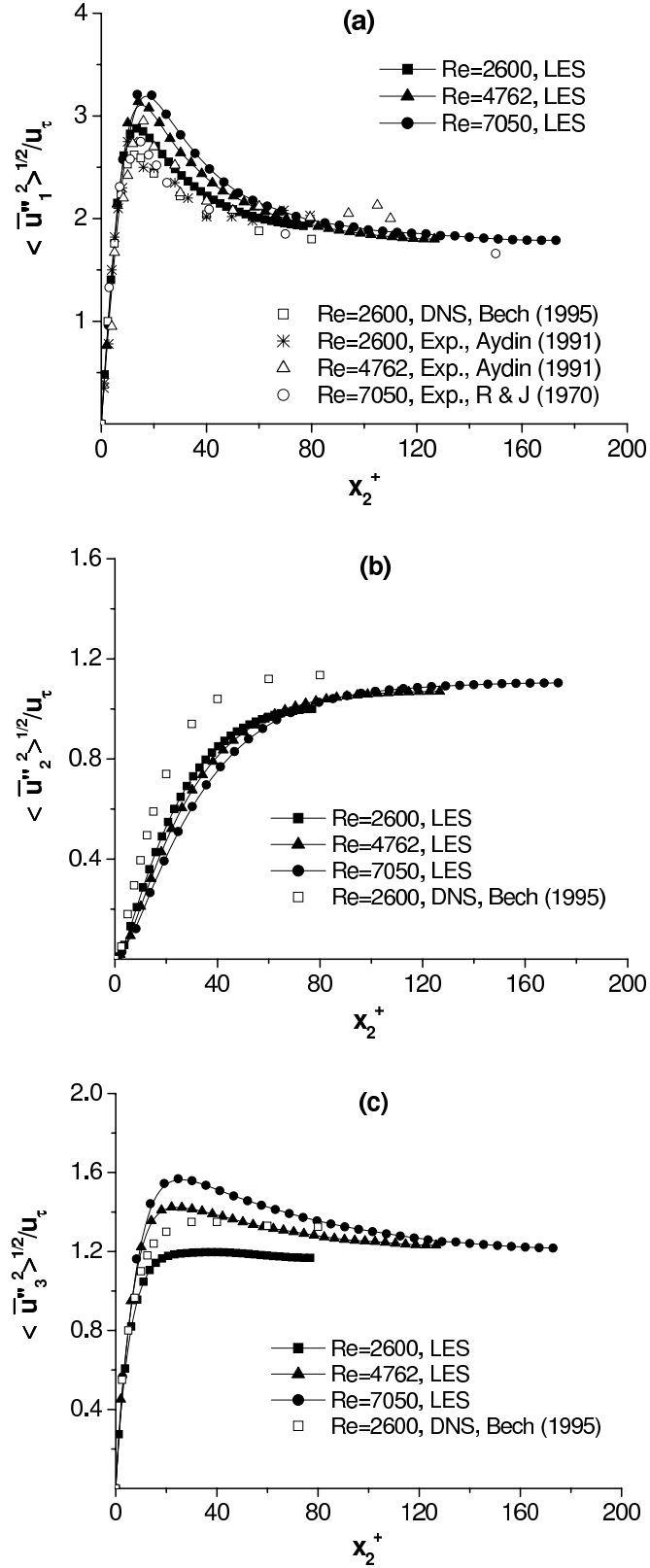


FIGURE 5.3: Averaged wall-normal distribution of resolved turbulence intensities (66^3 nodes).

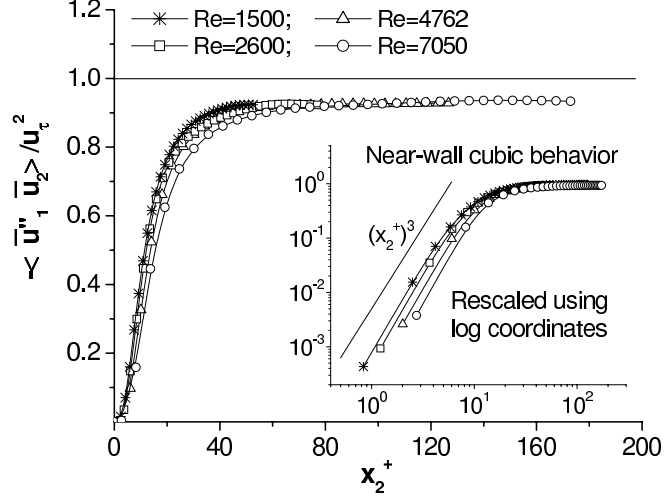


FIGURE 5.4: Averaged wall-normal profile of resolved Reynolds shear stress (66^3 nodes).

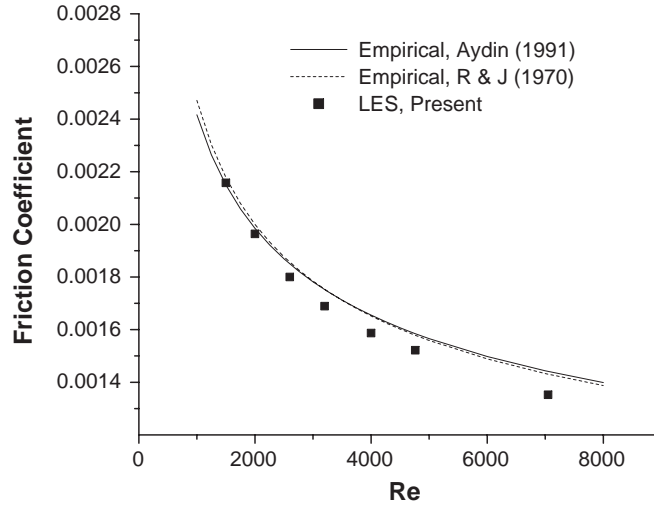


FIGURE 5.5: Variation of the skin-friction coefficient C_f with Reynolds number (66^3 nodes).

predicted using the PIE are somewhat lower than the DNS results ($Re = 2600$) of Bech *et al.* [124], while the streamwise component is slightly higher than those for the DNS and experimental results.

The viscous shear stress dominates in the near-wall region, while the resolved Reynolds shear stress dominates in the core of the channel. As expected, in Fig. 5.4, the resolved value of $-\langle \bar{u}_1'' \bar{u}_2' \rangle / u_\tau^2$ is flat and close to unity in the center of the channel.

TABLE 5.2: Near-wall cubic behavior of the resolved Reynolds shear stress ($Re = 1500$).

x_2^+	$-\langle \bar{u}_1'' \bar{u}_2 \rangle / u_\tau^2$	$(-\langle \bar{u}_1'' \bar{u}_2 \rangle / u_\tau^2) / y^{+3} \times 10^3$
0.822	4.11×10^{-4}	0.740
2.46	1.25×10^{-2}	0.834
4.11	5.84×10^{-1}	0.842
5.75	1.37×10^{-1}	0.719
7.39	2.36×10^{-1}	0.584
9.04	3.38×10^{-1}	0.459
10.7	4.35×10^{-1}	0.356

Near the wall, the resolved Reynolds shear stress varies following a ‘cubic law’ as indicated previously in chapter 3. In the near-wall region, the resolved Reynolds shear stress can be approximated as

$$-\langle \bar{u}_1'' \bar{u}_2 \rangle / u_\tau^2 = \mathcal{A} \cdot (x_2^+)^3 \quad (5.38)$$

Monin and Yaglom [3] estimated the value of \mathcal{A} to be about 0.001. Table 5.2 indicates that \mathcal{A} ranges from 0.00074 to 0.00084 in the viscous sublayer for $x_2^+ \leq 5$, which values are close to those reported by Kim *et al.* [135].

Figure 5.5 compares the predicted values for the skin friction coefficient with those of the two empirical friction laws for turbulent Couette flow, i.e. friction law of Aydin and Leutheusser [121] given by Eq.(3.5) and that of Robertson and Johnson [118] in the following form:

$$C_f = \frac{0.072}{4 \cdot [\log(2Re)]^2} \quad (5.39)$$

Figure 5.5 shows that the friction coefficient obtained from the LES results generally agrees with both Eqs.(5.39) and (3.5), although it tends to be somewhat lower at higher Reynolds numbers with a maximum deviation of approximately 8%.

5.3.3 Rate of SGS TKE Production, Modulus of Filtered Strain Rate Tensor, Model Coefficient and SGS Viscosity

In order to understand the characteristics of the model coefficient C_S and SGS viscosity ν_{sgs} , we need first to discuss the SGS TKE production rate \mathcal{P}_r , resolved viscous dissipation rate ε_r and modulus of the filtered strain rate tensor $|\bar{S}|$.

Figure 5.6 shows the mean distribution of \mathcal{P}_r along the wall-normal direction in terms of both dimensional and nondimensional values. We observe that \mathcal{P}_r exhibits a general anisotropy due to the restriction by the wall: it is lower in the central region and peaks in the near-wall region around $x_2^+ = 13$. From the dimensional diagram, we observe that the profile of \mathcal{P}_r is sensitive to the Reynolds number, i.e. the absolute value of \mathcal{P}_r increases dramatically as the Reynolds number increases. This is explained by the fact that for the same discrete grid system, a higher Reynolds number turbulent flow has ‘more’ net TKE to be transferred from the resolved to subgrid scales of motions. Figure 5.7 demonstrates the grid effect on the \mathcal{P}_r term. Clearly, as the grid becomes coarser, the nondimensional value of \mathcal{P}_r increases in the boundary layer region, especially around the peak location.

Equation (3.9) is a general definition for \mathcal{P}_r , which is applicable to any SGS constitutive relations. In general, e.g. for the dynamic two-parameter mixed models [44, 48, 50, 143, 148, 155] and quadratic nonlinear dynamic models [161, 162], the value of \mathcal{P}_r is decided by both the magnitudes of τ_{ij} , \bar{S}_{ij} (and other terms), as well as their relative tensorial geometrical relation. The importance of the tensorial geometry of the negative SGS stress and filtered strain rate tensors has lately been indicated by several studies based on *a priori* approaches [29, 70, 99, 100, 165] and *a posteriori* approaches [101–107]. Since $-\tau_{ij}$ is not necessarily aligned with \bar{S}_{ij} in the general case, various possibilities exist, one of which is the specific theoretical situation that an instantaneous orthogonality is allowed to exist between the $-\tau_{ij}$ and \bar{S}_{ij} such that their production is trivial, i.e. $\mathcal{P}_r = -\tau_{ij}^* \bar{S}_{ij} = 0$ (although the value of $|\tau_{ij}|$ and $|\bar{S}|$

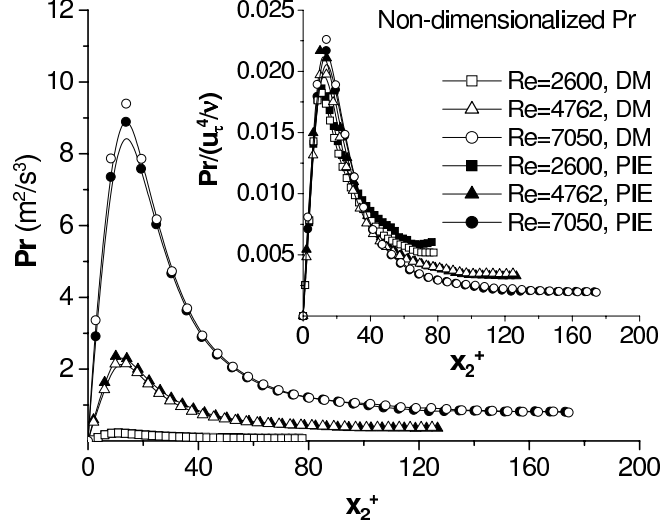


FIGURE 5.6: Averaged rate of SGS TKE production in the wall-normal direction (66^3 nodes).

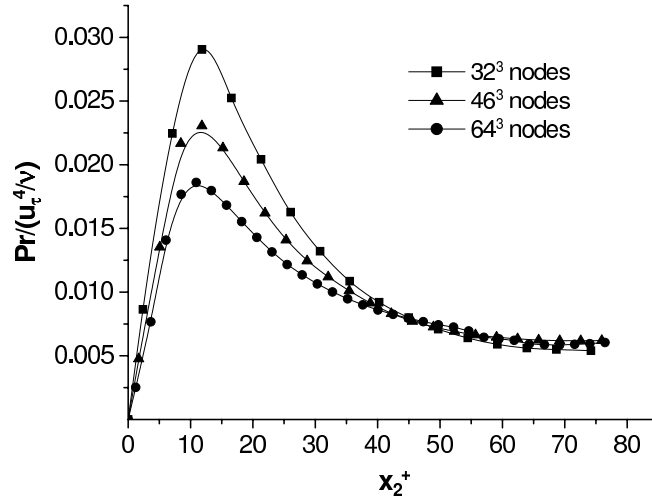


FIGURE 5.7: Grid effect on the rate of SGS TKE production ($Re = 2600$).

may be very large). For the Smagorinsky type models, the case that $\mathcal{P}_r = 0$ due to such an orthogonality never exists, since $-\tau_{ij}$ is always aligned with \bar{S}_{ij} . Furthermore, for the Smagorinsky type models, if $\mathcal{P}_r = 0$ and $\bar{\Delta} \neq 0$ then at least one of the two following conditions must be true: $C_S = 0$ and/or $|\bar{S}| = 0$. In general, a higher \mathcal{P}_r is not a sufficient condition for a larger value of C_S or ν_{sgs} , because the value of \mathcal{P}_r is decided not only by the relative tensorial magnitudes of τ_{ij} and \bar{S}_{ij} but also by the relative geometry between them as well. Notwithstanding the general case, in

the particular case of the Smagorinsky type models, \mathcal{P}_r takes the following form on substituting Eq.(1.12):

$$\mathcal{P}_r = \nu_{sgs} |\bar{S}|^2 = C_S \bar{\Delta}^2 |\bar{S}|^3 \quad (5.40)$$

Thus, for a particular turbulent flow with the Reynolds number specified, $\mathcal{P}_r = \mathcal{P}_r(\nu_{sgs}, |\bar{S}|) = \mathcal{P}_r(C_S, \bar{\Delta}, |\bar{S}|)$ when a Smagorinsky constitutive relation is adopted for the SGS model. From previous analysis, we understand that a higher Reynolds number corresponds to a higher level of \mathcal{P}_r . While from Eq.(5.40), it is understood that a higher level of \mathcal{P}_r does not necessarily correspond to larger values of C_S or ν_{sgs} , because the parameter $|\bar{S}|$ is also involved which responds to the Reynolds number independently.

The viscous dissipation rate at the filtered scale defined by Eq.(3.10) can be rearranged into

$$\varepsilon_r = 2\nu \bar{S}_{ij} \bar{S}_{ij} = \nu |\bar{S}|^2 \quad (5.41)$$

which indicates that $\varepsilon_r \propto |\bar{S}|^2$, i.e. ε_r is an indicator for the magnitude of the filtered strain rate tensor $|\bar{S}|$. Figures 5.8 and 5.9 plot the dimensional and non-dimensional profiles of the resolved viscous dissipation rate ε_r in the wall-normal direction for the entire channel and the core region. From the dimensional profiles, it is observed that both ε_r and \bar{S} increase with the Reynolds number. As shown in both the dimensional and non-dimensional diagrams, ε_r increases drastically as the wall is approached especially within $x_2^+ < 30$. This also indicates a strong anisotropic distribution of the modulus of the filtered strain rate tensor $|\bar{S}|$ along the wall-normal direction. The anisotropy of $|\bar{S}|$ is due to the behavior of the dominant velocity gradient component $\bar{u}_{1,2}$, whose value changes drastically in the near wall region and averagely reaches a maximum at the wall.

Figure 5.10 illustrates the mean distribution of the proposed model coefficient C_S along the wall-normal direction in comparison with those calculated using the conventional DM [20] and SM [13]. Figure 5.11 demonstrates the grid scale effect on the wall-normal distribution of the model coefficient calculated using the PIE. $C_S^{1/2}$ instead of C_S was used in Figs. 5.10 and 5.11, because the conventional SM [13]

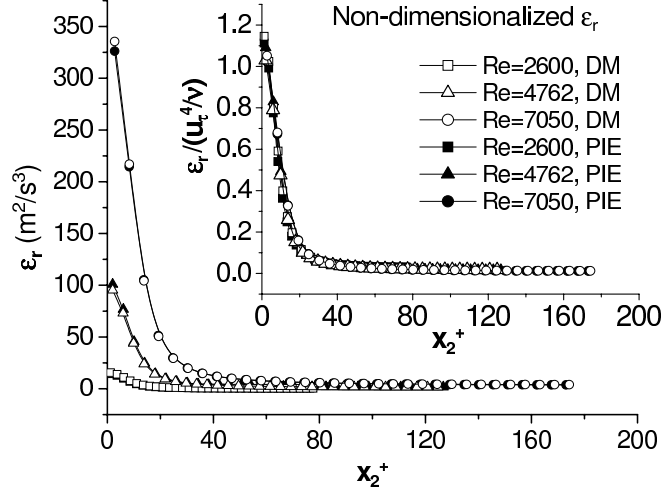


FIGURE 5.8: Resolved viscous dissipation in the wall-normal direction (66^3 nodes).

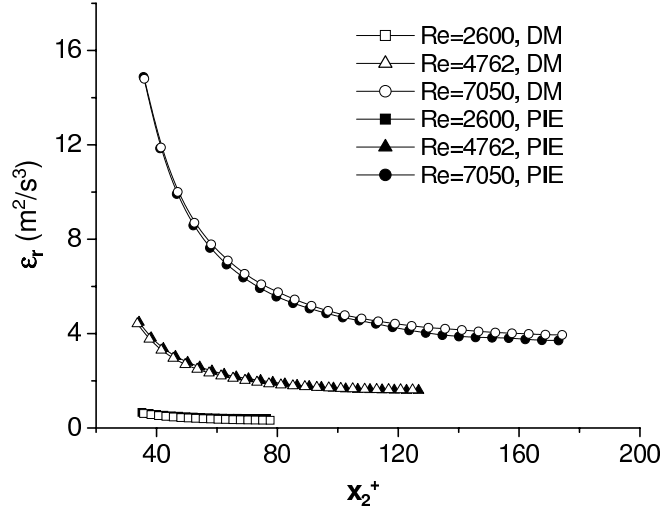


FIGURE 5.9: Resolved viscous dissipation rate in the core region (66^3 nodes).

uses C_S^2 (instead of C_S) to model the SGS stress tensor in Eq.(1.12). As shown in Fig. 5.10, the value of the Smagorinsky constant for the SM typically [1, 10, 139] ranges from 0.065 to 0.12, however, the $C_S^{1/2}$ value for the PIE ranges only from 0.014 ($Re = 7050$) to 0.026 ($Re = 2600$) in the core region. The model coefficient profile for both the DM and PIE vanishes at the wall, which is due to the requirement that the SGS viscosity must vanish at the wall ($\nu_{sgs}|_{x_2^+=0} \equiv 0$). This is intrinsically different than the approach of the SM, in which case this physical requirement is forced to be realized by an *ad hoc* geometric damping function instead of the model itself, for

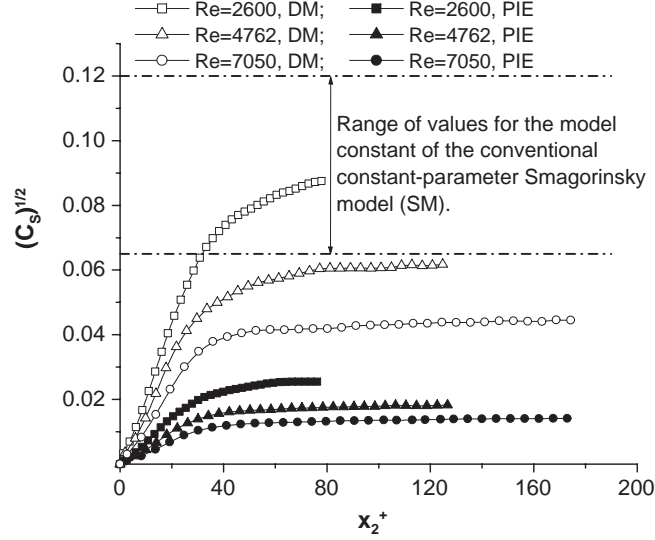


FIGURE 5.10: Mean distribution of the model coefficient in the wall-normal direction (66^3 nodes).

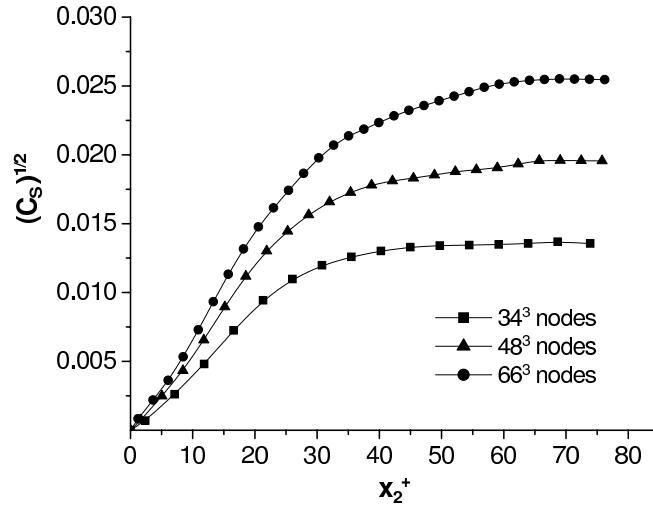


FIGURE 5.11: Grid effect on model coefficient ($Re = 2600$).

instance [38], $d(x_2^+) = [1 - \exp(-x_2^{+3}/25^3)]$. Also, as demonstrated in Fig. 5.10, for the three Reynolds numbers tested, the value of $C_s^{1/2}$ for the PIE is about 30% that of the DM, although both the DM and PIE are dynamic SGS models based on the same Smagorinsky constitutive relation. Furthermore, it is observed from Fig. 5.10 that as the Reynolds number increases, the value of C_s decreases for both the PIE and DM, which confirms our previous analysis that for the dynamic Smagorinsky model, a higher Reynolds number is not necessarily linked to a larger C_s because of

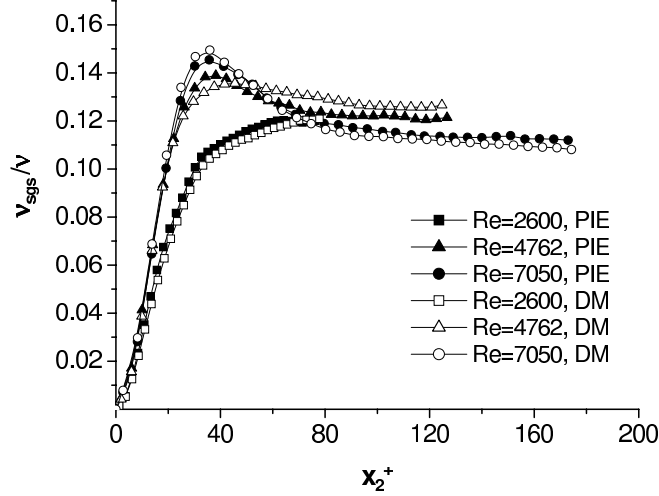


FIGURE 5.12: Mean SGS viscosity profile in the wall-normal direction (66^3 nodes).

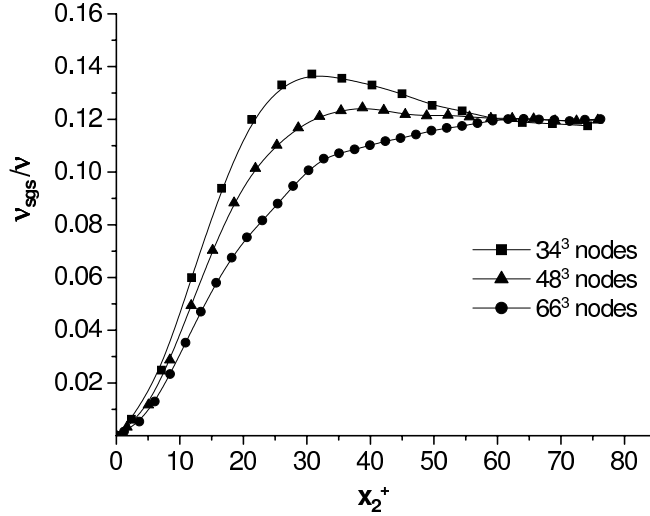


FIGURE 5.13: Grid effect on SGS viscosity ($Re = 2600$).

the involvement of $|\bar{S}|$ which is a function of Re (see Eq.(5.41) and Figs. 5.8 and 5.9).

Figure 5.12 demonstrates that as the Reynolds number increases, the profile of the SGS viscosity ν_{sgs} increases only slightly in the buffer region, which is in contrast to the large change in the C_S profile discussed in the previous paragraph. The explanation lies in the definition of ν_{sgs} , which indicates that for any particular instantaneous flow field (Re must be specified), ν_{sgs} is a function of the grid-level filter size, C_S and $|\bar{S}|$, i.e. $\nu_{sgs} = \nu_{sgs}(\bar{\Delta}, C_S, |\bar{S}|)$. Thus, it is clear that a larger value of ν_{sgs} does not necessarily correspond to a large value of C_S due to the involvement of $|\bar{S}|$ (if

$\bar{\Delta}$ is fixed). In fact, from Fig. 5.8 and 5.9, we understand that $|\bar{S}|$ increases drastically with Re , which explains the difference between the Reynolds number effects on C_S and ν_{sgs} . Figure 5.12 indicates that the buffer region (especially around $x_2^+ \approx 30$) responds to the Reynolds number more actively than other parts of the flow in terms of ν_{sgs} . Such an anisotropic behavior of ν_{sgs} is consistent with its definition (Eq.(1.13)) and the near-wall anisotropic effect of $|\bar{S}|$ and C_S as illustrated in Figs. 5.8 and 5.10, respectively. Figure 5.13 indicates that the buffer region also responds to the grid scale more sensitively than other regions in terms of the value of ν_{sgs} .

Finally, we briefly comment on the non-dimensionalization method for the SGS viscosity used in this research. From the Eqs.(5.41) and (5.40), we understand that ν_{sgs}/ν has a special meaning unique for the Smagorinsky constitutive relation: the ratio ν_{sgs}/ν actually describes the relative magnitudes of the two sinks for the TKE for the filtered motions, i.e. $\mathcal{P}_r/\varepsilon_r \equiv \nu_{sgs}/\nu$. Therefore, it is understood that the two non-dimensional parameters, i.e. $\mathcal{P}_r/\varepsilon_r$ used previously in Fig. 3.12 (for demonstrating the ILDM and DM) and ν_{sgs}/ν used currently in Figs. 5.12 and 5.13 (for demonstrating the PIE and DM) are equivalent.

5.4 Conclusions

This chapter provides a consistent mathematical treatment for localizing the coefficient C_S for the dynamic Smagorinsky SGS stress model, and also revisits the Smagorinsky relation in the concept of functional variation and function approximation. In contrast to the approach of Ghosal *et al.* [40], the local error density functional \mathcal{Q} has been successfully minimized without resorting to a global integration. The properties of the variations of the local error functional at different orders have been examined, and the possibilities of the non-extremum inflection and saddle points have been strictly excluded from the solution set of optimization. A theorem on the sufficient and necessary condition for localizing the dynamic Smagorinsky model using functional variational theory has been obtained, which is in the form of

an orthogonal condition (OC) and controls the localization model coefficient for the dynamic Smagorinsky SGS model. The OC is a useful tool in dynamic SGS modelling optimization, which unifies some conventional modelling formulations as its special theoretical solutions under different restrictions. These conventional approaches include the dynamic model of Germano *et al.* [19] and Lilly [20], and the Fredholm integral equation of the second kind (FIE2) [40].

From the integral form of the OC (IOC), a new Fredholm integral equation of the third kind or Picard's integral equation (PIE) has also been derived, which is necessary to make the local error density \mathcal{Q} minimum. Similar to the FIE2 [40], the obtained PIE holds locally at any point and needs to be solved only once for the entire domain. Further, the obtained PIE is more desirable in terms of the computational efficiency since it has one less convolution operation than the FIE2 introduced earlier by Ghosal *et al.* [40].

For the purpose of demonstrating the theoretical potential of the OC as well as the possibility of applying it in practice, numerical tests based on the PIE have been performed using turbulent Couette flow. Prototypical features of near-wall turbulent flow have been obtained and compared with the experimental and DNS results of other researchers, including the existence of a logarithmic mean velocity profile, the characteristic anisotropic wall-normal distribution of the resolved turbulent intensities, and a near-wall cubic behavior for the resolved Reynolds shear stress component. In order to solve the PIE effectively, a direct implicit solution scheme with an additional computational cost of less than 4% compared to the DM, has been developed by using the discrete Gaussian filter of Sagaut and Grohens [35]. Such an efficient implicit solution scheme for the PIE holds when it is acceptable to assume homogeneity in planes parallel to the walls. It should be noted that as the necessary and sufficient condition for localization, the OC has many theoretical applications, and the PIE is only one of its derivatives.

Physical meanings for such grid and test-grid level tensors as α_{ij} , β_{ij} , M_{ij} , M'_{ij} , \mathcal{L}_{ij}^{appr*} and \mathcal{L}_{ij}^{proj*} have been proposed by identifying their role in various constitutive

and constructive relations. The construction of the tensorial approximation space for the projection of the Leonard stress has also been discussed, including the tensorial approximation space of Lilly’s original [20] approach \mathfrak{M}_L^{orig} , that of the revised approach of Lilly \mathfrak{M}_L^{rev} , and that of the general localization approach \mathfrak{M}_0 . These tensorial approximation spaces for the Leonard stress are essential to the optimization methods adopted for deriving the dynamic localization models using the local minimal residual of the Germano identity as the criterion.

For the Smagorinsky constitutive relation, the modulus of the filtered strain rate tensor $|\bar{S}|$ plays the key role in determining the relative magnitudes of the SGS stress τ_{ij} , SGS TKE production rate \mathcal{P}_r , SGS viscosity ν_{sgs} , and model coefficient C_S . The value of $|\bar{S}|$ (indicated by the resolved viscous dissipation rate ε_r) changes dramatically with Reynolds number, especially within the near-wall region for $x_2^+ < 30$. Given that all the other test conditions are the same, the mean rate of SGS TKE production \mathcal{P}_r increases as the Reynolds number increases, indicating a larger net transfer of TKE between the filtered and subgrid scales of motions. From the definition of the SGS viscosity, it is understood that a large value of ν_{sgs} does not of itself require a large value of C_S because of the role of $|\bar{S}|$. For a specific flow (with the grid-level filter and Re specified), \mathcal{P}_r changes with C_S and $|\bar{S}|^3$, or with ν_{sgs} and $|\bar{S}|^2$, and therefore due to the involvement of $|\bar{S}|$, a higher level of \mathcal{P}_r does not necessarily imply a higher level of C_S or ν_{sgs} , although it is observed from the numerical simulation that it is true that ν_{sgs} increases slightly with Re (and thus with the level of \mathcal{P}_r) in the buffer region.

In general, this chapter attempts to investigate the properties of the localization SGS stress model within the framework of the Smagorinsky constitutive relation. An extensive discussion of this topic is always useful, because so far the (dynamic) Smagorinsky type models are still the most popular in the LES community. However, it should be indicated that many drawbacks of the (dynamic) Smagorinsky type models originate from its overly simplified constitutive relation based on the Boussinesq hypothesis. An increasing body of research [29, 99, 109, 158–162] suggests that instead of performing localization within the simple Smagorinsky constitutive frame-

work, which cannot correctly reflect the tensorial geometry of the SGS stress and usually results in a formulation that is relatively difficult to solve (e.g. an integral equation), improved methods should consider non-Smagorinsky constitutive relations in the dynamic modelling procedure [44, 48, 50, 143, 148, 155, 160–162]. The exploration of this topic will be continued in the next three chapters.

Chapter 6

A Novel Dynamic Nonlinear Subgrid Scale Stress Model

6.1 Introduction

In chapter 1, the classical Boussinesq hypothesis and its application in LES was briefly reviewed. The limitations of the conventional Smagorinsky constitutive relation were also discussed. For instance, since the Smagorinsky type models (e.g. DM and ILDM) are based on the Boussinesq hypothesis, a strict alignment between the principal axes of $-\tau_{ij}$ and \bar{S}_{ij} is required, which makes it impossible to mimic a realistic physical process that is strongly based on tensorial alignments, e.g. backscatter. In this chapter, we seek an improved dynamic SGS stress modelling approach based on an explicit nonlinear tensorial polynomial constitutive relation.

The idea of using an *explicit nonlinear tensorial polynomial constitutive relation* to connect the velocity gradient tensor and the unknown stress tensor to be modelled was originally proposed by Rivlin [166] in the area of non-Newtonian fluid mechanics. He also suggested that the normal components of the Reynolds stress of Newtonian fluids in turbulent flows may show a visco-elastic effect, in which case the fluids behave like a classical non-Newtonian medium undergoing a homogeneous deformation. Based on analogies with non-Newtonian fluids, the primary framework of a nonlinear constitutive relation for closing the Reynolds stress model in RANS was systematically set up by Lumley [158]. Using the theory of invariants (see Spencer [157]),

Pope [159] formulated a general expression for the Reynolds stress tensor relying on ten independent tensorial bases and five invariants derived from the full velocity gradient. Pope's pioneering general effective-viscosity hypothesis was only validated using a 2-D turbulent flow due to the complexity of the algebra involved. The extension of the modelling formulation from 2-D to 3-D turbulence was later accomplished by Taulbee [167], and Gatski and Speziale [109]. In the RANS literature, different numbers of nonlinear terms have been included in the explicit nonlinear tensorial polynomial constitutive relation. For instance, the nonlinear models of Yoshizawa [168], Horiuti [169], Speziale [108], Mompean [170], Speziale and Xu [171], and Rubinstein and Barton [172] are all quadratic, while the nonlinear models tested by Craft *et al.* [173] and Wall and Taulbee [174] take cubic and fifth order forms, respectively.

On observing the deficiencies of the linear (dynamic) Smagorinsky type models mentioned previously, nonlinear SGS modelling approaches were introduced into the LES community. Earlier works on the nonlinear model include the scale-similarity and related mixed models [18, 23, 175]. More related to this research, the explicit nonlinear tensorial polynomial stress modelling approach proposed by Rivlin [166], Lumley [158] and Pope [159] was implemented into LES in 1992 by Lund and Novikov [160], Meneveau *et al.* [176], and Wong [161]. The nonlinear model proposed by Lund and Novikov [160] takes a cubic form, which has five model coefficients that need to be determined. They evaluated their model coefficients using DNS data for homogeneous isotropic turbulence. The criterion for the least squares optimization used for determining the five coefficients in their *a priori* examination was the minimal norm of the difference between the SGS stress extracted from DNS data and that predicted by the model itself. This criterion is different than that used in the dynamic modelling procedure of Lilly [20], which is the minimal norm of the Germano identity residual based on a second test-grid filtering process [19]. Using a DNS database for isotropic turbulence, homogeneous shear flow and channel flow, Meneveau *et al.* [176] investigated the correlation between the SGS stress tensor, and the resolved strain rate and rotation rate tensors. Improved nonlinear models (including that of Lund and Novikov [160]) that parameterize the SGS stresses have been investigated using

a special statistical method, i.e. the projection pursuit regression method. Based on Holographic PIV (HPIV) measurements of a turbulent duct flow, Tao *et al.* [29, 99] analyzed the geometrical relations among the SGS stress tensor, strain rate tensor and vorticity vector. Horiuti [100] further examined the nonlinear constituent terms in regard to their tensorial principal alignment, and also their roles in vortex stretching and backscatter phenomena. Horiuti's research was based on *a priori* study using DNS data for incompressible homogeneous isotropic turbulence. Wong [161] adopted the quadratic constitutive relation of Speziale [108, 109] and implemented the dynamic procedure into the nonlinear SGS stress model that could be used for *a posteriori* studies. Wong's approach is characterized by use of the SGS TKE equation, two model coefficients, and lumping the two non-Smagorinsky nonlinear terms together (linearly) with equal weights. Canuto and Cheng [139] evaluated the value of the Smagorinsky model coefficient using the framework of a full nonlinear modelling approach proposed by Pope [159]. Kosović [162] also implemented the quadratic nonlinear constitutive relation of Speziale [108, 109] into LES. The three model coefficients in Kosović's approach were determined analytically using the assumption of isotropic equilibrium turbulence and Kolmogorov's $-5/3$ law for the inertial subrange.

One of the major objectives of this chapter is to propose a Dynamic Nonlinear SGS stress Model (DNM) which is able to eliminate the drawbacks of the (dynamic) Smagorinsky type models including the DM and ILDM which have been investigated in previous chapters. To be specific, it should allow the constituent terms the flexibility for self-calibration of their coefficients, admit various tensorial orientations of the SGS stress tensor, reflect both forward and backward TKE scattering processes between the resolved and unresolved scales of motions, and exhibit instantaneous local stability which removes the necessity for the conventional plane averaging technique. The remainder of the chapter is organized in the following way: the model will be formulated in section 6.2, results of numerical validations of the DNM using turbulent Couette flow will be presented in section 6.3, the geometrical characteristics of the DNM will be investigated in section 6.4, the properties of the tensorial eigensystem of the DNM will be studied in section 6.5, features of SGS TKE transfer between

filtered and subgrid scales including backscatter will be analyzed in section 6.6, and finally the conclusions for this chapter will be summarized in section 6.7.

6.2 A New Dynamic Nonlinear Model

Guided by the Smagorinsky model, one may assume that the generic SGS stress τ_{ij} is a function of the resolved velocity gradient, the cutoff filter size $\bar{\Delta}$ and the unit tensor δ_{ij} , which is [10]

$$\tau_{ij}^* = \tau_{ij} - \frac{\delta_{ij}}{3}\tau_{kk} = f(\bar{S}_{ij}, \bar{\Omega}_{ij}, \delta_{ij}, \bar{\Delta}) \quad (6.1)$$

where \bar{S}_{ij} and $\bar{\Omega}_{ij}$ are the resolved strain rate and rotation rate tensors, which represent the symmetric and antisymmetric parts of the filtered velocity gradient, respectively:

$$\begin{aligned} \bar{u}_{i,j} &= \frac{1}{2}(\bar{u}_{i,j} + \bar{u}_{j,i}) + \frac{1}{2}(\bar{u}_{i,j} - \bar{u}_{j,i}) \\ &\stackrel{\text{def}}{=} \bar{S}_{ij} + \bar{\Omega}_{ij} \end{aligned} \quad (6.2)$$

The resolved vorticity vector is defined as $\bar{\omega}_i = \varepsilon_{ijk}\bar{u}_{k,j} = \varepsilon_{ijk}\bar{\Omega}_{kj}$, where ε_{ijk} is the Levi-Civita permutation symbol. For brevity of expression, the following notations related to tensorial contractions are introduced [10]:

$$\begin{aligned} \mathbf{S}\boldsymbol{\Omega} &= \bar{S}_{ik}\bar{\Omega}_{kj} \\ \mathbf{S}^2 &= \bar{S}_{ik}\bar{S}_{kj} \\ \text{tr}(\mathbf{S}\boldsymbol{\Omega}^2) &= \bar{S}_{ij}\bar{\Omega}_{jk}\bar{\Omega}_{ki} \end{aligned} \quad (6.3)$$

A general explicit expression for Eq.(6.1) is a *tensorial polynomial* with an infinite number of tensors involving \mathbf{S} and $\boldsymbol{\Omega}$ of the form $\mathbf{S}^{m_1}\boldsymbol{\Omega}^{n_1}\mathbf{S}^{m_2}\boldsymbol{\Omega}^{n_2}\dots$, where m_i and n_i are positive numbers [160]. However, in accordance with the theory of invariants (Rivlin [166], Spencer [157]) and the Cayley-Hamilton theorem, Pope [159] obtained a general constitutive relation for closure of the Reynolds stress in RANS,

which has only a finite number of tensorial terms. Given the constitutive relation (6.1), Lund and Novikov [160] introduced an integrity set which has eleven independent symmetric tensorial elements related to the products of \mathbf{S} and $\mathbf{\Omega}$

$$\begin{aligned}
\mathbf{T}^{(1)} &= \mathbf{S} & \mathbf{T}^{(2)} &= \mathbf{S}^2 \\
\mathbf{T}^{(3)} &= \mathbf{\Omega}^2 & \mathbf{T}^{(4)} &= \mathbf{S}\mathbf{\Omega} - \mathbf{\Omega}\mathbf{S} \\
\mathbf{T}^{(5)} &= \mathbf{I}_d & \mathbf{T}^{(6)} &= \mathbf{S}^2\mathbf{\Omega} - \mathbf{\Omega}\mathbf{S}^2 \\
\mathbf{T}^{(7)} &= \mathbf{S}\mathbf{\Omega}^2 + \mathbf{\Omega}^2\mathbf{S} & \mathbf{T}^{(8)} &= \mathbf{\Omega}\mathbf{S}\mathbf{\Omega}^2 - \mathbf{\Omega}^2\mathbf{S}\mathbf{\Omega} \\
\mathbf{T}^{(9)} &= \mathbf{S}\mathbf{\Omega}\mathbf{S}^2 - \mathbf{S}^2\mathbf{\Omega}\mathbf{S} & \mathbf{T}^{(10)} &= \mathbf{S}^2\mathbf{\Omega}^2 + \mathbf{\Omega}^2\mathbf{S}^2 \\
\mathbf{T}^{(11)} &= \mathbf{\Omega}\mathbf{S}^2\mathbf{\Omega}^2 - \mathbf{\Omega}^2\mathbf{S}^2\mathbf{\Omega}
\end{aligned} \tag{6.4}$$

and *integrity bases* consisting of the six associated *irreducible tensorial invariants*

$$\begin{aligned}
I_1 &= \text{tr}(\mathbf{S}^2) & I_2 &= \text{tr}(\mathbf{\Omega}^2) \\
I_3 &= \text{tr}(\mathbf{S}^3) & I_4 &= \text{tr}(\mathbf{S}\mathbf{\Omega}^2) \\
I_5 &= \text{tr}(\mathbf{S}^2\mathbf{\Omega}^2) & I_6 &= \text{tr}(\mathbf{S}^2\mathbf{\Omega}^2\mathbf{S}\mathbf{\Omega})
\end{aligned} \tag{6.5}$$

where \mathbf{I}_d is the identity tensor. It should be noted that I_6 can be expressed using the other five invariants, however, with its sign undetermined. Thus, one can also argue in the mathematics that only the first five invariants are genuinely irreducible, as is commonly adopted in the RANS community (see Pope [32], Gatski and Speziale [109], and Wall and Taulbee [174]). In any event, the SGS stress tensor τ_{ij} can be linearly expressed using the above independent tensors, which is an explicit tensorial polynomial of \mathbf{S} and $\mathbf{\Omega}$:

$$\tau_{ij} = \sum_{k=1}^{11} G^{(k)} \mathbf{T}^{(k)} \tag{6.6}$$

where the scalar coefficients G^k are functions of the six irreducible tensorial invariants [159]. In both the RANS and LES communities, Eq.(6.6) with all eleven tensors is not used due to the demanding computational cost, complexity of the associated algorithm and undesirable performance of some tensorial terms in simulations. A popular approach is to use the first five tensors to construct a *nonlinear quadratic constitutive relation*. However, Speziale [108,109,177] eliminated terms related to $\mathbf{T}^{(3)}$

from the quadratic formulation because it yielded an erroneous prediction for isotropic turbulence subjected to a solid body rotation in a RANS approach. Speziale's observation [108, 109] has been utilized by Wong [161] and Kosović [162] to construct nonlinear SGS stress models for LES as noted previously. Also in the tests of Lund and Novikov [160], for their ten different SGS models constructed by using different combinations of independent tensors, the five worst scenarios all included $\mathbf{T}^{(3)}$ and the five best scenarios were generally not related to this term, with only one exception. For these reasons, the tensor $\mathbf{T}^{(3)}$ was not considered in the constitutive relation adopted in this research and instead Speziale's quadratic formulation of [108, 109, 161, 162] was employed. Thus, for the dynamic SGS modelling approach, the deviatoric grid-level and test-grid level stress tensors are proposed, respectively, to be

$$\tau_{ij}^* = -C_S \beta_{ij} - C_W \gamma_{ij} - C_N \eta_{ij} \quad (6.7)$$

and

$$T_{ij}^* = -C_S \alpha_{ij} - C_W \lambda_{ij} - C_N \zeta_{ij} \quad (6.8)$$

where the tensors α_{ij} and β_{ij} have been defined previously in Eqs.(1.19) and (1.20), respectively, and the new tensorial notations appearing in the above equations are

$$\begin{aligned} \gamma_{ij} &= 2\bar{\Delta}^2(\bar{S}_{ik}\bar{\Omega}_{kj} - \bar{\Omega}_{ik}\bar{S}_{kj}) \\ \lambda_{ij} &= 2\tilde{\Delta}^2(\tilde{S}_{ik}\tilde{\Omega}_{kj} - \tilde{\Omega}_{ik}\tilde{S}_{kj}) \\ \eta_{ij} &= 4\bar{\Delta}^2(\bar{S}_{ik}\bar{S}_{kj} - \frac{1}{3}\bar{S}_{mn}\bar{S}_{nm}\delta_{ij}) \\ \zeta_{ij} &= 4\tilde{\Delta}^2(\tilde{S}_{ik}\tilde{S}_{kj} - \frac{1}{3}\tilde{S}_{mn}\tilde{S}_{nm}\delta_{ij}) \end{aligned} \quad (6.9)$$

By minimizing the modulus of the Germano identity using the least squares approach (see Appendix A), a third order quadratic optimal DNM can be obtained

$$\left[\begin{array}{c|cc} M_{ij}M_{ij} & M_{ij}W_{ij} & M_{ij}N_{ij} \\ \hline W_{ij}M_{ij} & W_{ij}W_{ij} & W_{ij}N_{ij} \\ N_{ij}M_{ij} & N_{ij}W_{ij} & N_{ij}N_{ij} \end{array} \right] \cdot \left[\begin{array}{c} C_S \\ C_W \\ C_N \end{array} \right] = - \left[\begin{array}{c} \mathcal{L}_{ij}^* M_{ij} \\ \mathcal{L}_{ij}^* W_{ij} \\ \mathcal{L}_{ij}^* N_{ij} \end{array} \right] \quad (6.10)$$

or $\mathbf{AC} = \mathbf{B}$ for brevity. Here, $W_{ij} = \lambda_{ij} - \tilde{\gamma}_{ij}$ and $N_{ij} = \zeta_{ij} - \tilde{\eta}_{ij}$ are two *differential tensorial functions*. By comparing the above model formulation with the conventional DM formulation (Eq.(1.27)) of Lilly [20], we understand from the block matrix decomposition and multiplication shown in Eq.(6.10) that the conventional DM of Lilly [20] is the special case of the 1st order approximation for this 3rd order DNM.

6.3 Analysis of Numerical Results

Since a SGS model is usually applied locally at each node at every time step, its efficiency directly affects the general computational cost and practicability. A comparison has been made to study the relative computational cost among the proposed DNM, the standard DM of Lilly [20], and the conventional constant-parameter Smagorinsky model (SM) [13]. The comparative study was performed with the same code structure, and initial velocity and pressure fields. The cost was measured using the averaged computer Time for each Time Step (T/TS) relative to that of the conventional DM. An ALC PC (Pentium IV-2.66GHz) was used to perform the computations for the relative cost analysis. Table 6.1 indicates that the T/TS for the SM is only about 54—63% that of the standard DM, while the proposed DNM generally costs 23—30% more in terms of T/TS than the standard DM, which is not a substantial increase.

TABLE 6.1: Absolute and relative computational cost ($Re = 2600$)

Grid	66 ³ nodes		48 ³ nodes		34 ³ nodes	
Cost	T/TS (s)	Ratio	T/TS (s)	Ratio	T/TS (s)	Ratio
DNM	54.0	1.30	19.7	1.26	5.3	1.23
DM	41.5	1	15.6	1	4.3	1
SM	22.5	0.54	8.7	0.56	2.7	0.63

6.3.1 Basic Features of the Flow

In presenting the numerical results, the discussion will focus on those aspects that feature the proposed DNM and *a posteriori* research methodology regarding tensorial geometry, i.e. the characteristics of the DNM coefficients, local singularity condition of the DNM, relative tensorial geometric relation between the SGS stress and its constituent terms, and backscatter of TKE from the unresolved to the resolved scales of motions. The predicted features of the mean large scale velocity field for turbulent Couette flow only serve to validate the performance of the DNM, and are presented in the remainder of this subsection.

Figures 6.1 and 6.2 show the mean velocity profiles for two different Reynolds numbers using wall coordinates. As shown in the figures, the velocity profiles predicted by the DNM agree well with those predicted using the conventional DM [20], the experimental results of Aydin and Leutheusser [121], DNS results of Bech *et al.* [124], and the classical two-layer wall-law of von Kármán [140], i.e. Eq.(3.7). As shown in Fig. 6.1, the DNM is generally insensitive to changes in grid size for the three different grids tested in terms of the velocity profile. Figures 6.3 and 6.4 compare the resolved streamwise turbulence intensities with the experimental and DNS results reported in the literature. A characteristic anisotropic behavior is manifested by the fluctuating velocity component in both the near-wall and core regions. The peak value of $\langle \bar{u}_1''^2 \rangle^{1/2}/u_\tau$ is located at $x_2^+ = 13 \sim 14$ for both Reynolds numbers, which is close to the values reported by other researchers, i.e. $x_2^+ \approx 12$ for $Re = 2600$ by Bech *et al.* [124], and $x_2^+ \approx 11$ for $Re = 2600$ and $x_2^+ \approx 16$ for $Re = 4762$ by Aydin and Leutheusser [121]. As shown in Fig. 6.3, the values of $\langle \bar{u}_1''^2 \rangle^{1/2}/u_\tau$ on the two fine grid systems (using 48^3 and 66^3 nodes) are very close to each other, while the result predicted using the coarsest grid (34^3 nodes) is slightly higher. This is a prototypical characteristic of a coarse grid LES computation and is consistent with the result reported by Kravchenko *et al.* [138].

Figure 6.5 shows the budget of the shear stress for the grid system of 48^3 nodes. The mean contributions of the three normalized shear stress components, i.e.

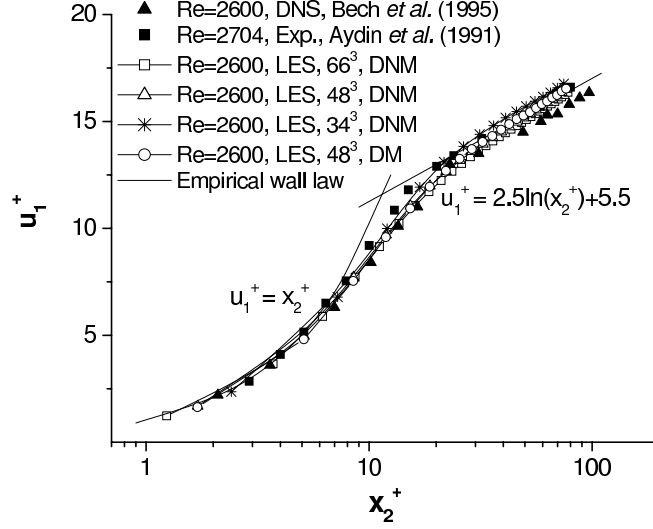


FIGURE 6.1: Mean velocity profile using wall coordinates.

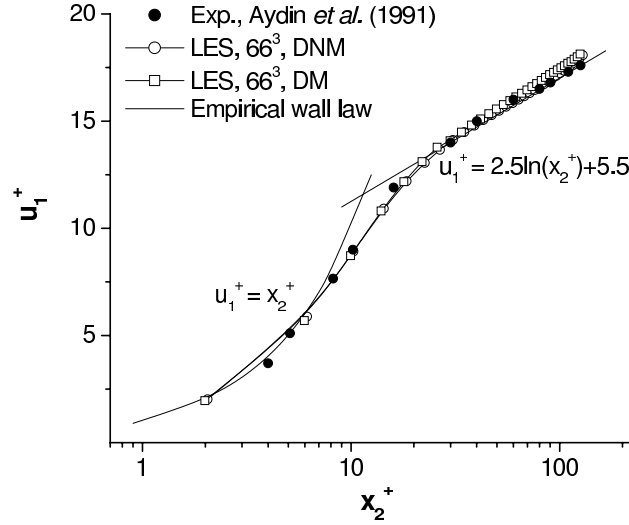


FIGURE 6.2: Mean velocity profile using wall coordinates ($Re = 4762$).

the resolved viscous shear stress, resolved Reynolds shear stress and subgrid scale shear stress (see Eq.(3.8)), to the total shear stress are demonstrated in the figure. The total mean shear stress is close to but slightly higher than unity. The resolved viscous shear stress is dominant in the near-wall region due to the large value of the resolved velocity gradient component $\langle \bar{u}_{1,2} \rangle$, while the resolved Reynolds stress $-\langle \bar{u}_1'' \bar{u}_2 \rangle$ dominates the other shear stress contributions in the core region. Close to the wall, the resolved Reynolds shear stress diminishes illustrating a strong near-wall

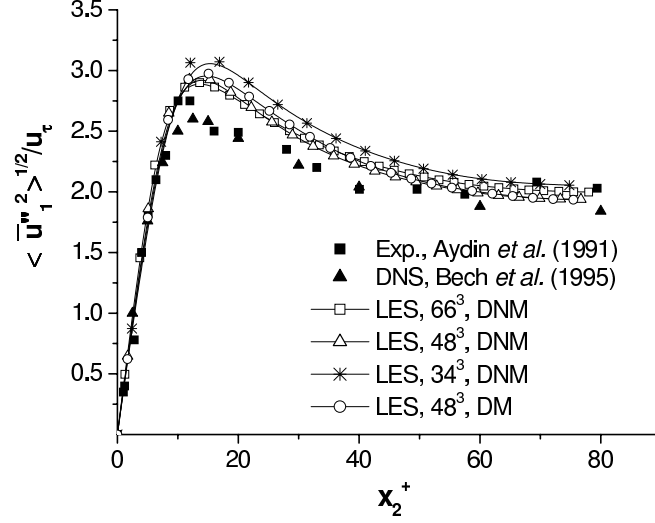


FIGURE 6.3: Resolved streamwise turbulence intensities ($Re = 2600$).

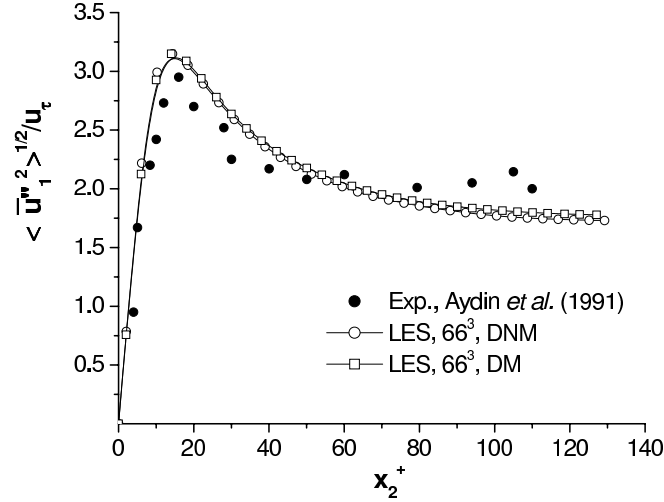


FIGURE 6.4: Resolved streamwise turbulence intensities ($Re = 4762$).

anisotropic effect. Figure 6.6 plots the resolved Reynolds shear stress distribution in the wall-normal direction for the three grid systems tested. In general, the grid effect on the resolved Reynolds stress is not striking. In the rescaled diagram of Fig. 6.6, a prototypical cubic behavior is observed for the resolved Reynolds stress, i.e. $-\langle \bar{u}_1'' \bar{u}_2 \rangle \propto x_2^{+3}$ for $0 \leq x_2^+ < 5$.

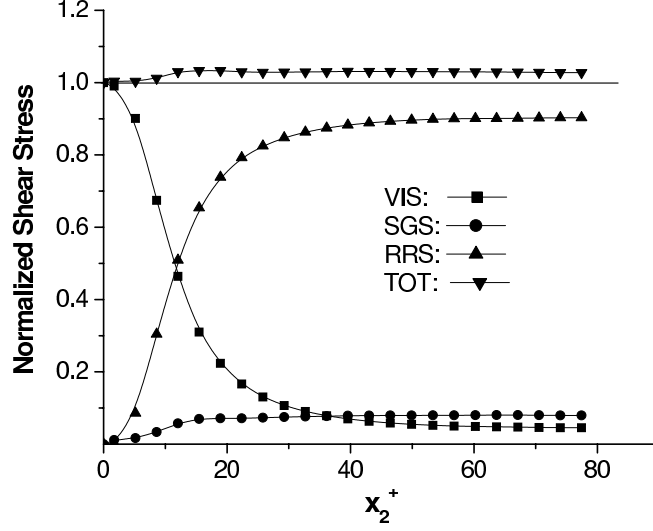


FIGURE 6.5: Budget of shear stresses ($Re = 2600$). VIS: viscous shear stress $\nu \langle \bar{u}_{1,2} \rangle / u_\tau^2$, SGS: subgrid shear stress $-\langle \tau_{12} \rangle / u_\tau^2$, RRS: resolved Reynolds shear stress, $-\langle \bar{u}_1'' \bar{u}_2 \rangle / u_\tau^2$, TOT: total shear stress.

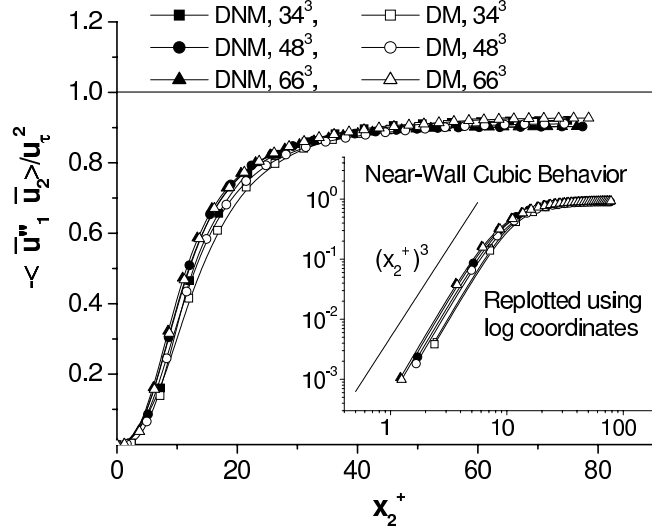


FIGURE 6.6: Resolved Reynolds shear stress distribution.

6.3.2 Numerical Stability of the Model

In the literature, for turbulence with a statistically homogeneous plane, the plane averaging technique is often adopted to obtain a stable solution for the model coefficient. This approach has been used to avoid a potential singularity problem in different simulations [19, 36, 38, 49, 50]. However, the plane averaging technique is

based on the assumption that the model coefficient varies only in the wall-normal direction and is instantaneously homogeneous in the other two directions, which is true only in a statistical sense. From the perspective of the physics of the flow, the plane averaging technique is inconsistent with the observation of instantaneous motions and eddy interactions in a 3-D manner.

An interesting and desirable feature of the numerical simulation performed with the proposed DNM is that the plane averaging technique is no longer necessary for achieving stability. From the proposition shown in Appendix A, *the DNM is locally non-singular, if and only if the three differential tensorial functions, M_{ij} , W_{ij} , and N_{ij} are linearly independent*. If they coincidentally are dependent, $\text{Rank}(\mathbf{A}) \leq 2$, $\det(\mathbf{A}) = 0$ and the system is singular. It would be very desirable if we could further prove that these three differential tensorial functions are linearly independent so that the DNM can be known to be absolutely locally non-singular at each time step. Encouraged by the stability exhibited by numerical simulations and an examination of the definitions of M_{ij} , W_{ij} and N_{ij} , the author suspects that these three differential tensorial functions are in fact independent. However, a strict analytical proof is not yet available to support such a conjecture, and it remains an open question for further analytical exploration. To compensate for the lack of a complete analytical proof, numerical approaches were employed to examine the property of the coefficient matrix \mathbf{A} in terms of its singularity. The *condition number* of \mathbf{A} , i.e. $\text{cond}(\mathbf{A}) = \|\mathbf{A}\|_{\infty} \cdot \|\mathbf{A}^{-1}\|_{\infty}$, was evaluated for such a purpose. Here, the norm of matrix \mathbf{A} is defined as

$$\|\mathbf{A}\|_{\infty} = \max_{1 \leq i \leq 3} \sum_{j=1}^3 |a_{ij}| \quad (6.11)$$

The condition number $\text{cond}(\mathbf{A})$ can be used for evaluating the stability of a linear system such as Eq.(6.10). As $\text{cond}(\mathbf{A})$ increases, the linear matrix system becomes less stable in numerical simulations, and in the worst-case scenario, the system becomes singular when $\text{cond}(\mathbf{A}) \rightarrow \infty$. Figure 6.7 shows both the averaged and instantaneous profiles of the condition number along the wall-normal direction. The instantaneous profiles show that typically the condition number is about 10 with a maximum value

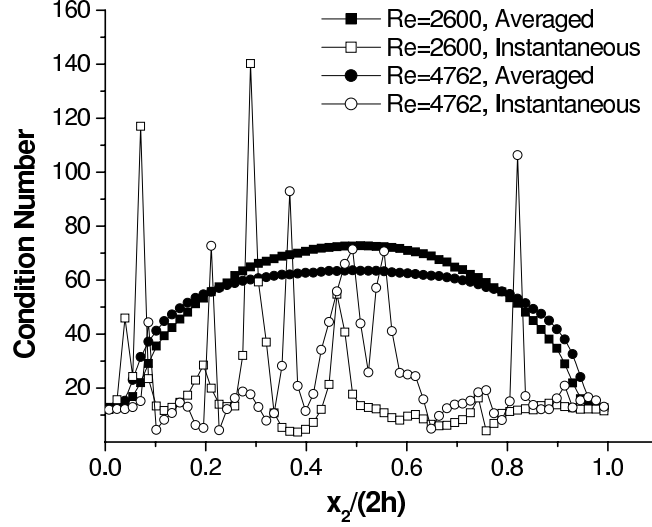


FIGURE 6.7: Averaged condition number $\text{cond}(\mathbf{A})$ along the wall-normal direction (66^3 nodes).

of 140. The fluctuation of $\text{cond}(\mathbf{A})$ relates to the local dynamical instantaneous small scale motions to be simulated. Due to the fluctuations, the averaged condition number ranges from 12 to 74. These profiles indicate that the stability of the linear matrix system $\mathbf{A}\mathbf{C} = \mathbf{B}$ for the DNM is generally good in the numerical simulations performed. However, since the second step of the analytical proof is not yet available, this conclusion obtained from the numerical tests should not be generalized for other wall-bounded flows at this stage.

Considering that $M_{ij}M_{ij}$ is only one of the nine elements of the coefficient matrix \mathbf{A} (see Eq.(6.10)), it is expected that the matrix system of DNM is more robust than the conventional DM formulation. It is difficult to imagine that all three complex differential tensorial functions could act coincidentally such that $\det(\mathbf{A}) = 0$, especially considering that the values of the elements of \mathbf{A} are determined by the instantaneous turbulent flow field. In fact, the author has performed multiple numerical tests, each with a significant number of time steps, and no singularity difficulty has ever been encountered. In contrast, in the numerical simulation performed using the conventional DM for the same test problems, a plane averaging technique is always necessary to maintain a stable calculation.

6.3.3 Model Coefficients

Figure 6.8 shows the averaged wall-normal distributions of the three model coefficients. From the figure, we can see that all three DNM coefficients reduce to zero at the wall and level off at their maximum magnitude in the core region. The profiles of the coefficients exhibit a clear anisotropy in the wall-normal direction due to the restriction by the walls. The averaged value is positive for coefficients C_S and C_W , but negative for C_N . As the Reynolds number increases from 2600 to 4762, the value of C_W in the core region remains approximately the same, while the absolute values of both C_S and C_N increase. All three DNM coefficients have the same order of magnitude, e.g. in the core region for the flow with $Re = 2600$, the values for the three DNM coefficients are $C_S = 0.035$, $C_W = 0.026$ and $C_N = -0.017$.

Figure 6.9 compares the model coefficients calculated for $Re = 2600$ using three different grid systems. Generally speaking, the values obtained using the three grid systems are slightly different to account for the grid effects. It should be indicated that there is no reason to expect that the dynamic model coefficients for LES are grid-invariant. To illustrate the difference between the DNM and the conventional single-constant-parameter SM [13], one could compare the value of C_S , though it is understood that the closure strategies for these two types of SGS models are significantly different. The conventional SM uses C_S^2 instead of C_S in its definition and generally ranges in value from [1, 139] 0.065 to 0.12 ($C_S^2 = 0.00425$ – 0.0144), which is smaller than the value of C_S for the DNM in the core region (see Figs. 6.8 and 6.9). The difference between these two modelling approaches exists not only in terms of their coefficients, but also in their capability of approximating τ_{ij} in terms of both the tensorial magnitude and orientation, which then influences the inertial inviscid scattering of TKE between the resolved and residual scales of motions. This topic will be discussed in a detailed manner later the sections 6.4–6.6.

Figure 6.10 illustrates the instantaneous wall-normal distribution of the three coefficients for $Re = 2600$ at a central location ($x_1/L_1 = x_2/L_2 = 0.49$). From the figure, the instantaneous coefficients are generally bounded, however with a fluctu-

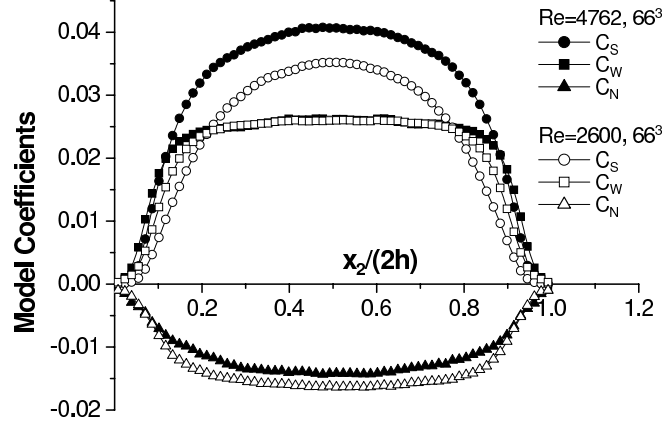


FIGURE 6.8: Distribution of model coefficients in the wall-normal direction.

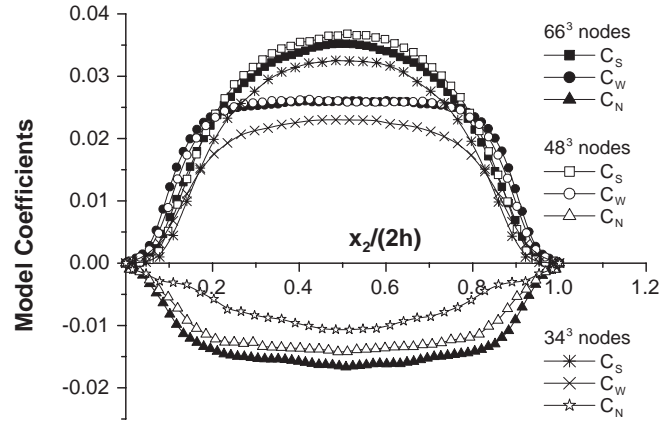


FIGURE 6.9: Sensitivity of the model coefficients to the grid size ($Re = 2600$).

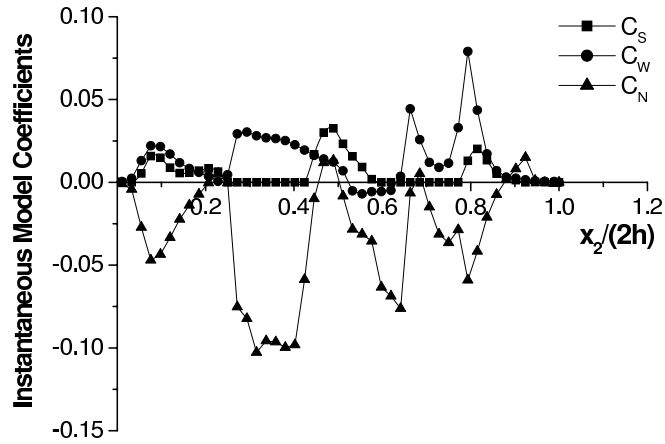


FIGURE 6.10: Instantaneous wall-normal distribution of the coefficients at central location: $x_1/L_1 = x_2/L_2 = 0.49$ ($Re = 2600$, 48^3 nodes).

ating amplitude about $0 \sim 8$ times the averaged values (shown previously). From Eq.(6.10), it is understood that the coefficients are flow dependent and determined by instantaneous tensors of a turbulence field. Therefore, the DNM coefficients should be considered as local turbulent quantities (via modelling), which account for the local structure and rapid small scale motions in a dynamic manner. Thus, truly localized dynamic modelling coefficients should fluctuate (or be variant) to reflect the local instantaneous flow structures and small scale motions; at the same time they must be bounded to avoid instability due to excessive backscatter or a potential singularity of the modelling formulation. Both features of the dynamic coefficients, i.e. being fluctuating and also being bounded, are important and must balance each other to make the simulation both realistic and stable. A plane averaging technique is helpful to make the simulation more stable, but the feature of the coefficients being locally variant and reflecting local flow structure is sacrificed. It should be indicated that although it is advantageous to be able to apply the DNM locally without plane averaging for the simulations performed in this study, one should be cautious in extending this conclusion to other cases.

6.4 Geometrical Characteristics of the DNM

Currently in both the RANS and LES communities, when one studies a new modelling approach using an *a posteriori* numerical approach, focus is often given to the model's capability to predict turbulence features in terms of the magnitude of a parameter, such as the mean velocity profile (e.g. using wall-coordinates to demonstrate the log law pattern) and the associated distributions of resolved turbulence intensities and shear stresses. However, it should be indicated that the magnitude and orientation are of equal importance in determining the properties of a tensor such as the resolved Reynolds stress tensor, SGS stress tensor, strain rate tensor and rotation rate tensor, which then influence the solution set of the momentum equation and physical processes such as backscatter. Therefore, it is argued in this research that *future improved a posteriori CFD studies should include consideration of the tensorial geometric rela-*

tions between the known and unknown terms in the constitutive relation. The recently reported geometrical alignment based SGS stress models by Pullin, Saffman, Misra and Voelkl [104, 106, 107] represent this new type of modelling approach. In the following context, attempts will be made to extend this type of research methodology to *a posteriori* studies based on the proposed DNM, and preliminary results on some selected parameters will be presented. It is hoped that the behavior of the DNM can be better understood by examining the role of each of the three constituent terms in terms of its relative tensorial orientation with the negative SGS stress tensor $-\tau_{ij}$.

6.4.1 Conventions on the Tensorial Eigensystem

From algebra (see Appendix B) it is understood that a second order real symmetric tensor, such as the SGS stress tensor and strain rate tensor, is always diagonalizable. In fact, its three eigenvalues represent the three *principal values* of the tensor, and its orthonormal eigenvectors represent the *principal axes*. In this study, the eigenvalues of a second order tensor are rearranged in a descending order represented by α , β and γ , respectively. The corresponding normalized eigenvectors are therefore likewise denoted by \mathbf{e}_α , \mathbf{e}_β and \mathbf{e}_γ . These three normalized eigenvectors are orthogonal to each other and form an *orthonormal eigenframe triad*. Throughout this dissertation, all the eigenframes are arbitrarily considered to be *dextral* (right-handed). For the resolved strain rate tensor (\bar{S}_{ij}) and negative SGS stress tensor ($-\tau_{ij}$), we have $\alpha_S \geq \beta_S \geq \gamma_S$ (the overbar on S is omitted in the subscript where no confusion is introduced thereby) and $\alpha_{-\tau} \geq \beta_{-\tau} \geq \gamma_{-\tau}$. These three eigenvalues arranged in a descending order are referred to as [29, 99] the *most extensive*, *intermediate*, and *most compressive* eigenvalues, respectively. The relations between the eigenvalues τ_{ij} and $-\tau_{ij}$ are: $\alpha_{-\tau} = -\gamma_\tau$, $\beta_{-\tau} = -\beta_\tau$ and $\gamma_{-\tau} = -\alpha_\tau$. Due to continuity, the following relation must hold for incompressible flows:

$$\alpha_S + \beta_S + \gamma_S = 0 \tag{6.12}$$

The following lists some basic concepts that are related to the eigenvalues of the resolved strain rate tensor:

- If $\beta_S > 0$, then there are two components of the principal axes of the strain rate tensor along which the fluid element is stretched while it is compressed in third principal direction, which taken together suggests that the local flow structure is *sheetlike*.
- If $\beta_S < 0$, then the fluid element is stretched in one principal direction and compressed in the other two principal directions, which suggests that the local flow structure is *tubelike* [62].
- If $\beta_S = 0$, the intermediate eigenvalue of the strain rate tensor vanishes and a 3-D flow degenerates to a *2-D flow* in terms of the principal deformation of the local fluid element.
- If the state of small $|\beta_S|$ prevails (i.e. $\beta_S \neq 0$, $|\beta_S| < |\alpha_S|$ and $|\beta_S| < |\gamma_S|$), the flow exhibits a *quasi-2-D* (QTD) behavior [78].
- If $\alpha_S = \beta_S > 0$, the local deformation pattern of the fluid material is *axisymmetric expansion*; whereas, if $0 > \beta_S = \gamma_S$, the local deformation pattern is *axisymmetric compression*.

6.4.2 Tensorial Alignment Feature of the DNM in Contrast to the Linear Smagorinsky Type Models

The objective of this subsection is to illustrate the fundamental difference between the proposed DNM and the conventional DM [20] in terms of their tensorial geometrical characteristics. The statistical results presented in this subsection are based on the simplest plane averaging method. A more strict analytical study of the tensorial eigensystem of the DNM will be explored later in section 6.5, while a refined investigation of the geometrical characteristics of the DNM will be performed in chapters 7 and

8 using the methodologies of the recently developed turbulence geometrical statistics and topology.

To illustrate the basic tensorial geometrical feature of the DNM, the *principal angles* between the principal axes of two eigenframes are studied. The three principal angles are represented by $\Lambda_\alpha(\mathbf{e}_{m\alpha}, \mathbf{e}_{n\alpha})$, $\Lambda_\beta(\mathbf{e}_{m\beta}, \mathbf{e}_{n\beta})$ and $\Lambda_\gamma(\mathbf{e}_{m\gamma}, \mathbf{e}_{n\gamma})$. Here the subscripts m and n are used to differentiate the two tensors involved in discussion, while α , β and γ are used to indicate the principal axes corresponding to the largest, intermediate, and smallest eigenvalues following the convention defined previously. To fully describe the relative rotation between two 3-D orthonormal frames, a 3×3 orthonormal *rotation matrix*, \mathbf{R} , formed by the direction-cosines should be considered (see Appendix B). The cosines of these three angles, i.e. $\cos(\Lambda_\alpha)$, $\cos(\Lambda_\beta)$ and $\cos(\Lambda_\gamma)$, are special since they are the three principal diagonal elements of the rotation matrix. The summation of these three cosine values is the trace of the rotation matrix, which determines the well known *Euler rotational angle* between the two eigenframes and is referred to as the *natural invariant* of the rotation matrix [178]. These three angles are chosen also because they serve the purpose of the research presented in this subsection, which is to illustrate the basic tensorial characteristics of the proposed DNM in comparison with those of the conventional DM of Lilly [20]. To be specific, the relative rotation between the two 3-D tensorial eigenframes of \bar{S}_{ij} and the 2nd or 3rd nonlinear terms, and that between the eigenframes of $-\tau_{ij}$ and each of the three constituent nonlinear terms, will be distinctly visualized.

Before discussing the geometrical properties of the tensorial eigenframe, the ambiguity in defining the alignment angle involving an eigenvector must be addressed. There appears to be some confusion in the literature in determining the interval for the angle involving an eigenvector, e.g. the angle between the vorticity vector ($\boldsymbol{\omega}$) and the intermediate eigenvector^a of the strain rate tensor ($\mathbf{e}_{S\beta}$). Some authors [62, 75, 76, 78, 85, 88, 91, 100] use $[0^\circ, 180^\circ]$ for the angle (or $[-1, 1]$ for the cosine value),

^aStrictly speaking, it should be referred to as the ‘eigenvector corresponding to the intermediate eigenvalue’. However, without bringing in any confusion, the term ‘intermediate eigenvector’ is adopted for brevity, as are the terms ‘the largest/most extensive eigenvector’ and ‘the smallest/most compressive eigenvector’.

some [29, 55, 77, 79, 99, 179] used $[0^\circ, 90^\circ]$ for the angle (or $[0, 1]$ for the absolute cosine value), some [73, 84] use both $[0^\circ, 180^\circ]$ and $[0^\circ, 90^\circ]$, while some [72, 74] even use $[-180^\circ, 180^\circ]$.

The aliasing of the $+/-$ sign of an eigenvector naturally derives from mathematics, since the eigenvector and its opposite (with an additional negative sign) share exactly the same eigenvalue for the same eigensystem. For instance, the eigensystem for $-\tau_{ij}$ corresponding to its largest eigenvalue is: $[-\tau_{ij}] \cdot \mathbf{e}_{-\tau\alpha} = \alpha \cdot \mathbf{e}_{-\tau\alpha}$, however, $(-\mathbf{e}_{-\tau\alpha})$ is also appropriate, i.e. $[-\tau_{ij}] \cdot (-\mathbf{e}_{-\tau\alpha}) = \alpha \cdot (-\mathbf{e}_{-\tau\alpha})$. As such, for the same eigenvalue α , the angle $\theta(\mathbf{e}_{-\tau\alpha}, \mathbf{e})$ is inevitably aliased with $[180^\circ - \theta(\mathbf{e}_{-\tau\alpha}, \mathbf{e})]$, $[180^\circ + \theta(\mathbf{e}_{-\tau\alpha}, \mathbf{e})]$ and $[360^\circ - \theta(\mathbf{e}_{-\tau\alpha}, \mathbf{e})]$. Here, \mathbf{e} represents an arbitrary eigenvector. Therefore, only the choice of $[0^\circ, 90^\circ]$ or the absolute cosine value of the angle is adopted in the statistics for this study, so that the results do not passively rely on any unexplained factors.

Three different grid systems were used in the study, i.e. 34^3 , 48^3 and 66^3 nodes. Since no obvious grid effect was observed, only the specific results related to 66^3 nodes for two different Reynolds numbers are presented in Figs. 6.11–6.15. Also, as it is clear in these figures that the profiles generally do not change significantly as the Reynolds number increases from 2600 to 4762, only the results of $Re = 2600$ are presented in Tables 6.2 and 6.3 for illustration. Another general impression from both the tables and Figs. 6.11–6.15 is that the geometrical orientation between the eigenframes of the SGS stress and each of the three nonlinear constituent tensors exhibits a strong anisotropic effect due to the existence of the wall.

(1) Principal Alignment between \bar{S}_{ij} and the 2nd and 3rd Nonlinear Terms

From Fig. 6.11, it is observed that Λ_α , which indicates the relative alignment between eigenvectors corresponding to the most extensive eigenvalues of \bar{S}_{ij} and γ_{ij} , is 45° at the wall demonstrating an *equiangular alignment pattern* in the near-wall region, and rises to a value of approximately 52° indicating a general *skewed alignment pattern* in the core region. The angle Λ_β between eigenvectors corresponding to the intermediate eigenvalues of \bar{S}_{ij} and γ_{ij} is 0° at the wall, showing an *parallel alignment pattern*, and

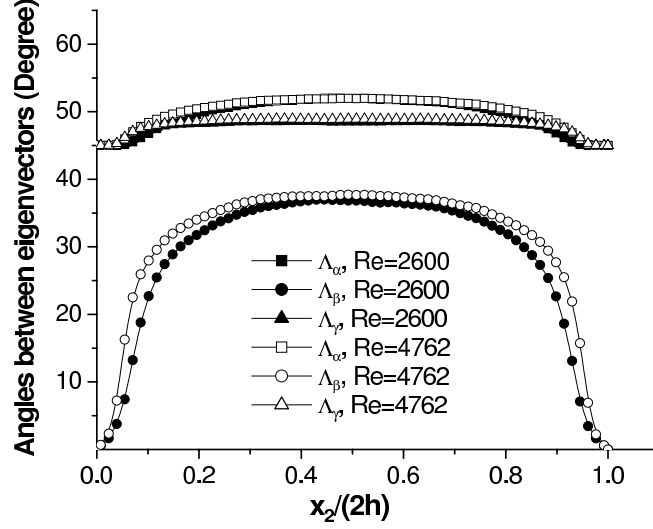


FIGURE 6.11: Averaged angles between the eigenvectors of the filtered strain rate tensor and second constituent term $(\bar{S}_{ij}, \gamma_{ij})$ for the case of 66^3 nodes.

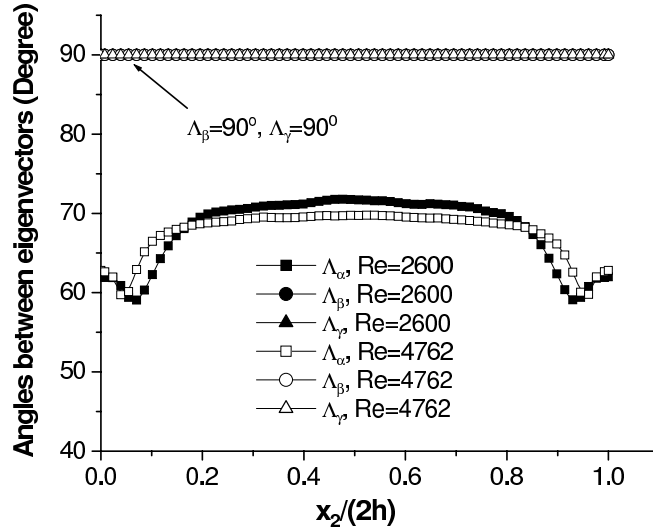


FIGURE 6.12: Averaged angles between the eigenvectors of the filtered strain rate tensor and third constituent term $(\bar{S}_{ij}, \eta_{ij})$ for the case of 66^3 nodes.

risers in the core region to an approximate value of 37° indicating a skewed pattern. The angle Λ_γ between eigenvectors corresponding to the most compressive eigenvalues of \bar{S}_{ij} and γ_{ij} demonstrates an equiangular pattern of 45° at the wall and a skewed (also regarded as a quasi-equiangular) pattern of 49° in the core region. From Figure 6.12, it is of interest to note that $\Lambda_\alpha \approx 62^\circ$ at the wall and 72° in the core region, both of which indicate a skewed alignment pattern between the eigenvectors corre-

TABLE 6.2: Averaged tensorial alignment between \bar{S}_{ij} and the 2nd and 3rd nonlinear terms ($Re = 2600$, 66^3 nodes).

Tensors	\bar{S}_{ij} and γ_{ij}			\bar{S}_{ij} and η_{ij}		
Angles (degrees)	Λ_α	Λ_β	Λ_γ	Λ_α	Λ_β	Λ_γ
Wall value:Comments	45:E	0:	45:E	62:S	90:⊥	90:⊥
Core value:Comments	52:S	37:S	49:S	72:S	90:⊥	90:⊥

Notations: ‘E’ for Equiangular, ‘||’ for Parallel, ‘⊥’ for Perpendicular, and ‘S’ for Skewed.

sponding to the largest eigenvalues. Otherwise, across the entire channel, $\Lambda_\beta \equiv 90^\circ$ and $\Lambda_\gamma \equiv 90^\circ$ both indicate an overall *perpendicular* alignment pattern between the eigenvectors corresponding to the intermediate and smallest eigenvalues. In the next subsection, it will be demonstrated analytically that these peculiar alignments observed in Fig. 6.12 are not a coincidence, but instead, determined by two particular flow configurations.

(2) Principal Alignment between $-\tau_{ij}$ and the Three Constituent Terms

From Fig. 6.13, it is observed that the relative alignment between the two eigenvectors corresponding to the most extensive eigenvalues of $-\tau_{ij}$ and β_{ij} , is equiangular with $\Lambda_\alpha = 45^\circ$ at the wall, and exhibits a skewed pattern of $\Lambda_\alpha \approx 54^\circ$ in the core region. The alignment between the two eigenvectors corresponding to the intermediate eigenvalues of $-\tau_{ij}$ and β_{ij} is almost parallel ($\Lambda_\beta = 1^\circ$) at the wall, but becomes skewed ($\Lambda_\beta \approx 58^\circ$) in the core region. From the profile of Λ_γ , it is found that the alignment between the eigenvectors corresponding to the most compressive eigenvalues of $-\tau_{ij}$ and η_{ij} is approximately equiangular both at the wall and in the core region. Since no data on the distribution of these angles for a wall-bounded flow are available in the literature, the author can only compare the obtained *a posteriori* numerical results with those obtained using isotropic turbulence through *a priori* analysis. Tao *et al.* [29,99] reported that according to their HPIV measurements, the most probable value for Λ_α in the core region of a square duct flow is 32° . However, Horiuti [100] obtained a different value, i.e. $\Lambda_\alpha = 45^\circ$, by analyzing DNS data for isotropic turbu-

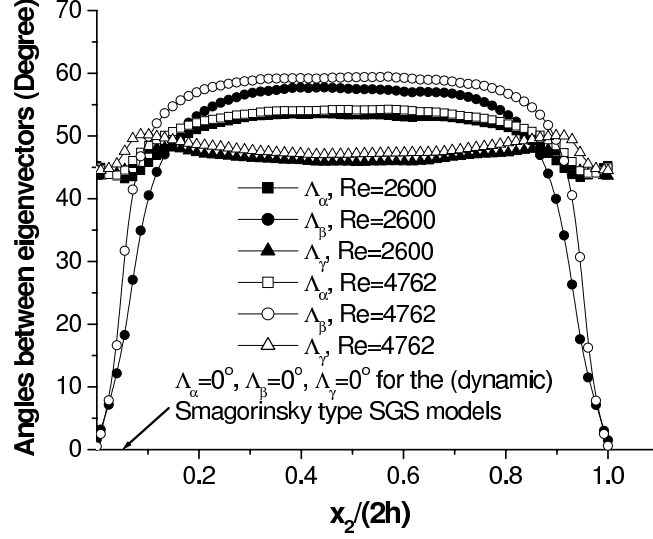


FIGURE 6.13: Averaged angles between the eigenvectors of the negative SGS stress and first constituent term $(-\tau_{ij}, \beta_{ij})$ or $(-\tau_{ij}, \bar{S}_{ij})$ for the case of 66^3 nodes.

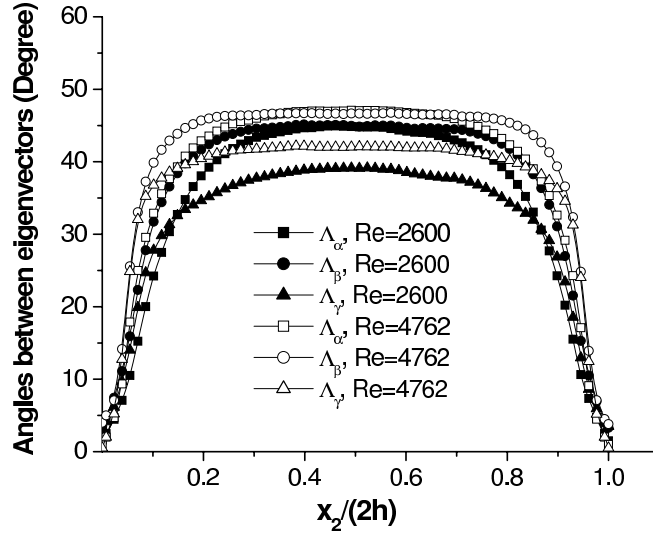


FIGURE 6.14: Averaged angles between the eigenvectors of the negative SGS stress and second constituent term $(-\tau_{ij}, \gamma_{ij})$ for the case of 66^3 nodes.

lence. Both the reported values of Tao [29, 99] and Horiuti [100] are different than the result of $\Lambda_\alpha \approx 54^\circ$ (in the core region) found in this research. The existence of these differences is not surprising for the following reasons: (i) as discussed earlier, Horiuti [100] used a different angle interval $[0^\circ, 180^\circ]$ for statistics, which has a direct influence on the final result; (ii) the Couette flow considered in this research is a wall-bounded anisotropic flow; (iii) the statistical result presented in this study is based

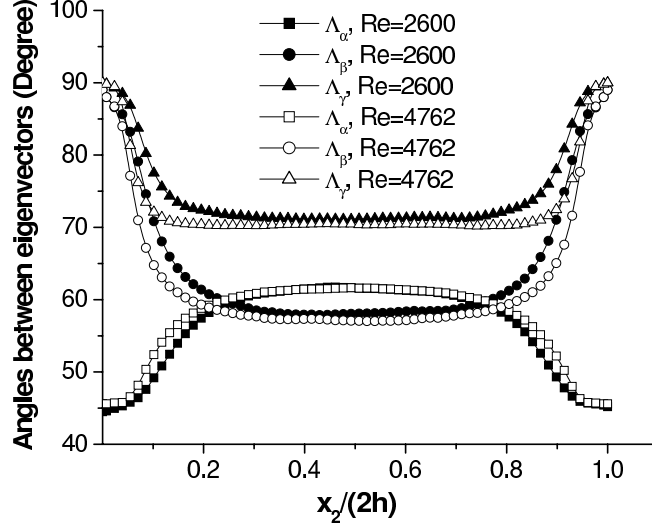


FIGURE 6.15: Averaged angles between the eigenvectors of the negative SGS stress and third constituent term $(-\tau_{ij}, \eta_{ij})$ for the case of 66^3 nodes.

on the plane averaging method, while the reported results [29, 99, 100] are based on probability density functions; and (iv) most importantly, both Tao [29, 99] and Horiuti [100] used an *a priori* approach, which implies a possible integrity set of 11 independent tensors in total in the constitutive relation shown in Eq.(6.6), whereas, the DNM considered in this *a posteriori* study is based on only 3 independent constituent tensors. As discussed earlier, a DNM based on all 11 independent tensors is impractical due to the complexity of the algorithm, high computational cost and the possibility of incorrectly representing the physics. Given the ambiguity of any comparison between the *a priori* and proposed *a posteriori* studies, the author has focused attention on comparison between two *a posteriori* approaches based on the (dynamic) Smagorinsky type models and proposed DNM. It is of interest to demonstrate in the next paragraph how drastically the nonlinear constituent terms change the tensorial geometry of the SGS stresses.

From the definition of β_{ij} it is understood that β_{ij} represents the linear Smagorinsky component of the SGS stress model, which is exactly aligned with \bar{S}_{ij} . The conventional single-parameter (dynamic) Smagorinsky type models require $-\tau_{ij}$ to be aligned with \bar{S}_{ij} with $\Lambda_\alpha \equiv 0^\circ$, $\Lambda_\beta \equiv 0^\circ$ and $\Lambda_\gamma \equiv 0^\circ$. However, from Fig. 6.13 it is observed that in the case of the DNM, the geometric relation between $-\tau_{ij}$ and β_{ij} (or

TABLE 6.3: Averaged tensorial alignment between $-\tau_{ij}$ and the nonlinear terms ($Re = 2600$, 66^3 nodes).

Tensors	$-\tau_{ij}$ and β_{ij}			$-\tau_{ij}$ and γ_{ij}			$-\tau_{ij}$ and η_{ij}		
Angles (degrees)	Λ_α	Λ_β	Λ_γ	Λ_α	Λ_β	Λ_γ	Λ_α	Λ_β	Λ_γ
Wall value:Comments	45:E	1:∥	45:E	1:∥	3:∥	3:∥	45:E	89:⊥	90:⊥
Core value:Comments	54:S	58:S	46:E	45:E	45:E	39:S	62:S	58:S	71:S

Notations: ‘E’ for Equiangular, ‘∥’ for Parallel, ‘⊥’ for Perpendicular, and ‘S’ for Skewed.

\bar{S}_{ij}) demonstrates a much more complicated anisotropic behavior. This suggests that the proposed DNM has more degrees of freedom to mimic the SGS stresses in terms of both tensorial magnitude and orientation, which in turn could influence the various turbulence transport processes between the resolved and subgrid scales of motions, e.g. the inertial inviscid cascade of TKE. Figures 6.14 and 6.15 further exhibit the complex tensorial geometric relation between the negative SGS stress $-\tau_{ij}$, and the second and third constituent terms in the nonlinear constitutive relation, i.e. γ_{ij} and η_{ij} , respectively. These two figures can be analyzed in a similar way to Fig. 6.13, and for the sake of brevity will not be discussed in detail. Generally, it is observed in Figs. 6.13–6.15 and specifically summarized in Table 6.3 that the value of these three angles is approximately either 0° , 45° or 90° at the wall. This indicates that the relative principal orientation between the negative SGS stress and three nonlinear tensors has only three scenarios at the wall: parallel, equiangular or perpendicular alignment. In contrast, the relative principal orientation in the core region is mainly either skewed or equiangular, and no perpendicular relative alignment pattern has been observed. It should be noted that all the tensorial alignment features discussed above are based on statistics obtained using the plane averaging technique. The discussion of this topic will be continued later in chapter 7 based on refined statistics using (joint) probability functions.

6.5 Properties of the Eigensystem

In the previous section the geometrical characteristics of the constitutive relation of the DNM have been investigated using numerical methods and some interesting results have been observed, e.g. the relative principal orientation between the principal axes of \bar{S}_{ij} and η_{ij} corresponding to the intermediate and smallest eigenvalues, are always perpendicular (see Fig. 6.12). In this section, the geometrical characteristics of the DNM constitutive relation will be revisited using an analytical approach. First, a tensorial identity that relates the first and third constituent terms will be proposed, which plays an important role in determining the flow configuration and rate of TKE transfer between the filtered and subgrid scales of motions.

6.5.1 An Eigensystem Identity

From Eqs.(6.4), (6.7) and (6.9), it is understood that the relation between the eigensystems of the first and third terms (i.e. β_{ij} and η_{ij} , respectively) is effectively decided by their tensorial parts, i.e. $\mathbf{S} = \bar{S}_{ij}$ and

$$\mathbf{\Gamma} \stackrel{\text{def}}{=} \mathbf{T}^{(2)*} \stackrel{\text{def}}{=} \bar{S}_{ik}\bar{S}_{kj} - \frac{1}{3}\bar{S}_{mn}\bar{S}_{nm}\delta_{ij} \quad (6.13)$$

Since \bar{S}_{ij} is a real symmetric tensor, it follows that $\bar{S}_{ik}\bar{S}_{kj} = \mathbf{S}\mathbf{S}$. Thus, the above system can be simplified to

$$\mathbf{\Gamma} = \mathbf{S}\mathbf{S} - \frac{1}{6}|\bar{S}|^2\delta_{ij} \quad (6.14)$$

Suppose that the eigensystem for \mathbf{S} is given by

$$\mathbf{S} \cdot \mathbf{e} = \lambda_S \cdot \mathbf{e} \quad (6.15)$$

where λ_S and \mathbf{e} are, respectively, the eigenvalue and eigenvector for \mathbf{S} . On left-multiplying both sides of the above equation with \mathbf{S} and then subtracting $\frac{1}{6}|\bar{S}|^2\delta_{ij}\mathbf{e}$

from both sides, the following formulation is obtained after some rearrangement:

$$(\mathbf{S}\mathbf{S} - \frac{1}{6}|\bar{S}|^2\delta_{ij}) \cdot \mathbf{e} = (\lambda_S^2 - \frac{1}{6}|\bar{S}|^2) \cdot \mathbf{e} \quad (6.16)$$

which is exactly the eigensystem equation for the second tensor $\mathbf{\Gamma}$, i.e. $\mathbf{\Gamma} \cdot \mathbf{e} = \lambda_{\Gamma} \cdot \mathbf{e}$. As such, it has been demonstrated that \mathbf{S} and $\mathbf{\Gamma}$ share the same eigenvectors (principal axes), and an identity that relates their eigenvalues (principal values) is obtained, i.e.

$$\lambda_{\Gamma} = \lambda_S^2 - \frac{1}{6}|\bar{S}|^2 \quad (6.17)$$

Since the three principal axes of the two tensors are the same, the scalar $\frac{1}{6}|\bar{S}|^2$ plays a dominant role in determining their geometrical relation. At this point, a question arises: if the first and third nonlinear term share the same three principal axes, how can their relative geometric orientation with the negative SGS stress $-\tau_{ij}$ be very different as shown in Fig. 6.13 and Fig. 6.15? The answer lies in the above identity, which implies a parabolic instead of a monotonic relation between λ_{Γ} and λ_S . This indicates that the sequence of eigenvectors corresponding to the descending order of the eigenvalues of \mathbf{S} , i.e. $\alpha_S \geq \beta_S \geq \gamma_S$, is not necessarily the same as that corresponding to $\alpha_{\Gamma} \geq \beta_{\Gamma} \geq \gamma_{\Gamma}$ for $\mathbf{\Gamma}$. In fact, the smallest eigenvalue for \mathbf{S} is often found to be negative with a large absolute value (see Table 6.4), which ‘switches’ the sequence of the eigenvalues of $\mathbf{\Gamma}$ when they are calculated from α_S , β_S and γ_S via the identity, i.e. Eq.(6.17). This sequence is decided by the instantaneous property of a turbulence field featured by quantities such as \bar{S}_{ij} . Table 6.4 presents the instantaneous eigensystems for the first (featured by \mathbf{S}) and third terms (featured by $\mathbf{\Gamma}$) for $Re = 2600$ at two specific locations. From the table, it is confirmed that the three eigenvectors for the first and third constituent terms are the same, however with a different sequence. At the first location, we have $|\gamma_S| > |\alpha_S| > |\beta_S|$, while at the second location we have $|\alpha_S| > |\gamma_S| > |\beta_S|$.

6.5.2 Mapping Characteristics of the Eigensystem Identity

In the previous subsection, we have found two types of mapping relations between the eigenvalues of the first and third nonlinear constituent tensors as demonstrated in Table 6.4. From the point of mathematics, the identity itself allows for six different scenarios for the mapping relation between the two tensorial eigensystems, which are illustrated in Fig. 6.16. However, in the following section it will be demonstrated that only the last two scenarios, represented by Figs. 6.16(e) and (f) are possible. The numerical demonstration of these two realistic scenarios is also illustrated in Table 6.4.

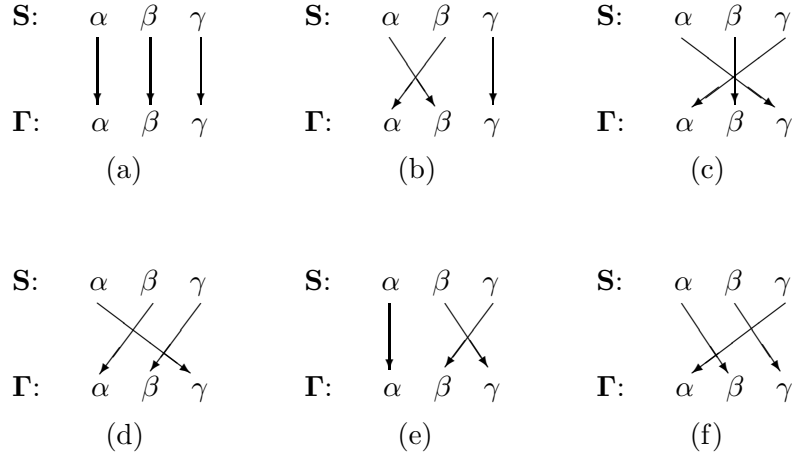


FIGURE 6.16: Scenarios for the mapping relation of the eigensystem identity.

Besides the identity, there are two additional restrictions to the eigensystems between the first and third nonlinear tensorial terms. Supposing that the eigenvalues of the second order tensor to be investigated are *distinct*, they can be distinguished using a descending order, i.e.

$$\begin{cases} \alpha_{\Gamma} > \beta_{\Gamma} > \gamma_{\Gamma} \\ \alpha_S > \beta_S > \gamma_S \end{cases} \quad (6.18)$$

If the eigenvalues of a second order tensor are not distinct, ambiguities becomes inevitable. Discussion on this topic will be left to the end of this section.

Considering that \mathbf{S} is a real symmetric 2nd order tensor, it must have three real eigenvalues (see Appendix B), which satisfy continuity, i.e. $\alpha_S + \beta_S + \gamma_S = 0$. Thus,

TABLE 6.4: Instantaneous tensorial eigensystem for the 1st and 3rd nonlinear terms ($Re = 2600$).

Location	1st term: S		3rd term: Γ		$ \bar{S} $	Relation	Local structure
	Eigenvalue	Eigenvector	Eigenvalue	Eigenvector			
$x_1/L_1 = 0.477$	$\alpha_S = 118.863$	$[0.621, 0.556, 0.552]^T$	$\alpha_\Gamma = 15706.146$	$[0.769, -0.567, -0.294]^T$	318.187	$\alpha_\Gamma = \gamma_S^2 - \frac{1}{6} \bar{S} ^2$	sheetlike
$x_2/L_2 = 0.477$	$\beta_S = 62.554$	$[-0.149, -0.608, 0.780]^T$	$\beta_\Gamma = -2745.332$	$[0.621, 0.556, 0.552]^T$		$\beta_\Gamma = \alpha_S^2 - \frac{1}{6} \bar{S} ^2$	
$x_3/L_3 = 0.477$	$\gamma_S = -180.499$	$[0.769, -0.567, -0.294]^T$	$\gamma_\Gamma = -12960.814$	$[-0.149, -0.608, 0.780]^T$		$\gamma_\Gamma = \beta_S^2 - \frac{1}{6} \bar{S} ^2$	
$x_1/L_1 = 0.477$	$\alpha_S = 190.689$	$[0.706, -0.016, 0.708]^T$	$\alpha_\Gamma = 13724.387$	$[0.706, -0.016, 0.708]^T$	368.548	$\alpha_\Gamma = \alpha_S^2 - \frac{1}{6} \bar{S} ^2$	tubelike
$x_2/L_2 = 0.914$	$\beta_S = -12.599$	$[-0.031, 0.998, 0.054]^T$	$\beta_\Gamma = 8754.768$	$[-0.707, -0.060, 0.704]^T$		$\beta_\Gamma = \gamma_S^2 - \frac{1}{6} \bar{S} ^2$	
$x_3/L_3 = 0.477$	$\gamma_S = -177.180$	$[-0.707, -0.060, 0.704]^T$	$\gamma_\Gamma = -22479.155$	$[-0.031, 0.998, 0.054]^T$		$\gamma_\Gamma = \beta_S^2 - \frac{1}{6} \bar{S} ^2$	

$\alpha_S > 0$ and $\gamma_S < 0$ and the sign of β_S is undetermined. Further, by applying system (6.18), the following inequalities are obtained:

$$\begin{cases} |\alpha_S| > |\beta_S| & \text{corresponding to } \alpha_S > |\beta_S| > 0 \\ |\gamma_S| > |\beta_S| & \text{corresponding to } \gamma_S < -|\beta_S| < 0 \end{cases} \quad (6.19)$$

Combining the identity with the above two inequalities, the first four scenarios illustrated in Fig. 6.16 can be excluded. For instance, for scenario (b) (i.e.: $\alpha_S \rightarrow \beta_\Gamma$, $\beta_S \rightarrow \alpha_\Gamma$, $\gamma_S \rightarrow \gamma_\Gamma$), the identity requires

$$\begin{cases} \alpha_\Gamma = \beta_S^2 - \frac{1}{6}|\bar{S}|^2 \\ \beta_\Gamma = \alpha_S^2 - \frac{1}{6}|\bar{S}|^2 \\ \gamma_\Gamma = \gamma_S^2 - \frac{1}{6}|\bar{S}|^2 \end{cases} \quad (6.20)$$

By applying the first inequality of (6.18), system (6.20) results in $|\beta_S| > |\alpha_S| > |\gamma_S|$, which is contradictory to both inequalities of system (6.19). The other five scenarios can be analyzed in a similar way. For brevity, only the results of the mathematical analysis are summarized in Table 6.5.

TABLE 6.5: Mapping scenarios for the tensorial eigensystems between \mathbf{S} and $\mathbf{\Gamma}$ (Distinct eigen-roots)

Mapping scenarios	Results from the identity and $\alpha_\Gamma > \beta_\Gamma > \gamma_\Gamma$	Existence	Comments	Local structure
(a)	$ \alpha_S > \beta_S > \gamma_S $	Impossible	Contradictory to the 2nd inequality of system (6.19)	—
(b)	$ \beta_S > \alpha_S > \gamma_S $	Impossible	Contradictory to both inequalities of system (6.19)	—
(c)	$ \gamma_S > \beta_S > \alpha_S $	Impossible	Contradictory the 1st inequality of system (6.19)	—
(d)	$ \beta_S > \gamma_S > \alpha_S $	Impossible	Contradictory to both inequalities of system (6.19)	—
(e)	$ \alpha_S > \gamma_S > \beta_S $	Possible	Corresponding to $\beta_S < 0$ (or $\alpha_S > 0 > \beta_S > \gamma_S$)	tubelike
(f)	$ \gamma_S > \alpha_S > \beta_S $	Possible	Corresponding to $\beta_S > 0$ (or $\alpha_S > \beta_S > 0 > \gamma_S$)	sheetlike

The major conclusions of this and previous subsections can be summarized using the following two properties:

Property 6.1: The eigensystems of the tensorial parts of the 1st and 3rd nonlinear constituent terms, i.e. \mathbf{S} and $\mathbf{\Gamma}$, respectively, share the same set of eigenvectors. Their eigenvalues are connected by an identity, i.e. $\lambda_{\Gamma} = \lambda_S^2 - \frac{1}{6}|\bar{S}|^2$.

Property 6.2: The mapping relation from the eigensystem of \mathbf{S} to that of $\mathbf{\Gamma}$ through the identity ($\lambda_{\Gamma} = \lambda_S^2 - \frac{1}{6}|\bar{S}|^2$), is either ($\alpha_S \rightarrow \alpha_{\Gamma}$, $\beta_S \rightarrow \gamma_{\Gamma}$, $\gamma_S \rightarrow \beta_{\Gamma}$) for a local tubelike structure when $\beta_S < 0$, or ($\alpha_S \rightarrow \beta_{\Gamma}$, $\beta_S \rightarrow \gamma_{\Gamma}$, $\gamma_S \rightarrow \alpha_{\Gamma}$) for a local sheetlike structure when $\beta_S > 0$.

Given the descending sequence of the eigenvalues of a second order tensor indicated by system (6.18), the corresponding eigenvectors form a dextral orthonormal triad (the choice of the dextral frame is optional, however, it follows the tradition of the engineering community.). With the previous observations, it is now possible to discuss the topological relation between the dextral eigenframes formed by the orthonormal eigenvectors of \mathbf{S} and $\mathbf{\Gamma}$. Such a discussion is necessary for understanding the tensorial geometrical characteristics of Speziale's nonlinear constitutive relation Eq.(6.7). From Property 6.1, it can be inferred that *the principal alignment between the principal axes of the eigenframe of \mathbf{S} and $\mathbf{\Gamma}$ are either orthogonal or parallel*, which then allows for six different topological relations. However, from Property 6.2, one can further limit the topological relations of the two dextral orthonormal eigenframes to only two scenarios corresponding to either local tubelike or sheetlike structures, both of which have been validated in the numerical simulations in this research (see Table 6.4). Furthermore, these two realistic scenarios are determined by the sign of the intermediate eigenvalue of \mathbf{S} , which admits two sequences of the eigenvalues, i.e. $\beta_S < 0$ (or $\alpha_S > 0 > \beta_S > \gamma_S$) or $\beta_S > 0$ (or $\alpha_S > \beta_S > 0 > \gamma_S$). An equivalent expression to Property 6.2 can be used to conclude the above discussion on the topological relation of the two eigenframes:

Property 6.2': The geometrical relation between the orthonormal dextral eigenframes of \mathbf{S} and $\mathbf{\Gamma}$ can only take one of the following two attitudes: ($\mathbf{e}_{\Gamma\alpha} \parallel \mathbf{e}_{S\alpha}$,

$\mathbf{e}_{\Gamma\gamma} \parallel \mathbf{e}_{S\beta}, \mathbf{e}_{\Gamma\beta} \parallel \mathbf{e}_{S\gamma}$) related to local tubelike structure if $\beta_S < 0$, or $(\mathbf{e}_{\Gamma\beta} \parallel \mathbf{e}_{S\alpha}, \mathbf{e}_{\Gamma\gamma} \parallel \mathbf{e}_{S\beta}, \mathbf{e}_{\Gamma\alpha} \parallel \mathbf{e}_{S\gamma})$ related to local sheetlike structure if $\beta_S > 0$.

With the above new conclusions, the previous question regarding the numerical result on the averaged principal alignment between \bar{S}_{ij} and the third nonlinear constituent term η_{ij} (see Fig.6.12) presented in subsection 6.4.2 can now be clearly answered. For both possible flow patterns indicated by Property 6.2' corresponding to Figs. 6.16(e) and (f), the intermediate eigenvectors of the first and third nonlinear constituent terms (\mathbf{S} and $\mathbf{\Gamma}$) are *always* orthogonal to each other, i.e. $\mathbf{e}_{S\beta} \perp \mathbf{e}_{\Gamma\beta}$; as are the smallest eigenvectors of \mathbf{S} and $\mathbf{\Gamma}$, i.e. $\mathbf{e}_{S\gamma} \perp \mathbf{e}_{\Gamma\gamma}$. The alignment between the largest eigenvectors of both \mathbf{S} and $\mathbf{\Gamma}$, i.e. $\mathbf{e}_{\Gamma\alpha} \parallel \mathbf{e}_{S\alpha}$ corresponding to Fig. 6.16(e) is the *only* realistic non-orthogonal principal alignment pattern for these two constituent terms.

6.5.3 Situation of Multiple Roots

The above discussion regarding the eigensystems of \mathbf{S} and $\mathbf{\Gamma}$ is based on the assumption that all three eigenvalues of the tensor are distinct. Thus, in the case that the characteristic equation of the tensor allows for multiple roots, some modification to the conclusion regarding the local tubelike and sheetlike flow patterns discussed above is expected. Fortunately, the situation of *triple roots* only relates to the *trivial flow configuration*, i.e. $\alpha_S = \beta_S = \gamma_S = 0$, since all other nontrivial situations, i.e. $\alpha_S = \beta_S = \gamma_S \neq 0$, can be excluded by the continuity equation. However, in the case of *dual roots*, the situation becomes more complicated and the eigensystems for \mathbf{S} and $\mathbf{\Gamma}$ must be differentiated. It can be demonstrated that if the characteristic equation of \mathbf{S} allows for dual roots, there are *only* two possible local flow configurations, i.e. $\alpha_S = \beta_S > 0$ (axisymmetric expansion) or $0 > \beta_S = \gamma_S$ (axisymmetric compression). While if the characteristic equation of $\mathbf{\Gamma}$ has dual roots, according to the parabolic relation indicated by the identity, Eq.(6.17), one more flow pattern corresponding to $\alpha_S = -\gamma_S > 0$ and $\beta_S = 0$ (degenerate 2-D flow configuration) becomes possible, in addition to the previous two flow configurations of axisymmetric expansion and

compression. In fact, a state of axisymmetric expansion has been found to be the most probable flow configuration in isotropic turbulence according to recent research of Lund and Rogers [59] and Tao *et al.* [29]. Further review and discussion related to this topic will be pursued in the next two chapters.

6.6 Characteristics of the SGS TKE Production Rate

6.6.1 Backscatter

The SGS TKE production rate for the proposed DNM has the particular form

$$\begin{aligned}\mathcal{P}_r &= C_S \beta_{ij} \bar{S}_{ij} + C_W \gamma_{ij} \bar{S}_{ij} + C_N \eta_{ij} \bar{S}_{ij} \\ &\stackrel{\text{def}}{=} \mathcal{P}_{rS} + \mathcal{P}_{rW} + \mathcal{P}_{rN}\end{aligned}\tag{6.21}$$

For comparison, \mathcal{P}_r for the conventional Smagorinsky type DM of Lilly [20] takes a different form

$$\mathcal{P}_r^{DM} = 2C_S \bar{\Delta}^2 |\bar{S}| \cdot \bar{S}_{ij} \bar{S}_{ij} = \nu_{sgs} |\bar{S}|^2 = C_S \bar{\Delta}^2 |\bar{S}|^3\tag{5.40}$$

as given previously in chapter 5. \mathcal{P}_r^{DM} is similar to \mathcal{P}_{rS} , however, the DM uses this term solely to account for all of the TKE transport processes between the resolved and unresolved scales. For the DM, the value of $|\bar{S}|$ is always positive, thus the sign of \mathcal{P}_r^{DM} is purely decided by the sign of C_S or ν_{sgs} , which implies that the TKE transport exhibits one of *two limiting situations*, i.e. either completely backward or completely forward scatter. A few researchers, e.g. Piomelli and Liu [49], Carati *et al.* [137] and Ghosal *et al.* [40], have noted that an unrealistic prediction of backscatter (especially in the situation of its overestimation) can directly result in instability and failure of a numerical simulation. As pointed out by Horiuti [100], backscatter is not generated by a negative eddy viscosity, but rather the relative geometrical alignment pattern

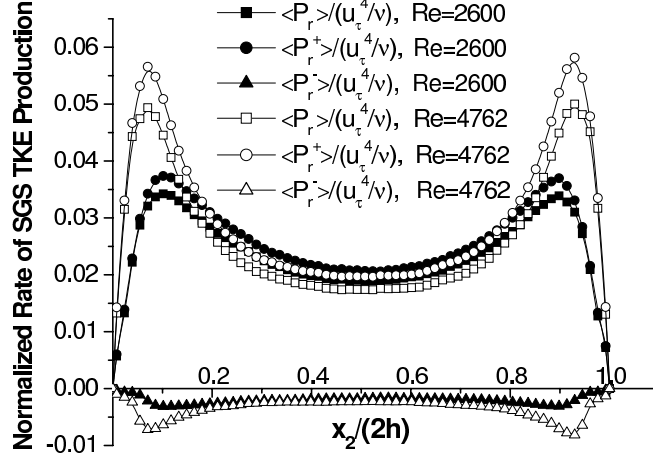


FIGURE 6.17: Mean profile of the non-dimensional SGS TKE production rate predicted using the DNM (66^3 nodes).

between the eigenvectors of the SGS stress and filtered strain rate tensors. Due to the deficiency of the Smagorinsky constitutive relation, which only admits two limiting SGS TKE transfer patterns, in some numerical applications involving the Smagorinsky type SGS models (e.g. Ghosal *et al.* [40], and Morinishi and Vasilyev [50]) numerical stability is achieved by employing a restriction of $C_S \geq 0$ or simply the adoption of C_S^2 (instead of C_S) to avoid excessive backscatter.

From Eq.(6.21), it is understood that the direction of the TKE transfer between the resolved and subgrid scales of motions is directly decided by both the sign of the coefficients (C_S , C_W and C_N), and the relative geometric orientation between the filtered strain rate tensor \bar{S}_{ij} and the constituent tensors β_{ij} , γ_{ij} and η_{ij} . Of course, one may also argue that the signs of the coefficients are eventually decided by the relative geometric relation of all the tensorial terms that appear in Eq.(6.10) in terms of both their relative magnitudes and orientations. Figure 6.17 plots the plane and time averaged wall-normal nondimensional profiles of SGS TKE production rate obtained using the DNM. From the figure, it is observed that the profiles for all three terms show a strong anisotropic effect in the wall-normal direction, and the Reynolds number effect is the most obvious in the buffer zone. The contributions of forward scatter $\langle \mathcal{P}_r^+ \rangle$ and backscatter $\langle \mathcal{P}_r^- \rangle$ to the general term $\langle \mathcal{P}_r \rangle$ are separated, which balance as $\langle \mathcal{P}_r^+ \rangle + \langle \mathcal{P}_r^- \rangle = \langle \mathcal{P}_r \rangle$. Fig. 6.17 shows that the averaged level of

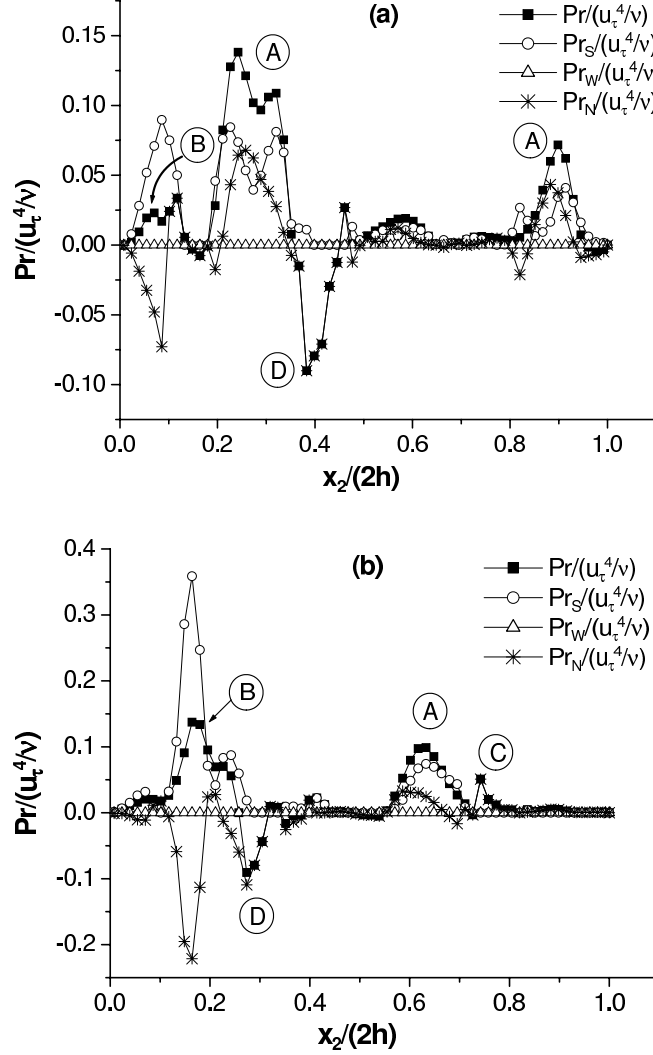


FIGURE 6.18: Instantaneous distribution of the non-dimensional SGS TKE production rate ($Re = 2600$, 66^3 nodes; relative location in the homogeneous plane: $x_1/L_1 = 0.570$ and $x_3/L_3 = 0.367$ for (a), $x_1/L_1 = 0.602$ and $x_3/L_3 = 0.461$ for (b)).

backscatter is about 10–15% that of forward scatter, and the net scattering effect of SGS TKE is from the resolved to the subgrid scales, i.e. $\langle \mathcal{P}_r \rangle \geq 0$.

Figures 6.18 and 6.19 show an instantaneous nondimensional profile of \mathcal{P}_r and the contribution of each of the three nonlinear constituent terms, i.e. \mathcal{P}_{rS} , \mathcal{P}_{rW} and \mathcal{P}_{rN} (see Eq. (6.21)), at specific locations for the two Reynolds numbers tested. These instantaneous figures clearly show both forward and backward scatter of TKE along the wall-normal direction. Some typical inertial TKE scattering peaks appearing in Figs. 6.18 and 6.19 can be approximately identified as follows: positive peaks

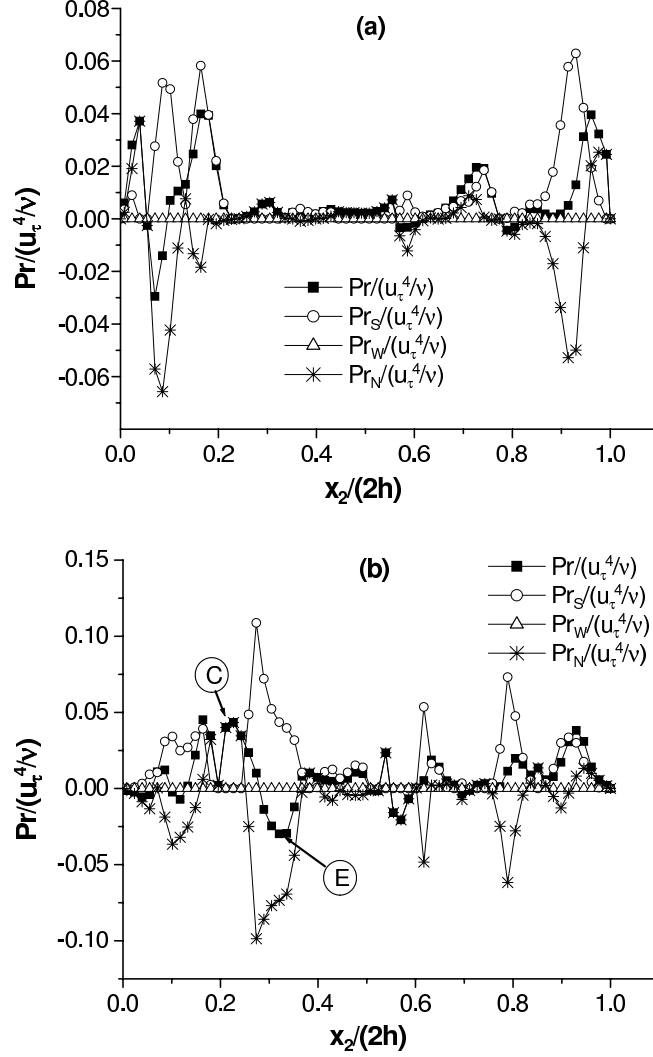


FIGURE 6.19: Instantaneous distribution of the non-dimensional SGS TKE production rate ($Re = 4762$, 66^3 nodes; relative location in the homogeneous plane: $x_1/L_1 = 0.383$ and $x_3/L_3 = 0.477$ for (a), $x_1/L_1 = 0.289$ and $x_3/L_3 = 0.180$ for (b)).

marked with a circled A in Fig. 6.18 indicate an instantaneous forward scatter of TKE contributed by both the first and third nonlinear terms; positive peaks marked with a circled B reflect an instantaneous net forward scatter of TKE from the balance of forward scatter of the first term and backscatter of the third term; positive peaks marked with a circled C in both Figures 6.18(b) and 6.19(b) indicate an forward scatter mainly due to the third term with negligible contributions from other terms; negative peaks marked with a circled D reflect a net instantaneous backscatter mainly contributed by the third term with negligible contributions from other terms; and the

negative peak marked with a circled E indicates an instantaneous net backscatter from the balance of the forward scatter due to the first term and backscatter (of relatively larger magnitude) due to the third term.

Based on Figs. 6.18 and 6.19 and an examination of many other similar instantaneous profiles, some general impressions are: the rate of SGS TKE production due to the first constituent term (the Smagorinsky component), \mathcal{P}_{rS} , predominates forward scatter of TKE from the resolved to the subgrid scales of motions; the rate of SGS TKE production attributed to the second nonlinear term, \mathcal{P}_{rW} , plays a trivial role in the total TKE transfer between the two scales; the backscatter phenomenon is preferentially linked to the third term, \mathcal{P}_{rN} . From the numerical tests, we observed that the instantaneous and time averaged value of \mathcal{P}_{rW} is always negligible ranging from 0 to 10^{-17} . A brief analytical explanation for this interesting phenomenon will be presented in the following subsection.

6.6.2 Rate of SGS TKE Production Due to the 2nd and 3rd Nonlinear Constituent Terms

In subsection 6.6.1 it has been observed that the rate of the SGS TKE production (\mathcal{P}_r) attributed to the second nonlinear term (\mathcal{P}_{rW}) is trivial as shown in Figs. 6.18 and 6.19. A concern then naturally emerges: is this just a numerical coincidence or an intrinsic characteristic of the DNM? The above concern is clarified by the following property:

Property 6.3: The strain rate tensor \bar{S}_{ij} is orthogonal to the second nonlinear constituent term of the SGS stress tensor, γ_{ij} , such that the rate of the SGS TKE production attributed to γ_{ij} is instantaneously zero at any location, i.e. $\mathcal{P}_{rW} = C_W \gamma_{ij} \bar{S}_{ij} \equiv 0$.

Proof: Neglecting the trivial solution of $C_W = 0$, the proof of this property requires $\gamma_{ij} \bar{S}_{ij} \equiv 0$, i.e. an orthogonal relation between γ_{ij} and S_{ij} with the inner product of two tensors defined in Appendix A. Thus, from the definition of γ_{ij} given in Eq.(6.9),

we have

$$\begin{aligned}
\gamma_{ij}\bar{S}_{ij} &= 2\bar{\Delta}^2(\bar{S}_{ik}\bar{\Omega}_{kj} - \bar{\Omega}_{ik}\bar{S}_{kj}) \cdot \bar{S}_{ij} \\
&= 4\bar{\Delta}^2\bar{\Omega}_{ki}\bar{S}_{kj}\bar{S}_{ji} \\
&\equiv 0
\end{aligned} \tag{6.22}$$

due to the fact that $\bar{\Omega}_{ij}$ is anti-symmetric, while both \bar{S}_{ij} and $\bar{S}_{kj}\bar{S}_{ji}$ are symmetric.

The performance of the third nonlinear constituent term (η_{ij}) is significantly different than the second term (γ_{ij}) in terms of \mathcal{P}_r , which is clearly indicated by Figs. 6.11 and 6.12. To clarify this issue analytically, we give the following property:

Property 6.4: \mathcal{P}_{rN} , the rate of SGS TKE production due to the third nonlinear constituent term (η_{ij}), is proportional to the *resolved strain skewness* $\bar{\mathcal{I}}_{S3}$, i.e. $\mathcal{P}_{rN} \equiv 4C_N\bar{\Delta}^2\bar{\mathcal{I}}_{S3}$. Here, the resolved strain skewness for incompressible flow is defined as

$$\bar{\mathcal{I}}_{S3} \stackrel{\text{def}}{=} \bar{S}_{ik}\bar{S}_{kj}\bar{S}_{ji} \equiv \alpha_S^3 + \beta_S^3 + \gamma_S^3 \tag{6.23}$$

which is a 3rd order invariant of \bar{S}_{ij} . Also in the following discussion, the *resolved strain product*, a 2nd order invariant of \bar{S}_{ij} will be used, which is defined as

$$\bar{\mathcal{I}}_{S2} \stackrel{\text{def}}{=} \bar{S}_{ij}\bar{S}_{ji} \equiv \alpha_S^2 + \beta_S^2 + \gamma_S^2 \tag{6.24}$$

Proof: The contribution to the SGS TKE production \mathcal{P}_r due to the third nonlinear constituent term \mathcal{P}_{rN} takes the following form:

$$\begin{aligned}
\mathcal{P}_{rN} &= C_N\eta_{ij}\bar{S}_{ij} \\
&= 4C_N\bar{\Delta}^2 \cdot (\bar{S}_{ik}\bar{S}_{kj} - \frac{1}{3}\bar{S}_{mn}\bar{S}_{nm}\delta_{ij})\bar{S}_{ij} \\
&\stackrel{\text{def}}{=} C'\mathcal{P}_{rN}^\circ
\end{aligned} \tag{6.25}$$

where $C' = 4C_N\bar{\Delta}^2$ and $\mathring{\mathcal{P}}_{rN}$ is

$$\begin{aligned}\mathring{\mathcal{P}}_{rN} &= (\bar{S}_{ik}\bar{S}_{kj} - \frac{1}{3}\bar{S}_{mn}\bar{S}_{nm}\delta_{ij})\bar{S}_{ij} \\ &= \bar{S}_{ik}\bar{S}_{kj}\bar{S}_{ji} - \frac{1}{6}|\bar{S}|^2\bar{S}_{ii} \\ &= \bar{\mathcal{I}}_{S3}\end{aligned}\tag{6.26}$$

In the above mathematical development, we used two properties specific for \bar{S}_{ij} , i.e. $\bar{S}_{ij} = \bar{S}_{ji}$ due to symmetry and $\bar{S}_{ii} \equiv 0$ due to continuity.

Actually, a result of Eq.(6.26) can be obtained more intuitively in terms of physics from the geometrical relation specified by Property 6.2', which results in

$$\mathring{\mathcal{P}}_{rN} = \begin{cases} \alpha_\Gamma\alpha_S + \gamma_\Gamma\beta_S + \beta_\Gamma\gamma_S & \text{for } \beta_S < 0 \text{ (tubelike)} \\ \beta_\Gamma\alpha_S + \gamma_\Gamma\beta_S + \alpha_\Gamma\gamma_S & \text{for } \beta_S > 0 \text{ (sheetlike)} \end{cases}\tag{6.27}$$

which explicitly expresses the SGS TKE production rate due to the 3rd nonlinear constituent terms ($\mathring{\mathcal{P}}_{rN}$) using the principal stresses of the 3rd term and the principal deformation (strain) rates. By applying the identity (Eq.(6.17)) in accordance with the two corresponding mapping relations indicated by Figs. 6.16(e) and (f), respectively, both equations in (6.27) result in

$$\mathring{\mathcal{P}}_{rN} = \alpha_S^3 + \beta_S^3 + \gamma_S^3 - \frac{1}{6}|\bar{S}|^2(\alpha_S + \beta_S + \gamma_S) = \bar{\mathcal{I}}_{S3}\tag{6.28}$$

which is the same as Eq.(6.26).

Thus, from Eq.(6.21) and properties 6.3 and 6.4, the following conclusion on the overall SGS TKE production rate \mathcal{P}_r is straightforward:

Property 6.5: The rate of SGS TKE production inherent to the DNM is a function of $\bar{\mathcal{I}}_{S2}$ and $\bar{\mathcal{I}}_{S3}$, the invariants of the filtered strain rate tensor, i.e.

$$\mathcal{P}_r \equiv C_S\bar{\Delta}^2(2\bar{\mathcal{I}}_{S2})^{3/2} + 4C_N\bar{\Delta}^2\bar{\mathcal{I}}_{S3}\tag{6.29}$$

6.7 Conclusions

A dynamic nonlinear model (DNM) based on Speziale’s three-term quadratic constitutive relation [108, 109] has been formulated, which admits a nonlinear anisotropic relation between the subgrid scale stress and the resolved strain rate and rotation rate tensors. The proposed DNM was tested using turbulent Couette flow and such phenomenological flow features as the logarithmic velocity profile, anisotropic wall-normal distribution of the resolved streamwise turbulence intensity, and cubic behavior of the resolved Reynolds shear stress in the near-wall region, have been obtained and compared with the results of other researchers. The additional computational cost of the DNM is approximately 23–30% that of the conventional DM of Lilly [20].

The proposed DNM demonstrates a variety of self-calibrating mechanisms in terms of its three coefficients and the tensorial geometric relations between the SGS stress and the three constituent terms, which in turn provides more degrees of freedom for predicting the forward and backward scattering processes of TKE. This is in contrast to the conventional DM [20], which can only reflect the TKE cascade in two extreme ways: either fully forward scatter or fully backscatter, and thus can induce numerical instability. The proposed DNM appears to be more robust than the conventional DM in the numerical simulation. In this study, the DNM can be applied locally and the simulation remains stable at each time step without the need for the ‘standard’ plane averaging technique to avoid a potential instability due to excessive backscatter or potential singularity of the modelling formulation. However, under the same test conditions, an additional plane averaging procedure is always necessary to maintain the simulation stable when the conventional DM [20] is applied.

The role of each of the three nonlinear constituent terms has been studied in terms of the relative principal orientation between its eigenframe and those of the negative SGS stress ($-\tau_{ij}$) and filtered strain rate tensors (\bar{S}_{ij}). To visualize the complex geometry between the eigenframes of the two tensors, three principal alignment angles, i.e. Λ_α , Λ_β and Λ_γ are investigated. The principal relative orientation of the eigenframes between the filtered strain rate and second and third nonlinear

constituent tensors (γ_{ij} and η_{ij} respectively), and that between the negative SGS stress and the three nonlinear constituent tensors exhibit strong anisotropy due to the presence of the wall. At the wall, the principal alignment between the two eigenvectors corresponding to the largest eigenvalue of \bar{S}_{ij} and γ_{ij} is equiangular, and so is that between the eigenvectors corresponding to their smallest eigenvectors. However, the principal alignment between the eigenvectors corresponding to the intermediate eigenvalues of \bar{S}_{ij} and γ_{ij} is parallel. In the core region, all these three principal alignments between \bar{S}_{ij} and γ_{ij} are skewed, but close to equiangular. The pattern of the principal alignment between \bar{S}_{ij} and η_{ij} is rather interesting in that the principal alignment between the eigenvectors corresponding to the largest eigenvalues are skewed in the wall-normal direction, whereas, the principal alignment between the eigenvectors corresponding to the intermediate eigenvalues and that corresponding to the smallest eigenvalues are always orthogonal. For the alignment between the eigenframes of $-\tau_{ij}$ and the three constituent terms, it is observed that the relative principal orientation pattern is parallel, equiangular or perpendicular at the wall, and either skewed or equiangular in the core region. In contrast, the (dynamic) Smagorinsky type models only allows the alignment pattern to be $\Lambda_\alpha \equiv \Lambda_\beta \equiv \Lambda_\gamma \equiv 0^\circ$ between the principal axes of $-\tau_{ij}$ and \bar{S}_{ij} .

Although the first and third constituent tensors are independent of each other and behave quite differently in terms of the distribution of the corresponding model coefficients and TKE scattering processes, they share the same set of eigenvectors and thus the alignment between the principal axes of these two constituent tensors can be only either parallel or orthogonal. An identity is found to relate the eigenvalues of their effective tensorial parts, i.e. \mathbf{S} and $\mathbf{\Gamma}$, respectively. Through this identity, it is found that among the six possible topological relations between the eigenframes of \mathbf{S} and $\mathbf{\Gamma}$, only two are realistic, which correspond to local tubelike and sheetlike structures if the roots of the characteristic equation of \mathbf{S} and $\mathbf{\Gamma}$ are distinct. If the characteristic equation of \mathbf{S} admits dual roots, the flow configuration of local axisymmetric expansion and compression become realistic. While if the characteristic equation of $\mathbf{\Gamma}$ admits dual roots, an additional local degenerate 2-D flow configuration

is included. It has been shown both numerically and analytically that the second nonlinear constituent term, γ_{ij} , is strictly orthogonal to the resolved strain rate tensor, \bar{S}_{ij} , and as such it does not make any contribution to the rate of SGS TKE production. However, the rate of SGS TKE production due to the third term is proportional to the resolved strain skewness, i.e. $\bar{\mathcal{L}}_{S3} = \alpha_S^3 + \beta_S^3 + \gamma_S^3$ for both realistic scenarios corresponding to local tubelike and sheetlike structures.

Chapter 7

Turbulence Geometrical Statistics

7.1 Introduction

Turbulence geometrical statistics is a recently developed methodology for studying geometrical properties of fluid flows such as the relative orientation between two fluid vectors and relative *attitude* [180] between two eigenframe triads. The attractiveness of this methodology is that it is useful for revealing invariant properties of fluid flows, since many of the relative geometrical alignments studied in turbulence geometrical statistics are *frame invariants* under any translations (Galilean) and rotations of the reference frame. For instance, the *enstrophy generation* which quantifies the alignment between the vorticity and vortex stretching vectors, and the previously discussed resolved strain skewness, are frame invariants.

Studies on the geometrical properties of fluid tensors can be traced back to the classical works of G. I. Taylor [181], A. A. Townsend [182] and R. Betchov [183]. Following these pioneering works, improved research approaches considering both eigenvalues and eigenvectors have become more active in the past two decades [51–55, 184], leading to the current research branch of so-called turbulence geometrical statistics [52–55, 76]. *A posteriori* applications of turbulence geometrical statistics in LES include the recent works of Saffman, Pullin, Misra, Voelkl and Chan [101–107] featured by their alignment-based SGS stress models, while *a priori* LES investigations on turbulence geometrical statistics are found in the recent works of Borue and

Orszag [165], Horiuti [100] and Tao *et al.* [29,99].

In this and the following chapters, the numerical results on turbulence geometrical statistics and *turbulence topology* will be presented, respectively. The approach adopted in both chapters is based on *a posteriori* LES of turbulent Couette flow using the proposed DNM SGS stress model, which is different than most other studies found in the literature based on *a priori* analysis of experimental or DNS data. In this context, the research presents a couple of challenges: (1) can a LES based on the DNM SGS stress model simulate a resolved turbulent wall-bounded flow to the extent that it captures not only the conventional turbulence scaling features but also geometrical and topological features of the flow? since it is advocated in this dissertation that in the future the CFD community should consider this as a criterion for a good turbulence model; and (2) what is the influence of near-wall anisotropy on the turbulence geometrical statistics and topology of the flow? The answers to these two questions will be addressed by analyzing the numerical results. Two types of statistical calculations are performed at each time step based on a simple plane average technique and using *Probability Functions* (PF) [185]. A PF (denoted by $P(s_i)$) is a real-valued function defined on a discrete sample space $\{s_1, s_2, \dots\}$ with properties: $P(s_i) \geq 0$ and $\sum_i P(s_i) = 1$. In the statistical calculations, 30 bins are used for the PF of a single variable, while 30×30 bins are used for the *Joint Probability Function* (JPF) [185] of a set of two independent variables. Before presenting any numerical results, it is necessary to first review some basic concepts and previous approaches of other researchers.

7.2 Basic Concepts Related to the Velocity Gradient Tensor

It is known that the small scales of turbulent flows are characterized by the gradients of the velocity instead of the velocity itself. The dynamical behavior of the velocity gradient tensor is of fundamental importance for understanding coherent structures

because it governs a variety of physical phenomena such as local vortex stretching and TKE dissipation. It also contains significant information through its *tensorial invariants*, which in turn determine the various local flow topologies [57, 58, 63, 186] and vectorial alignment patterns [54, 55, 76].

From the previous analysis, the velocity gradient tensor $u_{i,j}$ can be decomposed into a symmetric part and a skew-symmetric part, which are usually referred to as the strain rate tensor S_{ij} and rotation rate tensor Ω_{ij} , respectively. The vorticity vector $\boldsymbol{\omega}$ can be derived from the rotation rate tensor or directly from the velocity gradient as $\omega_i = \varepsilon_{ijk}\Omega_{kj} = \varepsilon_{ijk}u_{k,j}$. Besides S_{ij} , Ω_{ij} and ω_i , the velocity gradient also determines the vortex stretching vector, helicity density and enstrophy generation. The *helicity (density)* is defined as

$$H \stackrel{\text{def}}{=} u_i \omega_i \quad (7.1)$$

which quantifies helical motions. It is also known to play an important role in magnetohydrodynamics and is related to coherent structure, small scale intermittency, and topology of turbulence [53, 60, 61, 187]. The *relative helicity* normalized by its magnitude takes the form

$$h_n \stackrel{\text{def}}{=} \cos \Theta(\mathbf{u}, \boldsymbol{\omega}) = \frac{\mathbf{u} \cdot \boldsymbol{\omega}}{|\mathbf{u}| \cdot |\boldsymbol{\omega}|} \quad (7.2)$$

where $\Theta(\mathbf{u}, \boldsymbol{\omega})$ is the angle between the velocity and vorticity vectors. Since h_n is not a Galilean invariant, it is necessary to define what velocity is used in its definition. It is reported [53, 61] that there is a significant likelihood that the velocity and vorticity fields are aligned when the *total velocity* is adopted in the definition of h_n .

If the strain rate tensor produced by the velocity gradient tensor acts to stretch the material line element aligned with $\boldsymbol{\omega}$, then ω , the magnitude of $\boldsymbol{\omega}$, increases. This is the phenomenon of *vortex stretching*, and the corresponding *vortex stretching vector* \mathbf{w} is defined as [32]

$$w_i \stackrel{\text{def}}{=} \omega_j S_{ij} \quad (7.3)$$

which by definition clearly represents the response of $\boldsymbol{\omega}$ to S_{ij} in terms of the effect of deformation. The change of the vorticity by vortex stretching is a consequence of the conservation of angular momentum. The angular momentum of a material volume element remains constant if viscous effects are absent. If the fluid element is stretched so that its cross-sectional area and moment of inertia become smaller, the component of the angular velocity in the direction of the stretching must increase in order to conserve angular momentum [188]. This can also be understood from the transport equation for the *enstrophy* (ω^2), i.e. Eq.(C.2) in Appendix C, which shows that an instantaneous vortex stretching pattern ($\omega_i\omega_j S_{ij} > 0$) contributes to the transient increase of enstrophy or vorticity magnitude. A quantity that is closely related to vortex stretching is the so-called *enstrophy generation* defined as

$$\sigma \stackrel{\text{def}}{=} \boldsymbol{\omega} \cdot \mathbf{w} \equiv \omega_i \omega_j S_{ij} = \omega^2 \lambda_i \cos^2(\boldsymbol{\omega}, \mathbf{e}_i) = \sum_i \sigma_i \quad (7.4)$$

which is a third order frame invariant (or *geometrical invariant* [78,82]). In Eq.(7.4), λ_i and \mathbf{e}_i are the eigenvalue and eigenvector of the strain rate tensor, respectively. The subscript i runs from 1, 2 to 3, corresponding to the largest, intermediate and smallest eigenvalue, respectively. Following the conventions of the fluids community, the descending order of the eigenvalues mentioned above are represented by α , β and γ , respectively. In order to avoid any confusion in the subscripts, σ_α , σ_β and σ_γ instead of σ_1 , σ_2 and σ_3 , are used to represent these three enstrophy generation components in the following discussion. The relative orientation between \mathbf{w} and $\boldsymbol{\omega}$ can be represented using the *normalized enstrophy generation*, i.e.

$$\sigma_n \stackrel{\text{def}}{=} \cos \Theta(\boldsymbol{\omega}, \mathbf{w}) = \frac{\boldsymbol{\omega} \cdot \mathbf{w}}{|\boldsymbol{\omega}| \cdot |\mathbf{w}|} \quad (7.5)$$

For 2-D flows, both the vortex stretching vector and enstrophy generation vanish, i.e. $\mathbf{w}_{2D} \equiv \mathbf{0}$ and $\sigma_{2D} \equiv 0$, and the only non-zero component of vorticity evolves as a conserved scalar. Because of the absence of vortex stretching, 2-D turbulence is qualitatively different than 3-D turbulence [32].

Based on measurements of turbulent grid flow, Taylor [181] first demonstrated the positiveness of the mean enstrophy generation $\langle \sigma \rangle$ for isotropic turbulence. This conclusion is specific for (quasi-)homogeneous isotropic flows and has been more recently confirmed via experiments (e.g. Tsinober *et al.* [76]) and numerical tests using DNS (e.g. Ruetsch and Maxey [93, 94], Jiménez *et al.* [92], Andreotti [84], Tsinober *et al.* [77], Horiuti [88]). The predominant positiveness of the mean value of the enstrophy generation indicates that a most probable state for isotropic turbulence is related to vortex stretching instead of vortex compressing flow configuration. *Vortex compression* is the contraction of the vortex line related to a negative enstrophy generation.

Geometrical invariants are believed to be the most appropriate tool for studying physical processes in turbulent flows, since their properties and implied structures are universal [78, 82]. Another frequently used third order geometrical invariant is the *strain skewness* previously discussed in subsection 6.6.2, which is defined as

$$\mathcal{I}_{S3} = S_{ij}S_{jk}S_{ki} \quad (7.6)$$

Both enstrophy generation and strain skewness are odd moments of S_{ij} which represent the nonlinearity of turbulence and have a profound influence on local turbulence structures.

For the LES approach considered in the research, the resolved quantities are denoted using a overbar. For instance, the resolved relative helicity and normalized enstrophy generation are $\bar{h} = \cos \Theta(\bar{\mathbf{u}}, \bar{\boldsymbol{\omega}})$ and $\bar{\sigma}_n = \cos(\bar{\mathbf{w}}, \bar{\boldsymbol{\omega}})$, respectively.

7.3 Several Classical Topics in Turbulence Geometrical Statistics

Based on the concepts introduced above, some of the current research methodologies and reported results in the area of turbulence geometrical statistics can be reviewed. Due to the richness of the topic, only those that are closely related to this research can be highlighted, specifically the geometrical alignments between fluid vectors and the ratio of the eigenvalues of the resolved strain rate tensor.

7.3.1 Geometrical Alignments

The study of the relative orientation between the vorticity vector $\boldsymbol{\omega}$ and the eigenvectors of the strain rate tensor S_{ij} is one of the classical topics in the area of turbulence geometrical statistics. In his studies on DNS of isotropic turbulence, Kerr [54, 62] observed a strong tendency for alignment between the vorticity and the intermediate eigenvector of the strain rate tensor, i.e. $\mathbf{e}_{S\beta}$. Ashurst *et al.* [55] reported a similar result based on analysis of a DNS database of a low Reynolds number isotropic flow and homogeneous shear flow. The discovery of Kerr [54, 62] and Ashurst *et al.* [55] is rather “surprising” [77], since it is seemingly contradictory to the previous belief that $\boldsymbol{\omega}$ should be more likely aligned with $\mathbf{e}_{S\alpha}$, in which case, the explanation for the well acknowledged observation on positively skewed enstrophy generation would be easier to address (see Eq.(7.4)). The discovery of the preferential alignment between $\boldsymbol{\omega}$ and $\mathbf{e}_{S\beta}$ was later confirmed analytically by Cantwell [63] based on solving the restricted Euler equation, and experimentally by a number of researchers including: Tsinober *et al.* [76, 77] who measured the full velocity gradient of turbulent grid flow and boundary layer flow over a smooth plate using the 12- and 20-wire probes, Honkan and Andreopoulos [179] who measured boundary layer turbulence using three individual triple-wire gradient probes, and Tao *et al.* [29, 99] who measured the core region field of a square duct flow using HPIV and processed the data using *a priori* LES approaches. This unique alignment pattern has also been validated by a number

of numerical studies based on analysis of DNS databases, e.g. the works reported in Refs. [71–74, 77, 85, 88, 90, 94].

As discussed above, although the state of alignment between $\boldsymbol{\omega}$ and $\mathbf{e}_{S\beta}$ is strongly preferred, some refined research [71, 72, 74, 77, 78] indicates that other alignment patterns do exist. Tsinober *et al.* [77, 78] and Nomura and Post [71] pointed out that the flow regions which contribute most to the enstrophy generation are linked to the alignment between $\boldsymbol{\omega}$ and $\mathbf{e}_{S\alpha}$. It is further concluded from numerical [77, 85] and experimental [76–78] investigations that the enstrophy generation related to the most extensive eigenbasis is larger than but of the same order as that related to the intermediate eigenvalues, i.e. $\sigma_\alpha > \sigma_\beta$ (see Eq.(7.4)), which indicates that the majority of the enstrophy generation is associated with the most extensive eigenvalue α_S .

A strong alignment between the vorticity vector $\boldsymbol{\omega}$ and the vortex stretching vector \mathbf{w} has been reported by Tsinober *et al.* [77, 78] and Shtilman *et al.* [89]. Andreotti [84] also investigated this phenomenon using Burgers’ models. According to the research of Tsinober *et al.* [77, 78], it appears that both the alignment between $\boldsymbol{\omega}$ and $\mathbf{e}_{S\beta}$, and that between $\boldsymbol{\omega}$ and \mathbf{w} are the strongest when the magnitude of enstrophy (ω^2) is minimum. Similar results have been observed by Jiménez [92]. Tsinober *et al.* [77, 78] concluded that the background turbulence with the weakest excitation of vorticity is not a “random sea” without any structures. Various local alignment patterns exist in all regions with or without strong vorticity activities.

7.3.2 Relative Principal Values

Studies on the relative principal value of the strain rate tensor can be traced back to the pioneering work of Betchov [183], who analyzed the magnitude of the eigenvalues using some fundamental algebraic inequalities. Recent refined numerical investigations based on DNS of homogeneous turbulence by Ashurst *et al.* [55] and Kerr [62] show that the ratio of the principal values of the strain rate tensor is most likely to be $\alpha_S : \beta_S : \gamma_S = 3 : 1 : -4$. The statistical non-dimensional parameter adopted by

Ashurst *et al.* [55] and Kerr [62] was

$$\beta^* = \frac{\sqrt{6}\beta_S}{(\alpha_S^2 + \beta_S^2 + \gamma_S^2)^{1/2}} \quad (7.7)$$

The experiment of Tsinober *et al.* [76] based on hot-wire measurements of grid generated turbulence in a wind tunnel further confirmed the result of Ashurst *et al.* [55] and Kerr [62], i.e. $\beta^* \approx 0.4$ which corresponds to $\alpha_S : \beta_S : \gamma_S \approx 3.74 : 1 : -4.74$ (the ratio $3.1 : 1 : -3.8$ was instead presented in their paper). A similar observation was reported in the work of She *et al.* [90] based on analyzing a DNS database of homogeneous turbulence. Later, Lund and Rogers [59] indicated that the β^* -PF introduced by Ashurst *et al.* [55] and Kerr [62], appears to be inadequate, because it leads to the incorrect conclusion that a state of local axisymmetric expansion does not exist in turbulent flows. Lund and Rogers [59] proposed an improved non-dimensional parameter, i.e.

$$s^* = \frac{-3\sqrt{6}\alpha_S\beta_S\gamma_S}{(\alpha_S^2 + \beta_S^2 + \gamma_S^2)^{3/2}} \quad (7.8)$$

Besides s^* , Lund and Rogers [59] also proposed another non-dimensional parameter, β_S/α_S . Since there are only two independent eigenvalues for S_{ij} for incompressible flow, the most probable ratio of $\alpha_S : \beta_S : \gamma_S$ can be calculated using continuity given by Eq.(6.12) once the most probable value of either β^* , s^* or β_S/α_S is determined. For instance, a classical ratio of $3 : 1 : -4$ corresponds to $\beta^* = 0.480$, $s^* = 0.665$, or $\beta_S/\alpha_S = 0.333$.

With the new parameterization method, Lund and Rogers [59] investigated a DNS database of isotropic incompressible turbulence, and they obtained the interesting conclusion that a state of *axisymmetric expansion* ($s^* = 1$ and $\alpha_S : \beta_S : \gamma_S = 1 : 1 : -2$) is the most probable flow configuration, which is in sharp contrast to the previous conclusion of Ashurst *et al.* [55] and Kerr [62]. According to the result of Lund and Rogers [59], it appears that the statistics based on s^* do not support the classical ratio of $3 : 1 : -4$. Their refined statistical study indicated that the most probable state is $s^* = 1$ for a low dissipation rate, and $s^* = 0.9$ for regions with a high dissipation rate. The ratio corresponding to $s^* = 0.9$ is $\alpha_S : \beta_S : \gamma_S = 1.7 : 1 : -2.7$, which is

somewhat displaced from the state of axisymmetric expansion. Lund and Rogers [59] reported that for regions of high dissipation rate, the most probable values for β_S/α_S and β^* are 0.357 and 0.54, which correspond to $\alpha_S : \beta_S : \gamma_S = 2.8 : 1 : -3.8$ and $2.65 : 1 : -3.65$, respectively. Both these ratios are close to the previously discussed classical ratio of $3 : 1 : -4$. It is advocated by Lund and Rogers [59] that s^* -PF should be used for the purpose of understanding turbulent structures, and (β/α) -PF should only be used for determining the ratio $\alpha_S : \beta_S : \gamma_S$ itself. The result of Lund and Rogers [59] that the axisymmetric expansion is the most probable state has been confirmed by a number of researchers, including Horiuti [88] who analyzed DNS data of isotropic turbulence; Soria *et al.* [64] and Blackburn *et al.* [73] who studied the eigenvalue ratio using the phase plane of tensorial invariants (which will be discussed in the next chapter); and Tao *et al.* [29] who analyzed HPIV measurements using an *a priori* LES approach.

As mentioned earlier, there are two degrees of freedom in determining the relative principal values for a resolved strain rate tensor for incompressible flow. In addition to the three probability functions, i.e. β^* -PF, s^* -PF and (β/α) -PF, continuity provides a second constraint. In the special case of $\beta_S = 0$, the flow degenerates to 2-D and the relative eigenvalue ratio is usually determined to be $1 : 0 : -1$. Such a choice is *arbitrary*, since any choice $\lambda : 0 : -\lambda$ for all $\lambda \geq 0$ is valid. Strictly speaking, this is a *singular situation*. Furthermore, it should be pointed out that in the case of β_S being close to 0, the system of two constraints, continuity and one of the three statistical parameters, is very unstable and hence unreliable, since any small change in the value of the statistical quantity corresponding to the most probable state can result in a large difference in the result. Later in presenting the numerical result, it will be shown that this singular problem becomes very severe in the viscous sublayer, where β_S is statistically small.

7.4 Numerical Results on Geometrical Alignments

In this section, three types of relative alignments will be investigated, including the alignment between the velocity and vorticity vectors, that between vorticity vector and the eigenvector, and that between the vorticity and vortex stretching vectors.

7.4.1 Results on Helicity

As introduced previously, helicity by its definition describes the relative orientation between the velocity and vorticity vectors. If the value of the relative helicity density $h_n = \cos \Theta(\mathbf{u}, \boldsymbol{\omega}) = \mathbf{u} \cdot \boldsymbol{\omega} / (|\mathbf{u}| \cdot |\boldsymbol{\omega}|)$ is close to ± 1 , strong helical activity related to an alignment between \mathbf{u} and $\boldsymbol{\omega}$ becomes dominant, whereas at the same time $|\mathbf{u} \times \boldsymbol{\omega}|$ must be small ($\boldsymbol{\omega} \times \mathbf{u}$ is known as the *Lamb vector*). In the other case, if $h_n \rightarrow 0$, the level of $|\mathbf{u} \times \boldsymbol{\omega}|$ must be high (supposing that both $|\mathbf{u}|$ and $|\boldsymbol{\omega}|$ are nontrivial). Since the nonlinear term $\mathbf{u} \times \boldsymbol{\omega}$ is associated with the convection term in the N-S equations and its level indicates the rate of energy cascade to smaller scales, a high level of helicity inhibits nonlinear interactions as well as the cascade of energy due to $\mathbf{u} \times \boldsymbol{\omega}$ [60, 61].

Figures 7.1(a)–(c) show the *resolved helicity density* $\bar{h}_n = \cos \Theta(\bar{\mathbf{u}}, \bar{\boldsymbol{\omega}})$ at the filtered scale of motions in the three different flow regimes: viscous sublayer, buffer zone and logarithmic region. Figure 7.1(a) shows an overall “flat” helicity profile, which, however, turns up at $\bar{h}_n = \pm 1$. This tailing-up pattern indicates a slightly greater prevalence of resolved *helical structures* in the logarithmic region, which agrees with the DNS results reported by Pelz *et al.* [53], and Rogers and Moin [61]. From Figs. 7.1(b) and (c), it is observed that a state of $\bar{h}_n = 0$ becomes more and more probable as x_2^+ decreases, which indicates a *near-wall orthogonal alignment between $\bar{\mathbf{u}}$ and $\bar{\boldsymbol{\omega}}$* . Such a near-wall anisotropic effect of helicity has already been well documented based on DNS data analysis of Poiseuille channel flow [53, 61]. As concluded by Pelz *et al.* [53] that for the near wall region, the vorticity is mainly in the spanwise

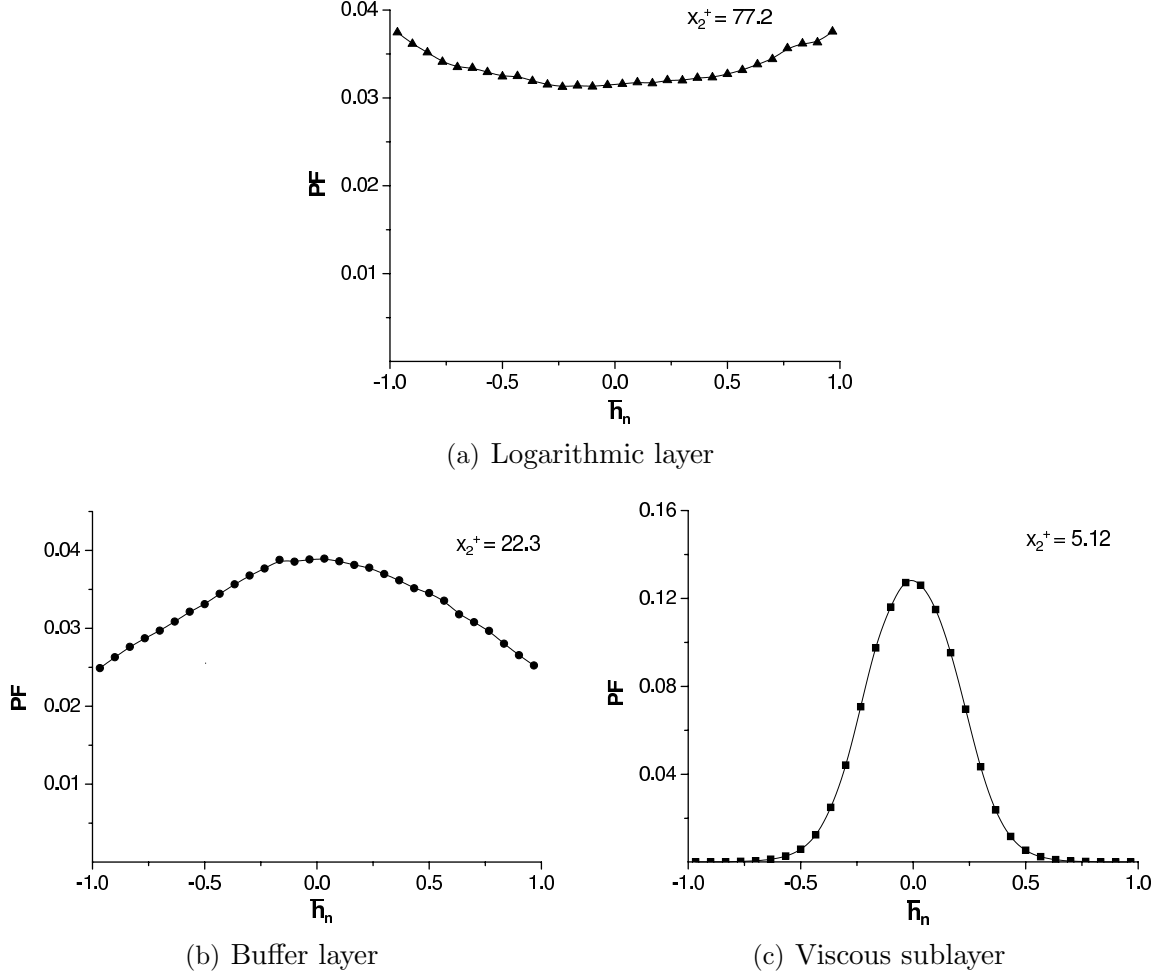


FIGURE 7.1: Time-averaged PF of resolved relative helicity density $\bar{h}_n = \cos(\bar{\mathbf{u}}, \bar{\boldsymbol{\omega}})$ ($Re = 2600$).

direction, while towards the center of the channel, the large scale vorticity tends to be convected by and aligned with the mean flow.

7.4.2 Results on Alignment between Vorticity and Eigenvectors

As reviewed earlier, the alignment pattern between the vorticity and the eigenvectors of the resolved strain rate tensor has become one of the canonical problems ever since the initial work of Kerr [54, 62] and Ashurst *et al.* [55] in the earlier 1980's. Tao *et*

al. [29, 99] first examined this alignment pattern in terms of large filtered motions using the LES approach. Their LES approach is *a priori* and based on analyzing HPIV measurements of a quasi-isotropic flow at the center of a square duct. In this subsection, this subject will be investigated via *a posteriori* LES predictions based on the proposed DNM. The relative orientation between the resolved vorticity vector and the eigenvectors of the negative SGS stress and the three constituent tensors will be explored. The anisotropic effect due to the presence of the wall will also be examined. As indicated previously, since an eigenvector by itself does not differentiate its direction, in presenting the statistical results, either the absolute cosine value or an angle interval of $[0^\circ, 90^\circ]$ is adopted.

Figures 7.2(a)–(d) present the plane and time averaged profiles of relative orientations between resolved vorticity $\bar{\omega}$, and the eigenvectors of the negative SGS stress and three constituent tensors. A general impression from all four diagrams is that the existence of the wall has a significant influence on the relative orientation. Also, it appears that the Reynolds number only slightly influences the profile in the buffer zone, and otherwise has no obvious effect. It is of interest to observe from Figs. 7.2(a)–(d) that the averaged angles between $\bar{\omega}$ and the eigenvectors of the negative SGS stress and all the three nonlinear constituent tensors are either parallel (0°) or perpendicular (90°) at the wall. From Fig. 7.2(a), it is observed that the averaged relative orientation between $\bar{\omega}$ and the most extensive eigenvector of $-\tau_{ij}$ shows a perpendicular pattern (90°) at the wall, becomes skewed as x_2^+ increases and finally levels off around 62° at the center of the channel for both Reynolds numbers tested. Similar relative orientation patterns are observed between $\bar{\omega}$ and the compressive eigenvector of $-\tau_{ij}$, except that the averaged core value for the latter is about 68° . The relative orientation between $\bar{\omega}$ and the intermediate eigenvector of $-\tau_{ij}$ exhibits a parallel pattern (0°) at the wall and reaches 42° in the core region for both Reynolds numbers. Figures 7.2(b) and (c) for the averaged relative orientations between $\bar{\omega}$ and the eigenvectors of the first and second constituent terms, i.e. β_{ij} (as well as \bar{S}_{ij}) and γ_{ij} , respectively, exhibit a similar behavior to that shown in Fig. 7.2(a). In Fig. 7.2(c), the overall characteristics of the eigenvectors corresponding to the largest

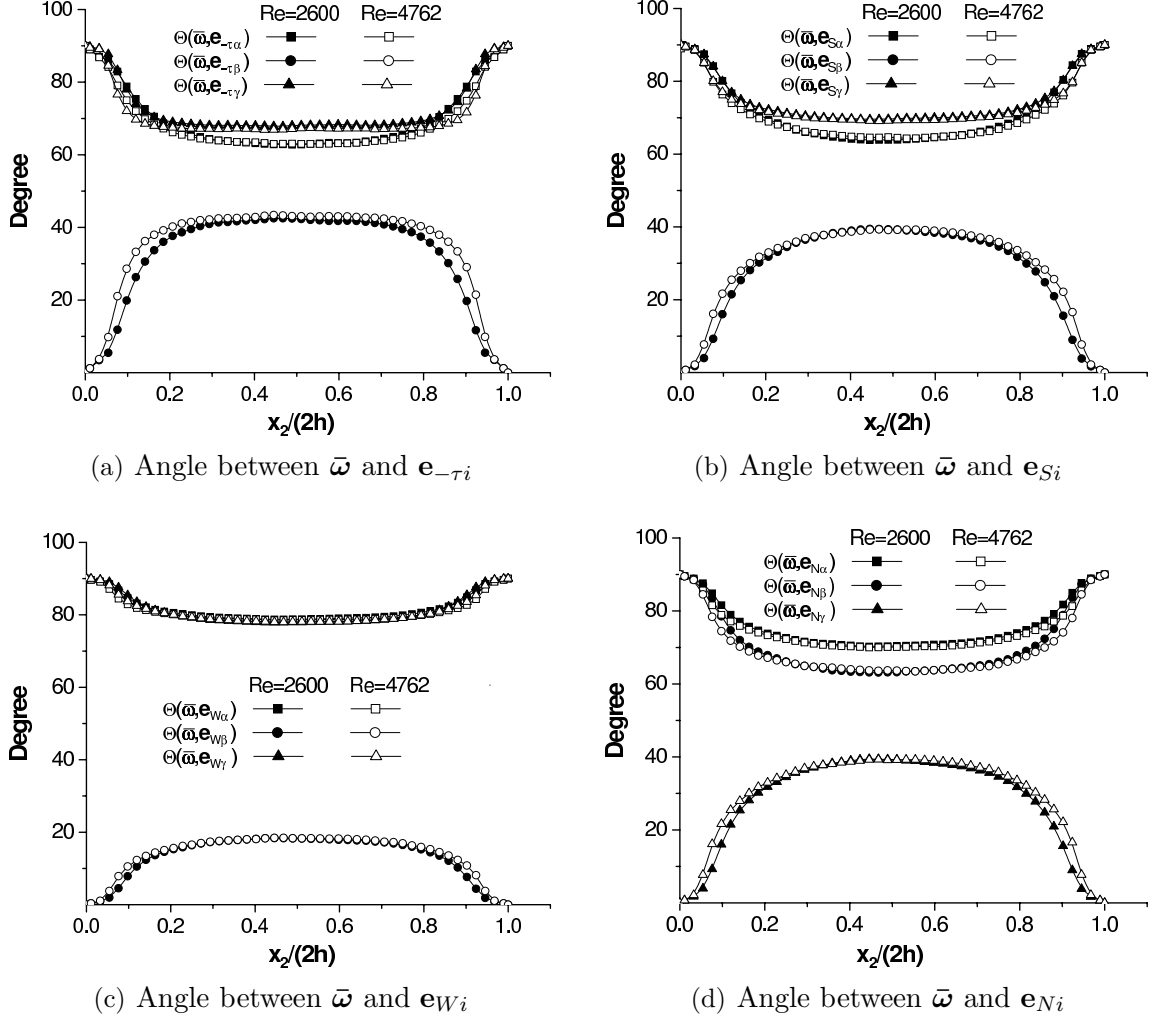


FIGURE 7.2: Averaged angle between the vorticity vector and eigenvectors.

and smallest eigenvalues of γ_{ij} are hardly distinguishable in terms of their averaged relative orientation with respect to $\bar{\omega}$.

The averaged relative alignment pattern between $\bar{\omega}$ and the eigenvectors of the third nonlinear constituent tensor η_{ij} shown in Fig. 7.2(d) are different than those shown in Figs. 7.2(a)–(c). The relative orientation between $\bar{\omega}$ and the largest eigenvector and that between $\bar{\omega}$ and the intermediate eigenvector exhibit a similar pattern, being perpendicular (90°) at the wall and skewed around 70° (corresponding to the largest eigenvector) and 63° (corresponding to the intermediate eigenvector) in the core region. The averaged alignment angle between $\bar{\omega}$ and the smallest eigenvector of η_{ij} is 0° at the wall, and rises to 40° in the center of the channel.

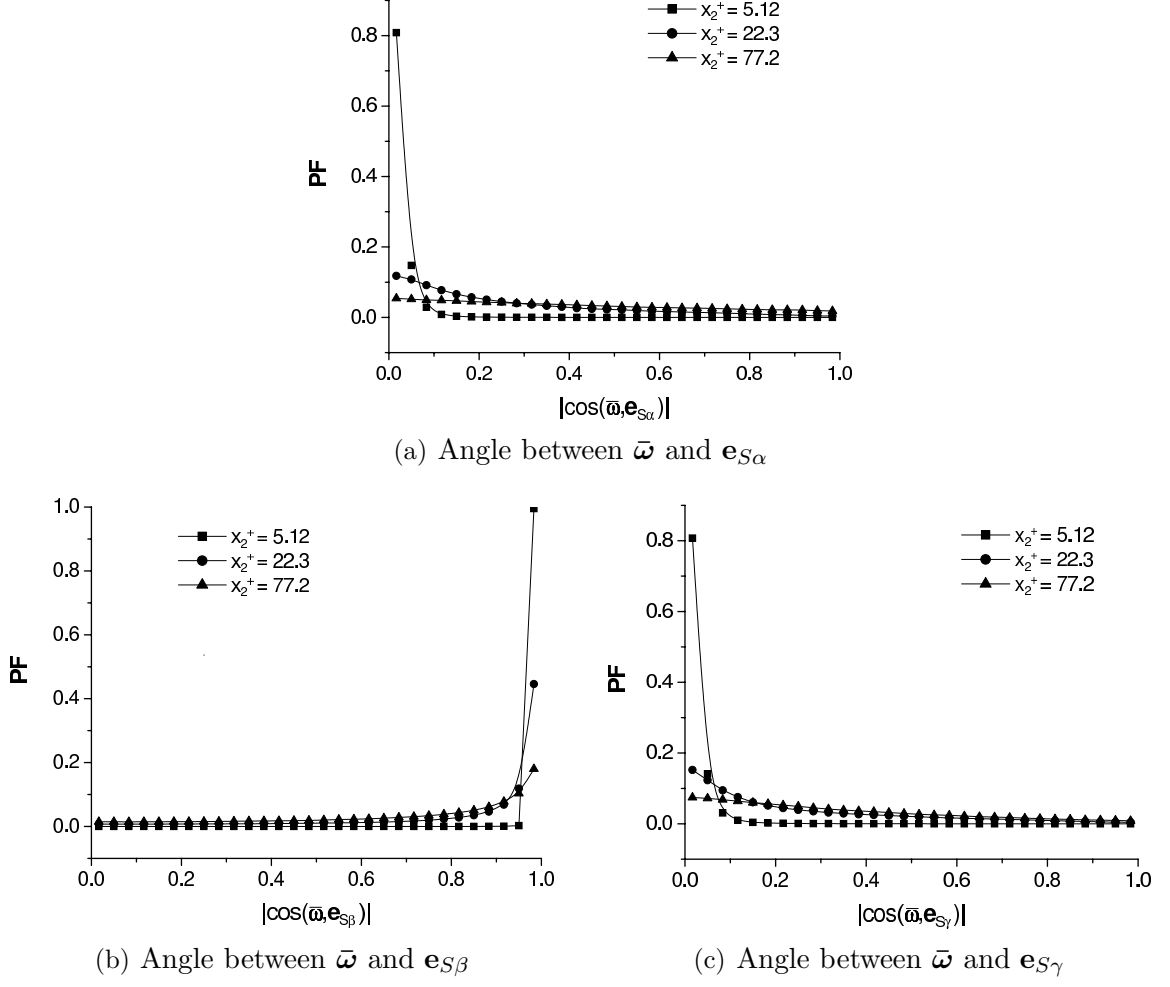


FIGURE 7.3: Time-averaged PF of the angle between the vorticity vector and the eigenvectors of filtered strain rate tensor ($Re = 2600$).

The above analysis of the angle between the resolved vorticity vector, and the eigenvectors of the negative SGS stress and three constituent tensors was based on plane and time averaged profiles. The following presents a refined analysis of these geometrical features based on probability functions. Figures 7.3(a)–(c) show the PF profiles of the absolute cosine value of the angle between $\bar{\omega}$ and the eigenvectors of \bar{S}_{ij} . Figure 7.3(a) indicates that the relative orientation between $\bar{\omega}$ and the most extensive eigenvector of \bar{S}_{ij} is the most probable for $|\cos(\bar{\omega}, \mathbf{e}_{S\alpha})| = 0$ (perpendicular pattern) for all three different flow regimes (sublayer, buffer zone and logarithmic region), regardless of differences in the PF levels. A similar alignment behavior is observed from Fig. 7.3(c) for the alignment between $\bar{\omega}$ and the most compressive eigenvector

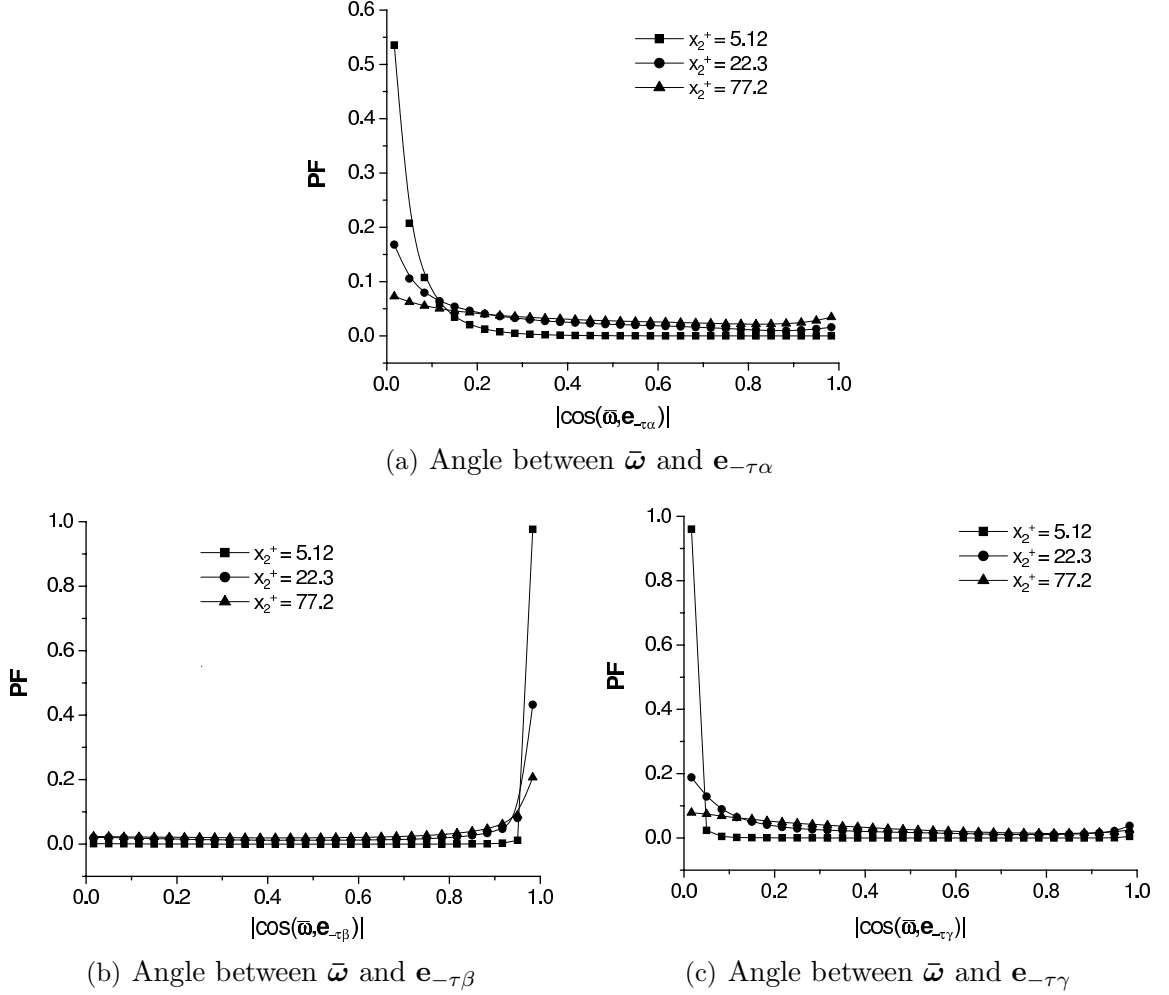


FIGURE 7.4: Time-averaged PF of the angle between the vorticity vector and eigenvectors of the negative SGS stress tensor ($Re = 2600$).

of \bar{S}_{ij} . However, in Fig. 7.3(b), it is observed that the relative orientation between $\bar{\omega}$ and the intermediate eigenvector of \bar{S}_{ij} is the most probable for $|\cos(\bar{\omega}, \mathbf{e}_{S\beta})| = 1$ (parallel). Therefore, it is concluded that $\bar{\omega}$ prefers to be aligned with $\mathbf{e}_{S\beta}$ while being perpendicular to $\mathbf{e}_{S\alpha}$ and $\mathbf{e}_{S\gamma}$. These phenomenological features are prototypical and consistent with other LES results [29, 99], DNS results [54, 55, 62, 73, 85] and experimental results [76, 77, 179]. In general, as shown in Fig. 7.3(a)–(c), the peak value of the PF corresponding to the most probable state increases drastically as x_2^+ decreases. This indicates that the alignment patterns identified above are actually more generic to the viscous sublayer rather than the logarithmic region, which agrees with the observation of Blackburn *et al.* [73].

Figures 7.4(a)–(c) illustrate the PF profiles of the relative alignment between $\bar{\omega}$ and the negative SGS stress. In general, the features shown in these figures are similar to those presented previously in Figs. 7.3(a)–(c). From the Figs. 7.4(a)–(c), it is observed that $\bar{\omega}$ prefers to be aligned with the intermediate eigenvector of $\mathbf{e}_{-\tau\beta}$, and perpendicular to the most extensive and compressive eigenvectors. The conclusion of $\bar{\omega}$ being perpendicular to $\mathbf{e}_{-\tau\gamma}$ is supported by the experimental results of Tao *et al.* [29, 99]. Tao *et al.* also indicated that there is no obvious preferred alignment pattern of $\bar{\omega}$ in the $(\mathbf{e}_{-\tau\alpha})$ – $(\mathbf{e}_{-\tau\beta})$ plane. However, according to the results presented in Figs. 7.4(a) and (b), it is found that $\bar{\omega}$ prefers to be aligned with $\mathbf{e}_{-\tau\beta}$ rather than $\mathbf{e}_{-\tau\alpha}$.

Since there are two degrees of freedom in determining an alignment pattern between two vectors, 2-D JPFs are advantageous for providing more insightful results. Figure 7.5 presents the time-averaged JPF contour for two angles formed by $\bar{\omega}$ and the intermediate and most compressive eigenvectors of the resolved strain rate tensor. It is very interesting to observe from both Fig. 7.5(a) and (b) that the JPF contour occupies only the upper-right triangular statistical domain, i.e.

$$90^\circ \leq \Theta(\bar{\omega}, \mathbf{e}_{S\beta}) + \Theta(\bar{\omega}, \mathbf{e}_{S\gamma}) \quad (7.9)$$

The straight line that separates the trivial and nontrivial JPF values in Fig. 7.5(b) corresponds to the equal sign in the above relation, and is hereby referred to as a “*natural bound*” due to the fact that such a pattern is not unique to the JPF contour being discussed, but instead a common feature of the relative orientation between a vector and an orthonormal triad. Figure 7.6 illustrates the geometry between an arbitrary vector ω and an arbitrary orthonormal triad $[\mathbf{e}_1, \mathbf{e}_2, \mathbf{e}_3]$. The *sides* of the spherical triangle shown in the figure are represented by A , B and C . From spherical trigonometry [189], it is known that $A + B + C \leq 360^\circ$, $A + B \geq C$ and $|A - B| \leq C$; whence if $C = 90^\circ$, the parameters A and B form the following “diamond-shape”

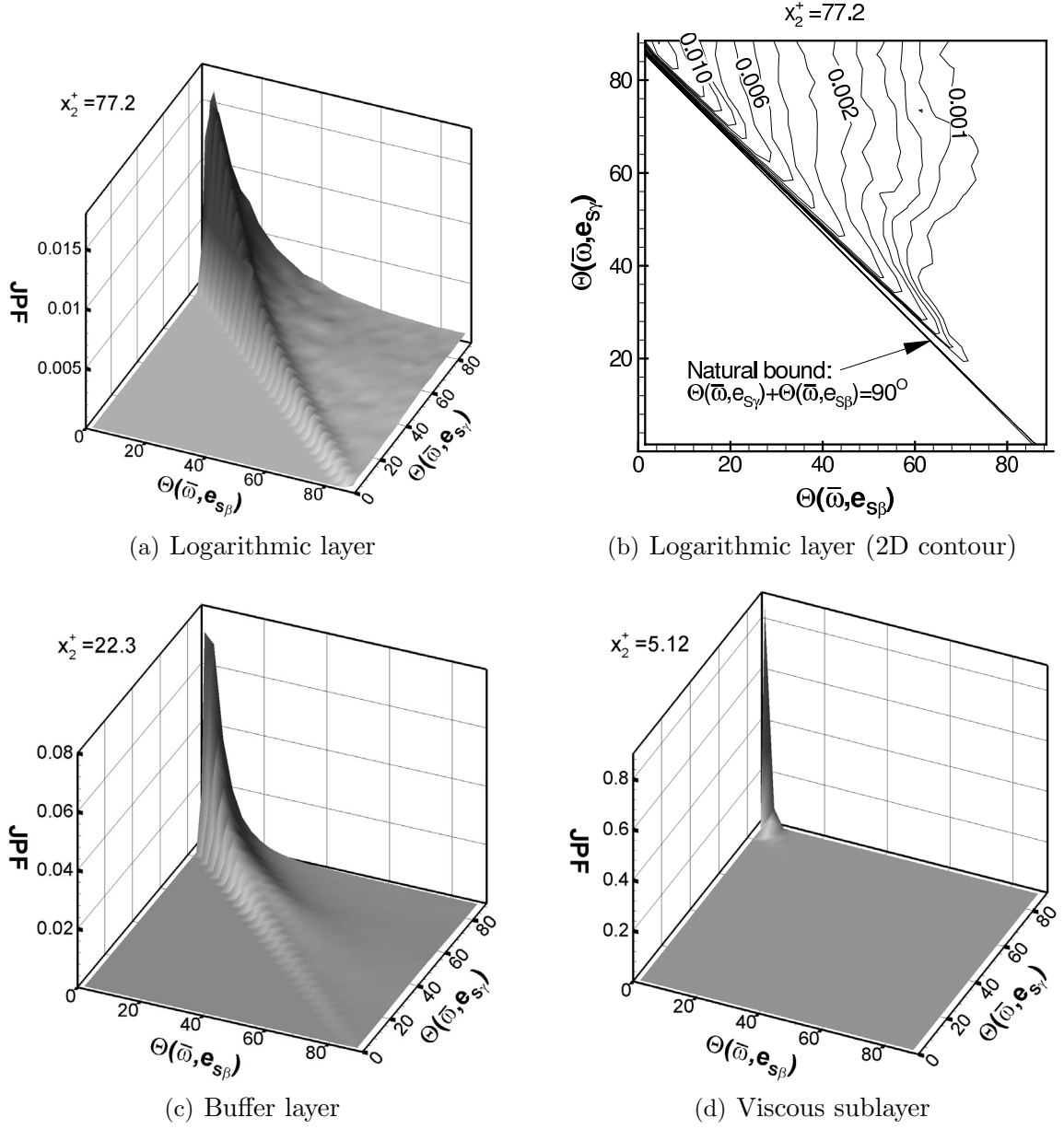


FIGURE 7.5: Time-averaged JPF between the $\Theta(\bar{\omega}, \mathbf{e}_{S\beta})$ and $\Theta(\bar{\omega}, \mathbf{e}_{S\gamma})$ ($Re = 2600$).

domain bounded by four straight lines (four “natural bounds”):

$$\begin{cases} 90^\circ \leq A + B \leq 270^\circ \\ -90^\circ \leq A - B \leq 90^\circ \end{cases} \quad (7.10)$$

The previous inequality (7.9) is included in the first of the above two general relations, and the triangular domain shown in Fig. 7.5(b) is only a quarter of this

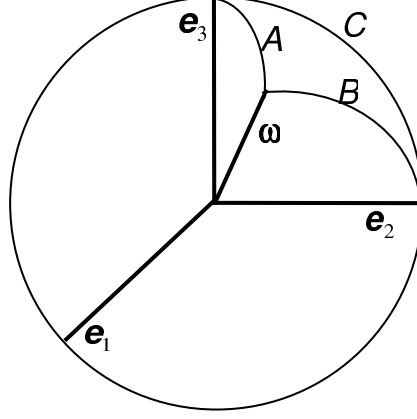


FIGURE 7.6: The spherical triangle related to a vector and an orthonormal triad.

general diamond-shape domain due to the restriction of $[0, 90^\circ]$ adopted in the statistical approach. It should be indicated that the line representing the “natural bound” in Fig. 7.5(b) is in fact not exactly the line: $\Theta(\bar{\omega}, \mathbf{e}_{S\beta}) + \Theta(\bar{\omega}, \mathbf{e}_{S\gamma}) = 90^\circ$, but instead the contour line corresponding to the lowest PF value. Theoretically speaking, no states should be shown in the right-left lower triangular region (corresponding to $\Theta(\bar{\omega}, \mathbf{e}_{S\beta}) + \Theta(\bar{\omega}, \mathbf{e}_{S\gamma}) < 90^\circ$), however, an uncertainty of $\pm 1.5^\circ$ is inevitable in the statistics due to the limited number of 30×30 bins adopted, and the smoothing (interpolating) property of the software package which also contributes to the error in graphic visualization.

From Fig. 7.5(a), it is observed that in the logarithmic core layer, the most jointly probable state corresponds to $\Theta(\bar{\omega}, \mathbf{e}_{S\beta}) = 0^\circ$ and $\Theta(\bar{\omega}, \mathbf{e}_{S\gamma}) = 90^\circ$. This indicates that the resolved vorticity vector is preferably aligned with the intermediate eigenvector, while being perpendicular to the most compressive eigenvector of the filtered strain rate tensor. Further, since there are only two degrees of freedom, the most probable alignment between the resolved vorticity and the most extensive eigenvector of \bar{S}_{ij} can only be perpendicular. Figure 7.5(c) shows that in the buffer zone, the strength of JPF peak increases, indicating a much stronger pattern of $\bar{\omega}$ being parallel to $\mathbf{e}_{S\beta}$ and perpendicular to $\mathbf{e}_{S\gamma}$. Finally, Fig. 7.5(d) demonstrates that in the viscous sublayer, the PF peak becomes very intense, indicating that such an alignment feature, i.e. $\Theta(\bar{\omega}, \mathbf{e}_{S\beta}) = 0^\circ$ and $\Theta(\bar{\omega}, \mathbf{e}_{S\gamma}) = 90^\circ$, is not confined to

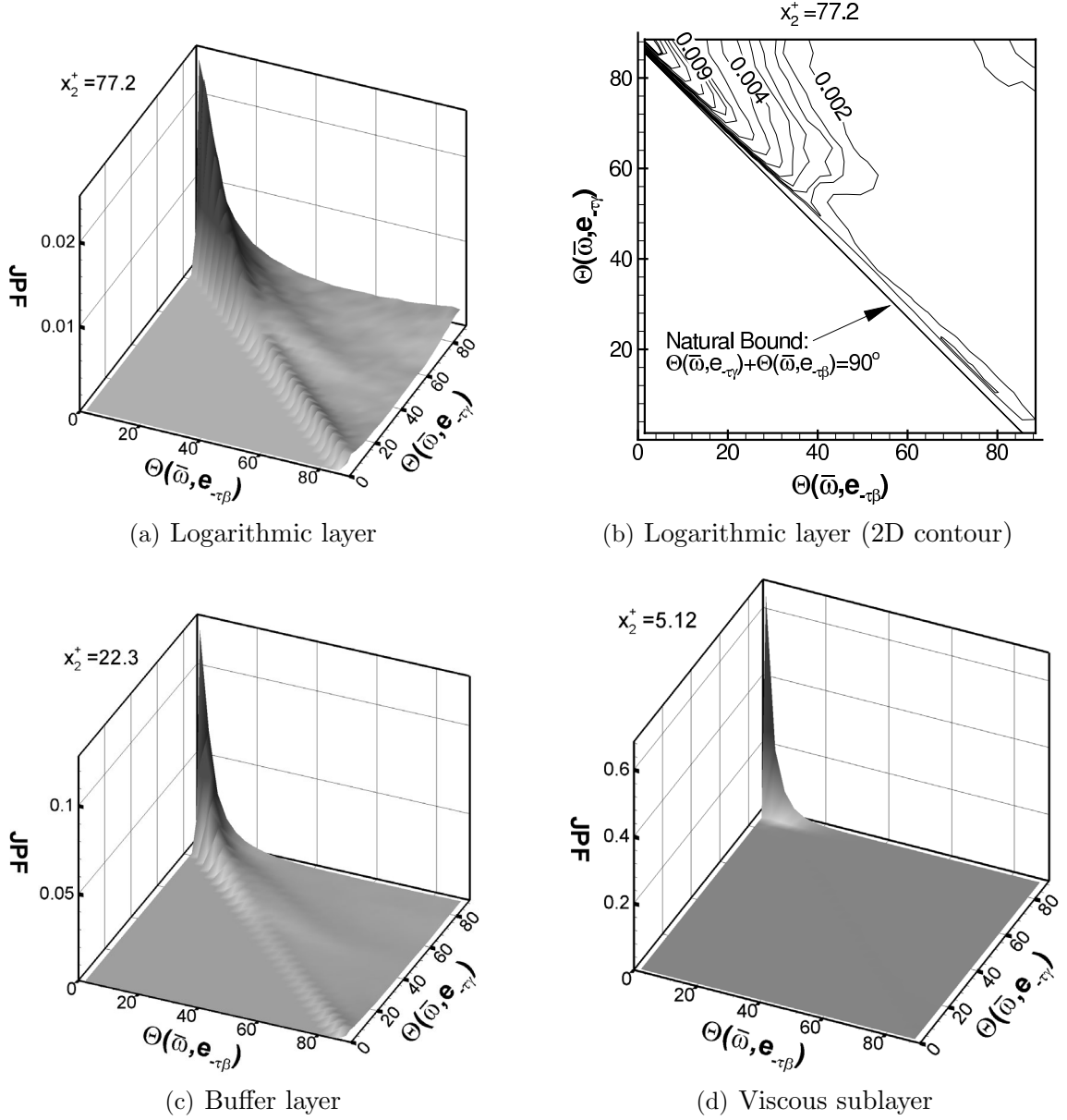


FIGURE 7.7: Time-averaged JPF between $\Theta(\bar{\omega}, \mathbf{e}_{-\tau\beta})$ and $\Theta(\bar{\omega}, \mathbf{e}_{-\tau\gamma})$ ($Re = 2600$).

the buffer and logarithmic layers, nor is such an alignment pattern a unique feature for (quasi-)isotropic turbulence as it is popularly claimed [29, 54, 55, 62, 71, 85, 90, 99]. Instead, it is argued in this thesis that such an alignment pattern is much more generic to the viscous sublayer.

Figures 7.7(a)–(d) demonstrate the relative orientation between $\bar{\omega}$ and the eigenvectors of the negative SGS stress. The characteristics shown in these fig-

ures are very similar to those in Figs. 7.5(a)–(d) which describe the relative orientation between $\bar{\omega}$ and the eigenvectors of the resolved strain rate tensor. In general, $\Theta(\bar{\omega}, \mathbf{e}_{-\tau\beta}) = 0^\circ$ and $\Theta(\bar{\omega}, \mathbf{e}_{-\tau\gamma}) = 90^\circ$ is the most probable state for all three flow regimes, i.e. viscous sublayer, buffer zone and logarithmic region, which indicates a prevalent alignment pattern that $\bar{\omega}$ is parallel to $\mathbf{e}_{-\tau\beta}$ and perpendicular to $\mathbf{e}_{-\tau\alpha}$ and $\mathbf{e}_{-\tau\gamma}$ across the entire channel. This preferred alignment pattern becomes stronger as x_2^+ decreases. Figures 7.7(a) shows that at the central layer of the channel where the flow is close to isotropic, the magnitude of the JPF peak is weaker than those in the buffer zone and sublayer, and the distribution of the JPF contour is more spread out. This indicates that besides the most probable state of $\bar{\omega}$ being aligned with $\mathbf{e}_{-\tau\beta}$, there is a considerable fraction of the vorticity being aligned at other angles in the $(\mathbf{e}_{-\tau\alpha})$ – $(\mathbf{e}_{-\tau\beta})$ plane (consider the restriction $\cos^2 \Theta(\bar{\omega}, \mathbf{e}_{-\tau\alpha}) + \cos^2 \Theta(\bar{\omega}, \mathbf{e}_{-\tau\beta}) + \cos^2 \Theta(\bar{\omega}, \mathbf{e}_{-\tau\gamma}) \equiv 1$). Similar results were reported by Tao *et al.* [29, 99] based on analyzing HPIV data of quasi-isotropic turbulence.

7.4.3 Results on Enstrophy and Enstrophy Generation

It is controversial whether concentrated vorticity has any significant influence on the overall behavior of turbulent flows. According to recent studies by Jiménez *et al.* [92] and Tsinober *et al.* [77, 78], the concentrated vorticity seems to be merely “a consequence rather than the dominating factor” of turbulence. Fluid quantities which closely relate to concentrated vorticity include the enstrophy ω^2 , vortex stretching vector \mathbf{w} and enstrophy generation σ . In their work [77, 78], Tsinober *et al.* proposed and explored several critical issues, e.g. (1) whether QTD turbulence can be treated as pure 2-D turbulence, and (2) whether the background turbulence (a flow regime with weak excitations, e.g. $\omega^2 \rightarrow 0$) is purely a “random sea” without any structures as was thought previously. These topics remain very attractive to the fluids community, since they relate to the statistical features and topologies of turbulence. In this subsection, the author presents some preliminary results related to these topics. However, in contrast to previous approaches based on DNS and experimental data analyses by

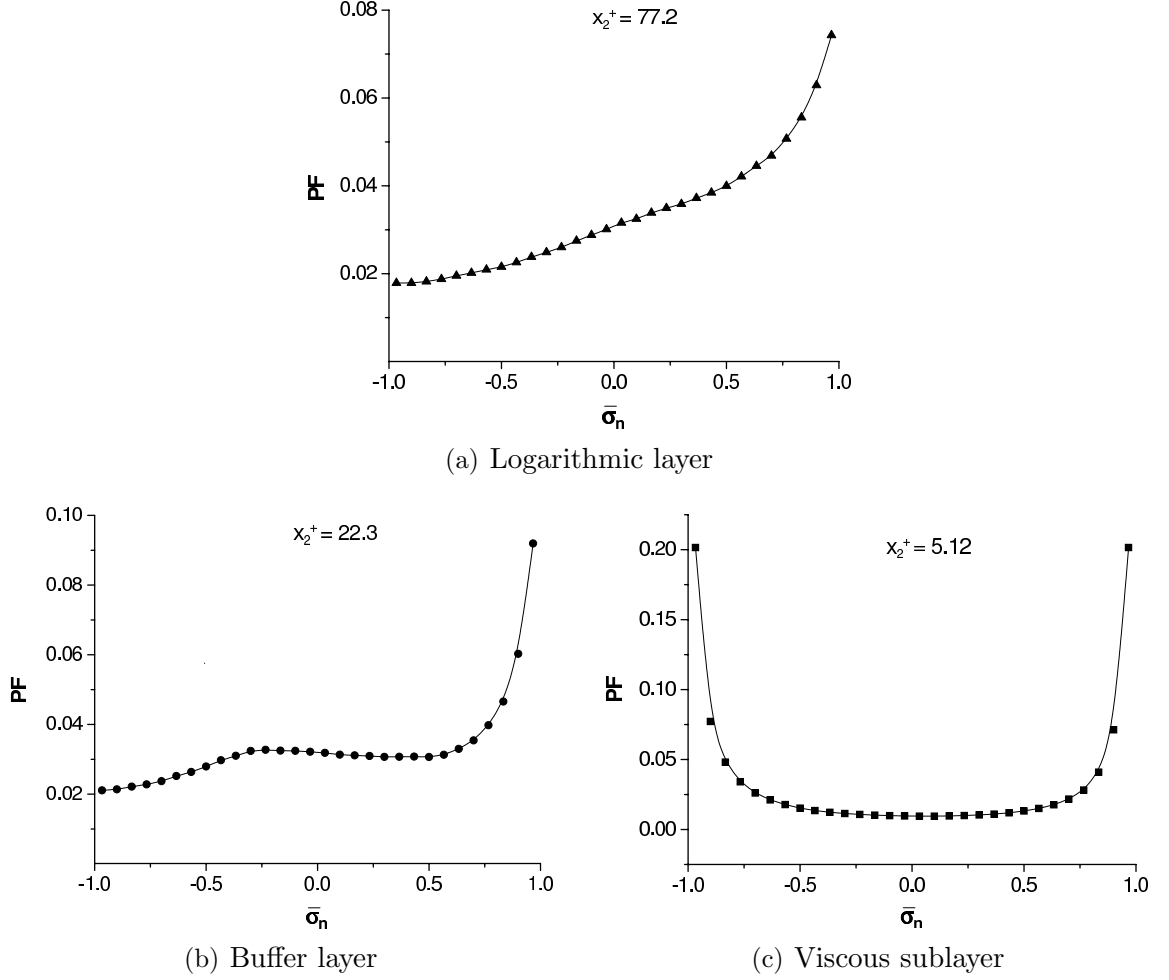


FIGURE 7.8: Time-averaged PF of the resolved normalized enstrophy generation $\bar{\sigma}_n = \cos(\bar{\omega}, \bar{\mathbf{w}})$ ($Re = 2600$).

other researchers [76–78, 89, 90, 92, 95], the results to be presented in the following context are based on the resolved large-scale motions calculated using the proposed DNM.

Figure 7.8 illustrates the PF profile of the normalized resolved enstrophy generation $\bar{\sigma}_n$. From Figs. 7.8(a) and (b), it is evident that in both the buffer and logarithmic regions, there is a strong alignment between the resolved vorticity and vortex stretching vectors suggesting a dominant local vortex stretching ($\bar{\omega} \cdot \bar{\mathbf{w}} > 0$) flow configuration, and closely related to this, the essential feature of positively skewed enstrophy generation for turbulence that has already been well documented in other works based on DNS and experimental approaches [76–78, 89, 92–94]. However, in the

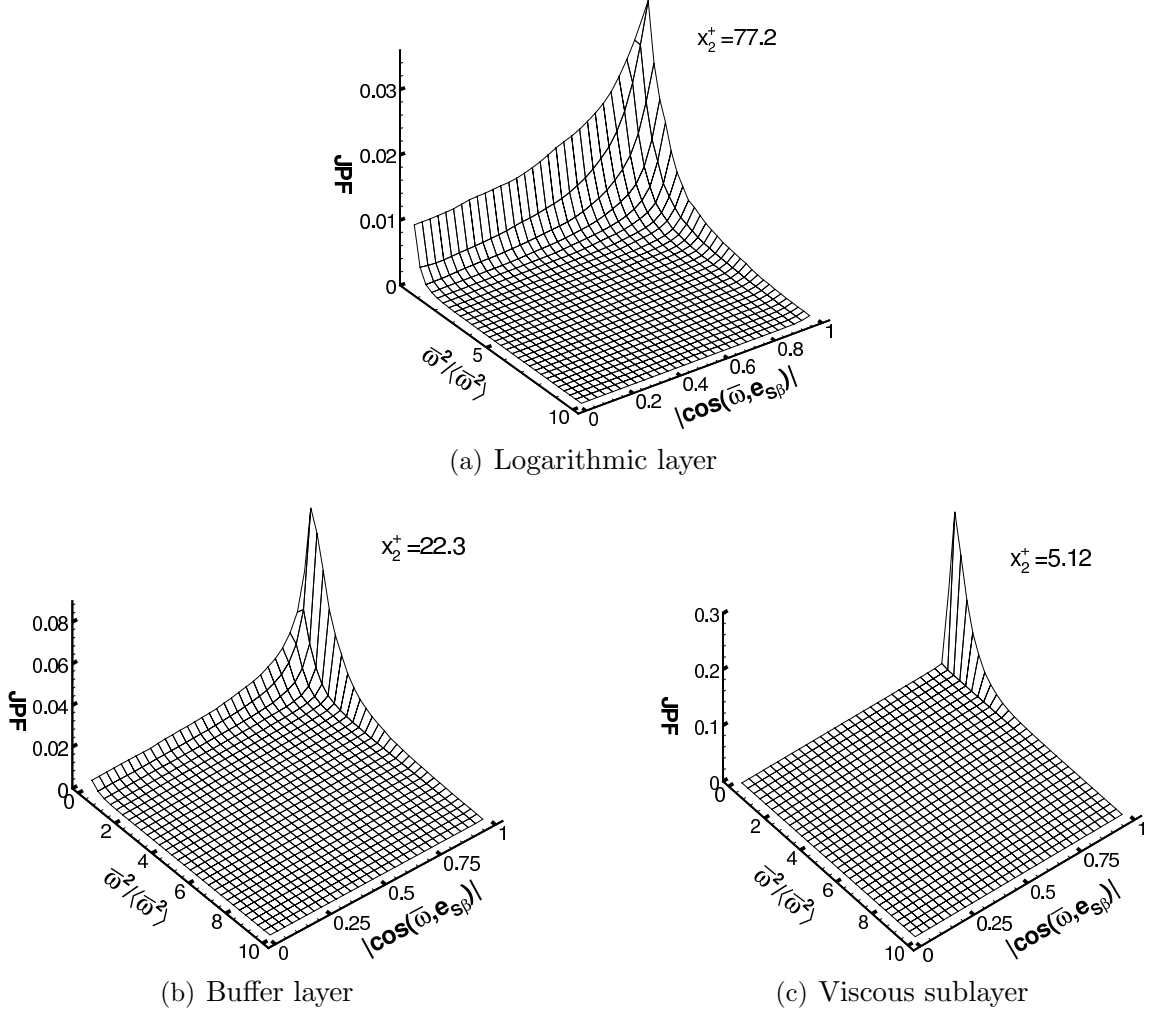


FIGURE 7.9: Time-averaged JPF between $\bar{\omega}^2/\langle\bar{\omega}^2\rangle$ and $|\cos(\bar{\omega}, \mathbf{e}_{S\beta})|$ ($Re = 2600$).

viscous sublayer, as shown in Fig. 7.8(c), both local vortex stretching and compressing ($\bar{\omega} \cdot \bar{\mathbf{w}} < 0$) configurations are highly probable as indicated by the two strong PF peaks observed at $\bar{\sigma}_n = \pm 1$. Such a symmetric pattern for the $\bar{\sigma}_n$ distribution was also observed by Chong *et al.* [67], who pointed out that there are as many vortex stretching states as vortex compressing states in the viscous sublayer.

Figures 7.9(a)–(c) show the JPF profile between the normalized enstrophy $\bar{\omega}^2/\langle\bar{\omega}^2\rangle$ and $|\cos(\bar{\omega}, \mathbf{e}_{S\beta})|$. Here $\langle\bar{\omega}^2\rangle$ represents the plane and time averaged resolved enstrophy. From the figure, it is evident that the alignment between $\bar{\omega}$ and the intermediate eigenvector of the filtered strain rate tensor, i.e. $\mathbf{e}_{S\beta}$, becomes strongest when $\bar{\omega}^2/\langle\bar{\omega}^2\rangle$ is small for all three flow regimes, i.e. the viscous sublayer, buffer

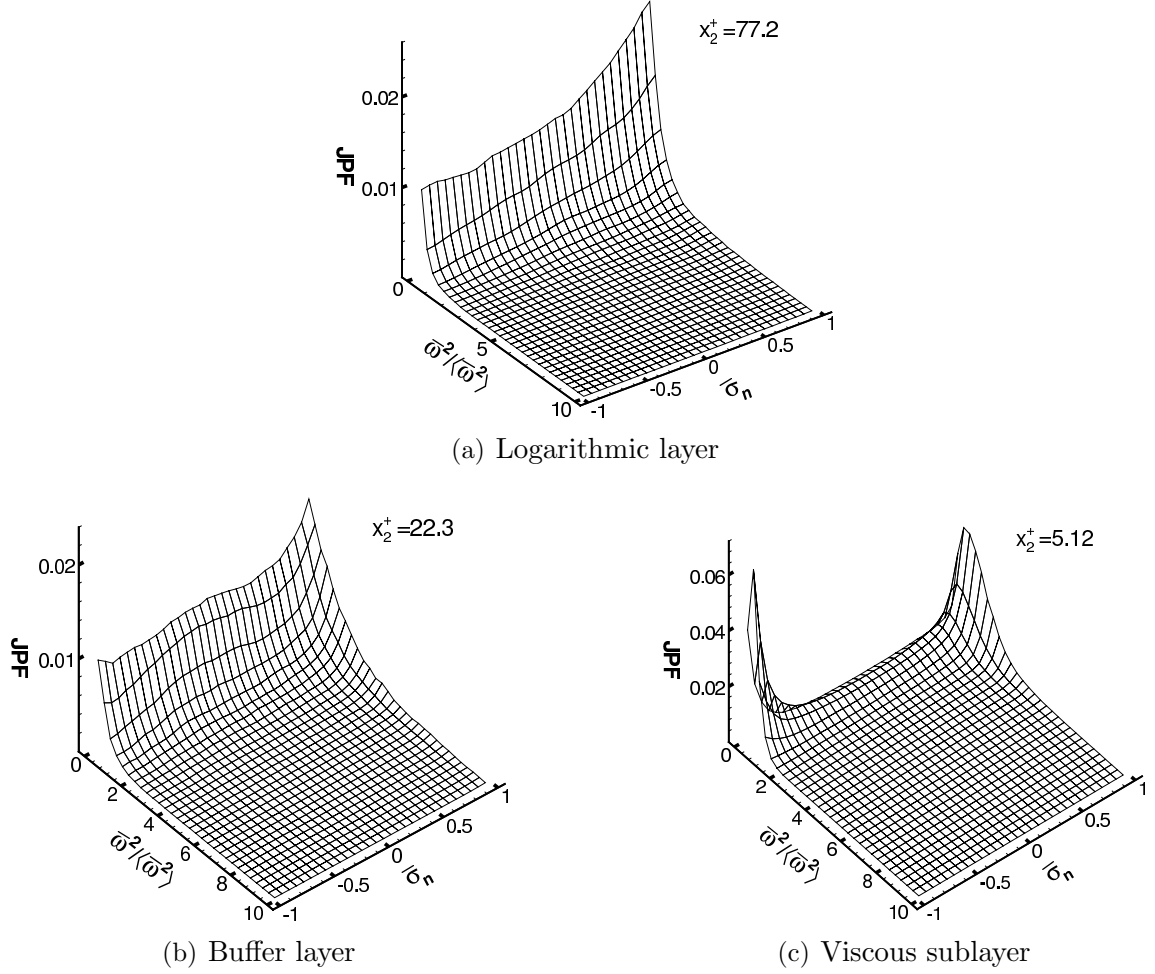


FIGURE 7.10: Time-averaged JPF between $\bar{\omega}^2/\langle\bar{\omega}^2\rangle$ and $\bar{\sigma}_n = \cos(\bar{\omega}, \bar{\mathbf{w}})$ ($Re = 2600$).

zone and logarithmic region. It is observed that the peak value of the JPF increases drastically as x_2^+ decreases and reaches its largest value in the sublayer. The pattern shown in Fig. 7.9(a) for the logarithmic layer is in good agreement with the result reported by Tsinober *et al.* [77, 78], who analyzed quasi-isotropic turbulence based on DNS as well as experimental measurements.

Figures 7.10(a)–(c) show the JPF between the normalized resolved enstrophy $\bar{\omega}^2/\langle\bar{\omega}^2\rangle$ and enstrophy generation $\bar{\sigma}_n$. From all three figures, it is generally observed that the strongest alignment between the resolved vorticity and vortex stretching vectors is related to the weakest resolved enstrophy. For the logarithmic and buffer regions, the state of vortex stretching flow configuration ($\bar{\sigma}_n > 0$) dominates any

other possible states. The major features indicated in Fig. 7.10(a) are consistent with the reported results of Tsinober *et al.* [77, 78], i.e. the most jointly probable state is $\bar{\omega}^2/\langle\bar{\omega}^2\rangle \rightarrow 0$ and $\bar{\sigma}_n \rightarrow 1$ in the quasi-isotropic flow regime. For the viscous sublayer, two most probable states are observed, i.e. both vortex stretching and vortex compressing flow configurations prevail. This observation is consistent with the previous result based on the 1-D PF as shown in Fig. 7.8(c).

From the previous discussion, it is known that the most probable state of alignment between $\bar{\omega}$ and the resolved vortex stretching vector $\bar{\mathbf{w}}$ corresponds to a positively skewed resolved enstrophy generation $\bar{\sigma}$. This has been demonstrated by a few studies, including the current one, to be a generic characteristic of turbulent flows. It is also known that for pure 2-D incompressible turbulent flows, $\bar{\sigma} \equiv 0$. Therefore, from Eq.(7.4), an overall positive value of $\bar{\sigma}$ implies two properties: (i) turbulence must not entirely be 2-D, and (ii) $\bar{\sigma}_\alpha$ based on the alignment between $\bar{\omega}$ and the most extensive eigenvector $\mathbf{e}_{S\alpha}$ should not be trivial. However, on the other hand, a QTD state of turbulence ($|\beta_S| < |\alpha_S|$, $|\beta_S| < |\gamma_S|$ and $\bar{\omega}$ being aligned with $\mathbf{e}_{S\beta}$) has also been observed as the most probable state for (quasi-)isotropic turbulence. As such, a “contradiction” appears. This relates to the first question listed at the beginning of the subsection. Tsinober *et al.* [77, 78] extensively investigated this problem. They indicated that most of the enstrophy generation is related to $\bar{\sigma}_\alpha$, and in fact a state of $\bar{\sigma}_\alpha > \bar{\sigma}_\beta$ and an alignment between $\bar{\omega}$ and $\mathbf{e}_{S\alpha}$ do exist. The latter has also been confirmed by this research. As shown in Fig. 7.5(a) for the core region, apart from the largest JPF peak corresponding to the most probable state that resolved vorticity is aligned with the intermediate eigenvector of \bar{S}_{ij} , the JPF values corresponding to all other states of alignments are obviously not trivial. Also from both Figs. 7.8(a) and 7.9(a), the strength of the JPF peak for the logarithmic region is much weaker than that for the viscous layer, and other states including vortex stretching do exist albeit with a lower probability. She *et al.* [90] and Tsinober *et al.* [77, 78] further indicated that a probable state of the vorticity vector being aligned with the intermediate eigenvector of the strain rate tensor tends to relate to a non-vanishing value of β_S and thus $\bar{\sigma}_\beta$ is not necessarily zero. This can be readily understood since nei-

ther of the following two frequently reported “most probable” eigenvalue ratios, i.e. $\alpha_S : \beta_S : \gamma_S = 1 : 1 : -2$ (corresponding to axisymmetric expansion) [29, 59] and $\alpha_S : \beta_S : \gamma_S = 3 : 1 : -4$ [55, 62, 76], suggests that $\beta_S = 0$ is highly probable. In this sense, the local QTD state of turbulence is qualitatively different from purely 2-D turbulence in that it possesses essential non-vanishing enstrophy generation and a finite intermediate eigenvalue of the (filtered) strain rate tensor.

Now, it is appropriate to return to the second question of Tsinober *et al.* [77, 78] listed at the beginning of this subsection. It is still commonly thought that the structure of turbulence is related to strong local excitations, such as intense concentrated vorticity [77]. The background of a turbulent field apart from these strong local events is considered to be Gaussian [77, 90, 92, 95], and for a Gaussian field $\langle \bar{\sigma} \rangle \equiv 0$ [76]. As discussed above, the alignment between $\bar{\omega}$ and $\mathbf{e}_{S\beta}$ (related to a local QTD state) and that between $\bar{\omega}$ and $\bar{\mathbf{w}}$ (related to a local vortex stretching pattern) both become highly probable when the local excitation of resolved vorticity is the weakest. As concluded by Tsinober *et al.* [77, 78], this implies that the background turbulence is not *locally* a structureless random sea; instead, various intense local structure patterns exist in all regions with or without high excitation of a specific quantity. Although the results presented in this section are based on the large resolved scale of motions, they support these comments, which in turn indicates that the proposed DNM performs well in terms of the prediction of these turbulence geometrical characteristics at the resolved scales.

7.5 Numerical Results on the Relative Principal Values

In this section, statistical results on the relative eigenvalues based on the time-plane averaging method, as well as the three probability functions, s^* -PF, β^* -PF and (β/α) -PF are presented. Figures 7.11(a)–(d) illustrate the plane and time averaged profiles of the relative principal values of the negative SGS stress and three constituent ten-

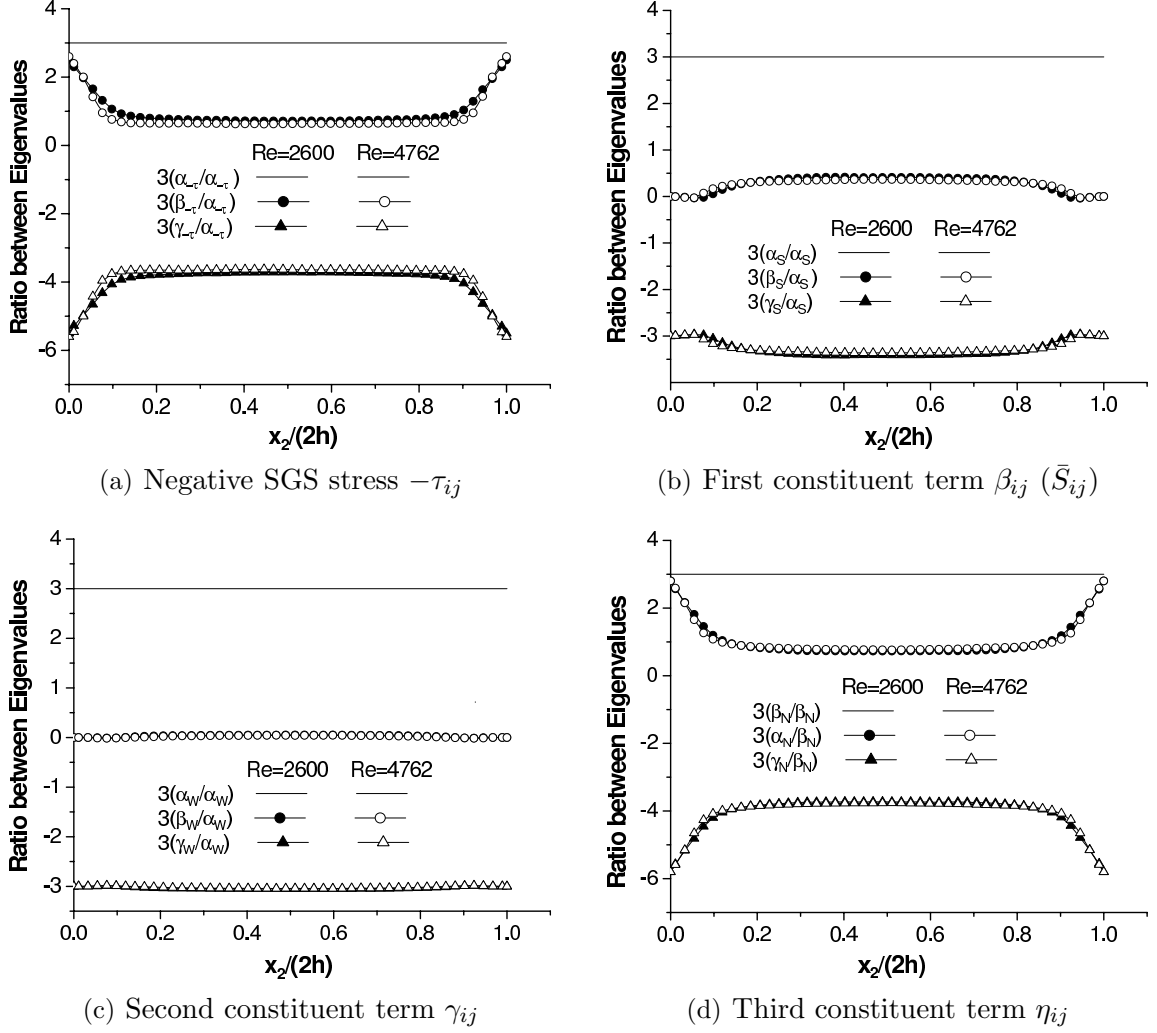


FIGURE 7.11: Averaged ratio between the eigenvalues of the negative SGS stress and three constituent tensors.

sors. Following convention, all the profiles presented in these four figures have been amplified by a factor of 3. In general, no obvious Reynolds number effect is observed in the figures. Figure 7.11(a) shows that the averaged ratio of the eigenvalues of the negative SGS stress $-\tau_{ij}$ is rather ‘flat’ around $\alpha_{-\tau} : \beta_{-\tau} : \gamma_{-\tau} = 3 : 0.8 : -3.8$ in the core region, and changes to $3 : 2.5 : -5.5$ at the wall for both Reynolds numbers tested. The locations for transition from the boundary to the flat core values are at about $x_2/(2h) \approx 0.12$ and 0.88 which corresponds to $x_2^+ = 25 \sim 30$. Figure 7.11(b) indicates that the averaged ratio of the eigenvalues of the filtered strain rate tensor (as well as for the first constituent term β_{ij}) is close to $\alpha_S : \beta_S : \gamma_S = 3 : 0.4 : -3.4$ in

the core region, and changes to $3 : 0 : -3$ (or $1 : 0 : -1$) at the wall which precisely reflects the 2-D nature of the near-wall flow. Figure 7.11(c) shows that the averaged ratio of the eigenvalues of the second nonlinear constituent tensor γ_{ij} is approximately $\alpha_W : \beta_W : \gamma_W = 3 : 0 : -3$. Finally, Fig. 7.11(d), which is similar to Fig. 7.11(a), indicates an averaged eigenvalue ratio of $\alpha_N : \beta_N : \gamma_N = 3 : 0.8 : -3.8$ in the core region and $3 : 2.8 : -5.8$ at the wall.

Figures 7.12, 7.13 and 7.14 illustrate 1-D PFs of the eigenvalue ratio of the filtered strain rate tensor \bar{S}_{ij} , i.e. s^* -PF, β^* -PF and (β/α) -PF, respectively. A general impression from all these figures is that there is an obvious “*viscous-shift*” of the most probable state as the wall is approached, i.e. the value of s^* , β^* or β/α corresponding to the most probable state decreases as x_2^+ decreases. Such a shift reflects the anisotropic effect due to the presence of the wall^a.

The β^* -PF profile illustrated in Fig. 7.12 shows that the most probable states are 0.41, 0.16 and 0.04 for the logarithmic region, buffer zone and viscous sublayer, respectively. These numbers correspond to relative eigenvalue ratios of $\alpha_S : \beta_S : \gamma_S = 3.6 : 1 : -4.6$ for $x_2^+ = 77.2$, $10 : 1 : -11$ for $x_2^+ = 22.3$ and $42 : 1 : -43$ for $x_2^+ = 5.12$. A most probable value of $\beta^* = 0.41$ matches very well with the experimental result reported by Tsinober *et al.* [76], and the corresponding ratio of $3.6 : 1 : -4.6$ is close to the classical one of $3 : 1 : -4$ ($\beta^* = 0.48$). The ratios $10 : 1 : -11$ and $42 : 1 : -43$ correspond to the singular situation when β_S is small, and as discussed earlier in subsection 7.3.2, both should be interpreted as an approximate 2-D state of $1 : 0 : -1$. Figure 7.13 indicates the most probable states are $\beta_S/\alpha_S = 0.15$, 0.08 and 0.03 for the logarithmic region, buffer zone and viscous sublayer, respectively, which correspond to eigenvalue ratios of $\alpha_S : \beta_S : \gamma_S = 6.6 : 1 : -7.6$, $14.3 : 1 : -15.3$ and $30 : 1 : -31$, respectively. Again since the value of β_S/α_S is very small in the buffer zone and viscous sublayer, the calculation procedure becomes unstable.

As noted previously, according to Lund *et al.* [59], both the β^* -PF and (β/α) -

^aA similar shifting behavior has been observed by some other researchers, e.g. She *et al.* [90] and Lund *et al.* [59]. However, those studies were based on isotropic turbulence, and the shift is due to the level of resolved TKE dissipation rate [59] (or simply $S_{ij}S_{ij}$ [90]) rather than wall anisotropy related to x_2^+ .

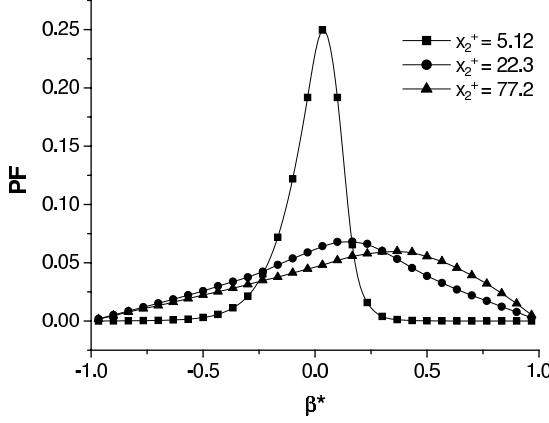


FIGURE 7.12: Time-averaged β^* -PF for the eigenvalue ratio of \bar{S}_{ij} ($Re = 2600$).

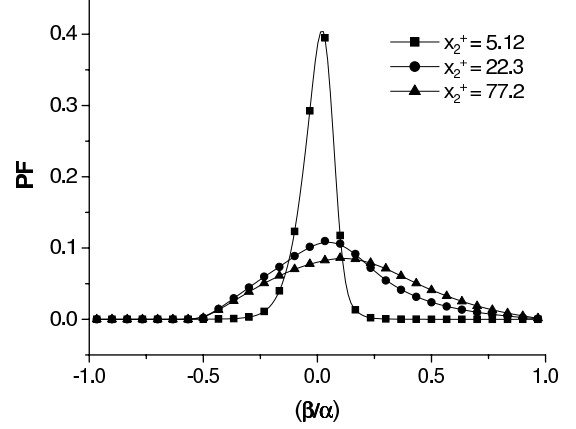


FIGURE 7.13: Time-averaged (β/α) -PF for the eigenvalue ratio of \bar{S}_{ij} ($Re = 2600$).

PF tail off at the two boundaries of the statistical interval and thus fail to predict the axisymmetric expansion ($\alpha_S : \beta_S : \gamma_S = 1 : 1 : -2$ and $s^* = 1$) flow configuration, which is actually regarded to be the most probable state for isotropic turbulence [29, 59, 64, 73, 88]. The results presented in Figures 7.14(a)–(c) are based on the s^* -PF. As shown in Fig. 7.14(a), the most probable value of $s^* = 0.9$ reported by Lund *et al.* [59] via analysis of DNS database has been reproduced in the core region at the filtered scale of motions. This indicates that a state of (quasi) axisymmetric expansion is the most probable in the core region. Figures 7.14(b) and (c) show a strong effect of a viscous-shift as x_2^+ decreases in comparison with Fig. 7.14(a). The most probable values in Figs. 7.14(b) and (c) are $s^* = 0.3$ (corresponding to $8 : 1 : -9$) and $s^* = 0.07$ (corresponding to $37 : 1 : -38$), respectively. Once again, a state of $s^* = 0.07 \rightarrow 0$ for the sublayer should be considered as singular, and the ratio $37 : 1 : -38$ should be interpreted approximately as $1 : 0 : -1$ reflecting the 2-D nature of the near-wall flow.

The 1-D PFs such as β^* -PF, s^* -PF and (β/α) -PF are appropriate for studying the relative eigenvalue ratio for the filtered strain rate tensor, since there are two constraints for the system of three independent parameters, i.e. the definition of the statistical quantity itself and the continuity condition that $\alpha_S + \beta_S + \gamma_S \equiv 0$ for incompressible flow. However, for the eigenvalue of the SGS stress, there is no

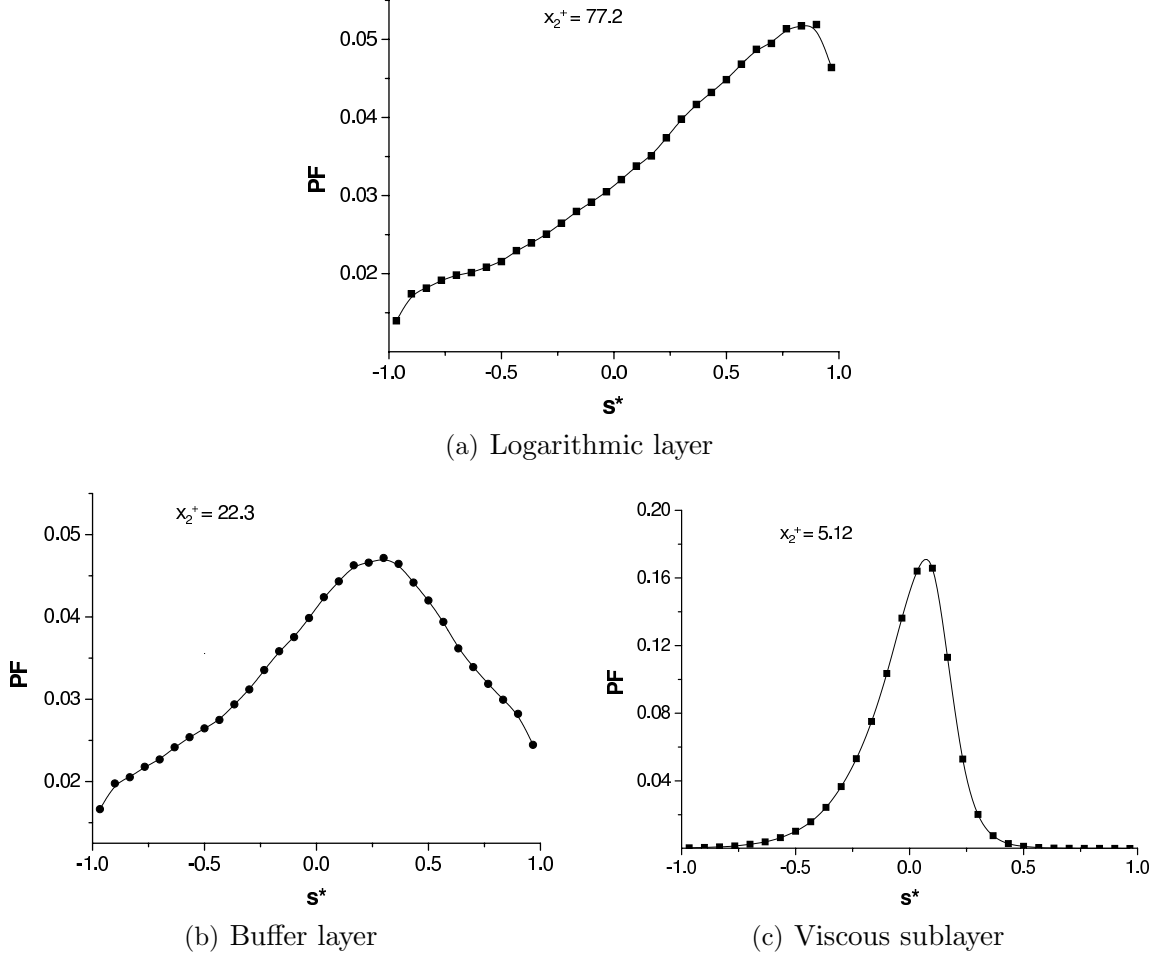


FIGURE 7.14: Time-averaged s^* -PF for the eigenvalue ratio of \bar{S}_{ij} ($Re = 2600$).

continuity equation which can be used as a constraint. Thus, a 2-D JPF should be considered for investigating the eigenvalue ratio for τ_{ij} . It is understood that τ_{ij} and τ_{ij}^* share the same eigenvector (eigenframe), with a difference of $\tau_{kk}/3$ in their eigenvalues. The justification of the above statement is straightforward. Suppose that the eigensystem of τ_{ij} is $\tau_{ij} \cdot e_j = \lambda \cdot e_i$. Subtract $(\tau_{kk}\delta_{ij}/3) \cdot e_j$ from both sides of the above equation, and the eigensystem for τ_{ij}^* is readily obtained, i.e. $(\tau_{ij} - \tau_{kk}\delta_{ij}/3) \cdot e_j = (\lambda - \tau_{kk}/3) \cdot e_i$ or simply $\tau_{ij}^* \cdot e_j = \lambda^* \cdot e_i$. Here the symbol λ is used to represent the eigenvalue in a general way. In the other parts of this chapter and the entire next chapter, there is no need to distinguish between τ_{ij} and τ_{ij}^* since only the properties related to the eigenvector are of concern. However, in this particular subsection, the difference needs to be mentioned since the eigenvalue itself is the

subject of study. Obviously, the eigenvalue ratio $\frac{\beta - \tau_{kk}/3}{\alpha - \tau_{kk}/3} \neq \frac{\beta}{\alpha}$ if $\tau_{kk} \neq 0$ or $\frac{\beta}{\alpha} \neq 1$. Notwithstanding the above difference, τ_{ij}^* instead of τ_{ij} is investigated in this subsection. For τ_{ij}^* , its tracefree property acts in a similar way to continuity (referred to here as *pseudo-continuity*), i.e. $\alpha_\tau + \beta_\tau + \gamma_\tau \equiv 0$, which indicates that a 1-D PF is sufficient for studying the relative eigenvalue ratio of τ_{ij}^* or $-\tau_{ij}^*$. However, the author is instead motivated to present the results based on the 2-D JPF due to some interesting geometrical properties it reveals.

Figure 7.15 illustrates the JPF of the relative eigenvalue ratio of the negative SGS stress tensor in the three layers: logarithmic region, buffer zone and viscous sublayer. It is interesting to observe that the JPF contour for the logarithmic region shown in Fig. 7.15(a) exhibits a regular symmetric geometrical shape: “a straight thin fin”, which in the $(\beta_{-\tau}/\alpha_{-\tau})$ — $(\gamma_{-\tau}/\alpha_{-\tau})$ plane becomes a “straight bar” as shown in Fig. 7.15(b). In fact, it is observed that the 2-D geometry of a straight bar is a general feature for all three layers, although the peak which represents the most probable state is not located at the symmetric center of the JPF contour for the viscous sublayer as shown in Fig. 7.15(d). The special straight line that the JPF contour is aligned with is the pseudo-continuity condition for $-\tau_{ij}^*$ as mentioned above. From Figs. 7.15(a) and (b) the most probable ratio reads $\alpha_{-\tau} : \beta_{-\tau} : \gamma_{-\tau} = 1 : 0.25 : -1.25$ (or $3 : 0.75 : -4.75$) for the core layer. Theoretically speaking, all states of statistics should fall on the pseudo-continuity line. The observed finite width of the straight bar is due to the interpolating error of the software package used for graphic visualization and also the limited number of 30×30 bins adopted in statistics which admits an uncertainty of ± 0.05 . Although in Fig. 7.15(c) the most probable state relates to $1 : 0.65 : -1.65$ (or $3 : 1.95 : -4.65$) for $x_2^+ = 22.3$, and the JPF contour is approximately flat at the top. In Fig. 7.15(d), the contour becomes a skewed sharp peak, which indicates a most probable ratio of $1 : 0.85 : -1.85$ (or $3 : 2.55 : -5.55$) for the viscous sublayer at $x_2^+ = 5.12$. As indicated earlier, due to the constraint of pseudo-continuity in addition to the definition of the statistical quantity, there is no need to apply the 2-D JPF to determine the relative eigenvalue ratio of $-\tau_{ij}$. However, it is desirable to find that the singularity problem encountered in the 1-D PFs (e.g. Fig. 7.13) has been avoided

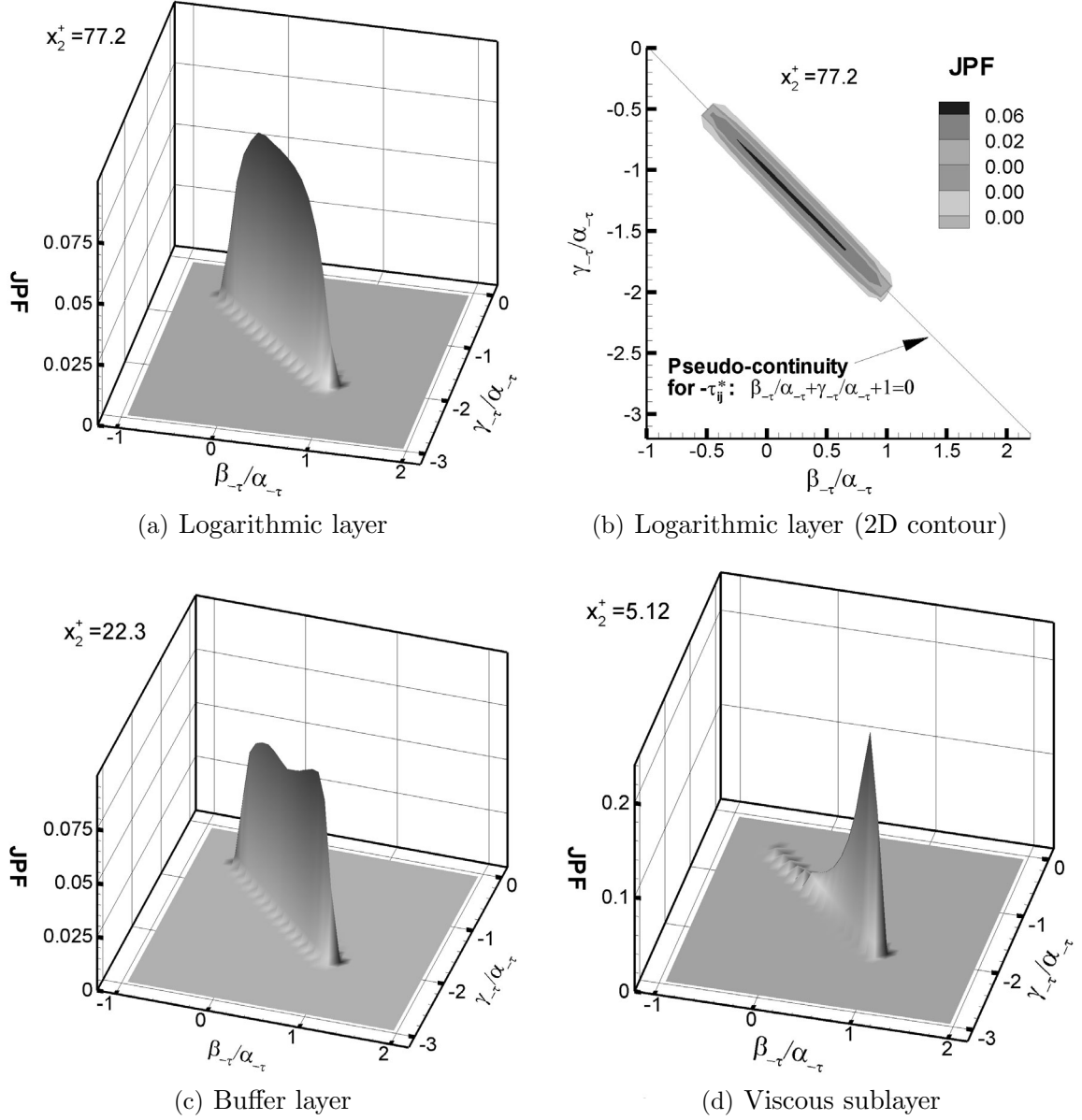


FIGURE 7.15: Time-averaged JPF between the relative eigenvalues of the negative SGS stress tensor ($Re = 2600$).

in the approach of utilizing the 2-D JPF. The calculation becomes stable and the eigenvalue ratio can be determined in a convergent way without any amplification of errors. Finally, it should be noted that this method for visualizing the geometry of a tracefree tensor represents an interesting approach which can be generally used for visualizing the trace of a second order tensor or the divergence of a vector, e.g. the strength of a local source or sink $u_{i,i}$ for mass flux.

7.6 Conclusions

In this chapter, the geometrical statistical characteristics of the resolved scales of motion have been investigated based on LES of turbulent Couette flow. The LES procedure relies on the DNM SGS stress model, which in the previous chapter, has been demonstrated to be capable of simulating a generic turbulence field in terms of conventional scaling features such as the resolved velocity field, turbulence intensity, Reynolds shear stress, etc. In this chapter, the LES results on the turbulence geometrical statistics have been compared with those based on DNS and experimental approaches as reported in the literature. The performance of the DNM is further validated since it is capable of predicting various prototypical geometrical statistical features such as helical behavior, the alignment between vorticity and the intermediate eigenvector of the filtered strain rate tensor, and that between vorticity and the vortex stretching vector. The effect of near-wall anisotropy due to the existence of the wall has been examined for three different flow regimes: the viscous sublayer, buffer zone and logarithmic region. The major conclusions are summarized as follows.

(i) Summary of Geometrical Alignments

Helicity by its definition quantifies the relative alignment between the velocity and vorticity vectors. In the logarithmic region, a prevalence of helical structure and a pattern of streamwise alignment of the resolved vorticity vector is observed. As the wall is approached, a state that the resolved vorticity vector $\bar{\omega}$ is perpendicular to the resolved velocity vector becomes more and more probable. This anisotropic effect due to the wall agrees with the reported results based on analyzing DNS data of Poiseuille channel flow [53, 61].

The alignment between the resolved vorticity vector and eigenvectors of the negative SGS stress and three constituent tensors are examined in this chapter based on three methods of statistics, i.e. plane average, 1-D PF and 2-D JPF profiles. The plane averaging method is advantageous for representing the general alignment across the entire channel, however, some important details are missed, e.g. the widely noted

alignment pattern between $\bar{\omega}$ and the intermediate eigenvector of the resolved strain rate tensor $\mathbf{e}_{S\beta}$. This prototypical feature is well captured by the 1-D PF for all three different flow regimes: sublayer, buffer zone and logarithmic region. It is also observed that $\bar{\omega}$ is preferentially aligned with the intermediate eigenvector of $-\tau_{ij}$, i.e. $\mathbf{e}_{-\tau\beta}$, and perpendicular to its most extensive and compressive eigenvectors in all three flow regimes. In general, as x_2^+ decreases, the peak of the PF corresponding to the most probable state increases drastically.

It is very interesting to observe a regular “triangle shape” 2-D JPF contour in the $(\Theta(\bar{\omega}, \mathbf{e}_{S\beta}))$ — $(\Theta(\bar{\omega}, \mathbf{e}_{S\gamma}))$ plane. This triangular shape represents the general characteristics inherent to the relative orientation between a vector and an orthonormal triad. In all three flow regimes, there is a dominant JPF peak corresponding to the most jointly probable state of two angles, i.e. $\Theta(\bar{\omega}, \mathbf{e}_{S\beta}) = 0^\circ$ and $\Theta(\bar{\omega}, \mathbf{e}_{S\gamma}) = 90^\circ$. This again demonstrates the canonical pattern that $\bar{\omega}$ is preferentially aligned with the intermediate eigenvector of \bar{S}_{ij} , while being perpendicular to its most compressive and extensive eigenvectors. In the sublayer, the magnitude of the JPF peak becomes the strongest, indicating that such an alignment feature, i.e. $\Theta(\bar{\omega}, \mathbf{e}_{S\beta}) = 0^\circ$ and $\Theta(\bar{\omega}, \mathbf{e}_{S\gamma}) = 90^\circ$, is not only valid for (quasi-)isotropic turbulence as it is popularly reported, but instead, is found by this research to be even more generic to the viscous sublayer.

In the logarithmic layer, a strong alignment between the resolved vorticity vector $\bar{\omega}$ and vortex stretching vector $\bar{\mathbf{w}}$ is predicted by the simulation, which suggests a dominant local vortex stretching flow configuration associated with positively skewed resolved enstrophy generation. This feature is expected and has been well documented in the literature based on DNS and experimental approaches [76–78, 89, 92–94]. However, in the viscous sublayer, both local vortex stretching and compressing flow configurations are highly probable.

The observed overall positive value of the resolved enstrophy generation suggests that turbulence must not entirely be 2-D, and $\bar{\sigma}_\alpha$, the component of resolved enstrophy generation contributed by the alignment between $\bar{\omega}$ and the most extensive

eigenvector $\mathbf{e}_{S\alpha}$, cannot be neglected. On the other hand, a QTD state of turbulence, i.e. $|\beta_S| < |\alpha_S|$, $|\beta_S| < |\gamma_S|$ and $\bar{\omega}$ being aligned with $\mathbf{e}_{S\beta}$, has also been identified as the most probable turbulence state. It is confirmed by this research that the local QTD state of turbulence is intrinsically different than a pure 2-D turbulence state, since it possesses a non-vanishing enstrophy generation and a nontrivial intermediate eigenvalue of the filtered strain rate tensor. It is observed in this research, as well in other studies based on DNS and experimental approaches [77, 78, 92], that the strongest alignment between $\bar{\omega}$ and $\mathbf{e}_{S\beta}$ and that between $\bar{\omega}$ and $\bar{\mathbf{w}}$ both become highly probable when the excitation of vorticity is the weakest, which implies that the background turbulence is not a random sea without any local structures. Instead, a variety of local structure patterns exist in all regions with or without high excitation of the resolved vorticity.

(ii) Summary of the Relative Principal Eigenvalues

Plane and time averaged profiles and three different statistical tools, i.e. s^* -PF, β^* -PF and (β/α) -PF, are used for investigating the relative eigenvalue ratio of the negative SGS stress and those of the three nonlinear constituent terms. The plane and time averaged profiles are advantageous for illustrating the general ratio between eigenvalues across the entire channel. For instance, the average ratio of the eigenvalues of the negative SGS stress $-\tau_{ij}$ is approximately $\alpha_{-\tau} : \beta_{-\tau} : \gamma_{-\tau} = 3 : 0.8 : -3.8$ in the core region, and changes to $3 : 2.5 : -5.5$ at the wall. The average ratio of the eigenvalues of the filtered strain rate tensor is approximately $\alpha_S : \beta_S : \gamma_S = 3 : 0.4 : -3.4$ in the core region, and changes to $3 : 0 : -3$ at the wall to be consistent with the 2-D nature of the near-wall flow.

Generally from 1-D PFs of the eigenvalue ratio of the filtered strain rate tensor, an obvious “viscous-shift” is observed in the most probable state as the x_2^+ decreases, which is due to the wall-normal anisotropic effect. The β^* -PF profile exhibits a most probable state of $\alpha_S : \beta_S : \gamma_S = 3.6 : 1 : -4.6$ in the core region, which matches well with the experimental result [76], and is close to the classical ratio of $3 : 1 : -4$ [54, 55, 62, 76]. The most probable value of $s^* = 0.9$ obtained from the s^* -PF,

also agrees well with the DNS result reported by Lund *et al.* [59]. A value of $s^* = 0.9$ indicates that a local quasi axisymmetric expansion pattern is the most probable in the core region. However, the result from the (β/α) -PF for the core region, i.e. $\alpha_S : \beta_S : \gamma_S = 6.6 : 1 : -7.6$, is different from the results obtained using β^* -PF and s^* -PF. It is identified during the research that in the case when β_S is close to 0 (e.g. in the viscous sublayer), all three statistical methods based on β^* -PF, s^* -PF and (β/α) -PF tend to become singular and the calculation of the relative eigenvalue ratio becomes unstable. A 2-D JPF is also adopted for investigating the eigenvalue ratio of $-\tau_{ij}^*$. Since $-\tau_{ij}^*$ is tracefree, the JPF contour is aligned with a regular straight line. The singularity problem encountered in the 1-D PF can be avoided by using the 2-D JPF, which determines the most probable eigenvalue ratio in an unambiguous way without the amplification of errors due to small values of $\beta_{-\tau} \rightarrow 0$. The most probable ratio predicted using the 2-D JPF for $-\tau_{ij}^*$ is $\alpha_{-\tau} : \beta_{-\tau} : \gamma_{-\tau} = 3 : 0.75 : -4.75$ for the core layer, $3 : 1.95 : -4.65$ for the buffer zone and $3 : 2.55 : -5.55$ for the sublayer.

Chapter 8

Tensorial Invariants and Turbulence Topology

8.1 Introduction

In chapters 6 and 7, the velocity gradient tensor was studied using geometrical statistical methods based on plane averaging and probability functions. It has been shown that the velocity gradient tensor is fundamental to a variety of important fluids quantities and processes such as the rotation and strain rate tensors, helical motions, enstrophy generation, vortex stretching, resolved dissipation rate, rate of SGS TKE production, etc. The pioneering works of Perry and Chong [56], Chong *et al.* [58], Chen *et al.* [57] and Cantwell [63,186] introduced another interesting methodology, i.e. *turbulence topology*, which investigates local small scales of turbulence by classifying flow topologies in terms of the three invariants of the velocity gradient or filtered strain rate tensors. Perry and Chong [56] implemented the concept of critical-point analysis of nonlinear physics into the description of eddying motions, which is fundamental to the development of the methodology of turbulence topology. This methodology has been studied using theoretical analysis based on tensorial invariants and restricted Euler dynamics [52, 58, 63, 65, 69, 184, 186], *a priori* LES approaches [29, 70, 165], and DNS analysis of a variety of turbulent flows [57, 64, 66–68, 190].

There are several good reasons to study the invariants of a velocity gradient tensor: (i) the geometry and structure obtained from the analysis are universal, i.e.

frame invariant under affine transformation [64, 78, 178]; (ii) in the case of incompressible flows, the analysis of a 3-D field can be conveniently reduced to a 2-D invariant analysis [64]; (iii) different length scales of turbulence corresponding to different magnitudes of the velocity gradient can be sorted in an unambiguous manner using the *invariant phase plane* [64]; and (iv) it has been shown by several studies [67, 68, 70, 73, 190] that the so-called turbulence invariant *discriminant* appears to be an effective quantity for flow structure visualization since it does not require any arbitrary thresholds. In this chapter, the methodology of turbulence topology for LES will be briefly introduced, and numerical results based on analyzing the data obtained using the proposed DNM will be presented.

In their paper, van der Bos *et al.* [70] indicated that a good SGS model should exhibit the capability to reproduce generic turbulence topological features in the invariant phase planes and also to predict turbulence quantities such as the statistically expected energy dissipation and various geometrical alignments between fluid vectors. The sound performance of the DNM in terms of conventional tests and geometrical statistics has been reported previously in chapters 6 and 7, respectively. As a continuation of the evaluation of the DNM, some preliminary results on turbulence topologies based on analyzing a Couette flow database ($Re = 2600$) obtained using the LES approach will be presented in this chapter. The methodology adopted follows the roadmap originally laid out by Chen *et al.* [57] based on analysis of DNS data, and also refers to the recent works on LES implementations by Borue and Orszag [165] and van der Bos *et al.* [70].

8.2 Basic Concepts Related to Tensorial Invariants and Flow Topologies

As is well known the velocity gradient tensor $A_{ij} \stackrel{\text{def}}{=} u_{i,j}$ can be decomposed into a symmetric strain rate tensor S_{ij} and skew-symmetric rotation rate tensor Ω_{ij} , i.e.

$A_{ij} = S_{ij} + \Omega_{ij}$. The eigenvalues of A_{ij} satisfy the *characteristic equation* [58, 69]

$$\lambda^3 + P_A \lambda^2 + Q_A \lambda + R_A = 0 \quad (8.1)$$

where P_A , Q_A and R_A are invariants of A_{ij} taking the following forms

$$\begin{cases} P_A \stackrel{\text{def}}{=} -\text{tr}(\mathbf{A}) \equiv -A_{ii} \\ Q_A \stackrel{\text{def}}{=} \frac{1}{2}\{[\text{tr}(\mathbf{A})]^2 - \text{tr}(\mathbf{A}^2)\} \equiv \frac{1}{2}P_A^2 - \frac{1}{2}A_{ik}A_{ki} \\ R_A \stackrel{\text{def}}{=} -\det(\mathbf{A}) \equiv -\frac{1}{3}P_A^3 + P_A Q_A - \frac{1}{3}A_{ik}A_{kn}A_{ni} \end{cases} \quad (8.2)$$

For incompressible flows, $P_A \equiv 0$ due to continuity and thus the local flow topology only relies on Q_A and R_A , which have the following simplified forms

$$\begin{cases} Q_A = -\frac{1}{2}A_{ik}A_{ki} = \frac{1}{4}(\omega_i\omega_i - 2S_{ij}S_{ji}) \\ R_A = -\frac{1}{3}A_{ik}A_{kn}A_{ni} = -\frac{1}{3}(S_{ij}S_{jk}S_{ki} + \frac{3}{4}\omega_i\omega_jS_{ij}) \end{cases} \quad (8.3)$$

The terms on the right hand side of the above equations are readily identifiable invariants with very clear physical meanings: the enstrophy $\omega^2 = \omega_i\omega_i = -2\Omega_{ij}\Omega_{ji}$, strain product (proportional to dissipation) $\mathcal{I}_{S2} = S_{ij}S_{ji} \propto \varepsilon_r = 2\nu S_{ij}S_{ji}$, strain skewness $\mathcal{I}_{S3} = S_{ij}S_{jk}S_{ki}$, and enstrophy generation $\sigma = \omega_i\omega_jS_{ij} = 4\Omega_{ij}\Omega_{jk}S_{ki}$. The behavior of these four invariants and the physical processes related to them will be discussed later in a detailed manner along with numerical illustrations in section 8.3.

Chong and Perry [58] have shown that when $P_A = 0$ (due to incompressibility), the nature of the roots of Eq.(8.1) is determined by a *discriminant* defined as

$$D_A = \frac{27}{4}R_A^2 + Q_A^3 \quad (8.4)$$

If $D_A > 0$, Eq.(8.1) admits one real and two complex-conjugate roots. In this case, vorticity dominates the rate of strain, the local streamlines swirl about the point and the flow pattern is referred to as a *focus* [56, 58]. If $D_A < 0$, the three roots of Eq.(8.1) are distinct and real, the rate of strain dominates the vorticity and the flow

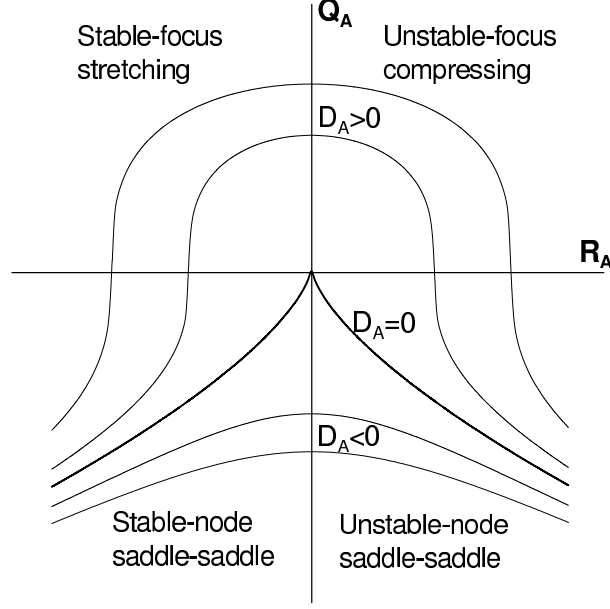


FIGURE 8.1: Solution space for invariants Q_A and R_A with lines corresponding to constant values of the discriminant D_A . The different subdomains are labelled according to the terminology of Chong and Perry [58].

pattern resembles a *stagnation point*. This type of flow geometry is referred to as a *node-saddle-saddle* [56, 58]. If $D_A = 0$, Eq.(8.1) has three real roots of which two are equal, which corresponds to two curves: $R_A = \pm(2\sqrt{3}/9)(-Q_A)^{3/2}$ as shown in Fig. 8.1. These two special curves are also sometimes referred to as the “*Vieillefosse line*” [191]. The sign of R_A can be used for a further classification of the flow topology: in the left half of the Q_A – R_A plane (the so-called *phase plane of invariants* of the velocity gradient tensor), the real parts of the complex-conjugate eigenvalues or two of the three real eigenvalues are negative and the critical points are classified as *stable*; in contrast, in the right half plane, the real parts of the complex-conjugate eigenvalues or two of the three real eigenvalues are positive and the critical points are classified as *unstable* [73]. The above mentioned three different solution sets corresponding to $D_A > 0$, $D_A < 0$ and $D_A = 0$, respectively, are illustrated in Fig. 8.1.

Upon taking the gradient of the N-S equation for incompressible flow, a transport equation for A_{ij} can be obtained [63], i.e.

$$D_t(A_{ij}) + (A_{ik}A_{kj})^* = \mathcal{H}_{ij} \quad (8.5)$$

As usual, the superscript $*$ indicates the tracefree form of a tensor, i.e. $(\)_{ij}^* = (\)_{ij} - (\)_{mm}\delta_{ij}/3$, the operation $D_t(\) = (\dot{\ }) + u_j \cdot (\)_{,j}$ represents the material derivative, and the tensor \mathcal{H}_{ij} in the above equation is defined as

$$\mathcal{H}_{ij} = -(p_{,ij})^*/\rho + \nu(A_{ij})_{,kk} \quad (8.6)$$

The two terms on the right hand side of the above equation represent the deviatoric part of the *pressure Hessian* and the *viscous diffusion* terms, respectively. If the effect of \mathcal{H}_{ij} is negligible, Eq.(8.5) reduces to a typical *homogeneous equation*, which is referred to as the *restricted Euler equation* [63]. By employing the rule of tensor contraction and Cayley-Hamilton theorem, Cantwell [63] deduced the following evolution equations for Q_A and R_A from Eq.(8.5):

$$\begin{cases} D_t(Q_A) = -3R_A - A_{ij}\mathcal{H}_{ji} \\ D_t(R_A) = \frac{2}{3}Q_A^2 - A_{ij}A_{jk}\mathcal{H}_{ki} \end{cases} \quad (8.7)$$

Multiply the 1st and 2nd equation of (8.7) with $\frac{2}{3}Q_A^2$ and $3R_A$, respectively, and then add the results to obtain the following relation under the restricted Euler condition (neglect \mathcal{H}_{ij}):

$$\frac{2}{3}Q_A^2 D_t(Q_A) + 3R_A D_t(R_A) = 0 \quad (8.8)$$

which, on applying Eq.(8.4), is simplified to

$$D_t(D_A) = 0 \quad (8.9)$$

which then results in a restricted Euler solution, i.e. $D_A = \text{constant}$ as shown in Fig. 8.1. The tangential direction of the restricted Euler solution vector (or the slope of the *solution trajectory* [63]) in the Q_A - R_A phase plane can therefore be determined as $dQ_A/dR_A = -9R_A/(2Q_A^2)$.

Although the restricted Euler equation is much simplified, as pointed out by

Cantwell [63,186], it is rather “remarkable” that its solution is close to DNS results for the N-S equations in terms of turbulence topology, which suggests that “the restricted Euler equation plays a role in real flows”. The above statement of Cantwell is strongly supported by various DNS based studies [57,64,66–68,190]. In the LES approach, an additional term \mathcal{B}_{ij} related to the SGS stress due to the filtering process appears in Eq.(8.5) which becomes [70]

$$D_t(\bar{A}_{ij}) + (\bar{A}_{ik}\bar{A}_{kj})^* = \bar{\mathcal{H}}_{ij} - \mathcal{B}_{ij}^* \quad (8.10)$$

where

$$\mathcal{B}_{ij} = \tau_{kj,ik} \quad (8.11)$$

Based on data analysis of the HPIV measurements of Tao *et al.* [29], van der Bos *et al.* [70] examined the effects of this additional SGS term. They concluded that the SGS stress has a certain influence on the discriminant and the slope of the solution trajectory (described as a “streamline” that follows the tangential direction of the resolved vector map in their paper), which deviates from the pattern admissible by the previously mentioned restricted Euler equation (sketched in Fig. 8.1). However, other features such as the resolved enstrophy generation, strain-skewness and energy flux quantified from the HPIV data agree with the previously reported DNS results of Chertkov *et al.* [191].

8.3 Numerical Results on Turbulence Topologies

8.3.1 Flow Topologies Related to Invariants of the Resolved Velocity Gradient Tensor

For LES of incompressible flows, the previously discussed three tensorial invariants of the velocity gradient tensor defined by Eq.(8.2) take the following forms at the

filtered scales:

$$\begin{cases} P_{A\Delta} \equiv 0 \\ Q_{A\Delta} = -\frac{1}{2}\bar{A}_{ik}\bar{A}_{ki} = \frac{1}{4}(\bar{\omega}_i\bar{\omega}_i - 2\bar{S}_{ij}\bar{S}_{ji}) \\ R_{A\Delta} = -\frac{1}{3}\bar{A}_{ik}\bar{A}_{kn}\bar{A}_{ni} = -\frac{1}{3}(\bar{S}_{ij}\bar{S}_{jk}\bar{S}_{ki} + \frac{3}{4}\bar{\omega}_i\bar{\omega}_j\bar{S}_{ij}) \end{cases} \quad (8.12)$$

Similar to Eq.(8.4), the Eulerian discriminant can be defined as

$$D_{A\Delta} = \frac{27}{4}R_{A\Delta}^2 + Q_{A\Delta}^3 \quad (8.13)$$

The tensorial invariants appearing in the above definitions of $Q_{A\Delta}$ and $R_{A\Delta}$ are the resolved enstrophy $\bar{\omega}^2 = \bar{\omega}_i\bar{\omega}_i = -2\bar{\Omega}_{ij}\bar{\Omega}_{ji}$, resolved strain product $\bar{\mathcal{I}}_{S2} = \bar{S}_{ij}\bar{S}_{ji}$, resolved strain skewness $\bar{\mathcal{I}}_{S3} = \bar{S}_{ij}\bar{S}_{jk}\bar{S}_{ki}$, and resolved enstrophy generation $\bar{\sigma} = \bar{\omega}_i\bar{\omega}_j\bar{S}_{ij}$. Before analyzing the statistical characteristics related to the $Q_{A\Delta}$ - $R_{A\Delta}$ phase plane, it is beneficial to explain some implications of these two invariants (i.e. $Q_{A\Delta}$ and $R_{A\Delta}$) and their connections to the local flow structures and physical processes. In addition to the previous introduction to the methodology of Perry and Chong [56,58] for classifying the flow topologies using these two invariants and the concept of critical points, it is worthwhile to note the following flow mechanisms for further clarification:

- It is well known that the resolved strain product relates to the resolved viscous dissipation, i.e. $\varepsilon_r = 2\nu\bar{S}_{ij}\bar{S}_{ji} = 2\nu\bar{\mathcal{I}}_{S2}$, which is different than the local rotational excitation (or the activity of concentrated vortical “worms” [78,92]) due to the resolved enstrophy. Thus, it is clear from its definition (Eq.(8.12)) that the invariant $Q_{A\Delta}$ is a measure of the relative weights of both the local straining and rotational parts of the resolved velocity gradient tensor: a large positive $Q_{A\Delta}$ corresponds to a large resolved enstrophy $\bar{\omega}^2$ dominating the resolved strain product (dissipation), while the reverse is true for the opposite case when $Q_{A\Delta}$ is large and negative [73].
- The invariant $R_{A\Delta}$ by definition accounts for the combined effects of two third order tensorial invariants, i.e. the resolved strain skewness $\bar{\mathcal{I}}_{S3}$ and the resolved

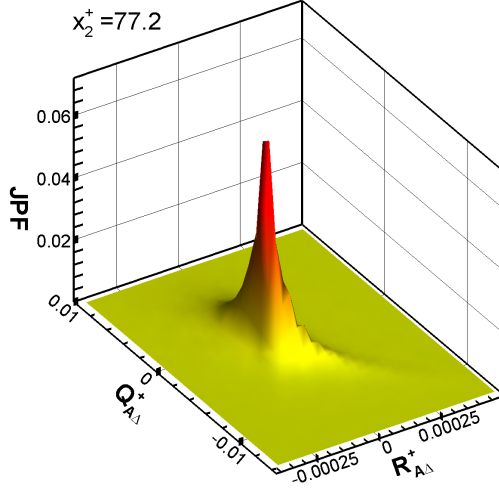
enstrophy generation $\bar{\sigma}$. According to the study of Tsinober *et al.* [81, 82], both resolved strain skewness and enstrophy generation are related to the transport equation of the resolved strain product $\bar{\mathcal{I}}_{S2}$ (equivalent to the dissipation equation, see Eq.(C.4) in Appendix C). The rate of energy dissipation ε_r is primarily associated with a negatively valued resolved strain skewness or $\bar{\mathcal{I}}_{S3} < 0$. Local vortex stretching ($\bar{\sigma} > 0$) suppresses the cascade of dissipation, however, vortex compression ($\bar{\sigma} < 0$) contributes to it. Although both negatively valued resolved strain skewness and enstrophy generation contribute to the local dissipation, they seem to counteract each other, since overall the resolved enstrophy generation is positively skewed (as discussed in detail previously in subsection 7.4.3) while the resolved strain skewness is negatively skewed (which will be discussed later in the $Q_{S\Delta}$ – $R_{S\Delta}$ phase plane based on the filtered strain rate tensor).

The above issues qualitatively characterize some fundamental statistical features of the flow topologies exhibited in the $Q_{A\Delta}$ – $R_{A\Delta}$ phase plane, which include the local straining process, (vortical) rotational excitation, vortex stretching/compression, and cascade of dissipation. Since all these features are based on tensorial invariants, they are expected to be generic to turbulence, independent of the observer/coordinate system and likely to be universal from one flow to another.

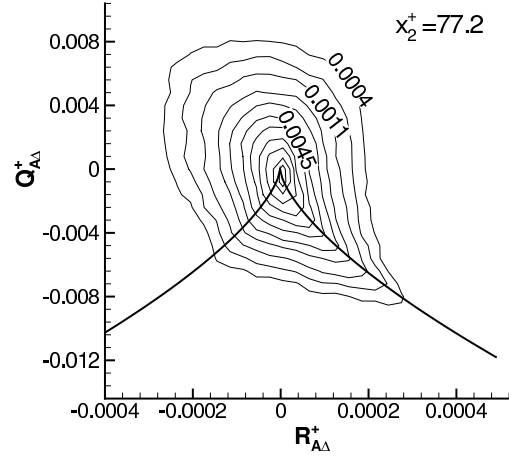
In presenting the results, the invariants $Q_{A\Delta}$ and $R_{A\Delta}$ for the resolved velocity gradient tensor (as well as those for the resolved strain rate tensor to be discussed later) are non-dimensionalized using ν and u_τ in analogy to the canonical wall coordinates u^+ and x_2^+ for wall flows:

$$\begin{cases} Q_{A\Delta}^+ = Q_{A\Delta}/(u_\tau^2/\nu)^2 \\ R_{A\Delta}^+ = R_{A\Delta}/(u_\tau^2/\nu)^3 \end{cases} \quad (8.14)$$

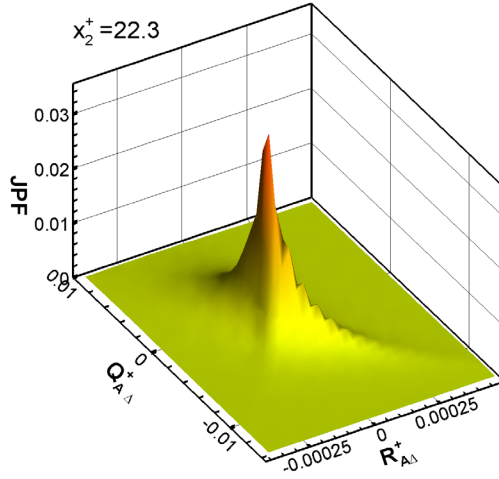
Figures 8.2(a)–(f) illustrate the JPF between $Q_{A\Delta}$ and $R_{A\Delta}$ for the sublayer, buffer zone and logarithmic region. A prototypical *self-similar* “pear-shape” [68] (also referred to as a “teardrop-shape” [67] or “elongated/roughly elliptical shape”



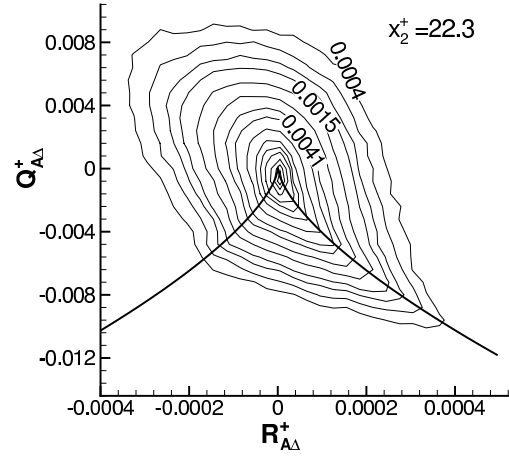
(a) Logarithmic layer



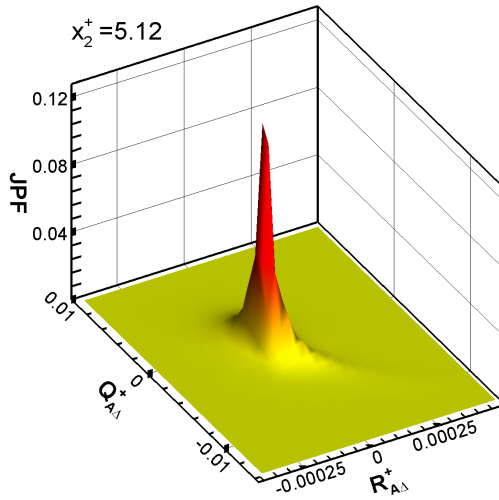
(b) Logarithmic layer (2-D contour)



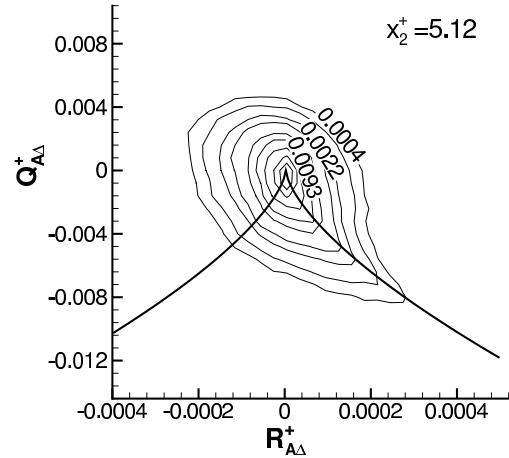
(c) Buffer layer



(d) Buffer layer (2-D contour)



(e) Viscous sublayer



(f) Viscous sublayer (2-D contour)

FIGURE 8.2: Time-averaged JPF between invariants $Q_{A\Delta}^+$ and $R_{A\Delta}^+$ of the filtered velocity gradient tensor ($Re = 2600$).

[64, 186, 190]) centered on the origin is apparent in all cases. It is evident from the figures that the most probable state is located at the origin. Apart from the origin, the 2-D pear-shape JPF contour has a preference for the 2nd and 4th quadrants, indicating the prevalence of stable-focus/stretching and unstable-node/saddle/saddle topologies, respectively. A comparison of Figs. 8.2(b), (d) and (f) based on the same minimum cut-off JPF contour level of 0.0004, indicates that the preference of the JPF for the origin is the most intense in the sublayer. This is also indicated by the largest 3-D JPF peak, which occurs in Fig. 8.2(e). Moving away from the wall, the pear-shape contour spreads out in the 2nd and 4th quadrants, and the magnitude of the corresponding peaks reduces. The dominance of the 2nd and 4th quadrants is the greatest in the buffer layer. Both the self-similarity of the JPF contour shape in different layers and the anisotropic effect due to the existence of the wall agree with the results reported by Blackburn *et al.* [73]. As pointed out by Cantwell [186], neither the commonly observed preference for $Q_{A\Delta}$ and $R_{A\Delta}$ to lie near the origin, nor the extension away from the origin along the “ridgeline” in the 2nd quadrant reported in earlier studies [57, 64, 186], are admissible to the restricted Euler equation (see Fig. 8.1).

As is apparent in Figs. 8.2(b), (d) and (f), there is a strong tendency for the JPF contour to gather around the right Vieillefosse line ($D_{A\Delta} = 0$ for $R_{A\Delta} \geq 0$), which in Figs. 8.2(a), (c) and (e) is represented by a 3-D ridge descending into the region of $D_{A\Delta} \leq 0$ and $R_{A\Delta} > 0$. Such a statistical phenomenological pattern is sometimes [70, 191] referred to as the “*Vieillefosse tail*”. Similar observations were reported in the *a posteriori* LES analysis of HPIV measurements of quasi-isotropic turbulence at the center of a square duct flow by van der Bos *et al.* [70], and various DNS studies of mixing layers by Chen *et al.* [57] and Soria *et al.* [64], channel flow by Blackburn *et al.* [73], turbulent boundary layer flow by Chong *et al.* [67] and Chacín *et al.* [190], stratified homogeneous shear flow by Diamessis and Nomura [74], homogeneous isotropic turbulent flow by Martin *et al.* [66], and forced isotropic turbulence by Ooi *et al.* [68]. It is very interesting to note that although the large scale motions of these flows differ, the statistical features in the $Q_{A\Delta}$ – $R_{A\Delta}$ phase

plane are similar. This suggests that the topological features shown in the $Q_{A\Delta}$ – $R_{A\Delta}$ phase plane are self-similar not only between different layers of a wall-bounded flow, but also between different types of flows as well, which according to Ooi *et al.* [68] and Martin *et al.* [66] indicates “a kind of universality for all turbulence flows, be they homogeneous or inhomogeneous”.

8.3.2 Flow Topologies Related to the Invariants of the Resolved Strain Rate Tensor

In the previous subsection, statistical features of the flow topology were investigated using the invariants of the resolved velocity gradient tensor for incompressible flows, i.e. $Q_{A\Delta}$ and $R_{A\Delta}$. As indicated earlier, both $Q_{A\Delta}$ and $R_{A\Delta}$ consider the combined effect of local resolved straining and vortical rotational processes, or to be more specific, the effects due to four invariants: the resolved enstrophy, strain product, strain skewness and enstrophy generation. In their roadmap paper, Chen *et al.* [57] also studied flow topology using the invariants of the strain rate tensor, which excludes (in a direct manner) the vorticity information (i.e. enstrophy and enstrophy generation) from the set of invariants. As such, the relation between the local flow topology and the straining process is highlighted, which in some cases is advantageous for clarifying flow topologies and processes. For instance, it will soon be demonstrated that this optional method is qualitatively more desirable when applied for illustrating the previously introduced relative eigenvalue ratio of the strain rate tensor and the local kinetic energy dissipation rate. The invariants of the filtered strain rate tensor for incompressible flows are

$$\begin{cases} P_{S\Delta} = \bar{S}_{ii} \equiv 0 \\ Q_{S\Delta} = -\frac{1}{2}\bar{S}_{ik}\bar{S}_{ki} \\ R_{S\Delta} = -\frac{1}{3}\bar{S}_{ik}\bar{S}_{kn}\bar{S}_{ni} \end{cases} \quad (8.15)$$

Clearly, the invariant $Q_{S\Delta}$ is a measure of the resolved viscous dissipation, i.e.

$$\varepsilon_r = 2\nu\bar{S}_{ij}\bar{S}_{ji} \equiv -4\nu Q_{S\Delta} \quad (8.16)$$

and $R_{S\Delta}$ is a measure of the resolved strain skewness, as well as an indicator for the sign of the intermediate eigenvalue of the resolved strain rate tensor, since

$$\bar{\mathcal{L}}_{S3} = \bar{S}_{ik}\bar{S}_{kn}\bar{S}_{ni} \equiv \alpha_S^3 + \beta_S^3 + \gamma_S^3 \equiv 3\alpha_S\beta_S\gamma_S \quad (8.17)$$

Given the convention $\alpha_S > \beta_S > \gamma_S$, it is straightforward from continuity that $\alpha_S > 0$ and $\gamma_S < 0$ are valid for any nontrivial situations (the trivial situation refers to $\alpha_S = \beta_S = \gamma_S = 0$). Therefore, if $R_{S\Delta} > 0$, then $\bar{S}_{ik}\bar{S}_{kn}\bar{S}_{ni} < 0$ and $\beta_S > 0$, and the local structure is sheetlike. This relation is one-to-one and the reverse is also true corresponding to a local tubelike structure. From the result presented previously in subsection 7.3.2, it is known that for the most probable ratios of either $\alpha_S : \beta_S : \gamma_S = 1 : 1 : -2$ (antisymmetric expansion) [29,59] or the classical result $3 : 1 : -4$ [55,62,76], β_S is positively skewed statistically, which in turn determines the invariant $R_{S\Delta}$ to be overall positively skewed and the resolved strain skewness to be overall negatively skewed. As discussed previously, it is known that an instantaneous negative value of the resolved strain skewness contributes to an increase of transient local dissipation rate ε_r (see Eq.(C.4)).

The discriminant for the $Q_{S\Delta}$ - $R_{S\Delta}$ phase plane is

$$D_{S\Delta} = \frac{27}{4}R_{S\Delta}^2 + Q_{S\Delta}^3 \quad (8.18)$$

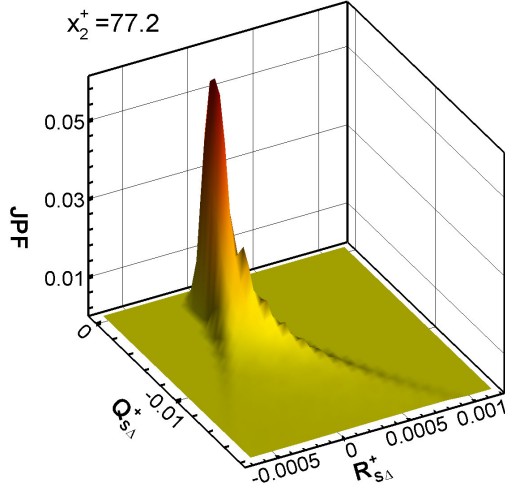
Since \bar{S}_{ij} is a real symmetric tensor, all of its three eigenvalues must be real. Therefore, according to the previous discussion in section 8.2, only the region corresponding to $D_{S\Delta} \leq 0$ in the $Q_{S\Delta}$ - $R_{S\Delta}$ phase plane is realistic for flow topological classification, which is significantly different than the property of the $Q_{A\Delta}$ - $R_{A\Delta}$ phase plane. As discussed earlier, the use of the invariant $Q_{S\Delta}$ is helpful to explicitly classify the different scales of motions according to the local dissipation rate. According to Black-

burn *et al.* [73], the $Q_{S\Delta}$ - $R_{S\Delta}$ phase plane is also very convenient for visualizing the relative eigenvalue ratio of the resolved strain rate tensor. Suppose that $r_a = \beta_S/\alpha_S$, then the curves corresponding to different eigenvalue ratios can be represented by

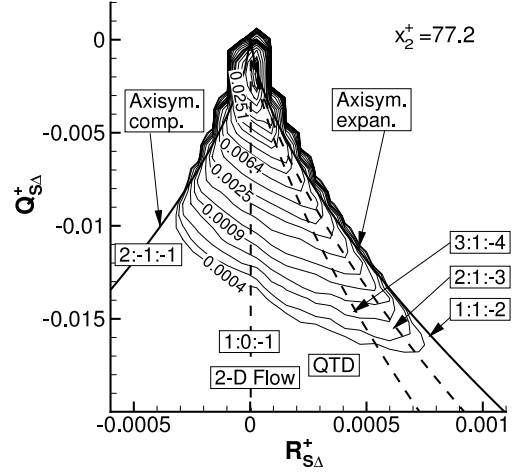
$$R_{S\Delta} = (-Q_{S\Delta})^{3/2} r_a (1 + r_a) (1 + r_a + r_a^2)^{-3/2} \quad (8.19)$$

Using the above relation, curves corresponding to $\alpha_S : \beta_S : \gamma_S = 1 : 1 : 2$ (axisymmetric expansion, the “right limiting” flow configuration), $2 : 1 : -3$, $3 : 1 : -4$ (the “classical ratio”), $1 : 0 : -1$ (2-D flow), and $-1 : -1 : 2$ (axisymmetric compression, the “left limiting” flow configuration) are illustrated in Fig. 8.3(b). The previously discussed preferred QTD state of flow configuration (related to small r_a) is also shown in the $Q_{S\Delta}$ - $R_{S\Delta}$ phase plane.

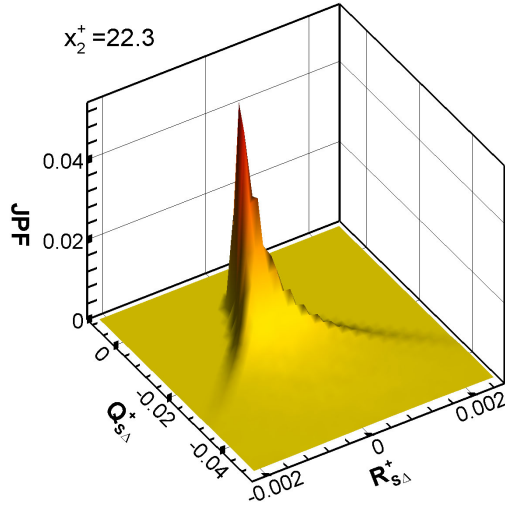
Figures 8.3(a)–(f) illustrate both the 3-D and 2-D JPF contours of the invariants $Q_{S\Delta}$ and $R_{S\Delta}$ for three different flow layers. All states of flow topologies are generally bounded by $D_{S\Delta} \leq 0$. However, some contours slightly extend across the boundary, which is a graphical error due to the limited number of bins (30×30) used for processing the statistics, and also the interpolating property of the software package available for graphic visualization. Generally, the flow topologies for the three layers shown in Fig. 8.3 are prototypical, and consistent with those reported in other studies of wall-bounded flows using DNS by Chong *et al.* [67] and Blackburn *et al.* [73]. The flow topology in the logarithmic region as shown in both Figures 8.3(a) and (b), shows a strong preference for the 4th quadrant ($R_{S\Delta} > 0$ and $Q_{S\Delta} < 0$), which according to previous discussion relates to a local dissipative pattern and positively skewed intermediate eigenvalue β_S . A general tendency towards the axisymmetric expansion pattern is also evident in Fig. 8.3(b), especially at low JPF value levels. As the JPF value increases, a state of eigenvalue ratio of $3 : 1 : -4$ becomes more probable. However, as the JPF value approaches its peak level, the contour patterns for determining the eigenvalue ratio become much smaller and less distinguishable. The above method for visualizing the eigenvalue ratio using the $Q_{S\Delta}$ - $R_{S\Delta}$ phase plane, which is very convenient and intuitive, was introduced by Blackburn *et al.* [73]. Howe-



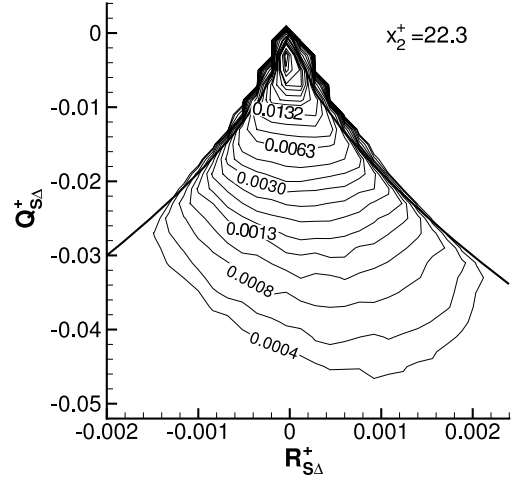
(a) Logarithmic layer



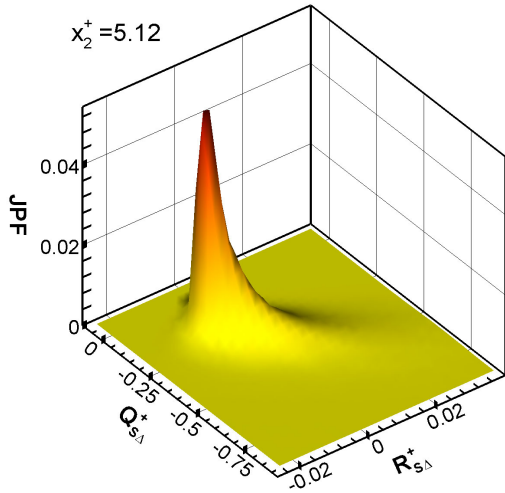
(b) Logarithmic layer (2-D contour)



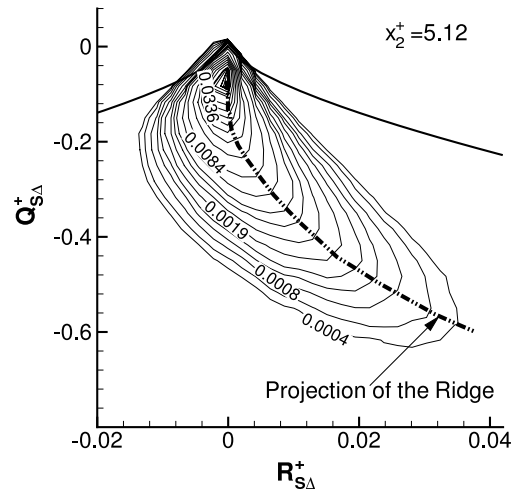
(c) Buffer layer



(d) Buffer layer (2-D contour)



(e) Viscous sublayer



(f) Viscous sublayer (2-D contour)

FIGURE 8.3: Time-averaged JPF between invariants $Q^+_{s\Delta}$ and $R^+_{s\Delta}$ of the filtered strain rate tensor ($Re = 2600$).

ver, it is argued in this dissertation that *it is inadequate to establish any quantitative analysis on the most probable eigenvalue ratio based on the JPF contour pattern exhibited in the $Q_{S\Delta}$ - $R_{S\Delta}$ phase plane*. This is because all states of high probability cluster around the peak location, where the different eigenvalue ratio curves specified by Eq.(8.19) are hardly distinguishable. In the regions away from the origin, the curves corresponding to different eigenvalue ratios become more distinguishable, however, the JPF value in these regions corresponding to lower probabilities. Thus, one cannot really rely on this method to quantify the most probable eigenvalue ratio of \bar{S}_{ij} in a manner as precise as the methodologies employed previously in chapter 7.

From Figs. 8.3(b), (d) and (f), it is observed that the most probable state is located around the origin, however, there is a shift of this location away from the origin along the negative $Q_{S\Delta}$ axis. From these three figures, it is observed that this negative shift from the origin enlarges as the wall is approached. The magnitude of the negative shift in the sublayer becomes as large as $Q_{S\Delta}^+ \approx -0.08$ in Fig. 8.3(f), which according to Blackburn *et al.* [73] is contributed by the wall anisotropic effect. Right at the wall, the boundary condition for \bar{S}_{ij} is given by Eq.(3.4), which results in

$$\begin{cases} Q_{S\Delta}|_{wall} = -\frac{1}{4}(\bar{u}_{1,2}^2 + \bar{u}_{3,2}^2)|_{wall} \\ R_{S\Delta}|_{wall} \equiv 0 \end{cases} \quad (8.20)$$

Since $Q_{S\Delta}$ is a direct indicator of local dissipation (see Eq.(8.16)), the term *near-wall dissipation shift in the $Q_{S\Delta}$ - $R_{S\Delta}$ phase plane* is coined here to describe this phenomenon. A more detailed discussion of this negative shifting effect will be explored in the next subsection together with the boundary condition and near-wall flow topology.

Also, the value of $R_{S\Delta} \equiv 0$ at the wall helps to explain the special pattern of the projection of the probable JPF contour ridge (the dash-dot-dot line) shown in Fig. 8.3(f), which becomes more and more “vertical” to the horizontal axis (thus more and more 2-D, see Fig. 8.3(b)) as the origin is approached. This feature is important, which demonstrates a generally understood characteristic of the near-wall flow: in

the sublayer the most probable states are very close to a 2-D pattern, whereas the two limiting flow configurations, i.e. axisymmetric compression/expansion, are the least probable due to their 3-D physical nature. This is in sharp contrast to the flow topology of the logarithmic layer where a state of axisymmetric expansion is highly probable as also concluded previously in chapter 7. The time-averaged JPF contour shown in Fig. 8.3(d) exhibits an interesting pattern: although the JPF contour for the buffer zone slightly prefers the 4th quadrant, none of the states from axisymmetric compression to 2D configuration and to axisymmetric expansion can be ignored. It is very desirable to see such a regular and universal flow topology for the buffer zone from Figs. 8.3(c) and (d) as well as previously from Figs. 8.2(c) and (d), with the aid of the phase plane of the tensorial invariants, since the buffer zone is still considered to be one of the most controversial flow regimes in wall-bounded turbulence.

8.3.3 Statistical Expectations of Resolved Quantities and Flow Topology

In this subsection, flow topologies related to the resolved quantities such as the resolved enstrophy, enstrophy generation and rate of SGS TKE production will be investigated. Since these quantities by their nature are scalars, a method is needed to relate them to the previously introduced invariant phase planes. Following van der Bos *et al.* [70], the *expectation* of a resolved scalar Π can be determined using $P(R_\Delta, Q_\Delta, \Pi)$, the JPF of a scalar quantity and two tensorial invariants, i.e.

$$E(\breve{\Pi}) = \sum_{\Pi} \Pi \cdot P(R_\Delta, Q_\Delta, \Pi) \quad (8.21)$$

Here, $(\breve{})$ is used to represent the actual *random variable*, and R_Δ and Q_Δ are generally used to indicate the invariants of either \bar{A}_{ij} or \bar{S}_{ij} . Based on Bayes's theorem [185],

the above equation can be further expressed as

$$\begin{aligned} E(\check{\Pi}) &= P(R_\Delta, Q_\Delta) \sum_{\Pi} \Pi \cdot P(\Pi | R_\Delta, Q_\Delta) \\ &= P(R_\Delta, Q_\Delta) \langle \Pi | R_\Delta, Q_\Delta \rangle_c \end{aligned} \quad (8.22)$$

where $P(\Pi | R_\Delta, Q_\Delta)$ is the *joint conditional distribution* [185] of $\check{\Pi}$ given $\check{R}_\Delta = R_\Delta$ and $\check{Q}_\Delta = Q_\Delta$, and $\langle \Pi | R_\Delta, Q_\Delta \rangle_c$ is the *conditional expectation* of the resolved scalar random variable $\check{\Pi}$. As such, the expectation of the non-dimensional resolved enstrophy generation takes the following form:

$$\sigma_E \stackrel{\text{def}}{=} N_B \cdot E(\check{\sigma}) = N_B \cdot P(R_\Delta, Q_\Delta) \cdot \langle \bar{\sigma}_n | R_\Delta, Q_\Delta \rangle_c \quad (8.23)$$

where $\bar{\sigma}_n = \bar{\sigma}/|\bar{\sigma}| = \cos(\bar{\boldsymbol{\omega}}, \bar{\mathbf{w}})$ is the resolved relative enstrophy generation. In the above equation $N_B = 30 \times 30$ is an arbitrary parameter, which is the number of the bins used for calculating statistics^a. In a similar way, the expectations of the normalized resolved enstrophy and SGS TKE production rate can be defined as

$$(\bar{\omega}^2)_E \stackrel{\text{def}}{=} N_B \cdot P(R_\Delta, Q_\Delta) \cdot \left\langle \frac{\bar{\omega}^2}{(u_\tau^2/\nu)^2} \middle| R_\Delta, Q_\Delta \right\rangle_c \quad (8.24)$$

and

$$\mathcal{P}_{rE} \stackrel{\text{def}}{=} N_B \cdot P(R_\Delta, Q_\Delta) \cdot \left\langle \frac{\mathcal{P}_r}{u_\tau^4/\nu} \middle| R_\Delta, Q_\Delta \right\rangle_c \quad (8.25)$$

8.3.3.1 Characteristics of the Expectation of Resolved Enstrophy

Figures 8.4(a), (b) and (c) illustrate the expectation of the resolved non-dimensional enstrophy, i.e. $(\bar{\omega}^2)_E$, in the $Q_{A\Delta}$ - $R_{A\Delta}$ phase plane. Generally speaking, the characteristics of the contour for $(\bar{\omega}^2)_E$ for the three different layers are similar to those of the JPF between $Q_{A\Delta}$ and $R_{A\Delta}$ shown previously in Figs. 8.2(b), (d) and (f). However, the contour of $(\bar{\omega}^2)_E$ in the viscous sublayer is more spread out than those in

^aThe constant multiplier N_B in the computer code is due to the consideration of amplifying some resultant effects. However, such a choice is optional.

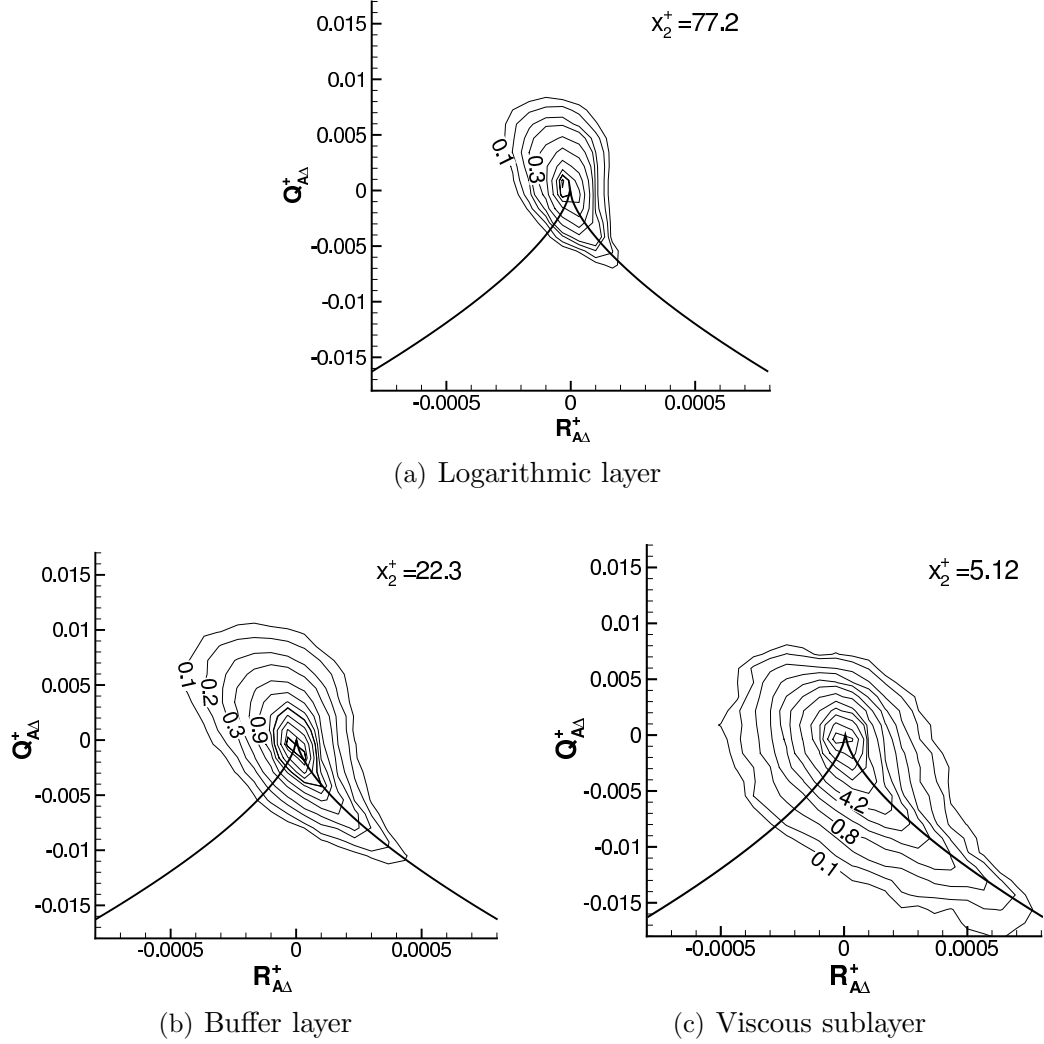


FIGURE 8.4: Time-averaged expectation of resolved non-dimensional enstrophy $(\bar{\omega}^2)_E$ associated with invariants $Q_{A\Delta}^+$ and $R_{A\Delta}^+$ ($Re = 2600$).

the buffer zone and logarithmic layer (based on the same minimum threshold of 0.1), whereas, as discussed previously, the contour in the buffer zone is the most spread out for the JPF between $Q_{A\Delta}$ and $R_{A\Delta}$. From Figs. 8.4(a), (b) and (c), it is observed that $(\bar{\omega}^2)_E$ peaks near the origin.

Figures 8.5(a), (b) and (c) replot $(\bar{\omega}^2)_E$ in the $Q_{S\Delta}$ – $R_{S\Delta}$ phase plane based on the invariants of the resolved strain rate tensor. The general patterns shown in these three figures for the three layers of wall-bounded Couette flow are very similar to those of the JPF between $Q_{S\Delta}$ and $R_{S\Delta}$ shown previously in Figs. 8.3(b), (d) and (f). As shown in Fig. 8.5(a), the contour of $(\bar{\omega}^2)_E$ in the logarithmic layer spreads out

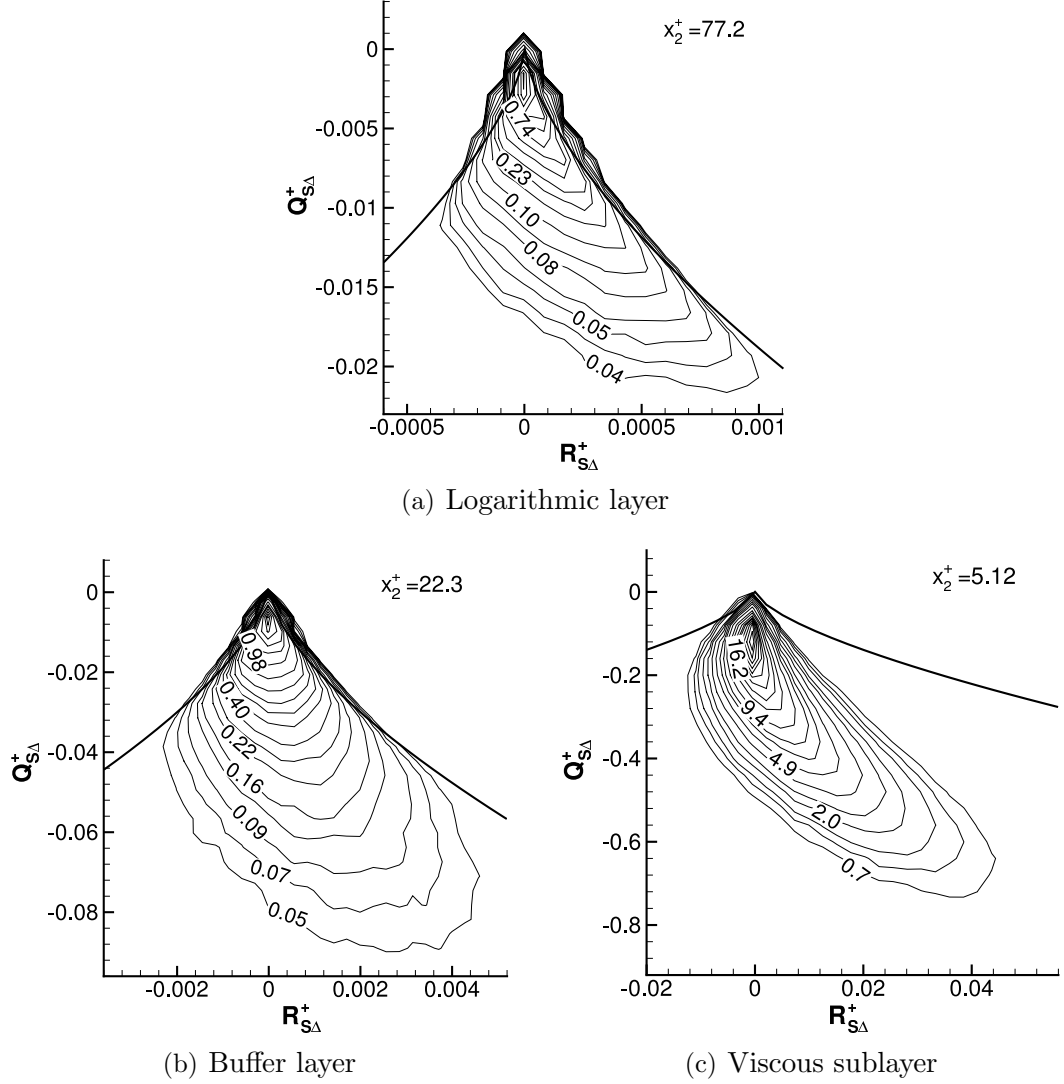


FIGURE 8.5: Time-averaged expectation of resolved non-dimensional enstrophy $(\bar{\omega}^2)_E$ associated with invariants $Q_{S\Delta}^+$ and $R_{S\Delta}^+$ ($Re = 2600$).

in the 4th quadrant and exhibits a strong preference for the axisymmetric expansion line ($D_{S\Delta} = 0$), while it peaks around the origin. This indicates that the strongest vorticity excitation is predominantly associated with a low local dissipation state, i.e. $\varepsilon_r = -4\nu Q_{S\Delta}$ is preferentially positive but close to zero. From Fig. 8.5(b), it is observed that $(\bar{\omega}^2)_E$ is more associated with the QTD states located in the 4th quadrant, but in general the contributions of all states ranging from the limiting 3-D axisymmetric compression pattern to the 2-D flow configuration and to the limiting 3-D axisymmetric expansion pattern on $(\bar{\omega}^2)_E$ are nontrivial. Figure 8.5(c) indicates

that the value of $(\bar{\omega}^2)_E$ is preferentially associated with the 2-D and QTD flow configurations in the viscous sublayer, with negligible contributions from the two limiting 3-D flow configurations. This again demonstrates the generic (quasi) 2-D feature of near-wall flow.

In contrast to the Figs. 8.4(b),(d) and (f) which have the highest $(\bar{\omega}^2)_E$ contour centered at the origin, it is obvious from Figs. 8.5(a), (b) and (c) that the contour corresponding to the largest value of $(\bar{\omega}^2)_E$ shifts vertically below the origin along the negative $Q_{S\Delta}$ axis, which is a familiar pattern that has been briefly discussed in the previous subsection 8.3.2 regarding the JPF contour. Previously, the discussion of this phenomenon only focused on the largest near-wall negative shift following Blackburn *et al.* [73]. It will now be discussed in a more general manner. From the definitions of the invariants, i.e. Eqs.(8.12) and (8.15), the following relations between the invariants of \bar{A}_{ij} and \bar{S}_{ij} can be obtained:

$$\begin{cases} Q_{S\Delta} = Q_{A\Delta} - \frac{1}{4}\bar{\omega}_i\bar{\omega}_i = Q_{A\Delta} - \frac{1}{4}\bar{\omega}^2 \\ R_{S\Delta} = R_{A\Delta} + \frac{1}{4}\bar{\omega}_i\bar{\omega}_j\bar{S}_{ij} = R_{A\Delta} + \frac{1}{4}\bar{\sigma} \end{cases} \quad (8.26)$$

whence, the origin condition in the $Q_{A\Delta}$ - $R_{A\Delta}$ plane, i.e. $Q_{A\Delta} = 0$ and $R_{A\Delta} = 0$, leads to

$$\begin{cases} Q_{S\Delta} = -\frac{1}{4}\bar{\omega}^2 \\ R_{S\Delta} = \frac{1}{4}\bar{\sigma} \end{cases} \quad (8.27)$$

Since $\bar{\omega}^2 \geq 0$, it is clear $Q_{S\Delta} \leq 0$ under the condition considered. Furthermore, since $Q_{S\Delta}$ is a measure of the local dissipation as show by Eq.(8.16), such a negative shift relates to a local dissipation magnitude of

$$\varepsilon_r = -4\nu Q_{S\Delta} = \nu\bar{\omega}^2 \quad (8.28)$$

Thus, it can be concluded that the origin of the $Q_{A\Delta}$ - $R_{A\Delta}$ phase plane, when mapped into the $Q_{S\Delta}$ - $R_{S\Delta}$ phase plane, corresponds to a negative shift along $Q_{S\Delta}$ axis, which is in the form of a local dissipation due to vortical excitations (enstrophy).

Now, we discuss the meaning of the second equation of (8.27). Although it is observed that $\bar{\sigma}$ is positively skewed in the logarithmic flow regime as well as in isotropic turbulence, both vortex stretching and compression are two realistic flow configurations and the sign of the instantaneous resolved enstrophy generation $\bar{\sigma}$ is undetermined (see Fig. 7.8). Therefore, the origin of the $Q_{A\Delta}-R_{A\Delta}$ phase plane, when mapped into the $Q_{S\Delta}-R_{S\Delta}$ phase plane, generates a horizontal coordinate, i.e. $R_{S\Delta} = \frac{1}{4}\bar{\sigma}$, whose sign can be either positive or negative. To summarize, a property is given as follows:

- In an incompressible flow regime where the resolved enstrophy is nontrivial, the origin of the $Q_{A\Delta}-R_{A\Delta}$ phase plane when mapped into the $Q_{S\Delta}-R_{S\Delta}$ phase plane, corresponds to $R_{S\Delta} = \frac{1}{4}\bar{\sigma}$ and $Q_{S\Delta} = -\frac{1}{4}\bar{\omega}^2$; the former can be either positive or negative, whereas the latter indicates a negative shift from the origin of the $Q_{S\Delta}-R_{S\Delta}$ phase plane along the $Q_{S\Delta}$ axis in the form of a local dissipation due to the vortical activity quantified as $\varepsilon_r = \nu\bar{\omega}^2$.

The above conclusion holds generally for any incompressible flow regime with vorticity excitations including the near-wall region. This conclusion is useful since the origin of the $Q_{A\Delta}-R_{A\Delta}$ phase plane is found [57, 64, 67, 68, 70, 73, 191] to be a special point that corresponds to the highest JPF level of the invariants $Q_{A\Delta}$ and $R_{A\Delta}$, and the largest value of the expectation of the resolved enstrophy, i.e. $(\bar{\omega}^2)_E$ as well.

We now focus on the near-wall behavior. Previously in subsection 8.3.2, the enlargement of the negative shift of the JPF in the $Q_{S\Delta}-R_{S\Delta}$ phase plane as the wall is approached, was reported and briefly explained following Blackburn *et al.* [73]. From Fig. 8.5, it is also observed that for $(\bar{\omega}^2)_E$, the negative shift in the sublayer is also larger than those in the buffer and logarithmic regions. However, a fine distinction between the two observed largest negative shifts of the JPF (i.e. $P(R_{S\Delta}, Q_{S\Delta})$) and $(\bar{\omega}^2)_E$ must be noted. From Eq.(8.24), it is clear that the value of $(\bar{\omega}^2)_E$ is decided not only by the JPF but also by the conditional expectation $\left\langle \frac{\bar{\omega}^2}{(u_\tau^2/\nu)^2} \middle| R_{S\Delta}, Q_{S\Delta} \right\rangle_c$. At

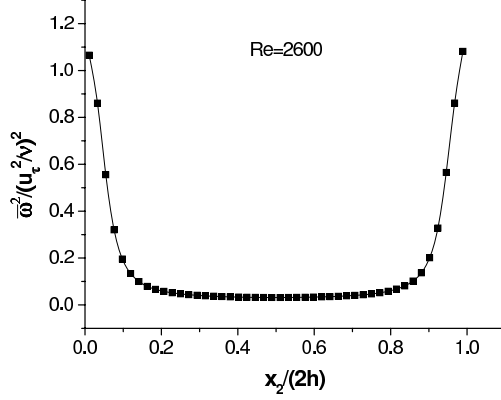


FIGURE 8.6: Plane and time-averaged profile for non-dimensional enstrophy.

the wall, the boundary condition for $\bar{\Omega}$ is given by

$$\bar{\Omega}_{ij}|_{wall} = \frac{1}{2} \begin{bmatrix} 0 & -\bar{u}_{1,2} & 0 \\ \bar{u}_{1,2} & 0 & \bar{u}_{3,2} \\ 0 & -\bar{u}_{3,2} & 0 \end{bmatrix}_{wall} \quad (8.29)$$

whence,

$$\bar{\omega}^2|_{wall} = 2(\bar{\Omega}_{ij}\bar{\Omega}_{ij})|_{wall} = (\bar{u}_{1,2}^2 + \bar{u}_{3,2}^2)|_{wall} > 0 \quad (8.30)$$

Furthermore, Fig. 8.6 indicates that the plane and time averaged value of $\bar{\omega}^2$ is overall maximum at the wall. From the boundary condition of \bar{S}_{ij} and $\bar{\Omega}_{ij}$ given by Eqs.(3.4) and (8.29), respectively, it can be determined that at the wall $Q_{A\Delta}|_{wall} = 0$ and $R_{A\Delta}|_{wall} = 0$. From the above analysis, it is concluded that:

- The state corresponding to the fluid regime right at the wall must occur at the origin of the $Q_{A\Delta}$ - $R_{A\Delta}$ phase plane, i.e. $Q_{A\Delta}|_{wall} = 0$ and $R_{A\Delta}|_{wall} = 0$. However, the reverse is not necessarily true, since it is clear from Eq.(8.26) that any states of $Q_{S\Delta} = -\bar{\omega}^2/4$ and $R_{S\Delta} = \bar{\sigma}/4$ are sufficient for $Q_{A\Delta}| = 0$ and $R_{A\Delta} = 0$.
- Among the contributions to the negative shift of the peak location of the enstrophy expectation from the origin along the $Q_{S\Delta}$ axis in the $Q_{S\Delta}$ - $R_{S\Delta}$ phase plane, that due to the wall condition is $Q_{S\Delta}|_{wall} = -(\bar{u}_{1,2}^2 + \bar{u}_{3,2}^2)|_{wall}/4$, which

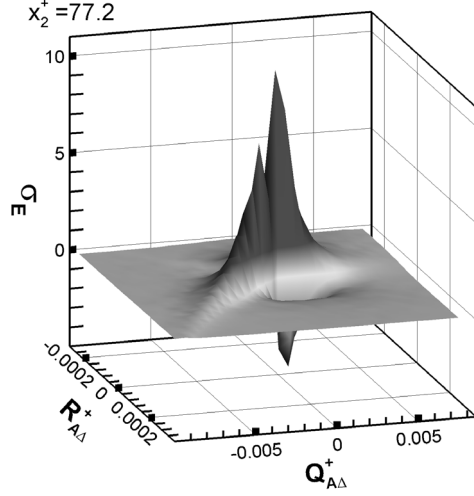
is linked to a wall dissipation rate through Eq.(8.16).

8.3.3.2 Characteristics of the Expectation of Resolved Enstrophy Generation

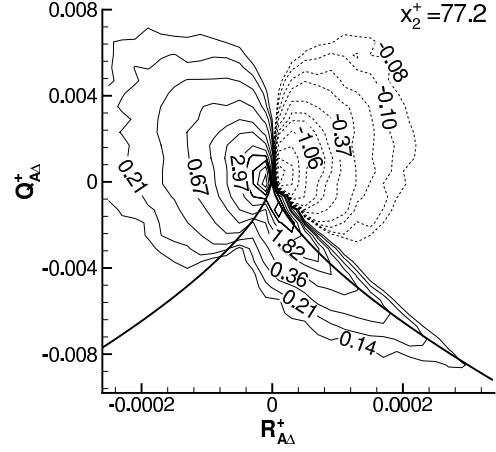
As we know, the resolved enstrophy generation $\bar{\sigma}$ is closely related to the process of local vortex stretching/compression and the cascade of kinetic energy dissipation. Currently, studies on the enstrophy and enstrophy generation using the method of turbulence geometrical statistics are popular, and numerical results based on this methodology have been presented systematically in chapter 7. Several research works on enstrophy and enstrophy generation based on the methodology of tensorial invariants and turbulence topology have also been seen in the literature, including the work of Chertkov *et al.* [191] based on a new special tetrad model and DNS analysis, and that of van der Bos *et al.* [70] based *a priori* LES analysis of HPIV measurements. In this subsection, some interesting phenomenological results on the resolved enstrophy generation and associated flow topologies will be discussed using the invariant phase planes. However, different than the approaches of Chertkov *et al.* [191] and van der Bos *et al.* [70], the method adopted in this study is based on *a posteriori* LES using the proposed DNM.

(i) Phenomenological Observation and the Flow Topology Classification

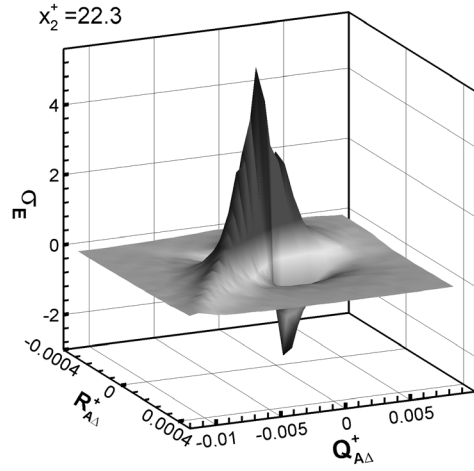
Figures 8.7(a)–(f) illustrate the expectation of resolved enstrophy generation σ_E (defined in Eq.(8.23)) in the $Q_{A\Delta}$ – $R_{A\Delta}$ phase plane. Compared with the features previously discussed for $(\bar{\omega}^2)_E$, the pattern of the σ_E contour is much more complex. For example, in Fig. 8.7(b) a “dragonfly-shape” contour is observed in the logarithmic layer rather than the previous pear-shape contour. Similar patterns of the σ_E expectation contour were also observed by Chertkov *et al.* [191] and van der Bos *et al.* [70]. The value of σ_E has two positive peaks corresponding to local vortex stretching flow configuration. Both positive peaks are close to the origin. The predominant positive peak in the region of $D_{A\Delta} > 0$ and $R_{A\Delta} < 0$ relates to the stable-focus/stretching



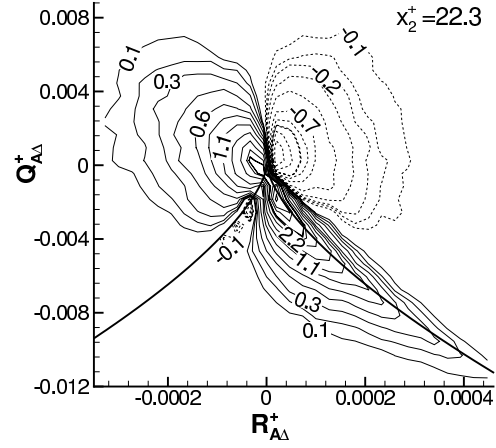
(a) Logarithmic layer



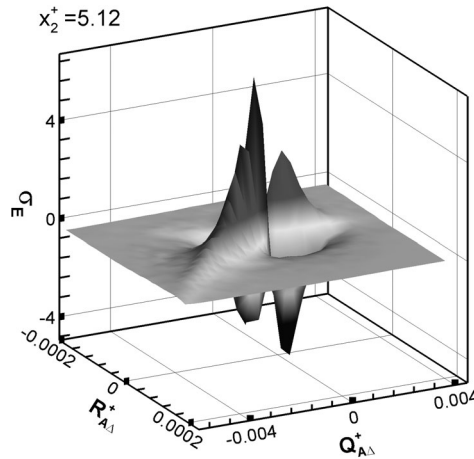
(b) Logarithmic layer (2-D contour)



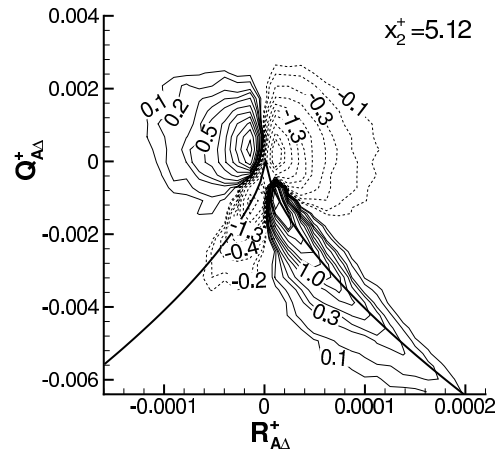
(c) Buffer layer



(d) Buffer layer (2-D contour)

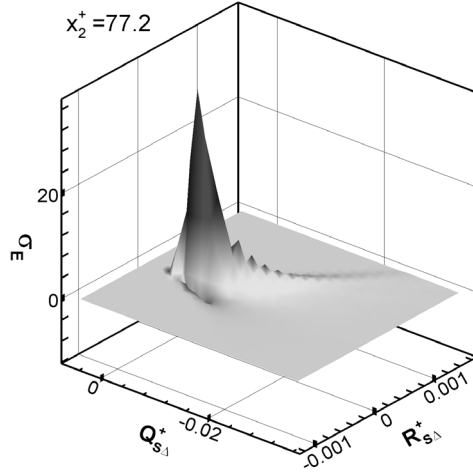


(e) Viscous sublayer

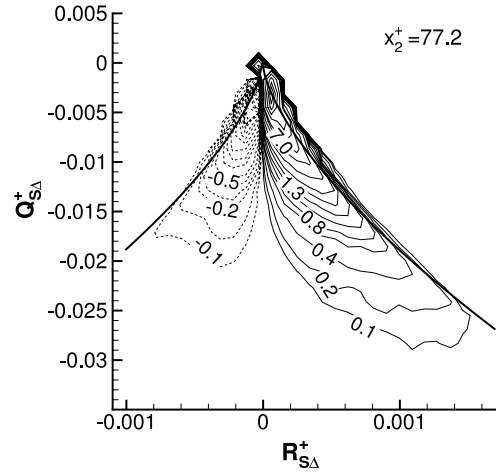


(f) Viscous sublayer (2-D contour)

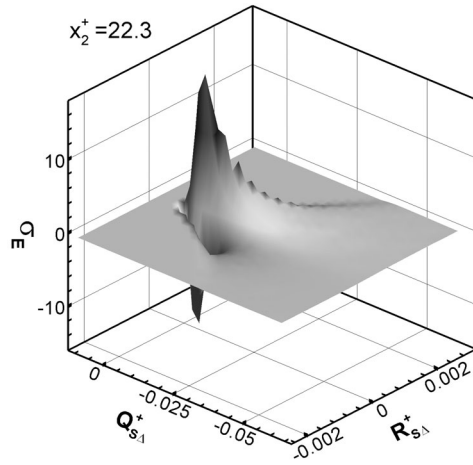
FIGURE 8.7: Time-averaged expectation of resolved non-dimensional enstrophy generation σ_E associated with invariants $Q_{A\Delta}^+$ and $R_{A\Delta}^+$ for $Re = 2600$ (positive values: solid lines, negative values: dashed line).



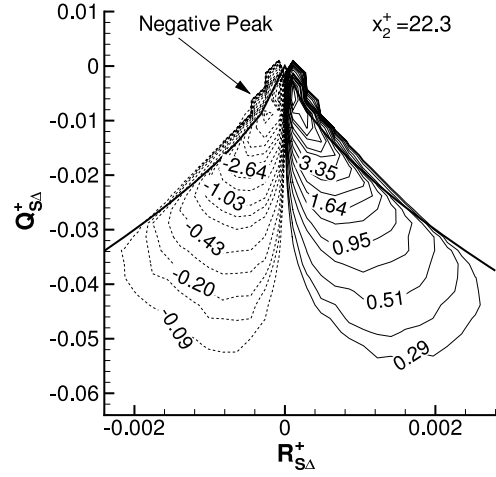
(a) Logarithmic layer



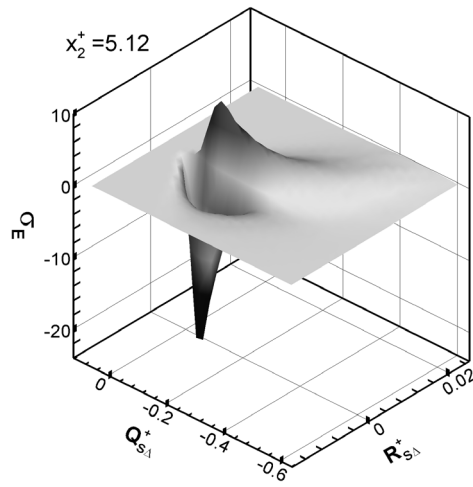
(b) Logarithmic layer (2-D contour)



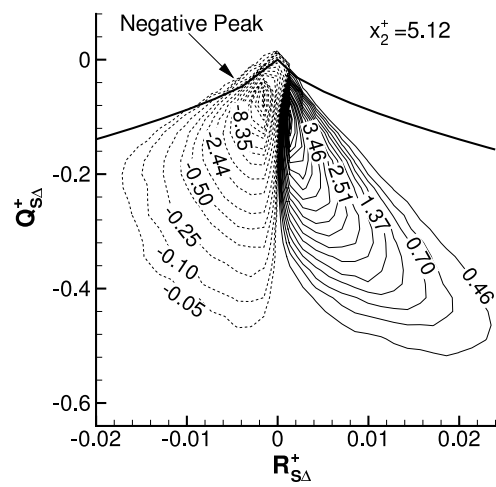
(c) Buffer layer



(d) Buffer layer (2-D contour)



(e) Viscous sublayer



(f) Viscous sublayer (2-D contour)

FIGURE 8.8: Time-averaged expectation of the resolved non-dimensional enstrophy generation σ_E associated with invariants $Q_{s\Delta}^+$ and $R_{s\Delta}^+$ for $Re = 2600$ (positive values: solid lines, negative values: dashed line).

flow topology, and the secondary positive peak in the 4th quadrant gathers around the right Vieillefosse line ($D_{A\Delta} = 0$). A negative σ_E peak is observed in the region of $D_{A\Delta} > 0$ and $R_{A\Delta} > 0$, which relates to the unstable-focus/compressing topology. Both the predominant positive contours and the predominant negative contours vividly form the shape of a pair of “eyes” of the “dragonfly”, while the secondary positive peak clinging to the Vieillefosse tail forms the “body” of the “dragonfly”.

Figures 8.7(c) and (d) for the buffer zone are generally similar to Figs. 8.7(a) and (b) for the logarithmic region. However, there are three differences: (1) the sequence of the two positive peaks is switched, i.e. the predominant peak is now located in the 4th quadrant along the right Vieillefosse line; (2) the “neck” of the dragonfly becomes thinner, indicating that the largest and the secondary positive peaks become more separate, although they are still connected at a low contour magnitude level; and (3) a small “mouth” of the dragonfly appears as a negative σ_E peak in the 3rd quadrant, corresponding to local vortex compression. In comparison with the topologies of the buffer zone, the above three tendencies are further amplified in the viscous sublayer, as shown in Figs. 8.7(e) and (f). The predominant peak located in the 4th quadrant increases in amplitude, and shifts away from the origin along the right Vieillefosse line $D_{A\Delta} = 0$. The neck of the dragonfly is now totally broken and in fact the four peaks (two positive and two negative) shown in Fig. 8.7(e) are entirely detached around the origin. Furthermore, the size of the “negative mouth” grows much larger.

Figures 8.8(a)–(f) show the expectation of the resolved enstrophy generation σ_E in the $Q_{S\Delta}$ – $R_{S\Delta}$ phase plane based on the resolved strain rate tensor. The pattern of the σ_E contour exhibited is very interesting. Generally, the previous “dragonfly-shape” contour with three or four peaks in the $Q_{A\Delta}$ – $R_{A\Delta}$ phase plane has now degenerated into a pair of “wings” in the $Q_{S\Delta}$ – $R_{S\Delta}$ phase plane: a negative wing located in the region of $D_{S\Delta} < 0$ and $R_{S\Delta} < 0$, and a positive wing located in the region of $D_{S\Delta} < 0$ and $R_{S\Delta} > 0$. The three limiting lines that separate the two wings correspond to: the left Vieillefosse line $D_{S\Delta} = 0$ (axisymmetric compression pattern), $R_{S\Delta}^+ = 0$ (2-D flow pattern), and right Vieillefosse line $D_{S\Delta} = 0$ (axisymmetric expansion pattern). In the logarithmic region, the positive peak dominates the negative

one as shown in Fig. 8.8(a), and the positive wing is longer than the negative one as shown in Fig. 8.8(b) (given the same threshold of $|\sigma_E| = 0.1$). Also in the logarithmic layer, the positive wing of the σ_E contour has a strong tendency toward the right Vieillefosse line which represents axisymmetric expansion, whereas, the negative wing shows a weak preference toward the left Vieillefosse line which represents axisymmetric compression. As shown in Figs. 8.8(c) and (d), in the buffer region, the negative and positive peaks for σ_E are about the same magnitude and therefore the two wings are more symmetric. It is observed that all flow topological states ranging from the axisymmetric compression pattern to the 2-D pattern for the negative wing, and from the 2-D pattern to the axisymmetric expansion pattern for the positive wing, are important for the σ_E distribution the $Q_{S\Delta}$ – $R_{S\Delta}$ phase plane. From Figs. 8.8(e) and (f), it is clear that in the viscous sublayer, the negative peak becomes dominant, and both wings move closer to the central 2-D line ($R_{S\Delta}^+ = 0$) and away from the left and right Vieillefosse lines. This indicates that in the sublayer, the local vortex compressing flow configuration becomes more significant. Also, both the vortex stretching and compressing configurations are preferentially associated with the 2-D and QTD flow patterns, with little influence from the 3-D axisymmetric expansion and compression patterns.

(ii) Further Discussion on the Contour Pattern of σ_E

From the above discussion on the statistical phenomenological results of σ_E , it is observed that there are generally two positive peaks, and one or two negative peaks of σ_E in the $Q_{A\Delta}$ – $R_{A\Delta}$ phase plane. It is also observed that there is always only one positive and one negative σ_E peak in the $Q_{S\Delta}$ – $R_{S\Delta}$ phase plane. As discussed earlier, all the positive and negative peaks shown in Fig. 8.7(a)–(f) gather around the origin of the $Q_{A\Delta}$ – $R_{A\Delta}$ phase plane. Considering Eq.(8.26), it is clear that the origin condition of $Q_{A\Delta} \rightarrow 0$ and $R_{A\Delta} \rightarrow 0$ corresponds to $Q_{S\Delta} \rightarrow -\frac{1}{4}\bar{\omega}^2 < 0$ and $R_{S\Delta} \rightarrow \frac{1}{4}\bar{\sigma}$. Thus, the states related to the largest σ_E values in the $Q_{A\Delta}$ – $R_{A\Delta}$ phase plane, when mapped into the $Q_{S\Delta}$ – $R_{S\Delta}$ phase plane must be within the region of $Q_{S\Delta} < 0$, while a further classification depends on the sign of $\bar{\sigma}$. Therefore, under

the considered condition, $R_{S\Delta} \rightarrow \frac{1}{4}\bar{\sigma}$, states of vortex stretching with large positive σ_E in the $Q_{A\Delta}$ - $R_{A\Delta}$ phase plane preferentially fall into the 4th quadrant of the $Q_{S\Delta}$ - $R_{S\Delta}$ phase plane, while states of vortex compression with large negative σ_E in the $Q_{A\Delta}$ - $R_{A\Delta}$ phase plane preferentially go into the 3rd quadrant of the $Q_{S\Delta}$ - $R_{S\Delta}$ phase plane. This explains the contour pattern of a pair of wings for the expectation of the resolved enstrophy generation in the $Q_{S\Delta}$ - $R_{S\Delta}$ phase plane.

8.3.3.3 Characteristics of the Expectation of Resolved SGS TKE Production Rate

In chapter 6, the characteristics of backscatter due to a negative rate of SGS TKE production ($\mathcal{P}_r = -\tau_{ij}^* \bar{S}_{ij}$) for the proposed DNM were investigated. In their paper, van der Bos *et al.* [70] proposed an interesting statistical technique for visualizing the forward and backward scatters of SGS TKE production rate in the invariant phase plane. The expectations for the forward scatter and backward scatter of non-dimensionalized SGS TKE (denoted as \mathcal{P}_{rE}^+ and \mathcal{P}_{rE}^- , respectively) can be defined by splitting Eq.(8.25) into two parts according to the sign of \mathcal{P}_r

$$\begin{aligned} \mathcal{P}_{rE}^+ &\stackrel{\text{def}}{=} N_B \cdot \sum_{\left(\frac{\mathcal{P}_r}{u_\tau^4/\nu}\right)} \left[\frac{\mathcal{P}_r}{u_\tau^4/\nu} \cdot P\left(\frac{\mathcal{P}_r}{u_\tau^4/\nu}, \mathcal{P}_r > 0, R_\Delta, Q_\Delta\right) \right] \\ &= N_B \cdot P(R_\Delta, Q_\Delta) \cdot \left\langle \frac{\mathcal{P}_r}{u_\tau^4/\nu} \middle| \mathcal{P}_r > 0, R_\Delta, Q_\Delta \right\rangle_c \cdot P(\mathcal{P}_r > 0 | R_\Delta, Q_\Delta) \end{aligned} \quad (8.31)$$

and

$$\begin{aligned} \mathcal{P}_{rE}^- &\stackrel{\text{def}}{=} N_B \cdot \sum_{\left(\frac{\mathcal{P}_r}{u_\tau^4/\nu}\right)} \left[\frac{\mathcal{P}_r}{u_\tau^4/\nu} \cdot P\left(\frac{\mathcal{P}_r}{u_\tau^4/\nu}, \mathcal{P}_r \leq 0, R_\Delta, Q_\Delta\right) \right] \\ &= N_B \cdot P(R_\Delta, Q_\Delta) \cdot \left\langle \frac{\mathcal{P}_r}{u_\tau^4/\nu} \middle| \mathcal{P}_r \leq 0, R_\Delta, Q_\Delta \right\rangle_c \cdot P(\mathcal{P}_r \leq 0 | R_\Delta, Q_\Delta) \end{aligned} \quad (8.32)$$

Again, the constant $N_B = 30 \times 30$ is arbitrary and both definitions can be used in accordance with the invariants of either \bar{A}_{ij} or \bar{S}_{ij} . From the above definitions, it is understood that $\mathcal{P}_{rE} = \mathcal{P}_{rE}^+ + \mathcal{P}_{rE}^-$.

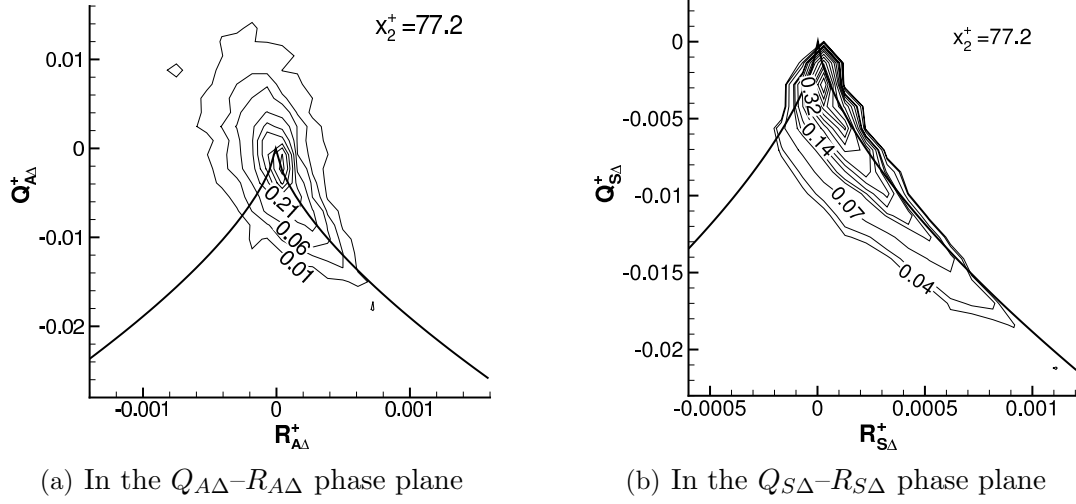


FIGURE 8.9: Time-averaged expectation of the resolved non-dimensional SGS TKE production rate \mathcal{P}_{rE} in the logarithmic region for $Re = 2600$.

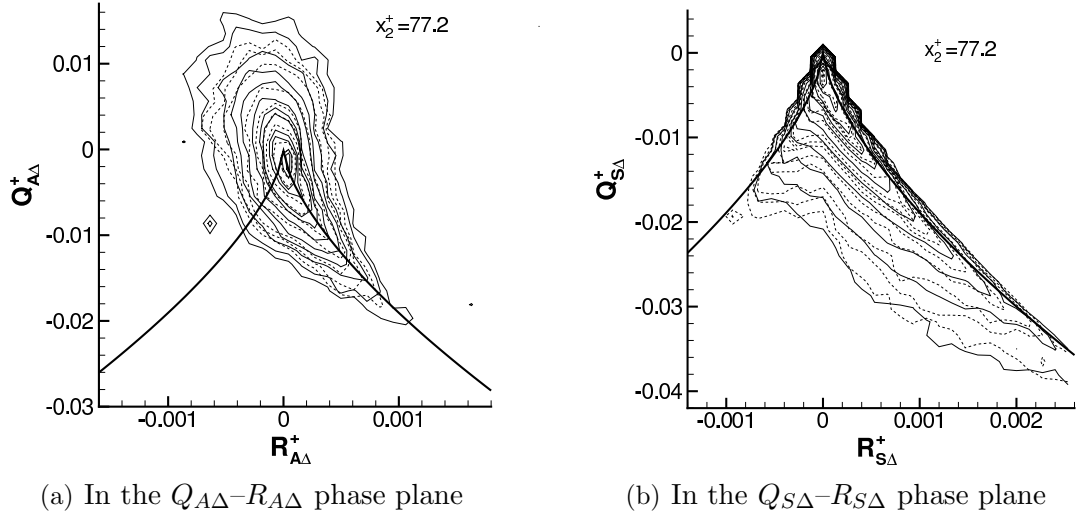
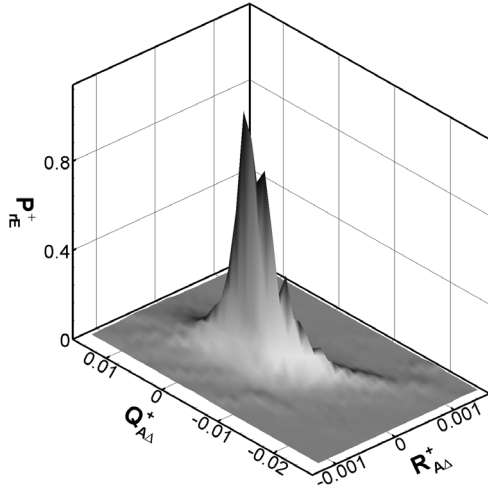
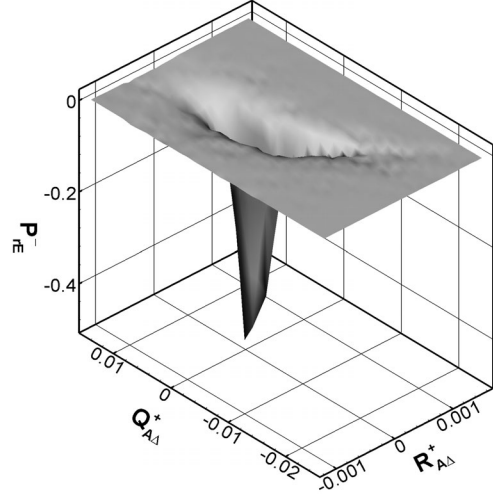


FIGURE 8.10: Time-averaged expectation of the resolved non-dimensional SGS TKE production rate \mathcal{P}_{rE} in the logarithmic region for $Re = 2600$ (Forward scatter \mathcal{P}_{rE}^+ and backward scatter \mathcal{P}_{rE}^- have been separated indicated by the solid and dashed contours, respectively).

Figures 8.9(a) and (b) illustrate the time-averaged expectation of the resolved \mathcal{P}_{rE} for the logarithmic region based on the DNM SGS stress model. Consistent with the previous illustration of \mathcal{P}_r in Fig. 6.17 based on plane and time averages, the overall SGS TKE transfer shown in Figs. 8.9(a) and (b) is positive, which indicates a net forward scattering of TKE from the filtered to the subgrid scales of motions. The

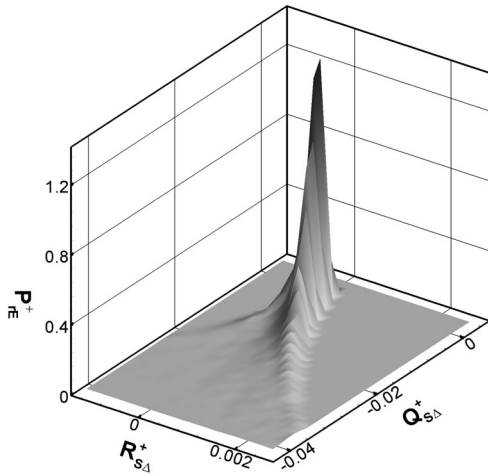


(a) Forward scatter

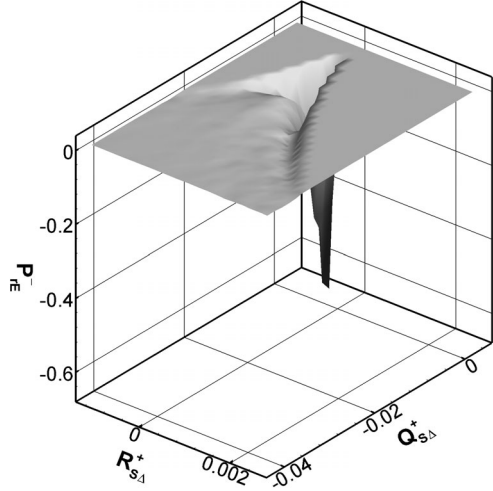


(b) Backscatter

FIGURE 8.11: Time-averaged expectation of the resolved SGS TKE production rate \mathcal{P}_{rE} in the $Q_{A\Delta}$ - $R_{A\Delta}$ phase plane ($x_2^+ = 77.2$, $Re = 2600$).



(a) Forward scatter



(b) Backscatter

FIGURE 8.12: Time-averaged expectation of the resolved SGS TKE production rate \mathcal{P}_{rE} in the $Q_{S\Delta}$ - $R_{S\Delta}$ phase plane ($x_2^+ = 77.2$, $Re = 2600$).

\mathcal{P}_{rE} contours shown in both Figs. 8.9(a) and (b) have a strong tendency to follow the right Vieillefosse lines of $D_{A\Delta} = 0$ and $D_{S\Delta} = 0$, and the latter indicates a local axisymmetric expansion flow configuration. Using Eqs.(8.31) and (8.32), the SGS TKE transfer rate is split into forward and backward scatters. Figures 8.10 (a) and (b) plot both net forward scatter and net backscatter contours in the two phase planes based on the invariants of both the resolved velocity gradient and strain rate tensors.

Clearly, the patterns of both the forward scatter and backscatter contours are similar to those of the general SGS TKE production rate shown in Figs. 8.9(a) and (b). These predicted features are consistent with the results reported by van der Bos *et al.* [70] based on *a priori* LES analysis of HPIV measurements. The net forward and backward scatters of SGS TKE in the logarithmic region are shown in Figs. 8.11 and 8.12 in a 3-D manner. From these 3-D figures, it clear that, although the magnitude of the peak value of backscatter is only about half of that of forward scatter, the effect of backscatter is significant. This in turn confirms the sound performance of the proposed DNM in terms of its capability of simulating the process of TKE transfer between the resolved and subgrid scales of motions.

8.4 Conclusions

In this chapter, turbulence flow topologies related to the invariants of both the resolved velocity gradient and strain rate tensors are studied. The analysis is based on *a posteriori* LES of turbulent Couette flow ($Re = 2600$) using the previously proposed DNM SGS stress model. As a further examination of the DNM in terms of its performance for predicting turbulence topological features, the obtained phenomenological results are compared with the reported conclusions based on DNS analysis [57, 64, 66–68, 73, 74, 190] and *a priori* LES process of experimental data [70]. Since tensorial invariants are used in the research, the results presented in the $Q_{A\Delta}$ – $R_{A\Delta}$ and $Q_{S\Delta}$ – $R_{S\Delta}$ phase planes are expected to be universal. The characteristics of the statistical expectation of enstrophy, enstrophy generation and SGS TKE transfer rate are also investigated and related to the local flow topologies.

(i) Summary of Flow Topologies in the Phase Plane of Tensorial Invariants

In the 2-D JPF contour diagram of $Q_{A\Delta}$ and $R_{A\Delta}$, a typical pear-shape contour pattern is observed in all three regimes: viscous sublayer, buffer zone, and logarithmic region. This pear-shape contour is centered at the origin and preferentially spreads into the 2nd and 4th quadrants, indicating the predominance of stable-focus/stretching

and unstable-node/saddle/saddle topologies, respectively. The preference of the JPF contour for the 2nd and 4th quadrants becomes the strongest in the buffer zone. There is a strong tendency for the JPF contour to cluster around the right Vieille-fosse line ($D_{A\Delta} = 0$). These features are as expected and consistent with the reported results [57, 64, 66–68, 70, 73, 74, 186, 190].

The $Q_{S\Delta}$ – $R_{S\Delta}$ phase plane based on the invariants of the filtered strain rate tensor is also useful for revealing the flow topology and geometrical characteristics, especially in visualizing local dissipation and relating flow topologies to the relative eigenvalue ratio of the filtered strain rate tensor, e.g. the axisymmetric expansion and compression, and 2-D and QTD flow patterns. On the other hand, it should be pointed out that the $Q_{S\Delta}$ – $R_{S\Delta}$ phase plane is not reliable for demonstrating the most probable eigenvalue ratio of \bar{S}_{ij} in a quantitative manner, since all states of high probability cluster around the origin, where the difference between the curves corresponding to different flow patterns is hardly distinguishable. Since \bar{S}_{ij} is a real symmetric tensor, all three eigenvalues must be real, which explains why all states of flow topologies identified in the simulations are bounded by $D_{S\Delta} \leq 0$. It is observed that in the logarithmic region, there is a strong tendency for axisymmetric expansion; in the buffer zone, all the states of flow configurations ranging from the axisymmetric compression pattern to the 2-D configuration and to the axisymmetric expansion pattern exist; in the sublayer, the most probable state of flow configuration is close to 2-D and deviates from the limiting 3-D patterns of axisymmetric expansion and compression. Such a feature of the sublayer profoundly reveals the (quasi) 2-D nature of near-wall turbulent flow.

(ii) Summary of the Characteristics of Enstrophy in the Phase Plane of Tensorial Invariants

The expectation of enstrophy $(\bar{\omega}^2)_E$ based on the JPF $P(R_\Delta, Q_\Delta, \bar{\omega}^2)$ is calculated and illustrated in both the $Q_{A\Delta}$ – $R_{A\Delta}$ and $Q_{S\Delta}$ – $R_{S\Delta}$ phase planes. Generally in the $Q_{A\Delta}$ – $R_{A\Delta}$ phase plane, a pear-shape contour of $(\bar{\omega}^2)_E$ is observed, which is consistent with the reported results [191]. In the $Q_{S\Delta}$ – $R_{S\Delta}$ phase plane, the contour of $(\bar{\omega}^2)_E$ for

the logarithmic layer spreads out in the 4th quadrant and shows a strong preference for the axisymmetric expansion line ($D_{S\Delta} = 0$); in the buffer zone, $(\bar{\omega}^2)_E$ is in general more associated with the QTD states located in the 4th quadrant of the $Q_{S\Delta}$ – $R_{S\Delta}$ phase plane, however, the effects of all states of flow configurations are noticeable; finally in the sublayer, $(\bar{\omega}^2)_E$ is preferentially associated with the QTD and 2-D flow configurations, which again validates the generic (quasi) 2-D nature of the near-wall flow.

It is concluded during the research that for a flow regime where the resolved enstrophy is nontrivial, the origin of the $Q_{A\Delta}$ – $R_{A\Delta}$ phase plane when mapped into the $Q_{S\Delta}$ – $R_{S\Delta}$ phase plane, corresponds to $R_{S\Delta} = \frac{1}{4}\bar{\sigma}$ and $Q_{S\Delta} = -\frac{1}{4}\bar{\omega}^2$, the latter indicating a negative shift from the origin along the $Q_{S\Delta}$ axis in the $Q_{S\Delta}$ – $R_{S\Delta}$ phase plane associated with a local dissipation due to vorticity excitations. The above conclusion holds generally for any flow regime with vorticity “worms”.

It is also concluded that the state corresponding to the fluid regime right at the wall must be located at the origin of the $Q_{A\Delta}$ – $R_{A\Delta}$ phase plane, i.e. $Q_{A\Delta}|_{wall} = 0$ and $R_{A\Delta}|_{wall} = 0$; however, the reverse is not necessarily true. Also, among the contributions to the negative shift of the peak location of the enstrophy expectation from the origin along the $Q_{S\Delta}$ axis in the $Q_{S\Delta}$ – $R_{S\Delta}$ phase plane, that due to the wall condition is $Q_{S\Delta}|_{wall} = -(\bar{u}_{1,2}^2 + \bar{u}_{3,2}^2)|_{wall}/4$, which is linked directly to the wall dissipation.

(iii) Summary of the Characteristics of Enstrophy Generation in the Phase Plane of Tensorial Invariants

The expectation of the non-dimensionalized enstrophy generation σ_E is studied in both the $Q_{A\Delta}$ – $R_{A\Delta}$ and $Q_{S\Delta}$ – $R_{S\Delta}$ phase planes. In the $Q_{A\Delta}$ – $R_{A\Delta}$ phase plane, the value of σ_E has two positive peaks, both close to the origin in the logarithmic region. The predominant positive peak is located in the region of $D_{A\Delta} > 0$ and $R_{A\Delta} < 0$ and is related to a stable-focus/stretching flow topology, while the secondary positive peak is in the 4th quadrant preferentially gathering around the right Vieillefosse

line ($D_{A\Delta} = 0$). The region of $D_{A\Delta} > 0$ and $R_{A\Delta} > 0$ is linked to an unstable-focus/compressing topology and is characterized by a negative σ_E peak. Generally, in the logarithmic layer, a “dragonfly-shape” contour is observed which agrees with the reported pattern [70, 191]. As the wall is approached, the magnitudes of the two positive peaks switch, i.e. the location for the largest one changes to the 4th quadrant of the $Q_{A\Delta}$ – $R_{A\Delta}$ phase plane. Also, a secondary negative σ_E peak begins to appear in the 3rd quadrant in the buffer zone and becomes strongest in the sublayer.

It is found that the sign of the resolved enstrophy generation plays an important role in the mapping relation between the $Q_{A\Delta}$ – $R_{A\Delta}$ phase plane and the $Q_{S\Delta}$ – $R_{S\Delta}$ phase plane in terms of the positive or negative σ_E peaks. In the $Q_{S\Delta}$ – $R_{S\Delta}$ phase plane, the σ_E contours have the shape of a pair of “wings”: the negative contours are confined between the left Vieillefosse line $D_{S\Delta} = 0$ (related to axisymmetric compression) and $R_{S\Delta} = 0$ (related to 2-D flow configuration), while the positive contour is confined between $R_{S\Delta} = 0$ and the right Vieillefosse line $D_{S\Delta} = 0$ (related to axisymmetric expansion). In the logarithmic region, the positive peak dominates the negative one and shows a strong tendency toward the right Vieillefosse line, whereas, the negative wing shows a weak preference for the left Vieillefosse line. In the buffer zone, both the negative and positive peaks for σ_E are about the same magnitude, and all states ranging from the limiting axisymmetric compression pattern to the 2-D pattern and to the limiting axisymmetric expansion pattern are important to σ_E . In the viscous sublayer, the negative σ_E peak becomes dominant and both wings approach closer to the 2-D line ($R_{S\Delta} = 0$) moving away from both the left and right limiting Vieillefosse lines, which again indicates the generic 2-D nature of near-wall flow. The wing-shape contours of σ_E in the $Q_{S\Delta}$ – $R_{S\Delta}$ phase plane and the 2-D topology of near-wall flow are very interesting and considered as important phenomenological results observed in this research.

(iv) Summary of the Characteristics of Forward and Backward Scatter of SGS TKE Transfer in the Phase Plane of Tensorial Invariants

The expectations for the forward and backward scatters of non-dimensional SGS TKE

are separated from each other and illustrated using both the $Q_{A\Delta}$ - $R_{A\Delta}$ and $Q_{S\Delta}$ - $R_{S\Delta}$ phase planes. The research focuses on turbulence in the core region of the channel. In both types of phase planes, the overall net TKE transfer rate from the resolved to the SGS scales is observed to be positive. In the $Q_{A\Delta}$ - $R_{A\Delta}$ phase plane, a prototypical pear-shape contour of the general term \mathcal{P}_{rE} is observed; furthermore, the contours of both the net forward and net backward scatters, i.e. \mathcal{P}_{rE}^+ and \mathcal{P}_{rE}^- , also show the pear-shape pattern independently and a strong tendency to follow the right Vieillefosse line ($D_{A\Delta} = 0$ for $R_{A\Delta} > 0$). In the $Q_{S\Delta}$ - $R_{S\Delta}$ phase plane, a similar tendency is observed that the contours corresponding to larger values of \mathcal{P}_{rE} , \mathcal{P}_{rE}^+ and \mathcal{P}_{rE}^- all cling to the right Vieillefosse line ($D_{S\Delta} = 0$ for $R_{S\Delta} > 0$), which explicitly indicates that SGS TKE flux is preferentially associated with the axisymmetric expansion flow configuration in the logarithmic region. Generally, the magnitude of the backscatter level is about half that of forward scatter in the invariant phase planes, indicating that the effect of backscatter is significant in a LES approach based on the proposed DNM SGS stress model.

Chapter 9

Conclusions and Future Work

This dissertation focuses on studying dynamic SGS stress models and the turbulence phenomenology of the resolved scale motions. It is based on six inter-related research topics, which were performed as independent research projects during the author's Ph.D. program. Due to the broad coverage of the subjects, these six topics are organized in a coherent as well as self-contained manner presented in chapters 3—8. In each of these six chapters, a detailed literature review and concluding remarks have been presented for the specific topic. In this chapter, a general review on the contributions of this dissertation and comments on future studies will be presented.

9.1 Review of Major Contributions

(i) A Direct Solution Scheme for the Integral Type Dynamic Localization SGS Model

In chapter 3, the integral type dynamic localization model in the form of a Fredholm integral equation of the second kind introduced by Ghosal *et al.* [40] has been applied for simulating turbulent Couette flow. Two efficient direct solution schemes, i.e. a penta-diagonal banded linear system (PDS) and a tri-diagonal banded linear system (TDS) based on the 3-D and 2-D discrete filters of Sagaut and Grohens [35] have been developed to solve the Fredholm integral equation of the second kind (FIE2). These two efficient solution schemes are applicable to turbulence with two homogeneous

dimensions. The computational cost for solving the FIE2 using the TDS and PDS is reduced to the same order as that for the DM of Lilly [20], which is substantially less than a conventional iterative solver [49, 137].

(ii) An Integral Type Dynamic Localization Two-Parameter Mixed Subgrid-Scale Model

In the current approaches using the C_L – C_S type dynamic two-parameter mixed SGS stress model (DMM2), a mathematical inconsistency exists due to the conventional assumption of incomplete spatial invariance (ISI) adopted in the procedure for developing the modelling formulation [37, 44, 48, 50, 143]. In chapter 4, the C_L – C_S type DMM2 has been localized using functional variational methods and the mathematical inconsistency has been avoided. A system of two integral equations has been obtained, which governs the instantaneous optimal spatial distribution of the two model coefficients of the DMM2. The proposed new modelling procedure is demonstrated to work very well in the numerical simulation of turbulent Couette flow using a relatively coarse grid. It can successfully predict many pertinent features such as the logarithmic velocity profile and the correct level of the friction coefficient. Attributed to both the scale similarity and SGS viscosity parts of the model, the new modelling approach has the desirable feature of self-adjusting forward and backward scatters of the SGS turbulence kinetic energy (TKE) between the resolved and subgrid scales of motions.

(iii) Consistent Localization and Constitutive Relation of the Dynamic Smagorinsky SGS Stress Model

Previous integral type dynamic localization SGS models [40, 137, 155] achieved the goal of localization by minimizing a globally integrated residual functional. In chapter 5, a consistent mathematical treatment is proposed for localizing the coefficient C_S of the dynamic Smagorinsky SGS stress model, and the Smagorinsky constitutive relation is revisited from the viewpoint of functional variation and function approximation. The proposed approach minimizes the local error density functional \mathcal{Q} directly without

resorting to a global integration. A theorem on the sufficient and necessary condition for localizing the dynamic Smagorinsky model has been obtained, which is in the form of an orthogonal condition (OC) and controls the localization model coefficient for the dynamic Smagorinsky SGS model. The OC is a useful tool for dynamic SGS modelling optimization, which unifies some conventional modelling formulations as its special theoretical derivatives under different restrictions, including the DM of Germano *et al.* [19] and Lilly [20], and the FIE2 of Ghosal *et al.* [40]. The OC also results in a new dynamic SGS stress model in the form of Picard’s integral equation (PIE). The new PIE is necessary to make the local error density \mathcal{Q} minimum. Since the new PIE has one less convolution operation than the FIE2 introduced earlier by Ghosal *et al.* [40], it is less expensive to compute.

Physical meanings for such grid and test-grid level tensors as α_{ij} , β_{ij} , M_{ij} , M'_{ij} , \mathcal{L}_{ij}^{appr*} and \mathcal{L}_{ij}^{proj*} have been proposed by identifying their role in various constitutive and constructive relations. The construction of the tensorial approximation space for the projection of the Leonard stress has also been discussed. These tensorial approximation spaces for the Leonard stress are essential to the optimization methods adopted for deriving the dynamic localization models. It is observed that the modulus of the filtered strain rate tensor $|\bar{S}|$ has a significant influence on the relative magnitudes of the SGS stress τ_{ij} , SGS TKE production rate \mathcal{P}_r , SGS viscosity ν_{sgs} , and model coefficient C_S .

Chapter 5 attempts to investigate the properties of the localization SGS stress model within the framework of the Smagorinsky constitutive relation. It is understood that many drawbacks of the (dynamic) Smagorinsky models originate from the simplicity of its adopted Boussinesq hypothesis, e.g. a strict requirement that the principal axes of the SGS stress tensor be aligned with those of the filtered strain rate tensor. The work presented in chapters 6—8 is motivated by a desire to find an improved non-Smagorinsky constitutive relation, which allows the dynamic SGS model to be able to simulate flows in a more realistic way in terms of the conventional scaling behavior, e.g. the velocity profile and resolved Reynolds shear stress distribution, as well as the advanced turbulence geometrical and topological properties of

the resolved scale motions.

(iv) A Novel Dynamic Nonlinear Subgrid-Scale Stress Model

In chapter 6, the explicit quadratic tensorial polynomial constitutive relation of Speziale [108, 109] is considered for building a dynamic nonlinear SGS model (DNM). The proposed DNM is observed to be more robust than the conventional DM [19, 20] and can be applied locally in a stable way without the need for the ‘standard’ plane averaging technique to avoid a potential singularity problem. The proposed DNM demonstrates a variety of self-calibrating mechanisms through its three coefficients and the tensorial geometric relations between the SGS stress and the three constituent tensors, which in turn provides more degrees of freedom for predicting the forward and backward scattering processes of the TKE flux between the resolved and subgrid scales. This is in contrast to the conventional DM, which can only reflect the SGS TKE scatter in two extreme ways: either fully forward or fully backward scatter, and thus can result in a numerical instability due to an unrealistic excessive prediction of backscatter.

Although the first and third nonlinear constituent terms are independent, they share the same set of eigenvectors and thus the alignment between the principal axes of these two constituent tensors can only be either parallel or orthogonal. An identity is found to relate the eigenvalues of their effective tensorial parts. If the roots of the characteristic equation of \mathbf{S} and $\mathbf{\Gamma}$ are distinct, the local flow configuration corresponds to tubelike and sheetlike structures; however, if the characteristic equations have dual roots, additional flow configurations of local axisymmetric expansion and compression, and local degenerate 2-D flow pattern (for $\mathbf{\Gamma}$ only) are included. The first constituent term (the Smagorinsky component), β_{ij} , predominates forward scatter of TKE from the resolved to the subgrid scales of motions. The second nonlinear constituent term, γ_{ij} , is strictly orthogonal to the resolved strain rate tensor, \bar{S}_{ij} , and thus, it does not make any contribution to the rate of SGS TKE production. In general, the backscatter phenomenon is preferentially associated with the third nonlinear constituent term, η_{ij} . The rate of SGS TKE production due to the third constituent

term is proportional to the resolved strain skewness, i.e. $\bar{\mathcal{I}}_{S3} = \alpha_S^3 + \beta_S^3 + \gamma_S^3$, for both scenarios of local tubelike and sheetlike structures.

(v) Turbulence Geometrical Statistics

In chapter 7, the recently developed research methodology of geometrical statistics has been utilized for examining the characteristics of the resolved scale motions of Couette flow. The research approach presented is new and featured by the concepts of *a posteriori* LES prediction, dynamic nonlinear SGS model, geometrical statistics and near-wall anisotropy, following the recent *a priori* LES reports by Tao *et al.* [29, 99] and Horiuti [100] on (quasi) isotropic flows. The *a posteriori* LES results obtained using the proposed DNM have been compared with those based on DNS, experimental and *a priori* LES approaches reported in the literature, and the sound performance of the DNM is further confirmed in terms of the predicted turbulence geometrical features.

In the logarithmic region, a prevalence of helical structures and a pattern of streamwise aligned resolved vorticity vector is observed. As the wall is approached, a state of $\bar{\omega}$ being perpendicular to the resolved velocity vector becomes highly probable. In the simulation, several important prototypical features are reproduced, e.g. the preferred alignment between the resolved vorticity vector $\bar{\omega}$ and the intermediate eigenvector of \bar{S}_{ij} . In general, as x_2^+ decreases, the peak of the PF corresponding to the most probable states increases drastically. An interesting pattern of a “triangle shape” 2-D JPF contour is observed in the $\Theta(\bar{\omega}, \mathbf{e}_{S\beta})$ – $\Theta(\bar{\omega}, \mathbf{e}_{S\gamma})$ plane, which represents a general characteristic inherent to the relative orientation between a vector and an orthonormal triad. It is argued in this dissertation that the preferred alignment pattern, i.e. $\Theta(\bar{\omega}, \mathbf{e}_{S\beta}) = 0^\circ$ and $\Theta(\bar{\omega}, \mathbf{e}_{S\gamma}) = 90^\circ$ is not limited to (quasi) isotropic turbulence as is popularly reported, but instead observed to be even more generic to the viscous sublayer.

In the logarithmic layer, a strong alignment between $\bar{\omega}$ and the resolved vortex stretching vector $\bar{\mathbf{w}}$ is predicted by the simulation, which suggests a dominant

local vortex stretching flow configuration associated with positively skewed resolved enstrophy generation. However, in the viscous sublayer, both local vortex stretching and compressing flow configurations are highly probable. It is confirmed in this research that the local QTD state of turbulence is intrinsically different than a pure 2-D turbulence since it possesses non-vanishing enstrophy generation and a nontrivial intermediate eigenvalue of the filtered strain rate tensor [77]. It is observed that the alignment between $\bar{\omega}$ and $\mathbf{e}_{S\beta}$ and that between $\bar{\omega}$ and $\bar{\mathbf{w}}$ both become highly probable when the excitation of vorticity is the weakest, which indicates that the background turbulence is not locally a “structureless random sea”. Various local structure patterns exist in all regions with or without high excitation of the resolved vorticity.

Plane and time-averaged profiles and three different statistical methods, i.e. s^* -PF, β^* -PF and (β/α) -PF, are used to investigate the relative eigenvalue ratio of the negative SGS stress and three constituent tensors. Generally from the 1-D PFs of the eigenvalue ratio of the filtered strain rate tensor, an obvious “viscous-shift” of the most probable state is observed as x_2^+ decreases, which is due to the wall-normal anisotropic effect. The β^* -PF profile shows that the most probable state corresponds to $\alpha_S : \beta_S : \gamma_S = 3.6 : 1 : -4.6$ in the core region, which matches very well with the experimental result [76]. The most probable value of $s^* = 0.9$ obtained from s^* -PF, agrees very well with the DNS result reported by Lund *et al.* [59], indicating that the most probable flow configuration in the core region is close to the axisymmetric expansion pattern. It is found during the research that in the case when β_S is close to 0 (especially in the viscous sublayer), all three statistical methods based on β^* -PF, s^* -PF and (β/α) -PF tend to become singular and the calculation of the relative eigenvalue ratio becomes unstable. A 2-D JPF is used to investigate the eigenvalue ratio for $-\tau_{ij}^*$, which avoids the singularity problem encountered in the 1-D PF. The most probable ratio predicted using the 2-D JPF for $-\tau_{ij}^*$ is found to be $\alpha_{-\tau} : \beta_{-\tau} : \gamma_{-\tau} = 3 : 0.75 : -4.75$ in the core region.

(vi) Turbulence Topology

As a further examination of the performance of the DNM, turbulence flow topologies related to the invariants of both the resolved velocity gradient and strain rate tensors have been studied in chapter 8. The research work presented in this chapter is novel since it proposes an approach to study turbulence topologies through *a posteriori* LES based on the SGS model. Some of the obtained phenomenological results are compared to those available in the literature. Besides these results, some new phenomenological results are also observed during the study, e.g. a contour pattern of a pair of wings for the expectation of the resolved enstrophy generation and the negative shift of the expectation of the resolved enstrophy in the tensorial invariant phase plane of \bar{S}_{ij} . These new results are very interesting and efforts have been made by the author for their analytical explanations. The observation of these new phenomenological results are to some extent, not surprising, since turbulence topology itself, as a newly developed research methodology, was introduced into the fluids community only about a decade ago marked by the pioneering works of Chong and Perry [58], Chen *et al.* [57] and Cantwell [63]; and its implementation into LES has even a shorter history following the *a priori* LES works of Borue and Orszag [165] and van der Bos *et al.* [70].

In the 2-D JPF contour diagram of $Q_{A\Delta}$ and $R_{A\Delta}$ (invariants of the resolved velocity gradient tensor), a typical pear-shape contour is observed in all three regimes: viscous sublayer, buffer zone and logarithmic region. The pear-shape contour is centered at the origin and preferentially spreads into the 2nd and 4th quadrants, indicating a prevalence of stable-focus/stretching and unstable-node/saddle/saddle topologies, respectively. It is also observed that the JPF contour is predominant along the right Vieillefosse line ($D_{A\Delta} = 0$ for $R_{A\Delta} > 0$). The $Q_{S\Delta}$ – $R_{S\Delta}$ phase plane (based on the invariants of the filtered strain rate tensor) is useful for visualizing local dissipation and relating flow topologies to the relative eigenvalue ratio of the filtered strain rate tensor in a qualitative manner. However, it is argued in this dissertation that the $Q_{S\Delta}$ – $R_{S\Delta}$ phase plane is not reliable for determining the most probable eigenvalue ratio of \bar{S}_{ij} , since all states of high probability cluster around the origin.

The expectation of the resolved normalized enstrophy $(\bar{\omega}^2)_E$ based on the JPF $P(R_\Delta, Q_\Delta, \bar{\omega}^2)$ has been investigated in both the $Q_{A\Delta}-R_{A\Delta}$ and $Q_{S\Delta}-R_{S\Delta}$ phase planes. Generally in the $Q_{A\Delta}-R_{A\Delta}$ phase plane, a pear-shape contour of $(\bar{\omega}^2)_E$ is observed. It is concluded in this dissertation that in a flow regime where the resolved enstrophy is nontrivial, the origin of the $Q_{A\Delta}-R_{A\Delta}$ phase plane if mapped into the $Q_{S\Delta}-R_{S\Delta}$ phase plane, corresponds to $R_{S\Delta} = \frac{1}{4}\bar{\sigma}$ and $Q_{S\Delta} = -\frac{1}{4}\bar{\omega}^2$; the latter indicates a negative shift from the origin along the $Q_{S\Delta}$ axis in the $Q_{S\Delta}-R_{S\Delta}$ phase plane in the form of a local dissipation due to vorticity excitations. The above conclusion holds generally for any flow regime with active vorticity excitations. It is also concluded that a state corresponding to the fluid regime right at the wall must be located at the origin of the $Q_{A\Delta}-R_{A\Delta}$ phase plane, however, the reverse is not necessarily true.

For the logarithmic region, the expectation of the non-dimensional enstrophy generation σ_E has two positive peaks, both close to the origin of the $Q_{A\Delta}-R_{A\Delta}$ phase plane. The predominant positive peak is located in the region of $D_{A\Delta} > 0$ and $R_{A\Delta} < 0$ and is related to a stable-focus/stretching flow topology; while the secondary positive peak is in the fourth quadrant of the $Q_{A\Delta}-R_{A\Delta}$ phase plane and relates to the local vortex stretching flow configuration. A negative σ_n peak is located in the region of $D_{A\Delta} > 0$ and $R_{A\Delta} > 0$ and linked to an unstable-focus/compressing topology. Generally, in the logarithmic layer, a “dragonfly-shape” contour is observed. As the wall is approached, the magnitudes of the two positive peaks switch. Also, a secondary negative σ_E peak begins to appear in the 3rd quadrant in the buffer zone and becomes strongest in the sublayer. In the $Q_{S\Delta}-R_{S\Delta}$ phase plane, the σ_E contours are found to possess a pattern of a pair of “wings” restricted by the three limiting flow configurations, i.e. the axisymmetric compression, 2-D flow pattern, and axisymmetric expansion. In the logarithmic region, the positive wing dominates the negative one and shows a strong tendency to approach the right Vieillefosse line ($D_{S\Delta} = 0$ for $R_{S\Delta} > 0$), whereas the negative wing shows a weak preference for the left Vieillefosse line ($D_{S\Delta} = 0$ for $R_{S\Delta} < 0$). In the buffer zone, all states ranging from the limiting axisymmetric compression pattern to the 2-D pattern and to the limiting

axisymmetric expansion pattern are significant to the σ_E distribution. In the viscous sublayer, the negative σ_E peak becomes dominant and both wings strongly approach the 2-D flow line, moving away from the curves corresponding to 3-D axisymmetric compression and expansion flow configurations. Such a feature in the sublayer is found to be important, since it reflects the 2-D nature of near-wall flows.

The expectation of the SGS TKE production rate (\mathcal{P}_{rE}) in the central logarithmic region has been studied using the invariant phase planes. Overall, \mathcal{P}_{rE} is observed to be positive indicating a general net TKE flux from the resolved to the subgrid scales. In the $Q_{A\Delta}-R_{A\Delta}$ phase plane, a prototypical pear-shape contour is observed for \mathcal{P}_{rE} . The net forward and net backward scatters, i.e. \mathcal{P}_{rE}^+ and \mathcal{P}_{rE}^- , can be obtained by splitting \mathcal{P}_r into the positive and negative parts using the conditional probability function. The contours of both \mathcal{P}_{rE}^+ and \mathcal{P}_{rE}^- also show the pear-shape pattern independently and a strong tendency to follow the right Vieillefosse line. In the $Q_{S\Delta}-R_{S\Delta}$ phase plane, a similar tendency is observed and the contours corresponding to larger values of \mathcal{P}_{rE} , \mathcal{P}_{rE}^+ and \mathcal{P}_{rE}^- cling to the right Vieillefosse line, which indicates that the possess of SGS TKE production is preferentially associated with the axisymmetric expansion flow configuration in the core region of the channel.

9.2 Comments on Future Studies

In this study, the proposed new SGS stress models were tested using turbulent Couette flow for a limited number of Reynolds numbers. Although good results have been obtained in the numerical simulations, it is understood that a thorough examination of these SGS modelling approaches should be based on a variety of flows with and without a homogeneous plane. Other canonical test flows such as the lid-driven cavity flow, Poiseuille channel flow, and flow passing over a cylinder can be considered in future studies. Also this dissertation only considers the fluid dynamics characteristics of the SGS models; it would also be of interest to examine their performance in turbulent flows involving scalar transport processes such as heat transfer and concen-

tration dispersion. The numerical results presented are based on a sequential code as described in chapter 2, and all computations were carried out using a personal computer. In future studies, a parallel code and high performance computation can be considered for applications in the areas such as boundary layer meteorology and environmental flows.

Based on the observation that the dynamic Smagorinsky type SGS model [19,20] has some drawbacks due to its overly simplified constitutive relation, an increasing body of research [44, 48, 50, 143, 148, 155, 160–162, 192] has proposed SGS modelling approaches based on nonlinear constitutive relations. The nonlinear feature of the SGS constitutive relations becomes very important from the modern viewpoint of turbulence geometrical statistics and topology, since the linear Smagorinsky relation fails to capture some advanced turbulence features such as the relative geometrical orientation between the tensorial eigenframes as demonstrated in chapter 6. Further research on nonlinear constitutive relations is anticipated to be introduced into LES in the future. It is suggested by this thesis and some recent work [70] that in the future the CFD community should consider an improved criterion for turbulence (SGS) models, i.e. being able to predict both conventional scaling characteristics such as the log law, and also the geometrical and topological features of turbulent flow, such as the alignment between the vorticity and vortex stretching vectors and the pear-shape JPF contour in the $Q_{AA}-R_{AA}$ invariant phase plane. In addition to the numerical validation of the proposed DNM performed in chapters 6–8, further diagnose of this dynamic nonlinear SGS stress model may consider the approach of *a priori* process of DNS and experimental data.

Turbulence geometrical statistics and topology are two relatively new research areas with only a short history of about twenty and ten years, respectively. The *a posteriori* LES applications of turbulence geometrical statistics include the recent works of Saffman, Pullin, Misra, Voelkl and Chan [101–107], while the *a priori* LES applications of both turbulence geometrical statistics and turbulence topology are found in the recent works by Borue and Orszag [165], Tao *et al.* [29,99] and van der Bos *et al.* [70]. Some new interesting phenomenological results on turbulence geometrical

statistics and topology have been observed in this study. For example, the dragonfly-shape and wing-shape contours of the expectation of the resolved enstrophy generation are found in the tensorial invariant phase planes; it is observed that in the buffer zone, all the states of flow configurations ranging from axisymmetric compression to 2-D pattern and to axisymmetric expansion have a significant influence on the flow topology; and the preferred alignment pattern, i.e. $\Theta(\bar{\omega}, \mathbf{e}_{S\beta}) = 0^\circ$ and $\Theta(\bar{\omega}, \mathbf{e}_{S\gamma}) = 90^\circ$ is found to be not unique for (quasi-)isotropic turbulence, but instead, even more characteristic for the viscous sublayer. Whether these new properties observed in this research are generic and universal for turbulence still needs further support from other LES, DNS, and experimental examinations.

References

- [1] U. Piomelli, *Large-Eddy and Direct Simulation of Turbulent Flows, Lecture Notes for CFD2001*. Kitchener, Ontario, May 27-29 2001. The 9th Annual Conference of the CFD Society of Canada.
- [2] J. L. Lumley and A. M. Yaglom, “A century of turbulence,” *Flow, Turb. Combust.*, vol. 66, pp. 241–286, 2001.
- [3] A. S. Monin and A. M. Yaglom, *Statistical Fluid Mechanics: Mechanics of Turbulence*, vol. 1. Cambridge, MA: MIT, 1971.
- [4] O. Reynolds, “An experimental investigation of the circumstances which determine whether the motion of water shall be direct or sinuous, and of the law of resistance in parallel channels,” *Philos. Trans. R. Soc. Lond. A*, vol. 174, pp. 935–982, 1883.
- [5] O. Reynolds, “On the dynamical theory of incompressible viscous fluids and the determination of the criterion,” *Philos. Trans. R. Soc. Lond. A*, vol. 186, pp. 123–164, 1895.
- [6] J. W. S. Rayleigh, “On the stability or instability of certain fluid motions—I (1880),” in *Scientific Papers*, vol. I, pp. 474–487, Cambridge Univ., 1899.
- [7] J. W. S. Rayleigh, “On the stability or instability of certain fluid motions—II (1887),” in *Scientific Papers*, vol. III, pp. 17–23, Cambridge Univ., 1902.

- [8] J. W. S. Rayleigh, “On the stability or instability of certain fluid motions—III (1895),” in *Scientific Papers*, vol. IV, pp. 203–209, Cambridge Univ., 1903.
- [9] J. W. S. Rayleigh, “Vortices in oscillating liquid (1908),” in *Scientific Papers*, vol. V, pp. 465–477, Cambridge Univ., 1912.
- [10] P. Sagaut, *Large Eddy Simulation for Incompressible Flows: An Introduction*. Berlin: Springer, 2nd ed., 2002.
- [11] S. A. Orszag and G. S. Patterson, “Numerical simulation of three-dimensional homogeneous isotropic turbulence,” *Phys. Rev. Lett.*, vol. 28, pp. 76–79, 1972.
- [12] J. Smagorinsky and S. Manabe, “Numerical model for study of global general circulation,” *Bull. Amer. Meteorol. Soc.*, vol. 43, pp. 673–673, 1962.
- [13] J. Smagorinsky, “General circulation experiments with the primitive equations, I. the basic experiment,” *Month. Weath. Rev.*, vol. 91, pp. 99–165, 1963.
- [14] J. W. Deardorff, “A numerical study of three-dimensional turbulent channel flow at large Reynolds numbers,” *J. Fluid Mech.*, vol. 41, pp. 453–480, 1970.
- [15] U. Schumann, “New subgrid scale motion model for numerical simulation of turbulent flows,” *Bull. Amer. Phys. Soc.*, vol. 18, pp. 1469–1469, 1973.
- [16] U. Schumann, “Subgrid scale model for finite difference simulations of turbulent flows in plane channels and annuli,” *J. Comp. Phys.*, vol. 18, pp. 376–404, 1975.
- [17] P. Moin, “Advances in large eddy simulation methodology for complex flows,” *Int. J. Heat Fluid Flow*, vol. 23, pp. 710–720, 2002.
- [18] J. Bardina, *Improved Turbulence Models Based on Large Eddy Simulation of Homogeneous, Incompressible, Turbulent Flows*. PhD thesis, Stanford Univ., 1983.

- [19] M. Germano, U. Piomelli, P. Moin, and W. H. Cabot, “A dynamic subgrid-scale eddy viscosity model,” *Phys. Fluids A*, vol. 3, pp. 1760–1765, 1991.
- [20] D. K. Lilly, “A proposed modification of the Germano subgrid-scale closure method,” *Phys. Fluids A*, vol. 4, pp. 633–635, 1992.
- [21] R. H. Kraichnan, “Eddy viscosity in two and three dimensions,” *J. Astronau. Sci.*, vol. 33, pp. 1521–1536, 1976.
- [22] O. Métais and M. Lesieur, “Spectral large-eddy simulations of isotropic and stably stratified turbulence,” *J. Fluid Mech.*, vol. 239, pp. 157–194, 1992.
- [23] R. A. Clark, J. H. Ferziger, and W. C. Reynolds, “Evaluation of subgrid-scale models using an accurately simulated turbulent flow,” *J. Fluid Mech.*, vol. 91, pp. 1–16, 1979.
- [24] O. J. McMillan and J. H. Ferziger, “Direct testing of subgrid-scale models,” *AIAA J.*, vol. 17, pp. 1340–1346, 1979.
- [25] S. Liu, C. Meneveau, and J. Katz, “On the properties of similarity subgrid-scale models as deduced from measurements in a turbulent jet,” *J. Fluid Mech.*, vol. 275, pp. 83–119, 1994.
- [26] S. Liu, J. Katz, and C. Meneveau, “Evolution and modelling of subgrid scales during rapid straining of turbulence,” *J. Fluid Mech.*, vol. 387, pp. 281–320, 1999.
- [27] R. J. Adrian, “Stochastic estimation of sub-grid scale motions,” *Appl. Mech. Rev.*, vol. 43, pp. S214–S218, 1990.

- [28] R. J. Adrian, C. Meneveau, R. D. Moser, and J. J. Riley, “Final report on ‘turbulence measurements for LES’ workshop,” tech. rep., Univ. of Illinois, Urbana-Champaign, 2000.
- [29] B. Tao, J. Katz, and C. Meneveau, “Statistical geometry of subgrid-scale stresses determined from holographic particle image velocimetry measurements,” *J. Fluid Mech.*, vol. 457, pp. 35–78, 2002.
- [30] M. Lesieur and O. Métais, “New trends in large-eddy simulations of turbulence,” *Ann. Rev. Fluid Mech.*, vol. 28, pp. 45–82, 1996.
- [31] C. Meneveau and J. Katz, “Scale-invariance and turbulence models for large-eddy simulation,” *Ann. Rev. Fluid Mech.*, vol. 32, pp. 1–32, 2000.
- [32] S. B. Pope, *Turbulent Flows*. Cambridge, UK: Cambridge Univ., 2000.
- [33] M. Germano, “A proposal for a redefinition of the turbulent stresses in the filtered Navier-Stokes equations,” *Phys. Fluids*, vol. 29, pp. 2323–2324, 1986.
- [34] J. Bardina, J. H. Ferziger, and W. C. Reynolds, “Improved subgrid-scale models for large-eddy simulation,” in *Proc. AIAA 13th Fluid & Plasma Dynamics Conference*, (Snowmass, Colorado), 1980. AIAA Paper 80-1357.
- [35] P. Sagaut and R. Grohens, “Discrete filters for large eddy simulation,” *Int. J. Numer. Meth. Fluids*, vol. 31, pp. 1195–1220, 1999.
- [36] P. Moin, K. Squires, W. Cabot, and S. Lee, “A dynamic subgrid-scale model for compressible turbulence and scalar transport,” *Phys. Fluids A*, vol. 3, pp. 2746–2757, 1991.
- [37] Y. Zang, R. L. Street, and J. R. Koseff, “A dynamic mixed subgrid-scale

- model and its application to turbulent recirculating flows,” *Phys. Fluids*, vol. 5, pp. 3186–3196, 1993.
- [38] U. Piomelli, “High Reynolds number calculations using the dynamic subgrid-scale stress model,” *Phys. Fluids A*, vol. 5, pp. 1484–1490, 1993.
- [39] J. T. Oden, *Applied Functional Analysis: A First Course for Students of Mechanics and Engineering Science*. Englewood Cliffs, NJ: Prentice-Hall, 1979.
- [40] S. Ghosal, T. S. Lund, P. Moin, and K. Akselvoll, “A dynamic localization model for large-eddy simulation of turbulent flows,” *J. Fluid Mech.*, vol. 286, pp. 229–255, 1995.
- [41] J. G. M. Kuerten, B. J. Geurts, A. W. Vreman, and M. Germano, “Dynamic inverse modelling and its testing in large-eddy simulations of the mixing layer,” *Phys. Fluids*, vol. 11, pp. 3778–3785, 1999.
- [42] Y. Morinishi and O. V. Vasilyev, “Vector level identity for dynamic subgrid scale modelling in large eddy simulation,” *Phys. Fluids*, vol. 14, pp. 3616–3623, 2002.
- [43] C. Ronchi, M. Ypma, and V. M. Canuto, “On the application of the Germano identity to subgrid-scale modeling,” *Phys. Fluids A*, vol. 4, pp. 2927–2929, 1992.
- [44] C. Meneveau and J. Katz, “Dynamic testing of subgrid models in large eddy simulation based on the Germano identity,” *Phys. Fluids*, vol. 11, pp. 245–247, 1999.
- [45] C. Brun and R. Friedrich, “Modelling of the test SGS tensor T_{ij} : an issue in the dynamic approach,” *Phys. Fluids*, vol. 13, pp. 2373–2385, 2001.

- [46] J. Kondo, *Integral Equations*. Oxford Applied Mathematics and Computing Science Series, Tokyo: Oxford Univ., 1991.
- [47] M. A. Golberg, “A survey of numerical methods for integral equations,” in *Solution Methods for Integral Equations: Theory and Applications* (M. A. Golberg, ed.), New York: Plenum, 1979.
- [48] M. V. Salvetti and S. Banerjee, “*A priori* Tests of a new dynamic subgrid-scale model for finite-difference large-eddy simulations,” *Phys. Fluids*, vol. 7, pp. 2831–2847, 1995.
- [49] U. Piomelli and J. Liu, “Large-eddy simulation of rotating channel flows using a localized dynamic model,” *Phys. Fluids*, vol. 7, pp. 839–848, 1995.
- [50] Y. Morinishi and O. V. Vasilyev, “A recommended modification to the dynamic two-parameter mixed subgrid scale model for large eddy simulation of wall bounded turbulent flow,” *Phys. Fluids*, vol. 13, pp. 3400–3410, 2001.
- [51] E. D. Siggia, “Numerical study of small-scale intermittency in three-dimensional turbulence,” *J. Fluid Mech.*, vol. 107, pp. 375–406, 1981.
- [52] P. Vieillefosse, “Internal motion of a small element of fluid in an inviscid flow,” *Physica A*, vol. 125, pp. 150–162, 1984.
- [53] R. B. Pelz, V. Yakhot, and S. A. Orszag, “Velocity-vorticity patterns in turbulent flows,” *Phys. Rev. Lett.*, vol. 54, pp. 2505–2508, 1985.
- [54] R. M. Kerr, “Higher-order derivative correlations and the alignment of small-scale structures in isotropic numerical turbulence,” *J. Fluid Mech.*, vol. 153, pp. 31–58, 1985.

- [55] W. T. Ashurst, A. R. Kerstein, R. M. Kerr, and C. H. Gibson, “Alignment of vorticity and scalar gradient with strain rate in simulated Navier-Stokes turbulence,” *Phys. Fluids*, vol. 30, pp. 2343–2353, 1987.
- [56] A. E. Perry and M. S. Chong, “A description of eddying motions and flow patterns using critical-point concepts,” *Ann. Rev. Fluid Mech.*, vol. 19, pp. 125–155, 1987.
- [57] J. H. Chen *et al.*, “A study of the topology of dissipating motions in direct numerical simulations of time-developing compressible and incompressible mixing layers,” in *Proc. CTR Summer Program*, pp. 139–164, Stanford Univ., 1990.
- [58] M. S. Chong, A. E. Perry, and B. J. Cantwell, “A general classification of three-dimensional flow fields,” *Phys. Fluids A*, vol. 2, pp. 765–777, 1990.
- [59] T. S. Lund and M. M. Rogers, “An improved measure of strain state probability in turbulent flows,” *Phys. Fluids*, vol. 6, pp. 1838–1847, 1994.
- [60] R. B. Pelz, L. Shtilman, and A. Tsinober, “The helical nature of unforced turbulent flows,” *Phys. Fluids*, vol. 29, pp. 3506–3508, 1986.
- [61] M. M. Rogers and P. Moin, “Helicity fluctuations in incompressible turbulent flows,” *Phys. Fluids*, vol. 30, pp. 2662–2671, 1987.
- [62] R. M. Kerr, “Histograms of helicity and strain in numerical turbulence,” *Phys. Rev. Lett.*, vol. 59, pp. 783–786, 1987.
- [63] B. J. Cantwell, “Exact solution of a restricted Euler equation for the velocity gradient tensor,” *Phys. Fluids A*, vol. 4, pp. 782–793, 1992.
- [64] J. Soria, R. Sondergaard, B. J. Cantwell, M. S. Chong, and A. E. Perry, “A

- study of the fine-scale motions of incompressible time-developing mixing layers,” *Phys. Fluids*, vol. 6, pp. 871–884, 1994.
- [65] J. Martín, C. Dopazo, and L. Valiño, “Dynamics of the velocity gradient invariants in turbulence: Restricted Euler and linear diffusion models,” *Phys. Fluids*, vol. 10, pp. 2012–2025, 1998.
- [66] J. Martín, A. Ooi, M. S. Chong, and J. Soria, “Dynamics of the velocity gradient tensor invariants in isotropic turbulence,” *Phys. Fluids*, vol. 10, pp. 2336–2346, 1998.
- [67] M. S. Chong, J. Soria, A. E. Perry, J. Chacin, B. J. Cantwell, and Y. Na, “Turbulence structures of wall-bounded shear flows found using DNS data,” *J. Fluid Mech.*, vol. 357, pp. 225–247, 1998.
- [68] A. Ooi, J. Martin, J. Soria, and M. S. Chong, “A study of the evolution and characteristics of the invariants of the velocity-gradient tensor in isotropic turbulence,” *J. Fluid Mech.*, vol. 381, pp. 141–174, 1999.
- [69] J. M. Chacin and B. J. Cantwell, “Dynamics of a low Reynolds number turbulent boundary layer,” *J. Fluid Mech.*, vol. 404, pp. 87–115, 2000.
- [70] F. van der Bos, B. Tao, C. Meneveau, and J. Katz, “Effects of small-scale turbulent motions on the filtered velocity gradient tensor as deduced from holographic particle image velocimetry measurements,” *Phys. Fluids*, vol. 14, pp. 2456–2474, 2002.
- [71] K. K. Nomura and G. K. Post, “The structure and dynamics of vorticity and rate of strain in incompressible homogeneous turbulence,” *J. Fluid Mech.*, vol. 377, pp. 65–97, 1998.

- [72] K. K. Nomura and P. J. Diamessis, “The interaction of vorticity and rate-of-strain in homogeneous sheared turbulence,” *Phys. Fluids*, vol. 12, pp. 846–864, 2000.
- [73] H. M. Blackburn, N. N. Mansour, and B. J. Cantwell, “Topology of fine-scale motions in turbulent channel flow,” *J. Fluid Mech.*, vol. 310, pp. 269–292, 1996.
- [74] P. J. Diamessis and K. K. Nomura, “Interaction of vorticity, rate-of-strain, and scalar gradient in stratified homogeneous sheared turbulence,” *Phys. Fluids*, vol. 12, pp. 1166–1188, 2000.
- [75] M. E. Brachet, M. Meneguzzi, A. Vincent, H. Politano, and P. L. Sulem, “Numerical evidence of smooth self-similar dynamics and possibility of subsequent collapse for three-dimensional ideal flows,” *Phys. Fluids A*, vol. 4, pp. 2845–2854, 1992.
- [76] A. Tsinober, E. Kit, and T. Dracos, “Experimental investigation of the field of velocity gradients in turbulent flows,” *J. Fluid Mech.*, vol. 242, pp. 169–192, 1992.
- [77] A. Tsinober, L. Shtilman, and H. Vaisburd, “A study of properties of vortex stretching and enstrophy generation in numerical and laboratory turbulence,” *Fluid Dyn. Res.*, vol. 21, pp. 477–494, 1997.
- [78] A. Tsinober, “Is concentrated vorticity that important?,” *Eur. J. Mech. B/Fluids*, vol. 17, pp. 421–449, 1998.
- [79] B. Protas, A. Babiano, and N. K.-R. Kevlahan, “On geometrical alignment properties of two-dimensional forced turbulence,” *Physica D*, vol. 128, pp. 169–179, 1999.

- [80] J. Jiménez, “Kinematic alignment effects in turbulent flows,” *Phys. Fluids A*, vol. 4, pp. 652–654, 1992.
- [81] A. Tsinober, M. Ortenberg, and L. Shtilman, “On depression of nonlinearity in turbulence,” *Phys. Fluids*, vol. 11, pp. 2291–2297, 1999.
- [82] A. Tsinober, “Vortex stretching versus production of strain/dissipation,” in *Turbulence Structure and Vortex Dynamics* (J. C. R. Hunt and J. C. Vassilicos, eds.), pp. 165–191, Cambridge, UK: Cambridge Univ., 2000.
- [83] J. D. Gibbon, B. Galanti, and R. M. Kerr, “Stretching and compression of vorticity in the 3D Euler equations,” in *Turbulence Structure and Vortex Dynamics* (J. C. R. Hunt and J. C. Vassilicos, eds.), pp. 23–34, Cambridge, UK: Cambridge Univ., 2000.
- [84] B. Andreotti, “Studying Burgers’ models to investigate the physical meaning of the alignments statistically observed in turbulence,” *Phys. Fluids*, vol. 9, pp. 735–742, 1997.
- [85] A. Vincent and M. Meneguzzi, “The dynamics of vorticity tubes in homogeneous turbulence,” *J. Fluid Mech.*, vol. 258, pp. 245–254, 1994.
- [86] K. Ohkitani, “Eigenvalue problems in three-dimensional Euler flows,” *Phys. Fluids A*, vol. 5, pp. 2570–2572, 1993.
- [87] K. Ohkitani and S. Kishiba, “Nonlocal nature of vortex stretching in an inviscid fluid,” *Phys. Fluids*, vol. 7, pp. 411–421, 1995.
- [88] K. Horiuti, “A classification method for vortex sheet and tube structures in turbulent flows,” *Phys. Fluids*, vol. 13, pp. 3756–3774, 2001.

- [89] L. Shtilman, M. Spector, and A. Tsinober, “On some kinematic versus dynamic properties of homogeneous turbulence,” *J. Fluid Mech.*, vol. 247, pp. 65–77, 1993.
- [90] Z.-S. She, E. Jackson, and S. A. Orszag, “Structure and dynamics of homogeneous turbulence: Models and simulations,” *Proc. R. Soc. Lond. A*, vol. 434, pp. 101–124, 1991.
- [91] B. Galanti and A. Tsinober, “Self-amplification of the field of velocity derivatives in quasi-isotropic turbulence,” *Phys. Fluids*, vol. 12, pp. 3097–3099, 2000.
- [92] J. Jiménez, A. A. Wary, P. G. Saffman, and R. S. Rogallo, “The structure of intense vorticity in isotropic turbulence,” *J. Fluid Mech.*, vol. 255, pp. 65–90, 1993.
- [93] G. R. Ruetsch and M. R. Maxey, “Small-scale features of vorticity and passive scalar fields in homogeneous isotropic turbulence,” *Phys. Fluids A*, vol. 3, pp. 1587–1597, 1991.
- [94] G. R. Ruetsch and M. R. Maxey, “The evolution of small-scale structures in homogeneous isotropic turbulence,” *Phys. Fluids A*, vol. 4, pp. 2747–2760, 1992.
- [95] Z.-S. She, E. Jackson, and S. A. Orszag, “Intermittent vortex structures in homogeneous isotropic turbulence,” *Nature*, vol. 344, pp. 226–228, 1990.
- [96] J. Jeong and F. Hussain, “On the identification of a vortex,” *J. Fluid Mech.*, vol. 285, pp. 69–94, 1995.
- [97] J. Zhou, R. J. Adrian, S. Balachandar, and T. M. Kendall, “Mechanisms for generating coherent packets of hairpin vortices in channel flow,” *J. Fluid Mech.*, vol. 387, pp. 353–396, 1999.

- [98] M. Lesieur, P. Comte, and O. Métais, “LES and vortex topology in shear and rotating flows,” in *Turbulence Structure and Vortex Dynamics* (J. C. R. Hunt and J. C. Vassilicos, eds.), pp. 269–288, Cambridge, UK: Cambridge Univ., 2000.
- [99] B. Tao, J. Katz, and C. Meneveau, “Geometry and scale relationships in high Reynolds number turbulence determined from three-dimensional holographic velocimetry,” *Phys. Fluids*, vol. 12, pp. 941–944, 2000.
- [100] K. Horiuti, “Alignment of eigenvectors for strain rate and subgrid-scale stress tensors,” in *Direct and Large-Eddy Simulation-IV* (B. J. Geurts *et al.*, eds.), pp. 67–72, Kluwer Academic, 2001.
- [101] P. G. Saffman and D. I. Pullin, “Anisotropy of the Lundgren-Townsend model of fine-scale turbulence,” *Phys. Fluids*, vol. 6, pp. 802–807, 1994.
- [102] P. G. Saffman and D. I. Pullin, “Calculation of velocity structure functions for vortex models of isotropic turbulence,” *Phys. Fluids*, vol. 8, pp. 3072–3084, 1996.
- [103] D. I. Pullin and P. G. Saffman, “On the Lundgren-Townsend model for turbulent fine scales,” *Phys. Fluids A*, vol. 5, pp. 126–145, 1993.
- [104] D. I. Pullin and P. G. Saffman, “Reynolds stresses and one-dimensional spectra for a vortex model of homogeneous anisotropic turbulence,” *Phys. Fluids*, vol. 6, pp. 1787–1796, 1994.
- [105] D. I. Pullin, “A vortex-based model for the subgrid flux of a passive scalar,” *Phys. Fluids*, vol. 12, pp. 2311–2319, 2000.

- [106] A. Misra and D. I. Pullin, “A vortex-based subgrid stress model for large-eddy simulation,” *Phys. Fluids*, vol. 9, pp. 2443–2454, 1997.
- [107] T. Voelkl, D. I. Pullin, and D. C. Chan, “A physical-space version of the stretched-vortex subgrid-stress model for large-eddy simulation,” *Phys. Fluids*, vol. 12, pp. 1810–1825, 2000.
- [108] C. G. Speziale, “On nonlinear $k-l$ and $k-\epsilon$ models of turbulence,” *J. Fluid Mech.*, vol. 178, pp. 459–475, 1987.
- [109] T. B. Gatski and C. G. Speziale, “On explicit algebraic stress models for complex turbulent flows,” *J. Fluid Mech.*, vol. 254, pp. 59–78, 1993.
- [110] J. H. Ferziger and P. M., *Computational Methods for Fluid Dynamics*. Berlin: Springer, 2nd ed., 1999.
- [111] A. J. Chorin, “Numerical solution of the Navier-Stokes equations,” *Math. Comp.*, vol. 22, pp. 745–762, 1968.
- [112] J. Kim and P. Moin, “Application of a fractional-step method to incompressible Navier-Stokes equations,” *J. Comp. Phys.*, vol. 59, pp. 308–323, 1985.
- [113] X. Huang, *Volume Average Technique for Turbulent Flow Simulation and Its Application to Room Airflow Prediction*. PhD thesis, Univ. of Saskatchewan, 1998.
- [114] B.-C. Wang and D. J. Bergstrom, “Application of multigrid schemes to 3-D Poisson equation,” in *Proc. 9th Annual Conference of the CFD Society of Canada, CFD2001* (G. E. Schneider, ed.), pp. 149–154, 2001.
- [115] S. V. Patankar, C. H. Liu, and E. M. Sparrow, “Fully developed flows and heat

- transfer in ducts having streamwise-periodic variations of cross-sectional area,” *ASME J. Heat Trans.*, vol. 99, pp. 180–186, 1977.
- [116] F. M. Najjar and D. K. Tafti, “Study of discrete test filters and finite difference approximations for the dynamic subgrid-scale stress model,” *Phys. Fluids*, vol. 8, pp. 1076–1088, 1996.
- [117] T. S. Lund, “On the use of discrete filters for large eddy simulation,” *Annu. Res. Briefs*, pp. 83–95, 1997. Center for Turbulence Research, Stanford Univ.
- [118] J. M. Robertson and H. F. Johnson, “Turbulence structure in plane Couette flow,” *ASCE J. Engng. Mech.*, vol. 96, pp. 1171–1182, 1970.
- [119] H. J. Leutheusser and V. H. Chu, “Experiments on plane Couette flow,” *ASCE J. Hydraul.*, vol. 97, pp. 1269–1284, 1971.
- [120] M. Aydin and H. J. Leutheusser, “Novel experimental facility for the study of plane Couette flow,” *Rev. Sci. Instrum.*, vol. 50, pp. 1362–1366, 1979.
- [121] E. M. Aydin and H. J. Leutheusser, “Plane-Couette flow between smooth and rough walls,” *Exper. Fluids*, vol. 11, pp. 302–312, 1991.
- [122] N. Tillmark and P. H. Alfredsson, “Experiments on transition in plane Couette flow,” *J. Fluid Mech.*, vol. 235, pp. 89–102, 1992.
- [123] N. Tillmark and P. H. Alfredsson, “Turbulence in plane Couette flow,” *Appl. Sci. Res.*, vol. 51, pp. 237–241, 1993.
- [124] K. Bech, N. Tillmark, P. H. Alfredsson, and H. I. Andersson, “An investigation of turbulent plane Couette flow at low Reynolds numbers,” *J. Fluid Mech.*, vol. 286, pp. 291–325, 1995.

- [125] A. Lundbladh and A. V. Johansson, “Direct simulation of turbulent spots in plane Couette flow,” *J. Fluid Mech.*, vol. 229, pp. 499–516, 1991.
- [126] J. M. Hamilton, J. Kim, and F. Waleffe, “Regeneration mechanisms of near-wall turbulence structures,” *J. Fluid Mech.*, vol. 287, pp. 317–348, 1995.
- [127] J. Komminaho, A. Lundbladh, and A. V. Johansson, “Very large structures in plane Couette flow,” *J. Fluid Mech.*, vol. 320, pp. 259–285, 1996.
- [128] D. V. Papavassiliou and T. J. Hanratty, “Interpretation of large-scale structures observed in a turbulent plane Couette flow,” *Int. J. Heat Fluid Flow*, vol. 18, pp. 55–69, 1997.
- [129] G. Kawahara and S. Kinda, “Periodic motion embedded in plane Couette turbulence: Regeneration cycle and burst,” *J. Fluid Mech.*, vol. 449, pp. 291–300, 2001.
- [130] J. Komminaho and M. Skote, “Reynolds stress budgets in Couette and boundary layer flows,” *Flow, Turb. Combust.*, vol. 68, pp. 167–192, 2002.
- [131] W.-W. Kim and S. Menon, “Application of the localized dynamic subgrid-scale model to turbulent wall-bounded flows,” in *Proc. 35th Aerospace Sciences Meeting & Exhibit*, (Reno, Nevada), pp. 1–12, 1997. AIAA Paper 97-0210.
- [132] W.-W. Kim and S. Menon, “An unsteady incompressible Navier-Stokes solver for large eddy simulation of turbulent flows,” *Int. J. Numer. Meth. Fluids*, vol. 31, pp. 983–1017, 1999.
- [133] V. C. Patel and M. R. Head, “Some observations on skin friction and velocity profiles in fully developed pipe and channel flows,” *J. Fluid Mech.*, vol. 38, pp. 181–201, 1969.

- [134] H. Eckelmann, “The structure of the viscous sublayer and the adjacent wall region in a turbulent channel flow,” *J. Fluid Mech.*, vol. 65, pp. 439–459, 1974.
- [135] J. Kim, P. Moin, and R. Moser, “Turbulence statistics in fully developed channel flow at low Reynolds number,” *J. Fluid Mech.*, vol. 177, pp. 133–166, 1987.
- [136] J. Jiménez and P. Moin, “The minimal flow unit in near-wall turbulence,” *J. Fluid Mech.*, vol. 225, pp. 213–240, 1991.
- [137] D. Carati, S. Ghosal, and P. Moin, “On the representation of backscatter in dynamic localization models,” *Phys. Fluids*, vol. 7, pp. 606–616, 1995.
- [138] A. G. Kravchenko, P. Moin, and R. Moser, “Zonal embedded grids for numerical simulations of wall-bounded turbulent flows,” *J. Comp. Phys.*, vol. 127, pp. 412–423, 1996.
- [139] V. M. Canuto and Y. Cheng, “Determination of the Smagorinsky-Lilly constant C_S ,” *Phys. Fluids*, vol. 9, pp. 1368–1378, 1997.
- [140] Th. von Kármán, “The analogy between fluid friction and heat transfer,” *Trans. ASME*, vol. 61, pp. 705–710, 1939.
- [141] P. Moin and J. Kim, “Numerical investigation of turbulence channel flow,” *J. Fluid Mech.*, vol. 118, pp. 341–377, 1982.
- [142] K. Horiuti, “A proper velocity scale for modelling subgrid-scale eddy viscosities in large eddy simulation,” *Phys. Fluids A*, vol. 5, pp. 146–157, 1993.
- [143] K. Horiuti, “A new dynamic two-parameter mixed model for large-eddy simulation,” *Phys. Fluids*, vol. 9, pp. 3443–3464, 1997.

- [144] V. C. Wong and D. K. Lilly, “A comparison of two dynamic subgrid closure methods for turbulent thermal convection,” *Phys. Fluids*, vol. 6, pp. 1016–1023, 1994.
- [145] A. Scotti and U. Piomelli, “Numerical simulation of pulsating turbulent channel flow,” *Phys. Fluids*, vol. 13, pp. 1367–1384, 2001.
- [146] F. Sarghini, U. Piomelli, and E. Balaras, “Scale-similar models for large-eddy simulations,” *Phys. Fluids*, vol. 11, pp. 1596–1607, 1999.
- [147] B. Vreman, B. Geurts, and H. Kuerten, “Large-eddy simulation of the turbulent mixing layer,” *J. Fluid Mech.*, vol. 339, pp. 357–390, 1997.
- [148] B. Vreman, B. Geurts, and H. Kuerten, “On the formulation of the dynamic mixed subgrid-scale model,” *Phys. Fluids*, vol. 6, pp. 4057–4059, 1994.
- [149] C. G. Speziale, “Galilean invariance of subgrid-scale stress models in the large-eddy simulation of turbulence,” *J. Fluid Mech.*, vol. 156, pp. 55–62, 1985.
- [150] K. Horiuti, “The role of the Bardina model in large eddy simulation of turbulent channel flow,” *Phys. Fluids A*, vol. 1, pp. 426–428, 1989.
- [151] Y. Dubief and F. Delcayre, “On coherent-vortex identification in turbulence,” *J. Turb.*, vol. 1, pp. 1–22, 2000.
- [152] P. Comte, J. H. Silvestrini, and P. Bégou, “Streamwise vortices in large-eddy simulations of mixing layers,” *Eur. J. Mech. B/Fluids*, vol. 17, pp. 615–637, 1998.
- [153] S. Menon, P.-K. Yeung, and W.-W. Kim, “Effect of subgrid models on the computed interscale energy transfer in isotropic turbulence,” *Comput. Fluids*, vol. 25, pp. 165–180, 1996.

- [154] J. Pallares and L. Davidson, “Large-eddy simulations of turbulent flow in a rotating square duct,” *Phys. Fluids*, vol. 12, pp. 2878–2894, 2000.
- [155] B.-C. Wang and D. J. Bergstrom, “An integral type dynamic localization two-parameter subgrid-scale model: Formulation and simulation,” *Int. J. CFD*, vol. 18, pp. 209–220, 2004.
- [156] R. P. Kanwal, *Generalized Functions: Theory and Technique*. Rensselaer, NY: Birkhäuser, 2nd ed., 1997.
- [157] A. J. M. Spencer, “Part III: Theory of invariants,” in *Continuum Physics, Volume I—Mathematics* (A. C. Eringen, ed.), New York: Academic, 1971.
- [158] J. L. Lumley, “Toward a turbulent constitutive relation,” *J. Fluid Mech.*, vol. 41, pp. 413–434, 1970.
- [159] S. B. Pope, “A more general effective-viscosity hypothesis,” *J. Fluid Mech.*, vol. 72, pp. 331–340, 1975.
- [160] T. S. Lund and E. A. Novikov, “Parameterization of subgrid-scale stress by the velocity gradient tensor,” *Annu. Res. Briefs*, pp. 27–43, 1992. Center for Turbulence Research, Stanford Univ.
- [161] V. C. Wong, “A proposed statistical-dynamic closure method for the linear and nonlinear subgrid-scale stresses,” *Phys. Fluids A*, vol. 4, pp. 1080–1082, 1992.
- [162] B. Kosović, “Subgrid-scale modelling for the large-eddy simulation of high-Reynolds-number boundary layers,” *J. Fluid Mech.*, vol. 336, pp. 151–182, 1997.
- [163] D. R. Smith, *Variational Methods in Optimization*. Englewood Cliffs, NJ: Prentice-Hall, 1974.

- [164] B.-C. Wang and D. J. Bergstrom, “An efficient solution scheme for applying the integral-type dynamic localization subgrid-scale model in turbulence with homogeneous directions,” *Numer. Heat Trans.: Part B*, vol. 45, pp. 201–220, 2004.
- [165] V. Borue and S. A. Orszag, “Local energy flux and subgrid-scale statistics in three-dimensional turbulence,” *J. Fluid Mech.*, vol. 366, pp. 1–31, 1998.
- [166] R. S. Rivlin, “The relation between the flow of non-Newtonian fluids and turbulent Newtonian fluids,” *Quart. Appl. Math.*, vol. 15, pp. 212–215, 1957.
- [167] D. B. Taulbee, “An improved algebraic Reynolds stress model and corresponding nonlinear stress model,” *Phys. Fluids A*, vol. 4, pp. 2555–2561, 1992.
- [168] A. Yoshizawa, “Statistical analysis of the deviation of the Reynolds stress from its eddy-viscosity representation,” *Phys. Fluids*, vol. 27, pp. 1377–1387, 1984.
- [169] K. Horiuti, “Higher-order terms in the anisotropic representation of Reynolds stresses,” *Phys. Fluids A*, vol. 2, pp. 1708–1710, 1990.
- [170] G. Mompean, “Numerical simulation of a turbulent flow near a right-angled corner using the Speziale non-linear model with RNG k - ε equations,” *Comput. Fluids*, vol. 27, pp. 847–859, 1998.
- [171] C. G. Speziale and X. H. Xu, “Towards the development of second-order closure models for nonequilibrium turbulent flows,” *Int. J. Heat Fluid Flow*, vol. 17, pp. 238–244, 1996.
- [172] R. Rubinstein and J. M. Barton, “Nonlinear Reynolds stress models and the renormalization group,” *Phys. Fluids A*, vol. 2, pp. 1472–1476, 1990.

- [173] T. J. Craft, B. E. Launder, and K. Suga, “Development and application of a cubic eddy-viscosity model of turbulence,” *Int. J. Heat Fluid Flow*, vol. 17, pp. 108–115, 1996.
- [174] K. M. Wall and D. B. Taulbee, “Application of a nonlinear stress-strain model to axisymmetric turbulent swirling flows,” *Int. J. Heat Fluid Flow*, vol. 17, pp. 116–123, 1996.
- [175] A. Leonard, “Energy cascade in large-eddy simulations of turbulent fluid flows,” *Adv. Geophys.*, vol. 18A, pp. 237–248, 1974.
- [176] C. Meneveau, T. S. Lund, and P. Moin, “Search for subgrid scale parameterization by projection pursuit regression,” in *Proc. CTR Summer Program*, pp. 61–81, Stanford Univ., 1992.
- [177] C. G. Speziale, “Second-order closure models for rotating turbulent flows,” *Quart. Appl. Math.*, vol. 45, pp. 721–733, 1987.
- [178] J. Angeles, *Rational Kinematics*, vol. 34 of *Springer Tracts in Natural Philosophy*. New York: Springer-Verlag, 1988.
- [179] A. Honkan and Y. Andreopoulos, “Vorticity, strain-rate and dissipation characteristics in the near-wall region of turbulent boundary layers,” *J. Fluid Mech.*, vol. 350, pp. 29–96, 1997.
- [180] P. C. Hughes, *Spacecraft Attitude Dynamics*. New York: Wiley, 1986.
- [181] G. I. Taylor, “Production and dissipation of vorticity in a turbulent fluid,” *Proc. R. Soc. Lond. A*, vol. 164, pp. 15–23, 1938.
- [182] A. A. Townsend, “On the fine-scale structure of turbulence,” *Proc. R. Soc. Lond. A*, vol. 208, pp. 534–542, 1951.

- [183] R. Betchov, “An inequality concerning the production of vorticity in isotropic turbulence,” *J. Fluid Mech.*, vol. 1, pp. 497–504, 1956.
- [184] E. D. Siggia, “Invariants for the one-point vorticity and strain rate correlations functions,” *Phys. Fluids*, vol. 24, pp. 1934–1936, 1981.
- [185] W. A. Rosenkrantz, *Introduction to Probability and Statistics for Scientists and Engineers*. New York, NY: McGraw-Hill, 1997.
- [186] B. J. Cantwell, “On the behavior of velocity gradient tensor invariants in direct numerical simulations of turbulence,” *Phys. Fluids A*, vol. 5, pp. 2008–2013, 1993.
- [187] M. Lesieur, *Turbulence in Fluids*. Dordrecht: Kluwer Academic, 2nd ed., 1990.
- [188] H. Tennekes and J. L. Lumley, *A First Course in Turbulence*. Cambridge, MA: MIT, 1972.
- [189] K. L. Nielsen and J. H. Vanlonkhuyzen, *Plane and Spherical Trigonometry*. New York: Barnes and Noble, 1954.
- [190] J. M. Chacin, B. J. Cantwell, and S. J. Kline, “Study of turbulent boundary layer structure using the invariants of the velocity gradient tensor,” *Exper. Thermal Fluid Sci.*, vol. 13, pp. 308–317, 1996.
- [191] M. Chertkov, A. Pumir, and B. I. Shraiman, “Lagrangian tetrad dynamics and the phenomenology of turbulence,” *Phys. Fluids*, vol. 11, pp. 2394–2410, 1999.
- [192] G. S. Winckelmans, A. A. Wray, O. V. Vasilyev, and H. Jeanmart, “Explicit-filtering large-eddy simulation using the tensor-diffusivity model supplemented by a dynamic Smagorinsky term,” *Phys. Fluids*, vol. 13, pp. 1385–1403, 2001.

- [193] B. R. Gelbaum, *Linear Algebra: Basics, Practice and Theory*. New York: North-Holland, 1989.
- [194] C. Cullen, *Matrices and Linear Transformations*. Reading, MA: Addison-Wesley, 1966.
- [195] G. E. Shilov, *Linear Algebra*. New York: Dover, 1977.
- [196] W. K. Nicholson, *Elementary Linear Algebra with Applications*. Boston: PWS-Kent, 2nd ed., 1990.
- [197] R. M. Murray, Z. Li, and S. S. Sastry, *A Mathematical Introduction to Robotic Manipulation*. Boca Raton: CRC, 1994.
- [198] R. H. Battin, *An Introduction to the Mathematics and Methods of Astrodynamics*. AIAA Education Series, New York: Springer, revised ed., 1999.

Appendix A

Formulations and Singularity Condition for the DNM

In this appendix, the modelling formulation for the DNM will be first developed using the least squares method, and then its local singularity condition will be investigated.

(1) The DNM Formulation

The mathematical procedure to obtain the DNM follows the least squares approach introduced by Lilly [20], which uses the assumption that $\widetilde{C_S\beta_{ij}} \approx C_S\tilde{\beta}_{ij}$. For the three-parameter DNM, this assumption needs to be extended to treat $\widetilde{C_W\gamma_{ij}}$ and $\widetilde{C_N\eta_{ij}}$ in a similar way. On substituting Eqs.(6.7) and (6.8) into the Germaino identity Eq.(1.17), the following relation is obtained as an approximation to the deviatoric part of the Leonard stress tensor:

$$\mathcal{L}_{ij}^* \approx \mathcal{L}_{ij}^{appr*} = -C_S\alpha_{ij} - C_W\lambda_{ij} - C_N\zeta_{ij} + \widetilde{C_S\beta_{ij}} + \widetilde{C_W\gamma_{ij}} + \widetilde{C_N\eta_{ij}} \quad (\text{A.1})$$

Using the assumptions above and the previously introduced expressions for the differential tensorial functions M_{ij} , W_{ij} and N_{ij} , the above equation can be simplified to

$$\begin{aligned} \mathcal{L}_{ij}^{appr*} &= -C_S(\alpha_{ij} - \tilde{\beta}_{ij}) - C_W(\lambda_{ij} - \tilde{\gamma}_{ij}) - C_N(\zeta_{ij} - \tilde{\eta}_{ij}) \\ &= -C_SM_{ij} - C_WW_{ij} - C_NN_{ij} \end{aligned} \quad (\text{A.2})$$

Thus, the local error tensor has the following specific form:

$$\begin{aligned}
E_{ij} &= \mathcal{L}_{ij}^* - \mathcal{L}_{ij}^{appr*} \\
&= \mathcal{L}_{ij}^* + C_S M_{ij} + C_W W_{ij} + C_N N_{ij} \\
&= \mathcal{L}_{ij}^* + C_m F_{ij}^m
\end{aligned} \tag{A.3}$$

where the index m runs from 1 to 3 (replacing subscripts S , W and N) to indicate the three nonlinear terms, and the tensor F_{ij}^m is used to represent M_{ij} , W_{ij} and N_{ij} . The local error density function defined by Eq.(1.21) becomes

$$Q = E_{ij} E_{ij} = C_m C_n F_{ij}^m F_{ij}^n + 2C_m F_{ij}^m \mathcal{L}_{ij}^* + \mathcal{L}_{ij}^* \mathcal{L}_{ij}^* \tag{A.4}$$

Define the *inner product of two tensors* as their tensorial contraction, i.e.

$$(F_{ij}^m, F_{ij}^n) = F_{ij}^m F_{ij}^n \tag{A.5}$$

It is well known from algebra that for an extremum value of Q determined by the least squares method, it is necessary for $\partial Q / \partial C_i$ to vanish ($i = 1, 2, 3$), which requires E_{ij} to be orthogonal to F_{ij}^n [193], i.e.

$$(E_{ij}, F_{ij}^n) = E_{ij} F_{ij}^n = 0 \tag{A.6}$$

for $n = 1, 2, 3$. By substituting Eq.(A.3) into the above equation, the following *normal equations* for the coefficients are obtained:

$$(F_{ij}^m, F_{ij}^n) C_m = -\mathcal{L}_{ij}^* F_{ij}^n \tag{A.7}$$

for $m, n = 1, 2, 3$. This is the modelling formulation for the DNM, which is necessary for Q to be minimal. It can be equivalently expressed using matrices as

$$\begin{bmatrix} M_{ij} M_{ij} & M_{ij} W_{ij} & M_{ij} N_{ij} \\ W_{ij} M_{ij} & W_{ij} W_{ij} & W_{ij} N_{ij} \\ N_{ij} M_{ij} & N_{ij} W_{ij} & N_{ij} N_{ij} \end{bmatrix} \cdot \begin{bmatrix} C_S \\ C_W \\ C_N \end{bmatrix} = - \begin{bmatrix} \mathcal{L}_{ij}^* M_{ij} \\ \mathcal{L}_{ij}^* W_{ij} \\ \mathcal{L}_{ij}^* N_{ij} \end{bmatrix} \tag{A.8}$$

or $\mathbf{AC} = \mathbf{B}$ for brevity.

(2) Singularity Condition

At this stage, one may naturally ask the question: is the system of the DNM, i.e. Eq.(A.7) or (A.8), singular? We have shown that the DNM is necessary for a locally minimum Q . Furthermore, since it is well understood that such a solution of the DNM can also be a maximum or inflection ‘point’ for Q , is the DNM also sufficient for Q to be minimal? Fortunately, both questions can be answered using the following proposition:

Proposition: The set of model coefficients as the solution to the DNM must exist and be unique iff the differential tensorial functions $M_{ij}(\mathbf{x})$, $W_{ij}(\mathbf{x})$ and $N_{ij}(\mathbf{x})$ are linearly independent, such that the local error density function $Q(\mathbf{x})$ is minimal.

Proof:

Consider the quadratic form $(F_{ij}^m, F_{ij}^n)C_m C_n$ for the DNM coefficients C_m for $m = 1, 2, 3$. We have

$$(F_{ij}^m, F_{ij}^n)C_m C_n = (C_m F_{ij}^m, C_n F_{ij}^n) = (C_m F_{ij}^m, C_m F_{ij}^m) \geq 0 \quad (\text{A.9})$$

which indicates that the quadratic form is positive semidefinite. It can be zero, iff $C_m F_{ij}^m = 0$ and its linear combination is nontrivial (i.e. the DNM coefficients C_m for $m = 1, 2, 3$ are not all zero). Actually, given that the tensorial functions are linearly independent,

$$C_m F_{ij}^m \neq 0 \quad (\text{A.10})$$

if the linear combination is nontrivial. As such, we obtain

$$(F_{ij}^m, F_{ij}^n)C_m C_n > 0 \quad (\text{A.11})$$

which further indicates that the quadratic form is positive definite, and thus

$$\det(\mathbf{A}) = \det([F_{ij}^m F_{ij}^n]) > 0 \quad (\text{A.12})$$

So far, we have proven that the DNM is locally non-singular with a unique solution set for the model coefficients at each time step, iff the three differential tensorial

functions are linearly independent. Now we continue to answer the second question by demonstrating that the DNM is also sufficient for Q to be minimum. Supposing the Leonard stress can also be approximated using a different set of coefficients D_m for $m = 1, 2, 3$, i.e.

$$\mathcal{L}_{ij}^* \approx \mathring{\mathcal{L}}_{ij}^{appr*} = -D_m F_{ij}^m \quad (\text{A.13})$$

the local error tensor then is expressed as

$$\mathring{E}_{ij} = \mathcal{L}_{ij}^* - \mathring{\mathcal{L}}_{ij}^{appr*} = \mathcal{L}_{ij}^* + D_m F_{ij}^m \quad (\text{A.14})$$

and the local error density function is

$$\begin{aligned} \mathring{Q} &= \mathring{E}_{ij} \mathring{E}_{ij} \\ &= (\mathcal{L}_{ij}^* - \mathring{\mathcal{L}}_{ij}^{appr*}, \mathcal{L}_{ij}^* - \mathring{\mathcal{L}}_{ij}^{appr*}) \\ &= (\mathcal{L}_{ij}^* - \mathcal{L}_{ij}^{appr*} + \mathcal{L}_{ij}^{appr*} - \mathring{\mathcal{L}}_{ij}^{appr*}, \mathcal{L}_{ij}^* - \mathcal{L}_{ij}^{appr*} + \mathcal{L}_{ij}^{appr*} - \mathring{\mathcal{L}}_{ij}^{appr*}) \\ &= (\mathcal{L}_{ij}^* - \mathcal{L}_{ij}^{appr*}, \mathcal{L}_{ij}^* - \mathcal{L}_{ij}^{appr*}) + 2(\mathcal{L}_{ij}^* - \mathcal{L}_{ij}^{appr*}, \mathcal{L}_{ij}^{appr*} - \mathring{\mathcal{L}}_{ij}^{appr*}) \\ &\quad + (\mathcal{L}_{ij}^{appr*} - \mathring{\mathcal{L}}_{ij}^{appr*}, \mathcal{L}_{ij}^{appr*} - \mathring{\mathcal{L}}_{ij}^{appr*}) \end{aligned} \quad (\text{A.15})$$

Considering that

$$\mathcal{L}_{ij}^{appr*} - \mathring{\mathcal{L}}_{ij}^{appr*} = (D_m - C_m) F_{ij}^m \quad (\text{A.16})$$

and from the orthogonal condition (Eq.(A.6)), we obtain

$$(\mathcal{L}_{ij}^* - \mathcal{L}_{ij}^{appr*}, \mathcal{L}_{ij}^{appr*} - \mathring{\mathcal{L}}_{ij}^{appr*}) = (D_m - C_m)(F_{ij}^m, E_{ij}) \equiv 0 \quad (\text{A.17})$$

Thus from Eq.(A.15), the following relation holds

$$\begin{aligned} \mathring{Q} &= (\mathcal{L}_{ij}^* - \mathcal{L}_{ij}^{appr*}, \mathcal{L}_{ij}^* - \mathcal{L}_{ij}^{appr*}) + (\mathcal{L}_{ij}^{appr*} - \mathring{\mathcal{L}}_{ij}^{appr*}, \mathcal{L}_{ij}^{appr*} - \mathring{\mathcal{L}}_{ij}^{appr*}) \\ &= Q + (\mathcal{L}_{ij}^{appr*} - \mathring{\mathcal{L}}_{ij}^{appr*}, \mathcal{L}_{ij}^{appr*} - \mathring{\mathcal{L}}_{ij}^{appr*}) \\ &\geq Q \end{aligned} \quad (\text{A.18})$$

As such, it has been shown that the DNM is not only necessary but also sufficient for Q to be minimum and the proof of the proposition is hereby completed.

Appendix B

Orthogonal and Rotation Matrices

B.1 Similar and Orthogonal Transformations

In the following section, we limit our discussion mainly to be within the *set of real numbers* \Re . We use the symbol $V_n(\Re)$ to represent the *n-dimensional vector space* associated with \Re and symbol \Re_n to represent the *set for all $n \times n$ matrices over \Re* . If only a second order tensor is involved, $n = 3$. The material presented are basically from textbooks [193–196].

Definition B.1: Two matrices \mathbf{A} and \mathbf{B} are *similar* if there exists a nonsingular matrix \mathbf{C} , such that $\mathbf{B} = \mathbf{C}^{-1}\mathbf{B}\mathbf{C}$.

Definition B.2: $\mathbf{A} \in \Re_n$ is called an *orthogonal matrix* if $\mathbf{A}^T \mathbf{A} = \mathbf{I}_d$, where \mathbf{I}_d is the identity matrix.

Definition B.3: Matrices \mathbf{A} and $\mathbf{B} \in \Re_n$ are *orthogonally similar* if there exists an orthogonal matrix \mathbf{R} such that $\mathbf{B} = \mathbf{R}^T \mathbf{A} \mathbf{R}$.

Property B.1: Every symmetric matrix is orthogonally similar to a diagonal matrix.

Property B.2: A matrix $\mathbf{T} \in \Re_n$ is similar to a diagonal matrix iff there exists a basis for $V_n(\Re)$ consisting of eigenvectors of \mathbf{T} .

Property B.3: A real symmetric matrix has only real eigenvalues.

Property B.4: For a real symmetric matrix, its eigenvectors, associated with distinct eigenvalues, are orthogonal to each other.

Property B.5: Similar matrices have the same eigenvalues, i.e. if $\mathbf{A} = \mathbf{C}^{-1}\mathbf{B}\mathbf{C}$,

$$\lambda_A = \lambda_B.$$

Property B.6: The trace of a matrix \mathbf{A} equals to the summation of its eigenvalues, i.e. $\text{tr}(\mathbf{A}) = \sum_{i=1}^n (\lambda_A)_i$.

From Property B.5 and B.6, it is straightforward [193] that similar matrices share the same trace.

Corollary B.1: The trace of a matrix is an invariant under similar transformation, i.e. if $\mathbf{A} = \mathbf{C}^{-1}\mathbf{B}\mathbf{C}$, then $\text{tr}(\mathbf{A}) = \text{tr}(\mathbf{B})$.

B.2 Rotation Matrix

Let $\mathcal{E} = [\mathbf{e}_1, \mathbf{e}_2, \mathbf{e}_3]$ and $\mathcal{E}' = [\mathbf{e}'_1, \mathbf{e}'_2, \mathbf{e}'_3]$ represent two orthonormal frame bases, such that a vector can be represented using either of the frames: $\mathbf{v} = x_i \mathbf{e}_i = x'_i \mathbf{e}'_i$, where x_i and x'_i are the corresponding coordinates. The *direction-cosine matrix* $\mathbf{R} \in \mathfrak{R}_3$ is formed by the bases \mathcal{E} and \mathcal{E}' by

$$R_{ij} = \mathbf{e}'_i \cdot \mathbf{e}_j \quad (\text{B.1})$$

which is the co-called *rotation matrix*, a typical orthonormal matrix linking the frame \mathcal{E} and \mathcal{E}' via orthogonal transformations. Therefore,

$$\mathbf{R}\mathbf{R}^T = \mathbf{I}_d, \quad \mathbf{R}^{-1} = \mathbf{R}^T, \quad \det(\mathbf{R}) = \pm 1 \quad (\text{B.2})$$

$$x'_i = R_{ij}x_j, \quad x_i = R_{ji}x'_j \quad (\text{B.3})$$

and

$$\mathbf{e}'_i = R_{ij}\mathbf{e}_j, \quad \mathbf{e}_i = R_{ji}\mathbf{e}'_j \quad (\text{B.4})$$

An orthonormal matrix corresponding to $\det(\mathbf{R}) = +1$ is called *proper*, otherwise, *improper*. An proper \mathbf{R} represents rotations, while an improper one involves reflections.

A rotation matrix \mathbf{R} can be used for representing the *frame attitude*, however, it has 6 extra redundant parameters. An second method, i.e. *Euler axis/angle*

representation is based the on the famous Euler Theorem [178,197],

The Theorem of Euler (1776): Any proper orientation $\mathbf{R} \in \mathfrak{R}_3$ is equivalent to a rotation about a fixed axis \mathbf{q} through an angle χ .

The fixed axis \mathbf{q} is not a free vector, and is known as the *Euler equivalent axis*. Euler's theorem can be understood from its eigensystem [180]: $\mathbf{R}\mathbf{e} = \lambda\mathbf{e}$. The characteristic equation for \mathbf{R} is [198]:

$$|\mathbf{R} - \lambda\mathbf{I}_d| = -\lambda^3 + \text{tr}(\mathbf{R})\lambda^2 - \text{tr}(\mathbf{R})\lambda + \mathbf{I}_d = 0 \quad (\text{B.5})$$

which results in three eigenvalues:

$$\lambda = +1, \quad e^{i\chi}, \quad e^{-i\chi} \quad (\text{B.6})$$

where $i = \sqrt{-1}$. The Euler equivalent axis \mathbf{q} corresponds to the eigenvector of the proper real eigenvalue $\lambda = +1$. However, χ the *angle of rotation* (or *Euler rotational angle* introduced here for clarity) is characterized by the *phase* of the other two eigenvalues. From Eq.(B.6), we obtain

$$\text{tr}(\mathbf{R}) = \lambda_1 + \lambda_2 + \lambda_3 = 1 + 2\cos\chi \quad (\text{B.7})$$

Thus, if the trace $\text{tr}(\mathbf{R}) \neq +3$ or -1 , the Euler rotational angle χ can be uniquely determined from it. Furthermore, it can be shown [180] that

$$\mathbf{q}^\times = \frac{1}{2\sin\chi}(\mathbf{R}^T - \mathbf{R}) \quad (\text{B.8})$$

The rotation matrix \mathbf{R} can be inversely calculated using the Euler axis/angle as

$$\mathbf{R} = \cos\chi\mathbf{I}_d + (1 - \cos\chi)\mathbf{q}\mathbf{q}^T - \sin\chi\mathbf{q}^\times \quad (\text{B.9})$$

The operation \mathbf{q}^\times used above is defined as

$$\mathbf{q}^\times = \begin{bmatrix} 0 & -q_3 & q_2 \\ q_3 & 0 & -q_1 \\ -q_2 & q_1 & 0 \end{bmatrix} \quad (\text{B.10})$$

Appendix C

Transport Equations for the Moments of the Strain Rate Tensor and Vorticity Vector

In this appendix, the transport equations for vorticity vector ω_i , enstrophy $\omega^2 = \omega_i \omega_i$, strain rate tensor S_{ij} , strain product $\mathcal{I}_{S2} = S_{ij} S_{ji}$, enstrophy generation $\sigma = \omega_i \omega_j S_{ij}$, and strain skewness $\mathcal{I}_{S3} = S_{ij} S_{jk} S_{ki}$ from Refs. [81, 82] are listed, which is helpful to understand the mechanism of these quantities in a both quantitative and qualitative manner.

$$D_t(\omega_i) = \omega_j S_{ij} + \nu \omega_{i, kk} \quad (\text{C.1})$$

$$\frac{1}{2} D_t(\omega_i \omega_i) = \omega_i \omega_j S_{ij} + \nu \omega_j \omega_{j, kk} \quad (\text{C.2})$$

$$D_t(S_{ij}) = -S_{ik} S_{kj} - \frac{1}{4}(\omega_i \omega_j - \omega_k \omega_k \delta_{ij}) - p_{,ij} + \nu S_{ij, kk} \quad (\text{C.3})$$

$$\frac{1}{2} D_t(2S_{ij} S_{ji}) = -2 \left(S_{ik} S_{kj} S_{ji} + \frac{1}{4} \omega_i \omega_j S_{ij} + S_{ij} p_{,ij} \right) + 2\nu S_{ij} S_{ij, kk} \quad (\text{C.4})$$

$$D_t(\omega_i \omega_j S_{ij}) = \omega_j S_{ij} \omega_k S_{ik} - \omega_i \omega_j p_{,ij} + \nu (2\omega_i S_{ij} \omega_{j, kk} + \omega_i \omega_j S_{ij, kk}) \quad (\text{C.5})$$

$$D_t(S_{ij} S_{jk} S_{ki}) = 3 \left[-S_{ik} S_{kj} S_{il} S_{lj} + \frac{1}{4} (S_{ij} S_{ij} \omega_k \omega_k - \omega_j S_{ij} \omega_k S_{ik}) - p_{,ij} + \nu S_{ik} S_{kj} S_{ij, kk} \right] \quad (\text{C.6})$$

where $D_t(\cdot) = (\dot{\cdot}) + u_j \cdot (\cdot)_{,j}$ is the material derivative.